

# **Growth and Excitation Dynamics of Epitaxial 2D Materials and Molecular Layers Studied by Electron and Momentum Microscopy**

Miriam Elisabeth Rath

Information

Band / Volume 123

ISBN 978-3-95806-892-6

Mitglied der Helmholtz-Gemeinschaft

 **JÜLICH**  
Forschungszentrum





Forschungszentrum Jülich GmbH  
Peter Grünberg Institut (PGI)  
Quantum Nanoscience (PGI-3)

# **Growth and Excitation Dynamics of Epitaxial 2D Materials and Molecular Layers Studied by Electron and Momentum Microscopy**

Miriam Elisabeth Raths

Schriften des Forschungszentrums Jülich  
Reihe Information / Information

Band / Volume 123

---

ISSN 1866-1777

ISBN 978-3-95806-892-6

Bibliografische Information der Deutschen Nationalbibliothek.  
Die Deutsche Nationalbibliothek verzeichnet diese Publikation in der  
Deutschen Nationalbibliografie; detaillierte Bibliografische Daten  
sind im Internet über <http://dnb.d-nb.de> abrufbar.

Herausgeber  
und Vertrieb:                   Forschungszentrum Jülich GmbH  
  Zentralbibliothek, Verlag  
  52425 Jülich  
  Tel.: +49 2461 61-5368  
  Fax: +49 2461 61-6103  
  zb-publikation@fz-juelich.de  
  www.fz-juelich.de/zb

Umschlaggestaltung:   Grafische Medien, Forschungszentrum Jülich GmbH

Druck:                               Grafische Medien, Forschungszentrum Jülich GmbH

Copyright:                       Forschungszentrum Jülich 2026

Schriften des Forschungszentrums Jülich  
Reihe Information / Information, Band / Volume 123

ISSN 1866-1777  
ISBN 978-3-95806-892-6

Vollständig frei verfügbar über das Publikationsportal des Forschungszentrums Jülich (JuSER)  
unter [www.fz-juelich.de/zb/openaccess](http://www.fz-juelich.de/zb/openaccess).



This is an Open Access publication distributed under the terms of the [Creative Commons Attribution License 4.0](https://creativecommons.org/licenses/by/4.0/),  
which permits unrestricted use, distribution, and reproduction in any medium, provided the original work is properly cited.

# License Notice

This dissertation is published under the license Creative Commons Attribution 4.0 International License (CC BY 4.0). Unless otherwise indicated, the contents of this work may be freely shared, adapted, and reused, provided appropriate credit is given.

The CC BY 4.0 license of this work does not extend to third-party materials, such as figures reproduced or adapted from published sources, which are included with permission from the original copyright holders. Any reuse of these materials requires permission from the respective rights holders and must comply with the original copyright terms.



# Abstract

The properties of modern nanomaterials are governed by their atomic structure, as well as by electronic interactions at their surfaces and internal interfaces. The present thesis is situated within this contemporary field of research and focuses on the synthesis and analysis of two model systems of functional surface structures. The first project is located in the field of twistrionics and studies the growth of unconventionally oriented graphene layers on silicon carbide (SiC). The second project focuses on probing the transiently occupied orbitals of surface-adsorbed organic molecules in time and space.

The first project aims for a better understanding of an already established growth process for the production of unconventionally oriented monolayer graphene on SiC, which offers a promising route to produce 30°-twisted bilayer graphene. The growth process involves two preparation steps, namely, the chemical vapor deposition of a BN layer and its replacement by graphene upon annealing at increasingly high temperatures. The mechanism that determines the orientation of the graphene layer is of particular interest, as well as the influence of the preparation parameters on the composition and quality of the BN layer, and therefore also the quality of the resulting graphene. These aspects were investigated by employing low-energy electron microscopy (LEEM), a powerful technique to probe the crystalline structure and domain configuration of surfaces, and to investigate growth processes *in situ* and in real time. It is demonstrated that the BN layer's composition and quality – and thus the quality of the resulting unconventionally oriented graphene – depend sensitively on the heating rate during BN synthesis.

In the second project, photoemission orbital tomography (POT) was combined with time-resolved photoelectron spectroscopy to image transiently occupied orbitals of surface-adsorbed organic molecules on ultrafast timescales for the first time. A monolayer of perylene-3,4,9,10-tetracarboxylic dianhydride (PTCDA) molecules on oxygen-passivated Cu(001) serves as the sample. The oxide layer decouples the molecules from the substrate, enabling observation of ultrafast excitation dynamics. Using time-resolved POT (tr-POT), the population of the lowest unoccupied molecular orbital (LUMO) after optical excitation was visualized in a time- and momentum-resolved manner.

Overall, this work demonstrates that precise control over the growth of layered nanomaterials contributes to a better understanding of complex growth mechanisms and can facilitate the development of new characterization techniques.



# Kurzfassung

Diese Dissertation leistet einen Beitrag zur Erforschung moderner Nanomaterialien, deren Eigenschaften maßgeblich von ihrer atomaren Struktur sowie elektronischen Wechselwirkungen an ihren Oberflächen und internen Grenzflächen geprägt werden. Im Fokus steht die gezielte Synthese und Analyse zweier Modellsysteme von Nanomaterialien, die in unabhängigen Projekten dazu dienen, einerseits den Wachstumsmechanismus von unkonventionell orientiertem Graphen zu untersuchen, und andererseits die zeitaufgelöste Dynamik angeregter Molekülorbitale im Impulsraum sichtbar zu machen.

Der Schwerpunkt des ersten Projekts ist die Untersuchung des Wachstums der zweidimensionalen Materialien Bornitrid (BN) und Graphen auf Siliziumkarbid (SiC). Ziel ist es, einen bereits etablierten Wachstumsprozess für die Herstellung von unkonventionell orientiertem Monolagen-Graphen auf SiC besser zu verstehen, der eine vielversprechende Grundlage für die epitaktische Herstellung von 30°-verdrehtem, zweilagigem Graphen bietet. Dieser Prozess umfasst die chemische Gasphasenabscheidung einer BN-Schicht und deren Umwandlung in Graphen. Dabei ist der Mechanismus der Orientierung der Graphenschicht bestimmt von besonderem Interesse, sowie der Einfluss der Präparationsparameter auf die Zusammensetzung und Qualität der BN- und der Graphen-Schicht. Zur Untersuchung dieser Aspekte wurde niederenergetische Elektronenmikroskopie (LEEM) eingesetzt, die sich ideal für die Bildgebung, Strukturanalyse und das Studium dynamischer Oberflächenprozesse eignet. Dabei wurde demonstriert, wie die Heizrate während der BN-Synthese entscheidend die Qualität und Zusammensetzung der BN-Schicht und der daraus entstehenden Graphen-Schicht beeinflusst.

Im Rahmen des zweiten Projekts wurde Photoemissions-Orbitaltomografie (POT) erstmals mit zeitaufgelöster Photoelektronenspektroskopie kombiniert, um die Dynamik vorübergehend besetzter Molekülorbitale zu untersuchen. Als Probensystem dient eine einzelne Lage des organischen Moleküls 3,4,9,10-Perylentetracarbonsäuredianhydrid (PTCDA) auf sauerstoff-passiviertem Cu(001). Dabei entkoppelt die Oxidschicht die Moleküle elektronisch und physikalisch vom Substrat und ermöglicht so die Beobachtung der ultraschnellen Anregungsdynamik. Mittels zeitaufgelöster POT (tr-POT) konnte so erstmals die Besetzung des niedrigsten unbesetzten Molekülorbitals (LUMO) durch optische Anregung zeit- und impulsaufgelöst visualisiert werden.

Insgesamt wird verdeutlicht, wie die präzise Kontrolle über das Wachstum von Schichtsystemen unterschiedlicher Nanomaterialien entscheidend dazu beiträgt, das Verständnis komplexer Wachstumsprozesse zu vertiefen und die Entwicklung neuartiger Charakterisierungsmethoden zu ermöglichen.



# Contents

<b>License Notice</b>	<b>i</b>
<b>Abstract</b>	<b>iii</b>
<b>Kurzfassung</b>	<b>v</b>
<b>List of Figures and Tables</b>	<b>xi</b>
<b>List of Acronyms</b>	<b>xv</b>
<b>1 Motivation and Outline</b>	<b>1</b>
<b>2 Experimental Principles and Methods</b>	<b>7</b>
2.1 Probing surfaces with low-energy electron scattering processes . . . .	8
2.2 Low-energy electron diffraction (LEED) . . . . .	10
2.2.1 The reciprocal lattice . . . . .	10
2.2.2 Experimental setup . . . . .	11
2.2.3 Notation and examples . . . . .	12
2.3 Low-energy electron microscopy (LEEM) . . . . .	16
2.3.1 Experimental setup and electron optics . . . . .	16
2.3.2 Contrast mechanisms and imaging parameters . . . . .	20
2.3.3 Bright-field and dark-field LEEM . . . . .	24
2.4 Probing surfaces with photoemission techniques . . . . .	26
2.5 Angular-resolved photoemission spectroscopy (ARPES) . . . . .	29
2.6 Photoemission orbital tomography (POT) . . . . .	31
2.7 Time-resolved photoemission experiments . . . . .	33
2.7.1 Two-photon photoemission processes . . . . .	33
2.7.2 Density matrix formalism for a three-level system . . . . .	35
2.7.3 Experimental setup . . . . .	38
<b>3 Boron Nitride on 6H-SiC(0001)</b>	<b>41</b>
3.1 Introduction to the experiment . . . . .	42
3.1.1 The Si-rich ( $3 \times 3$ ) surface reconstruction of 6H-SiC(0001) . .	43
3.1.2 Terrace configuration and step bunching on 6H-SiC(0001) . .	46
3.2 In-situ study of BN growth . . . . .	52
3.3 Structure of BN on SiC(0001) . . . . .	54
3.3.1 Structural overview . . . . .	54
3.3.2 Domain structure . . . . .	57

3.4	Temperature dependence . . . . .	68
3.4.1	BN on Sample 2 after fast annealing in Borazine . . . . .	68
3.4.2	Discussion of BN growth characteristics . . . . .	72
3.5	Conclusion . . . . .	75
<b>4</b>	<b>Graphene on 6H-SiC(0001)</b>	<b>77</b>
4.1	Introduction to the experiment . . . . .	78
4.1.1	Gr- $R30^\circ$ and Gr- $R0^\circ$ on SiC(0001) in literature . . . . .	78
4.1.2	The in-situ LEEM experiment . . . . .	81
4.2	Graphitization of BN on SiC(0001) upon annealing in UHV . . . . .	83
4.2.1	Structural overview . . . . .	83
4.2.2	Replacement of $B_xN_y-R0^\circ$ by Gr- $R0^\circ$ . . . . .	86
4.2.3	Emergence of conventional Gr- $R30^\circ$ . . . . .	91
4.2.4	Replacement of the $(\sqrt{7} \times \sqrt{7})-R19.1^\circ$ reconstruction by mixed Gr- $R0^\circ$ /Gr- $R30^\circ$ . . . . .	93
4.2.5	Formation of $30^\circ$ -tBLG . . . . .	98
4.3	Conclusion . . . . .	104
<b>5</b>	<b>Electron Dynamics of Molecular Orbitals in Time and Space</b>	<b>107</b>
5.1	Introduction to the experiment . . . . .	108
5.1.1	On decoupling organic adsorbates from metal supports . . . . .	110
5.1.2	Choosing a suitable sample system . . . . .	111
5.2	The sample preparation in Jülich . . . . .	111
5.2.1	Experimental setup . . . . .	112
5.2.2	The metal substrate - Cleaning and sample handling . . . . .	112
5.2.3	Calibration of the PTCDA evaporator . . . . .	114
5.2.4	Oxygen induced reconstruction of the Cu(001) surface . . . . .	116
5.2.5	Structure of PTCDA on the oxidized Cu(001) surface . . . . .	119
5.3	The tr-POT experiment in Marburg - Results and discussion . . . . .	128
5.3.1	Observing transiently occupied molecular states . . . . .	130
5.3.2	Determination of the inelastic lifetime $T_1$ of the LUMO . . . . .	132
5.3.3	Real-space excitation pathways . . . . .	134
5.4	Conclusion . . . . .	138
<b>6</b>	<b>Summary and Outlook</b>	<b>141</b>
<b>A</b>	<b>Challenges in LEEM Imaging at High Sample Temperatures</b>	<b>147</b>
<b>B</b>	<b>Second Layer Formation of PTCDA Deposited on Ag(110)</b>	<b>151</b>
<b>C</b>	<b>Review: The Oxygen Reconstruction of the Cu(001) Surface</b>	<b>153</b>
	<b>Bibliography</b>	<b>I</b>
	<b>List of Own Publications</b>	<b>XXV</b>

*Contents*

<b>Acknowledgments</b>	<b>XXVII</b>
<b>Eidesstattliche Erklärung</b>	<b>XXIX</b>



# List of Figures and Tables

## List of Figures

1.1	Structure and electronic properties of graphene. . . . .	2
2.1	Interaction of low-energy electrons with matter . . . . .	9
2.2	Ewald's sphere construction and principle of LEED . . . . .	11
2.3	Examples for surface structures and their LEED patterns . . . . .	13
2.4	Multiple scattering and formation of moiré patterns in LEED. . . . .	15
2.5	Picture of the AC-SPELEEM instrument . . . . .	17
2.6	LEEM electron optics . . . . .	19
2.7	Energy dependency of contrast in LEEM . . . . .	20
2.8	Phase contrast in LEEM . . . . .	22
2.9	Influence of the focusing condition on LEEM contrast . . . . .	23
2.10	Schematics of BF-LEEM and DF-LEEM imaging modes . . . . .	24
2.11	DF-LEEM characterization of one layer hBN on Ni(111) . . . . .	25
2.12	The photoemission process . . . . .	27
2.13	Angular-resolved photoemission spectroscopy (ARPES) . . . . .	29
2.14	ARPES data of graphene on SiC(0001) measured with the LEEM instrument. . . . .	30
2.15	Theoretical calculation of orbital tomography maps . . . . .	31
2.16	Orbital tomography of PTCDA on Ag(110) . . . . .	32
2.17	The two-photon photoemission experiment . . . . .	34
2.18	Polarization and population terms derived by perturbation theory . . . . .	38
2.19	Experimental setup for time-resolved momentum microscopy . . . . .	39
3.1	The Si-rich (3×3) surface reconstruction . . . . .	45
3.2	LEEM-I(V) characterization of the Si-rich (3×3) surface reconstruc- tion . . . . .	46
3.3	Structure of 6H-SiC . . . . .	47
3.4	Terrace configuration of (3×3)-Si reconstructed 6H-SiC in DF-LEEM . . . . .	48
3.5	Step retraction model at the 6H-SiC(0001) surface . . . . .	49
3.6	Step retraction during BN growth . . . . .	50
3.7	Terrace and domain configuration of Sample 1 and Sample 2 . . . . .	51
3.8	BN Growth on SiC(0001) . . . . .	53
3.9	Overview of BN on Sample 1 . . . . .	54
3.10	LEED of BN on SiC(0001) . . . . .	55
3.11	LEEM-I(V) spectra of BN on SiC(0001) . . . . .	57

List of Figures and Tables

3.12	Identification of different surface regions with LEEM-I(V) . . . . .	58
3.13	DF-LEEM on $B_xN_y-R0^\circ$ . . . . .	60
3.14	LEEM-I(V) profiles of different $B_xN_y-R0^\circ$ regions in the island free area . . . . .	61
3.15	DF-LEEM on the $(\sqrt{7} \times \sqrt{7})-R19.1^\circ$ reconstruction . . . . .	63
3.16	$\mu$ LEED on the $(\sqrt{7} \times \sqrt{7})-R19.1^\circ$ reconstruction . . . . .	64
3.17	DF-LEEM on the $(\sqrt{7} \times \sqrt{7})-R19.1^\circ$ reconstruction . . . . .	65
3.18	DF-LEEM composite of $B_xN_y-R0^\circ$ and $(\sqrt{7} \times \sqrt{7})-R19.1^\circ$ . . . . .	66
3.19	DF-LEEM characterization of the misoriented minority phase . . . . .	67
3.20	Overview of BN on Sample 2 . . . . .	69
3.21	Domain structure of Sample 2 . . . . .	71
3.22	Temperature-versus-time plots during BN preparation . . . . .	73
4.1	Gr- $R30^\circ$ on SiC(0001), grown by thermal decomposition . . . . .	79
4.2	Surface structures obtained by annealing a $(3 \times 3)$ -Si reconstructed SiC(0001) surface in borazine at increasingly higher temperatures . . . . .	80
4.3	BN on Sample 2 before and after annealing in UHV . . . . .	82
4.4	Graphene on Sample 2 . . . . .	84
4.5	Graphene on Sample 1 . . . . .	85
4.6	Replacement of $B_xN_y-R0^\circ$ by Gr- $R0^\circ$ . . . . .	87
4.7	DF-LEEM data recorded from Sample 2 after the first annealing in UHV . . . . .	88
4.8	DF-LEEM data recorded from Sample 2 after the second annealing in UHV . . . . .	89
4.9	ARPES data, recorded on Sample 2 . . . . .	90
4.10	Determination of the multilayer thickness of Gr- $R30^\circ$ on Sample 2 . . . . .	92
4.11	$\mu$ LEED measurements on an island on a $S_2$ terminated terrace of Sample 2 . . . . .	93
4.12	LEEM-I(V) profiles of islands on Sample 2 after the first annealing in UHV . . . . .	94
4.13	Different graphene monolayer configurations on Sample 2 after the second annealing in UHV . . . . .	95
4.14	ARPES data recorded on the islands on Sample 2 after the second annealing in UHV . . . . .	97
4.15	Inhomogeneity of the domains revealed by LEEM-I(V) . . . . .	97
4.16	Bilayer graphene, domains and terrace configuration on Sample 2 . . . . .	99
4.17	LEEM-I(V) data of Graphene on Sample 1 . . . . .	101
4.18	DF-LEEM data recorded from Sample 1 after graphitization . . . . .	103
5.1	1PPE Results for PTCDA on Ag(110) . . . . .	109
5.2	Experimental setup for sample preparation in Jülich . . . . .	113
5.3	Structure of PTCDA on the Ag(110) surface . . . . .	115
5.4	Formation of the Cu(001)- $(\sqrt{2} \times 2\sqrt{2})R45^\circ-2O$ surface reconstruction . . . . .	117
5.5	LEED of PTCDA on Cu(001)-MR-2O, comparison with literature . . . . .	120

5.6	LEED measurements for different preparations of PTCDA on oxygen reconstructed Cu(001) . . . . .	122
5.7	Temperature profile during the optimized oxidation process . . . . .	125
5.8	Structure of PTCDA on the Cu(001)-MR-2O surface . . . . .	127
5.9	Femtosecond time-resolved photo- emission tomography of molecular orbitals . . . . .	129
5.10	Momentum maps of the frontier orbitals . . . . .	131
5.11	Lifetime of the excited electron in the LUMO . . . . .	133
5.12	Momentum-resolved LUMO dynamics for different excitation pathways . . . . .	135
A.1	Thermal electrons . . . . .	147
A.2	Spot profile of the electron beam . . . . .	149
A.3	LEEM imaging at high T with optimized settings . . . . .	149
B.1	LEED of the PTCDA bilayer structure on Ag(110) . . . . .	152
C.1	LEED of different oxygen induced reconstructions of the Cu(001) surface . . . . .	154
C.2	Structure of the $c(2 \times 2)$ oxygen surface reconstruction . . . . .	156
C.3	The “4-spot” surface structure . . . . .	158
C.4	Experimental data on the order-disorder phase transition by Iddir et al. . . . .	159
C.5	Structure model of the temperature-induced order-disorder phase transition of the Cu(001)-MR-2O structure . . . . .	161

## List of Tables

A.1	Available contrast apertures and energy slits at the AC-SPELEEM .	148
-----	---	-----



# List of Acronyms

2D	two-dimensional
1PPE	one-photon photoemission
2PPE	two-photon photoemission
AC-SPELEEM	aberration corrected spectroscopic photo emission and low-energy electron microscopy
ARPES	angle-resolved photoemission spectroscopy
BF-LEEM	bright-field low-energy electron microscopy
BN	boron nitride
BW	brick wall
CA	contrast aperture
CCD	charge-coupled device
CVD	chemical vapor deposition
DF-LEEM	dark-field low-energy electron microscopy
DFT	density functional theory
EDC	energy distribution curve
ES	energy slit
fcc	face-centered cubic
FL	field lens
FoV	field of view
Gr	graphene
HB	herringbone
hBN	hexagonal boron nitride
HHG	high-harmonic generation
HOMO	highest occupied molecular orbital
HV	high-voltage
IA	illumination aperture
IL	intermediate lens
LEED	low-energy electron diffraction
LEEM	low-energy electron microscopy
lq	low-quality
LUMO	lowest unoccupied molecular orbital
f-LUMO	partially filled (former) LUMO
MCP	microchannel plate
MR	missing row
MS	multiple scattering
NIXSW	normal incidence X-ray standing wave
OLED	organic light-emitting diode

*List of acronyms*

OFET	organig field-effect transistor
P1	projective lens 1
PEEM	photoemission electron microscopy
PES	photoemission spectroscopy
PGI-3	Peter Grünberg Institut 3
POT	photoemission orbital tomography
PT	perturbation theory
PTCDA	perylene-3,4,9,10-tetracarboxylic dianhydride
QIP	quantum interference peak
R30°	rotated by 30°
SAA	selected area aperture
SFB	Sonderforschungsbereich
SHG	second harmonic generation
SiC	silicon carbide
STM	scanning tunneling microscopy
tBLG	twisted bilayer graphene
TMDCs	transition-metal dichalcogenides
tr-POT	time-resolved photoemission orbital tomography
UHV	ultrahigh vacuum
UPS	ultraviolet photoelectron spectroscopy
UV	ultaviolet
vdW	van der Waals
XPS	X-ray photoelectron spectroscopy
XRD	X-ray diffraction
ZLG	zeroth layer graphene

# Chapter 1

## Motivation and Outline

Modern electronics are evolving rapidly, driven by the relentless pursuit of smaller, faster, and more efficient devices, along with the demand for new functionality and tailored properties [1, 2]. As device dimensions shrink to the nanometer scale and below, conventional bulk material descriptions are no longer adequate [3]. Instead, the atomic and electronic structures of surfaces and interfaces – accompanied by quantization effects arising from electron confinement, as well as intriguing phenomena such as chirality, superconductivity, and magnetism – emerge as key determinants of material properties [4–6]. The variety of physical effects and resulting material properties attracts significant interest also in fundamental research. This drives advances in fabrication techniques to produce new functional materials [7, 8]. In addition, characterization methods are refined and expanded to probe the properties of these materials and investigate the underlying phenomena [9].

In this work, two independent research projects are presented, each addressing a different model system of functional surface structures. The first project is located in the field of twistrionics, the study of electronic properties arising from the relative orientation of stacked two-dimensional (2D) materials. By means of electron microscopy, the growth and structure of unusually oriented graphene layers on the semiconductor silicon carbide (SiC) are investigated with the goal to produce twisted bilayer graphene. The second project is located in the field of organic adsorbates. Orbital tomography, a method for visualizing the orbitals of surface adsorbed molecules, is being used for the first time to image transiently occupied molecular orbitals.

### **Growth of unusually oriented graphene layers on SiC**

A group of materials with great potential for applications in modern electronics are 2D materials, which includes e. g. graphene, hexagonal boron nitride (hBN) and transition-metal dichalcogenides (TMDCs). These are crystalline materials of only one or few atomic layer thickness, where every atom is part of the surface or interface.

After being first isolated as a sheet of one atomic layer from graphite by mechanical exfoliation by Novoselov and Geim in 2004 [10], graphene quickly became the most extensively studied 2D material [7]. It consists solely of carbon atoms, arranged in a honeycomb lattice as illustrated in Fig. 1.1(a). Graphene's unique bandstructure [cf. Fig. 1.1(b,c)] is characterized by the linear dispersion of the  $\pi$

bands near the so-called Dirac points, which causes its charge carriers to behave like massless Dirac fermions and results in an exceptionally high carrier mobility exceeding that of silicon [11–13]. Because of its unique combination of electronic [10–15], optical [16–19], thermal [20–22], and mechanical [23–25] properties, graphene is a promising material for many applications, such as high-speed transistors and flexible devices [13, 26, 27]. Another prominent 2D material is hBN. It exhibits a honeycomb lattice similar to graphene, but consisting of alternating boron and nitrogen atoms. Due to its structural and electronic properties, particularly its insulating nature, it is of high interest in heteroepitaxial systems combined with graphene and other 2D materials [7, 28–30].

Combining 2D materials in so-called van der Waals heterostructures opens up opportunities for ultrathin devices and tailoring functionality of new artificial materials [7]. The combination possibilities are endless, given the pool of available 2D materials, their stacking sequence, layer thickness, and orientation angles, as well as different supporting structures and surface modifications that can be used as free parameters. In these layered systems, not only are the properties of the individual elements combined, but new and exciting properties emerge from interactions between the layers.

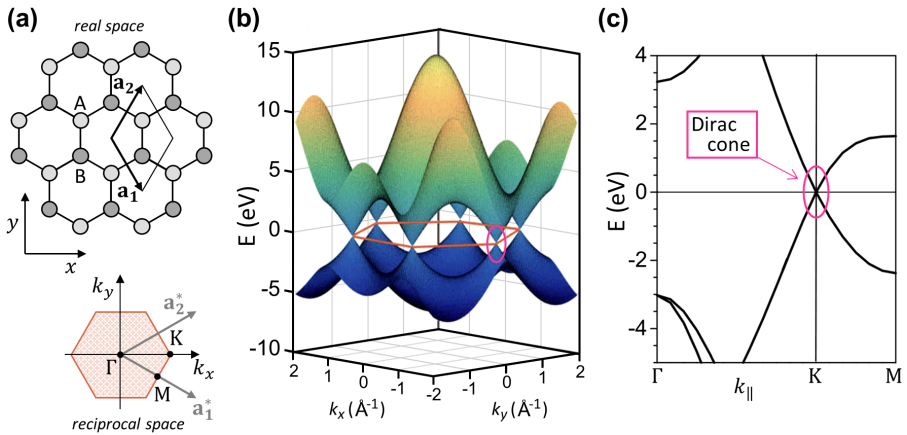


**Figure 1.1: Structure and electronic properties of graphene.** (a) Honeycomb lattice of monolayer graphene in real space (top) and the corresponding Brillouin zone in reciprocal space (bottom). Light and dark gray circles indicate carbon atoms on A and B sites, respectively. The real space (and reciprocal) lattice vectors  $\mathbf{a}_1$  and  $\mathbf{a}_2$  ( $\mathbf{a}_1^*$  and  $\mathbf{a}_2^*$ ) are drawn with black (gray) arrows.  $\Gamma$ , M and K mark high symmetry points in reciprocal space. (b) Simulated 3D electronic dispersion of ideal free monolayer graphene and (c) simulated band map in the vicinity of the Fermi level. The Dirac cone is highlighted in pink. Image in panel (b) adapted from Ref. [31], licensed under CC-BY 4.0. Image in panel (c) adapted from Ref. [32], licensed under CC-BY 4.0.

This is particularly evident in the properties of twisted bilayer graphene (tBLG) where the electronic properties depend sensitively on the rotation angle between the two layers [33]. Especially tBLG of small rotation angles attract high interest due to strong interlayer coupling and moiré effects, which come along with intriguing phenomena such as unconventional superconductivity, correlated insulating states, the anomalous quantum Hall effect, topological states, and tunable band gaps [33–39]. With increasing twist angle, the interlayer coupling weakens, and the bilayers behave almost like two independent monolayers. However, at the largest twist angle of exactly  $30^\circ$ , strong interaction reemerges. With its unique dodecagonal quasicrystallinity, nearly flat bands, and mirrored Dirac cones,  $30^\circ$ -tBLG exhibits intriguing properties that attract considerable interest in both experimental and theoretical studies [40–48].

A crucial prerequisite for the investigation of these materials is their synthesis. For research purposes, combining mechanical exfoliation with manual assembly of 2D heterostructures is often the most practical approach. This method provides exceptional crystalline quality, precise control over layer thickness, and the ability to choose twist angles deliberately [7, 13]. However, it is also time-consuming, the yield and size of exfoliated flakes is limited, and reproducibility – especially with respect to precise twist-angle control – remains challenging. With the prospect of future industrial implementation in mind, efforts are directed toward establishing scalable synthesis routes [7, 13, 49]. For graphene synthesis, epitaxial growth on silicon carbide (SiC) by thermal sublimation has proven highly promising [13, 49]. In this process, graphene grows in a single orientation, rotated by  $30^\circ$  with respect to the SiC substrate (referred to as Gr- $R30^\circ$ ) enabling the production of single- or multilayer graphene directly on an industry-relevant semiconductor without requiring a transfer step [50, 51]. Recently, a complementary method was developed that produces epitaxial graphene on SiC in an unconventional orientation, i.e., aligned with the substrate lattice (Gr- $R0^\circ$ ) [MR5, 41, 52–54]. Combined with conventional Gr- $R30^\circ$  growth, this approach offers a promising pathway for the large-scale, high-quality production of  $30^\circ$ -tBLG [41, 53, 54].

The key to preparing the unconventionally oriented Gr- $R0^\circ$  layer is the exposure of a SiC(0001) surface to borazine at elevated temperatures. Two preparation routes have been established. One is the growth of a boron nitride (BN) layer that is subsequently transformed into Gr- $R0^\circ$  by annealing at higher temperatures in UHV. The other is to directly heat the SiC(0001) surface in borazine up to temperatures at which Gr- $R0^\circ$  emerges. It is suggested that in this dynamic process, transient BN nuclei act as a surfactant, guiding the graphene to adopt the unconventional orientation. Either way, the underlying growth mechanisms are of high scientific interest. Therefore, this work aims to expand the understanding of the formation of unconventionally oriented Gr- $R0^\circ$  on SiC by studying BN growth and its replacement by graphene. To this end low-energy electron microscopy (LEEM) is employed. This characterization technique has proved to be a powerful tool to investigate growth processes of 2D materials *in situ*, in real time, and with lateral resolution [MR1, MR3, MR6].

## Imaging orbitals on ultrafast time scales

One of the most intriguing questions is how electron interactions give rise to the properties of functional materials. This drives the continuous refinement and expansion of traditional characterization techniques. By directly probing the electronic structure of solids in momentum space, angle-resolved photoemission spectroscopy (ARPES) has emerged as the ideal tool for investigating electronic properties of materials [9, 55, 56]. As such, it has played a central role in the discovery, characterization, and understanding of quantum materials [55]. Over the past two decades, ARPES has grown far beyond static band mapping, with ongoing improvements in instrumentation and expansion into new experimental domains [55, 56]. Among these developments, photoemission orbital tomography and time-resolved ARPES form the basis of the experimental approach in this work.

Photoemission orbital tomography (POT) is a combined experimental and theoretical approach which investigates the electronic structure of surface adsorbed molecules [57]. By measuring the momentum- and energy-resolved photoemission intensity, POT makes molecular orbitals directly visible, allowing them to be identified and localized in momentum space. Comparison with theoretical predictions from density functional theory (DFT) then enables quantitative reconstruction of orbital shapes and determination of orbital energy ordering. This makes POT an exceptionally powerful tool for studying both the geometric and electronic structures of surface-adsorbed semiconducting organic molecules [58–60]. With their tunable electronic properties and potential for low-cost, large-area fabrication, this class of nanomaterials is the basis of applications such as organic light-emitting diodes (OLEDs), organic field-effect transistors (OFETs), and organic photovoltaics [61, 62]. Advances in synthesis, processing, and theory continue to make organic semiconductors a highly active research area [63, 64].

Although the electron distribution of occupied orbitals can be imaged in momentum space by POT, it has so far been impossible to follow the momentum-space dynamics of a molecular orbital in time, for example during an excitation process or a chemical reaction. However, the emergence and refinement of femtosecond lasers in the past 20 years, capable of producing ultrashort coherent light pulses, has enabled the development and advancement of time-resolved ARPES techniques [9]. Thus ARPES became capable of mapping the temporal evolution of the electron system in momentum space [65–69].

In this thesis, time-resolved photoemission is combined with POT to realize a proof-of-principle experiment, enabling, for the first time, the observation of excitation dynamics of surface-adsorbed molecules in both time and momentum space. The primary objective of this work is the selection and preparation of a suitable model system to serve as the sample for the experiment. The crucial requirements – well-defined molecular orientation for orbital mapping, yet weak molecule-substrate interaction to slow excitation dynamics – are met by a monolayer of the prototype organic molecule 3,4,9,10-perylenetetracarboxylic dianhydride (PTCDA) deposited on an oxygen-passivated Cu(001) surface.

## Outline

Following this introduction, the experimental approaches employed in this work are introduced in Chapter 2. Adsorption structures of different sample systems are characterized by the well-established technique of low energy electron diffraction (LEED). *In situ* growth experiments and studies of lateral domain configurations are performed with low-energy electron microscopy (LEEM). The electronic structure of graphene and molecules is accessed with photoemission-based techniques, namely, angular-resolved photoemission spectroscopy (ARPES) and photoemission orbital tomography (POT). The latter is combined with two photon photoemission (2PPE) to realize a time-resolved POT (tr-POT) experiment.

The first project of this thesis discusses the epitaxial growth of Gr- $R0^\circ$  for  $30^\circ$ -tBLG production on SiC in two separate steps: The growth of BN, presented in Chapter 3, and the graphitization of the BN template, presented in Chapter 4. BN is grown by exposing the hot SiC(0001) surface to borazine in Chapter 3. This process is investigated *in situ* and in real time using LEEM, thereby providing new insights into the growth mechanism. A detailed analysis of the structure and domain configuration of three different BN surface phases is performed. Furthermore, it is shown that increasing the heating rate during BN growth improves the quality of the BN template. Subsequently, the BN layers serve as templates to grow Gr- $R0^\circ$  in Chapter 4. LEEM is utilized to analyze the structural change of the BN layer upon graphitization. Thus, information is provided on how the domain configuration and the structural quality of the BN template, as well as the sample morphology, influence the graphitization process.

Chapter 5 represents the second project of this thesis and is dedicated to the proof-of-principle experiment that combines time-resolved photoemission with POT. The focus lies on the selection and preparation of the model system that serves as the sample. Furthermore, the experimental results are presented and discussed, proving that this experiment enables the observation of excitation dynamics of surface-adsorbed molecules in both time and momentum space for the first time.

Finally, this work closes with a summary of the main results and a discussion of avenues for future research.



# Chapter 2

## Experimental Principles and Methods

This chapter introduces the basic principles of the different experimental techniques and theoretical approaches which have been used to study the structure, growth and electronic properties of different surfaces in this work.

First, the interaction process of low-energy electrons with matter is discussed. Their surface sensitivity and structural sensitivity due to diffraction make low-energy electrons a versatile probe for surface science. With low-energy electron diffraction (LEED), a simple diffraction experiment is introduced as standard technique to investigate the surface structure of crystalline surfaces. It allows to directly access the periodic structure of the surface via the reciprocal lattice. With a more advanced optical setup, low-energy electron microscopy (LEEM) is realized as an imaging technique with lateral resolution down to a few nm. The combination of surface microscopy with the structural sensitivity of LEED provides complementary information on the lateral surface composition and the crystalline structure. Moreover, experiments on adsorbate formation and structural transitions at surfaces can be investigated both *in situ* and in real-time.

When low-energy electrons are generated through photoemission, information on the electronic structure of surfaces becomes accessible. With angular resolved photoemission spectroscopy (ARPES), the momentum- and energy-resolved reciprocal band structure of bulk surfaces and adsorbate layers can be mapped directly. In photoemission orbital tomography (POT), the ARPES signal of surface adsorbed organic molecules is used to map the molecule's orbitals. Information on the interaction between molecule and surface can be obtained by comparing experimental photoemission data with theoretical predictions. When using pulsed photon sources, two-photon photoemission (2PPE) experiments make it possible to probe the unoccupied electronic structure of surfaces and surface adsorbates. With the time-resolved measurement mode, the dynamics of transiently occupied states can be probed. For a quantitative analysis of the time-resolved 2PPE signal, a theoretical model is introduced. By combining 2PPE with POT a time-resolved POT (tr-POT) experiment is realized.

## 2.1 Probing surfaces with low-energy electron scattering processes

Generally, a surface characterization technique must fulfill two conditions, namely surface sensitivity and surface specificity. As the surface of a material is defined only by the outermost few atomic layers, the sensitivity requirement arises simply from the small amount of material within the limited lateral range of the probe. A more demanding need is surface specificity. Without, the signal originating from the surface is superimposed and thus obscured by the signal of the bulk, which would make up by far the largest amount of probed material.[70]

Due to their surface specificity, low-energy electrons are a well suited probe for the structural investigation of solid surfaces and thin adsorbate layers. Electrons are considered to have low kinetic energy  $E_{kin}$  in the range of  $\sim 10 - 500$  eV (and very low energy if  $E_{kin} \leq 10$  eV) [71]. The short penetration depth of low energy electrons is a result of two dominant and roughly equally strong contributing interaction effects, namely inelastic scattering and elastic backscattering[70].

Inelastic scattering processes of low-energy electrons in solids appear mainly through interaction with plasmons (collective vibrational excitations of the valence electrons), and single electron excitations (electron-hole pair interaction)[3, 71]. In diffraction based techniques, the electrons which undergo inelastic scattering are lost for surface characterization. The corresponding attenuation effect due to all inelastic scattering processes can be described by a parameter called inelastic mean free path  $\lambda_i$  [72]. It corresponds to the distance an electron wave can travel in a solid before its intensity has decreased by a factor  $1/e$ . Experimentally,  $\lambda_i$  is found to depend on the electron's kinetic energy, following the empirical law

$$\lambda_i[\text{\AA}] = c_1 E_{kin}[\text{eV}]^{-2} + c_2 \sqrt{E_{kin}[\text{eV}]} \quad , \quad (2.1)$$

with material specific constants  $c_1$  and  $c_2$  [73]. As can be extracted from Fig. 2.1(a),  $\lambda_i$  is in the range of  $\sim 5 - 10$  \AA for low-energy electrons in elemental crystals. Consequently, electrons that penetrate more than a few atomic layers have a high probability of losing energy and coherence to the incident beam so that elastically backscattered electrons stem from the first few atomic surface layers [3].

Moreover, elastic scattering itself does also contribute to the surface specificity. As the incident electron beam is progressively scattered out of the surface from each layer, the contribution of deeper layers to diffraction decreases [70]. In analogy to the inelastic mean free path  $\lambda_i$ , an energy dependent elastic mean free path  $\lambda_e$  is defined. One way to demonstrate the energy-dependent interplay of  $\lambda_i$  and  $\lambda_e$  is to compare a solid's specular reflectivity with its unoccupied electronic band structure perpendicular to the surface [74], as shown for a W(110)-surface in Fig. 2.1(b). At electron energies where no electronic states are accessible for the free electron to scatter with inelastically [cf. Fig. 2.1(b), band gap between 1 eV and 5 eV above the vacuum level  $E_V$ ],  $\lambda_i$  becomes large. Therefore, the sampling depth depends mainly on the magnitude of  $\lambda_e$ . As the electrons are likely to undergo elastic scattering, a maximum in reflectivity occurs. In analogy, a reflection minimum

## 2.1 Probing surfaces with low-energy electron scattering processes

corresponds to a high density of states. The increased amount of possible inelastic scattering processes results into a short  $\lambda_i$  which causes strong attenuation [cf. Fig. 2.1(b), at energy of 10 eV above  $E_V$ ].

Finally, a coherent electron beam that is elastically scattered at a crystalline surface gives rise to diffraction, provided that the periodicity of the probed structure and the wavelength of the electrons are of comparable length scale. The electron wave length can be determined by employing the de Broglie relation

$$\lambda = \frac{h}{p} \quad \text{and} \quad p = mv = \sqrt{2mE_{kin}} \quad . \quad (2.2)$$

A substitution of the parameters with values of appropriate fundamental constants leads to the expression

$$\lambda[\text{\AA}] = \sqrt{150.4/E_{kin}[\text{eV}]} \quad . \quad (2.3)$$

Thereby, the range of typically 20-300 eV used in low-energy electron diffraction experiments corresponds to electron wavelengths of  $\sim 1 \text{\AA}$ , which is ideal for diffraction from crystalline solids. Electron waves that are reflected from consecutive crystal planes with lattice spacing  $d$  and incident angle  $\theta$  interfere constructively when their path length difference is an integer multiple of the de Broglie wavelength

$$n\lambda = 2d\sin\theta \quad , \quad (2.4)$$

a relation commonly known as Bragg's law. [70]

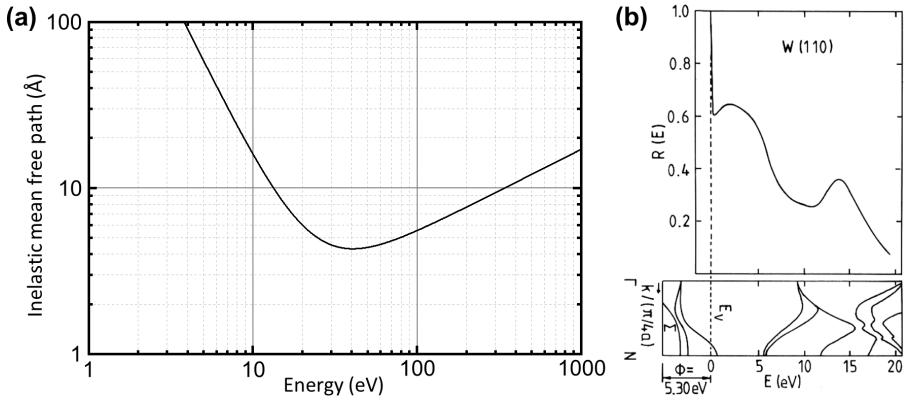


**Figure 2.1: Interaction of low-energy electrons with matter.** (a) Inelastic mean free path  $\lambda_i$  of electrons in a solid as a function of electron energy. The displayed profile was determined by Eq. 2.1, using the parameters  $c_1 = 1430$  and  $c_2 = 0.54$  for elemental solids, as provided by Ref. [73]. (b) Normal incidence reflectivity of electrons at a (110)-oriented tungsten surface (top) and the band structure along the surface normal (bottom). Fig. 2.1(b) originally from Ref. [75], reproduced from Ref. [74] with permission. Licensed by Springer Nature Customer Service Center GmbH. This material is not covered by the terms of the CC BY 4.0 license (see License Notice).

## 2.2 Low-energy electron diffraction (LEED)

LEED is a standard technique for the structural characterization of crystalline surfaces. Thereby, the atomic lattice serves as a diffraction grating for the surface sensitive low-energy electrons. The recorded diffraction pattern gives direct access to the reciprocal lattice of the investigated material.

### 2.2.1 The reciprocal lattice

In three dimensions, a crystal's reciprocal lattice is described by the Laue condition

$$\mathbf{k} = \mathbf{k}_0 + \mathbf{G}_{hkl} \quad , \quad (2.5)$$

which is the general condition for constructive interference at a crystalline solid and basically describes momentum conservation of the incident and scattered wave vectors  $\mathbf{k}_0$  and  $\mathbf{k}$  of the probe. Constructive interference occurs only for discrete points in reciprocal space, given by the reciprocal lattice vectors  $\mathbf{G}_{hkl} = h\mathbf{a}_1^* + k\mathbf{a}_2^* + l\mathbf{a}_3^*$  with the integer-value Miller indices  $(h, k, l)$  and the primitive reciprocal-space translation vectors  $(\mathbf{a}_1^*, \mathbf{a}_2^*, \mathbf{a}_3^*)$ . When low-energy electrons are used as probe in the diffraction experiment, the penetration depth is short and information on the crystal's periodicity along the dimension of the surface normal is lost. Consequently, momentum conservation stays valid only for  $\mathbf{k}^{\parallel}$ , the momentum component parallel to the surface:

$$\mathbf{k}^{\parallel} = \mathbf{k}_0^{\parallel} + \mathbf{G}^{\parallel} \quad \text{with} \quad \mathbf{G}^{\parallel} = \mathbf{g}_{hk} = h\mathbf{a}_1^* + k\mathbf{a}_2^* \quad . \quad (2.6)$$

Here,  $\mathbf{a}_1^*$  and  $\mathbf{a}_2^*$  are defined parallel and  $\mathbf{a}_3^*$  perpendicular to the surface. The reciprocal translation vectors parallel to the surface plane,  $\mathbf{a}_1^*$  and  $\mathbf{a}_2^*$ , are related to the translation vectors of the real-space lattice parallel to the surface plane,  $\mathbf{a}_1$  and  $\mathbf{a}_2$ , by

$$\mathbf{a}_1^* = 2\pi \frac{\mathbf{a}_2 \times \mathbf{n}}{A} \quad , \quad \mathbf{a}_2^* = 2\pi \frac{\mathbf{n} \times \mathbf{a}_1}{A} \quad , \quad A = \mathbf{a}_1 \cdot \mathbf{a}_2 \times \mathbf{n} \quad , \quad (2.7)$$

with  $\mathbf{n}$  being the unit vector normal to the surface. The momentum component  $\mathbf{k}^{\perp}$  perpendicular to the surface is not conserved. Therefore, the discrete reciprocal lattice points of bulk scattering transform into infinite reciprocal lattice rods perpendicular to the surface, also called diffraction rods. As illustrated in Fig. 2.2(a), these are identified with the number index  $(hk)$ . Note that the probing depth is not exactly two-dimensional but has a finite probing depth. Therefore, the intensity along the rods is modulated. [70]

In a LEED experiment, the incident electron beam  $\mathbf{k}_0$  is monochromatic and energy conservation must be fulfilled:

$$|\mathbf{k}_0| = |\mathbf{k}| = \frac{2\pi}{h} p = \frac{2\pi}{h} \sqrt{2mE} \quad . \quad (2.8)$$

For a fixed energy  $E$ , this defines all points in reciprocal space which are accessible in a LEED measurement by a sphere with radius  $\frac{2\pi}{h} \sqrt{2mE}$ , the so-called Ewald's sphere [cf. Fig. 2.2(a)]. [76]

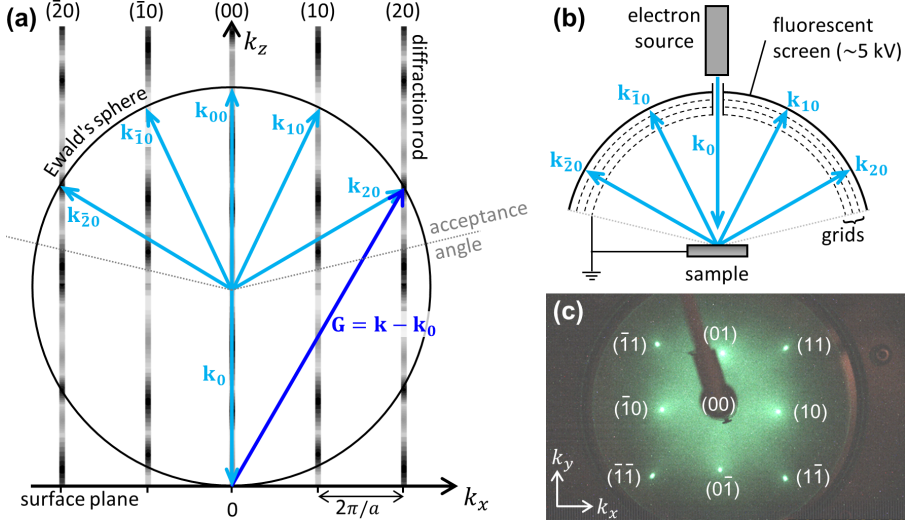


**Figure 2.2: Ewald's sphere construction and principle of LEED.** (a) 2D-lattice in reciprocal space. In a diffraction experiment, constructive interference appears when the Ewald's sphere intersects with the diffraction rods ( $hk$ ). (b) Schematic of the LEED experiment, based on Ref. [70]. (c) LEED pattern of the Cu(001) surface. The (00)-spot is shadowed by the electron source.

### 2.2.2 Experimental setup

In Fig. 2.2(b) the experimental setup of a LEED instrument is displayed schematically. A monochromatic electron beam  $k_0$  is generated by an electron gun and directed onto the sample under normal incidence. The typical probing diameter is  $\sim 0.5$ -1 mm [77, 78]. A system of grids is used to control the electric fields in the setup. In this way, a field free area around the sample is created and inelastically scattered electrons are repelled [79]. The elastically backscattered electrons are detected by a fluorescent screen. Fig. 2.2(c) displays a LEED pattern recorded by directing a camera on the fluorescent screen from behind the electron source. In this geometry, the lattice rods (marked with corresponding number indices) are imaged as LEED spots. The LEED pattern is a direct projection of a two-dimensional map of reciprocal space, defined by the surface of the Ewald's sphere and the acceptance angle [cf. Fig. 2.2(a,b)]. As a consequence, the magnification is determined by the incident electron energy, making the LEED spots move towards the center upon increasing the energy and therefore, the radius of the Ewald's sphere. Note that, the LEED instrument used in this work has a flat detection geometry which results into a distortion of the LEED pattern [72][cf. Figs. 2.2(c) and 2.3(a)]. However, it allows the use of a microchannel plate to enhance the signal. Due to the higher detection sensitivity, lower beam currents can be applied which reduces beam damage on organic samples.

### 2.2.3 Notation and examples

In the following, the notation used for the description of crystalline surface structures is introduced and examples for different surface structures and their respective LEED features are presented, based on Ref. [70]. The provided information is selected by its relevance for the present work and focuses on qualitative effects. For more details refer to standard text books [3, 70, 77, 79, 80] and cited literature.

**The unit cell** Any crystalline surface structure is described completely by the arrangement of the surface atoms within a unit cell spanned by the translation vectors  $\mathbf{a}_1$  and  $\mathbf{a}_2$  as introduced above. The assignment of a unit cell is not unambiguous. Usually, a unit cell containing the smallest possible area, the so-called primitive unit cell, is chosen. The reciprocal-space translation vectors  $\mathbf{a}_1^*$  and  $\mathbf{a}_2^*$  are then obtained directly from Eq. 2.7. Fig. 2.3(a) shows an exemplary real-space structure model (left), which represents the topmost atomic layer of a simple cubic (sc) or face centered cubic (fcc) (001)-surface. From its primitive unit cell, the corresponding reciprocal lattice results as shown on the right.

**Superlattice and superstructure** Upon adsorbate formation, LEED structures become more complicated as the substrate's structure is superimposed with the adsorbate's structure. The latter is commonly described by a matrix  $M$ , which relates the unit cell vectors of substrate  $\mathbf{a}_1, \mathbf{a}_2$  and adsorbate  $\mathbf{b}_1, \mathbf{b}_2$  by:

$$\begin{pmatrix} \mathbf{b}_1 \\ \mathbf{b}_2 \end{pmatrix} = M \begin{pmatrix} \mathbf{a}_1 \\ \mathbf{a}_2 \end{pmatrix} = \begin{pmatrix} m_{11} & m_{12} \\ m_{21} & m_{22} \end{pmatrix} \begin{pmatrix} \mathbf{a}_1 \\ \mathbf{a}_2 \end{pmatrix} . \quad (2.9)$$

When the matrix elements  $m_{ij}$  are rational numbers, the superstructure is called commensurate, otherwise incommensurate[70]. An example for a commensurate adsorbate structure is shown in Fig. 2.3(b). Here, every second hollow site of the structure model from Fig. 2.3(a) is occupied by an adsorbate atom. The primitive unit cell of the superlattice is drawn with solid gray lines and the corresponding superstructure matrix is  $\begin{pmatrix} 1 & \\ & 1 \end{pmatrix}$ . In Wood notation, this superstructure is given by  $(\sqrt{2} \times \sqrt{2})R45^\circ$  [77]. This term describes the geometric relation of the superlattice's to the substrate's primitive unit cell, namely a scaling of the respective lattice vectors by  $\sqrt{2}$  and a rotation by  $45^\circ$ . Another expression in Wood notation for the same superstructure is the more commonly used  $c(2 \times 2)$  [77]. It relates to the conventional centered ('c') and in size doubled (non-primitive) unit cell as indicated with a dashed square in Fig. 2.3(b). In reciprocal space, the superstructure spots (gray) are superimposed with the substrate spots (black), adding additional 1/2-order spots. Note that as a consequence of Eq. 2.7, the size ratio of the substrate's and the adsorbate's reciprocal unit cells is inverted with respect to real space.

**Disorder effects** Each type of defect in the crystalline lattice gives rise to particular features in the diffraction pattern, according to the structure of the defect and its embedding into the surface matrix [3]. Exemplary, the effect of anti-phase

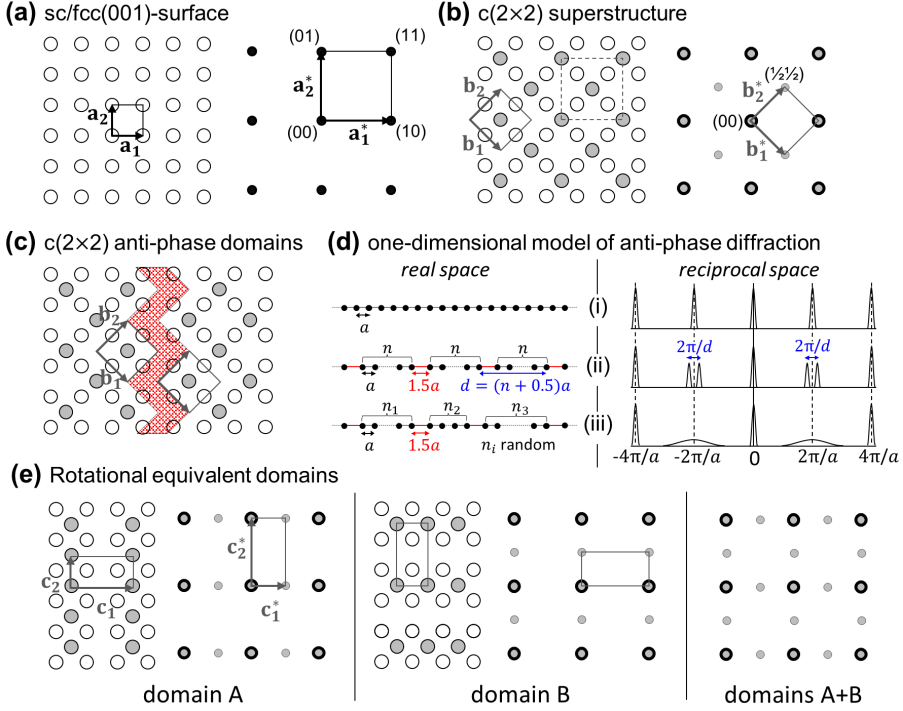


**Figure 2.3: Examples for surface structures and their LEED patterns.** (a) Real-space (left) and reciprocal-space (right) structure models for the topmost layer of an sc(001) or fcc(001)-surface. The unit cells and translation vectors are drawn with black lines and arrows, respectively. (b) Same as (a), but with additional adatoms (gray) occupying every second hollow site. The primitive unit cell of the superlattice and the corresponding reciprocal-space structure are drawn in gray. Dashed lines indicate the  $c(2 \times 2)$  superstructure unit cell. (c) Real-space structure model of a phase boundary (red shaded area) between the two anti-phase domains of the  $c(2 \times 2)$  superstructure. (d) Anti-phase diffraction. The calculated diffraction intensities (right) are shown for scattering at one-dimensional lattice models (left) of (i) a large number  $N$  of atoms with spacing  $a$ ; (ii) several groups of  $n$  atoms, each with spacing  $a$  and distance between the groups of  $d = (n + 0.5)a$ ; (iii) Several groups of atoms of varying size  $n_i$  but otherwise as for (ii). (e) Adsorption structure on the (001)-surface with adatoms occupying every second hollow site by forming rows. Domain A ( $2 \times 1$ ) and domain B ( $1 \times 2$ ) are symmetrically equivalent by a rotation of  $90^\circ$ . When both domains are present in the investigated surface region, the reciprocal structures superimpose in LEED (right). The schematics in (a-e) are based on Ref. [70].

domain formation is introduced. The real-space model in Fig. 2.3(b) represents an idealized  $c(2 \times 2)$  adsorption structure. Considering that every hollow site of the (001)-surface is symmetrically equivalent, the surface registry allows two energetically equivalent domains to form, as shown in Fig. 2.3(c). These have unit cells of identical dimensions but do not fulfill translational symmetry, which results in domain boundaries (red shaded area). In terms of interference, the two domain registries are out of phase, therefore called anti-phase domains. Depending on size and distribution of the anti-phase domains, different interference effects can be observed in diffraction patterns [70]. This is illustrated for three exemplary cases in Fig. 2.3(d). Here, scattering intensities in reciprocal space (right) have been simulated using simplified one-dimensional scattering models in real space (left) [70, 81]. Example (i) represents an ideal lattice without anti-phase domains. Arranging  $N$  atoms in a row with spacing  $a$ , the basic periodicity of the diffraction pattern is  $\Delta \mathbf{k}_{\parallel} = 2\pi/a$ . The width of the intensity maxima scales with  $1/N$ . Example (ii) is a periodic arrangement of alternating anti-phase domains of  $n$  atoms, each with spacing  $a$  and distance  $d = (n + 0.5)a$  between the groups. The simulated diffraction intensity exhibits a splitting by  $2\pi/d$  [82] of alternating diffraction spots. If the domain sizes  $n$  become randomized (iii), a peak broadening occurs instead. In a general context, weakened and broadened fractional-order spots and diffuse intensity distributions are commonly associated with disorder effects [77]. Importantly, these can only be observed when the respective domain structures appear on length scales smaller than the lateral coherence length of the electron beam, also called transfer width. The latter is in the order of  $\sim 100 \text{ \AA}$  for typical LEED instruments [70].

**Rotational domains** Another effect of domain formation is observed when the adsorbate's superstructure exhibits lower symmetry than the substrate. This is illustrated in Fig. 2.3(e). Here, adatoms form a  $(2 \times 1)$  rectangular mesh (domain A) on the square lattice of the (001)-substrate. As a consequence of Eq. 2.7, length scales are inverted in reciprocal space, resulting into a  $(1/2 \times 1)$  reciprocal mesh. Due to the substrate's higher symmetry, a  $90^\circ$  rotated and symmetrical equivalent domain B arises. When both domains coexist on the investigated surface area, the diffraction patterns of the respective domains superimpose in the LEED measurement [cf. Fig. 2.3(e) right].

**Multiple scattering** So far, only single scattering events have been considered, as illustrated in Fig. 2.4(a). Here, electrons are scattered only once, either from adsorbate or substrate. This results simply in the superposition of their LEED patterns, resembled by the sets of two dimensional reciprocal lattice vectors  $\{\mathbf{g}_a^{\parallel}\}$  and  $\{\mathbf{g}_s^{\parallel}\}$ . However, due to the short elastic mean free path of low-energy electrons, successive elastic scattering from several surface atoms makes an important contribution to LEED patterns [79]. Exemplary, the effect of multiple scattering (MS) on LEED patterns is discussed for a double scattering event ( $1^{\text{st}}$ -order MS), involving both substrate and adsorbate, as illustrated in Fig. 2.4(b). Considering

Eq. 2.6, the resulting reciprocal scattering vectors of the described 1<sup>st</sup>-order MS event are simply obtained by all possible linear combinations of  $\{\mathbf{g}_s^{\parallel}\}$  and  $\{\mathbf{g}_a^{\parallel}\}$ , which fulfill energy conservation [83]. These are referred to as  $\{\mathbf{g}_s^{\parallel} + \mathbf{g}_a^{\parallel}\}$ . When no adsorbate is present or when all reciprocal lattice vectors of the adsorbate's structure are in common with the substrate's,  $\{\mathbf{g}_s^{\parallel} + \mathbf{g}_a^{\parallel}\}$  is identical with the union of the two sets:  $\{\mathbf{g}_s^{\parallel}\} \cup \{\mathbf{g}_a^{\parallel}\}$ . In this case, multiple scattering (MS) solely alters the LEED spots' intensities. Otherwise, additional LEED spots arise which cannot be explained by single scattering events. This effect is well known for example from the so-called moiré patterns commonly observed in LEED for two hexagonal lattices being rotated with respect to each other and/or having slightly different lattice constants [84]. The latter case is illustrated in Fig. 2.4(c). In the schematic example (i), the reciprocal lattices of substrate and adsorbate are represented by gray and red spots, respectively. A 1<sup>st</sup>-order MS event involving  $\mathbf{g}_s^{\parallel}$  and  $\mathbf{g}_a^{\parallel}$  results into a new LEED spot at  $\mathbf{g}_s^{\parallel} + \mathbf{g}_a^{\parallel}$ . Similarly, all additional LEED spots up to 3<sup>rd</sup>-order MS are deduced and indicated by blue spots of different shades. The scattering intensity of MS spots usually decreases with increasing order of MS events, as becomes obvious in the LEED measurement (ii).

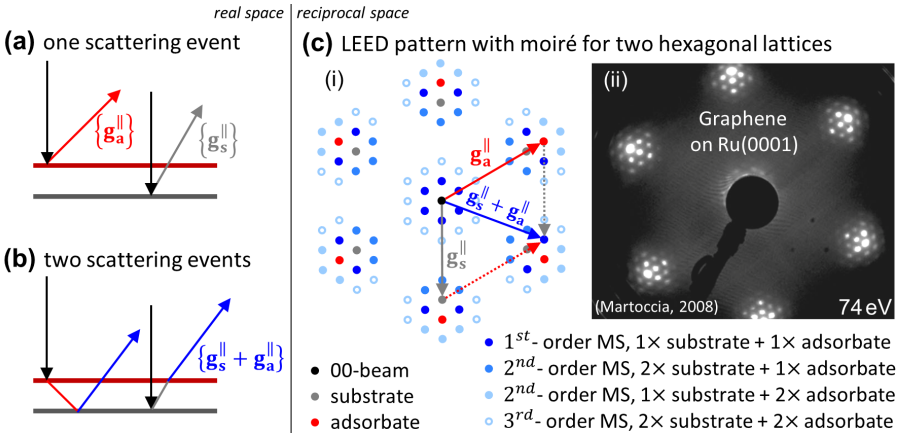


**Figure 2.4: Multiple scattering and formation of moiré patterns in LEED.** (a) Single scattering results into the two-dimensional reciprocal lattice vectors  $\{\mathbf{g}_a^{\parallel}\}$  (adsorbate) and  $\{\mathbf{g}_s^{\parallel}\}$  (substrate). (b) Double scattering, which involves substrate and adsorbate, results into additional scattering vectors  $\{\mathbf{g}_s^{\parallel} + \mathbf{g}_a^{\parallel}\}$ . (c) Multiple scattering (MS) at two hexagonal lattices with the same orientation but slightly different lattice constants  $a_s$  (substrate) and  $a_a$  (adsorbate). (i) Simulated LEED pattern for  $a_a : a_s = 15 : 18$ . Under 1<sup>st</sup>-order multiple scattering, additional LEED spots appear as exemplarily illustrated by  $\mathbf{g}_s^{\parallel} + \mathbf{g}_a^{\parallel}$ . Increasing the number of involved scattering events, a so-called moiré pattern forms. (ii) LEED measurement of a monolayer graphene (*Gr*) on a Ru(0001)-surface (*Ru*) with  $a_{Gr} : a_{Ru} = 23 : 25$ , showing a moiré pattern due to MS. Fig. 2.4(ii) adapted with permission from Ref. [85]. © 2008 by the American Physical Society (see License Notice).

**Interpretation of LEED data** Although LEED offers direct access to the reciprocal surface structure, the given examples underline that information on the real-space surface structure is not trivial to deduce from complex LEED patterns. Moreover, two important aspects limit the power of conventional LEED. Firstly, LEED averages the structural information of a large surface area ( $\sim 0.5\text{-}1\text{ mm}$ ) while the structural quality can be judged only for length scales below the transfer width ( $\sim 100\text{ \AA}$ ). Secondly, the reciprocal lattice vectors alone do only yield information on the dimensions and the symmetry of the unit mesh in real space and not on the geometric positions of surface atoms within the unit cell [79]. Worth mentioning is that quantitative techniques have been developed to further extend the power of LEED. For example, a quantitative analysis of energy dependent LEED spot intensity profiles (LEED-I(V), I: Intensity, V: acceleration voltage of the electrons) makes information on the geometric positions of surface atoms accessible. More commonly, LEED is used as a convenient tool to control the structural quality of samples in preparation for other surface characterization techniques. In this work, LEED was mainly used to control the structural quality of already known adsorbate-substrate systems or in combination with the surface imaging technique LEEM.

## 2.3 Low-energy electron microscopy (LEEM)

In LEEM, elastically backscattered low-energy electrons are used for surface imaging. Due to the complex interaction process of low-energy electrons with matter, namely the structural and material-specific sensitivity as well as the strong and nonmonotonic energy-dependency [cf. Section 2.1], contrast can be established between almost any surface structures. Moreover, the combination of LEED with the spatial resolution of LEEM provides access to complementary real-space and reciprocal-space information on surface structures. Finally, in contrast to other surface techniques like scanning tunneling microscopy (STM), large scale surface areas (less than  $1\mu\text{m}$  up to  $\sim 100\mu\text{m}$ ) can be imaged *in situ* and in real time (without scanning) [86]. All these properties make LEEM an ideal tool both for surface characterization and for the investigation of dynamic processes such as adsorbate formation and structural transitions at surfaces.

### 2.3.1 Experimental setup and electron optics

The concept of LEEM was developed by Ernst Bauer and experimentally demonstrated in 1962 [87]. The first working instrument with a resolution of  $20\text{ nm}$  followed in 1985 [88]. To access both spatial and momentum information of the electrons, LEEM affords a more advanced optical system than conventional LEED. In the following, the instrumental realization of LEEM is introduced along with the experimental setup, based on Refs. [76, 89, 90].

The instrument used in this work, and shown in Fig. 2.5, is an aberration-corrected spectroscopic photoemission and low-energy electron microscope (AC-

### 2.3 Low-energy electron microscopy (LEEM)

SPELEEM III), produced by 'Elmitec Elektronenmikroskopie GmbH'. It is operated under ultra high vacuum (UHV) conditions with a base pressure in the range of  $10^{-10}$  mbar as required for electron optics and production and storage of UHV clean samples. Three chambers can be separated by valves: The sample preparation chamber with a storage, the main chamber with measuring stage and the electron optics column. An overview of the most important optical components is provided in Fig. 2.6. In order to keep the overview of the microscope's optics simple, some elements are not depicted. These are for example deflectors, which are used to align the beam along the optical axis of the microscope. Other elements, as the beam separators, the aberration correction mirror and the energy analyzer are much more complex than presented here. For more detailed information on electron optics, consider Refs. [74, 89].

A Schottky field emitter serves as electron source, providing a highly coherent electron beam with low energy dispersion. In order to keep optical aberrations low, the emitted electrons are accelerated to 20 keV and pass the electron optical

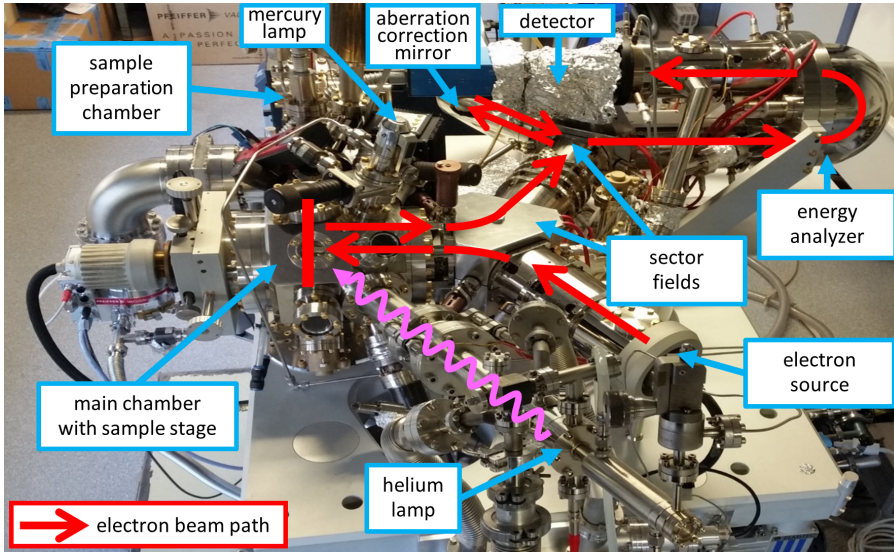


**Figure 2.5: Picture of the AC-SPELEEM instrument.** The setup consists of three UHV chambers: The sample preparation chamber, the main chamber with measuring stage, and the electron optics column. The latter consists of the electron source, two sector fields, the correction mirror, the energy analyzer and the detector. The beam path of the electrons is indicated by red arrows. It passes the electron optics column from source to detector, only entering the main chamber for interaction with the sample after passing the first sector field for the first time. Additionally, a helium lamp and a mercury lamp can be used for photoemission experiments.

components along the beam path as indicated by red lines in Fig. 2.5 and Fig. 2.6(a). After being focused into the back focal plane of the objective lens by the illumination optics, the beam is directed onto the sample in the main chamber. In contrast to other conventional electron microscope techniques, LEEM requires a normal incidence reflection geometry, and slow electrons to interact with the sample. The first aspect is realized by a magnetic sector field with a deflection angle of  $60^\circ$ , which serves as a beam separator for the incident and reflected electron beam. Passing through the objective lens at the entrance of the main chamber, the electrons hit the sample as a parallel beam. An electric field between objective lens and sample slows down the electrons from 20 keV to the required interaction energy of a few eV. After interacting with the sample's surface, the same electric field reaccelerates the electrons, which are then refocused in the back focal plane of the objective lens.

Being deflected by the first sector field again, the beam passes the intermediate optics towards a second sector field. Here, an aberration correction mirror is connected with the electron optics column in a similar geometry as the main chamber. The correction mirror allows to correct for spherical and chromatic aberrations which are caused mainly by the decelerating and accelerating field of the objective lens. Thereby, the lateral resolution can be improved to less than 2 nm [90, 91]. Depending on the operation mode of the second magnetic sector field, the LEEM instrument can be operated with or without correction mirror. Either way, the electrons leave the second sector field into the imaging column.

The lenses of the imaging column serve mainly for magnification and projection. As illustrated in Fig. 2.6(b,c), basically the focal length of the illumination lens (IL) decides if an image of the sample's surface or a diffraction plane is projected into the first projective lens (P1) and finally onto the detector. In this way, the operation mode of the instrument is changed between LEEM and LEED mode. Compared to conventional LEED (as introduced in the previous section), LEED measurements at a LEEM setup go along with a number of advantageous features. Due to the high acceleration of the electrons after interacting with the sample, the acceptance angle is almost  $180^\circ$  and LEED spots do not move when changing the electron energy, as it is the case in conventional LEED instruments [76]. Another feature are so-called  $\mu$ LEED measurements. By introducing the illumination aperture IA in the first sector field [cf. Fig. 2.6(a)], the spot size of the beam on the sample can be reduced to a minimum spot diameter of  $\sim 0.2 \mu\text{m}$ . In this way, small surface areas of different structures can be probed with LEED separately. Last but not least, the electron gun does not appear as a shadow in the pattern.

Subsequent to the imaging column, the electrons pass the hemispherical energy analyzer. With the energy slit at its exit, inelastically scattered electrons can be filtered. Moreover, it enables to use the setup also for photoemission electron spectroscopy (PES) experiments, as discussed in succeeding sections. Finally, the electron beam is projected onto a detector similar to the LEED setup: A microchannel plate (MCP) multiplies the electrons before the electrons hit the fluorescent screen which is imaged by a CCD camera from behind.

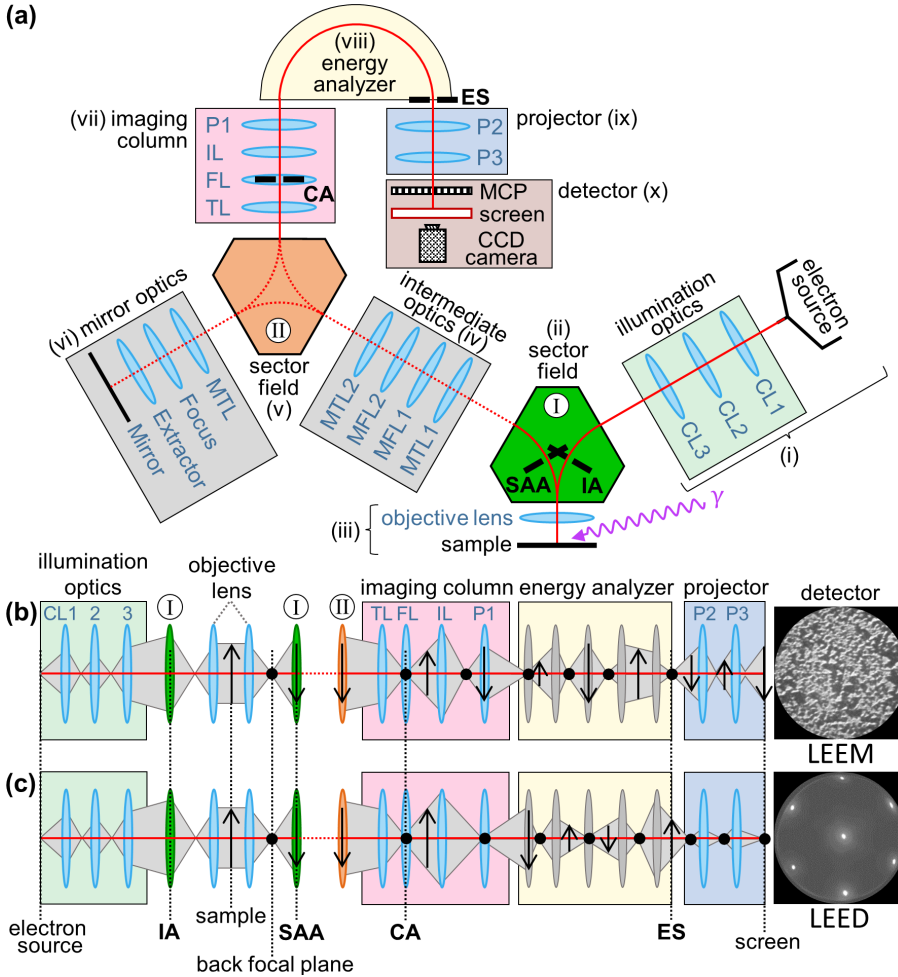


**Figure 2.6: LEEM electron optics.** (a) Overview of the most important components along the geometric beam path: (i) Electron source and illumination optics with three condenser lenses CL1-3. (ii) First sector field with illumination aperture (IA) and selected area aperture (SSA). (iii) Objective lens, sample and photon source ( $\gamma$ ). (iv) Intermediate optics with mirror field lenses (MFL1, MFL2) and mirror transfer lenses (MTL1, MTL2). (v) Second sector field. (vi) Mirror optics with mirror transfer lens (MTL), focus, extractor and mirror. (vii) Image column with transfer lens (TL), field lens (FL), contrast aperture (CA), illumination lens (IL) and projective lens (P1). (viii) Energy analyzer with energy slit (ES). (ix) Projector with projective lenses (P2 and P3). (x) Detector with microchannel plate (MCP), fluorescent screen and camera. (b) Reduced schematic of the LEEM operation mode. Black arrows represent image planes and black dots diffraction planes. An image of the sample's surface is projected onto the detector. (c) Same as (b) but for the LEED operation mode. Instead of the image plane, the back focal plane is projected onto the detector. The schematics in (b,c) are based on Ref. [92].

### 2.3.2 Contrast mechanisms and imaging parameters

A LEEM measurement basically records the specular reflectivity of a surface with spatial resolution. Consequently, contrast in LEEM imaging originates primarily from reflectivity variations between adjacent areas of different chemical and structural composition. This contrast mechanism is called amplitude or diffraction contrast. As discussed in Section 2.1, the reflectivity of a surface is not only structure- and material-specific but also depends strongly and nonmonotonically on the electrons' interaction energy. Therefore, the latter is a crucial parameter to generate contrast in LEEM. Experimentally, the electrons' interaction energy is resembled by the parameter  $U_{start}$ , which can be tuned by changing the bias between objective lens and sample. Note that LEEM is mainly conducted with very low-energy electrons as the high reflection intensities in this energetic range are beneficial for fast image acquisition [76]. In the following, the most important aspects of LEEM contrast and imaging are introduced, selected by relevance to the present work. For more detailed information refer to Refs. [76, 90, 93] and other cited literature.

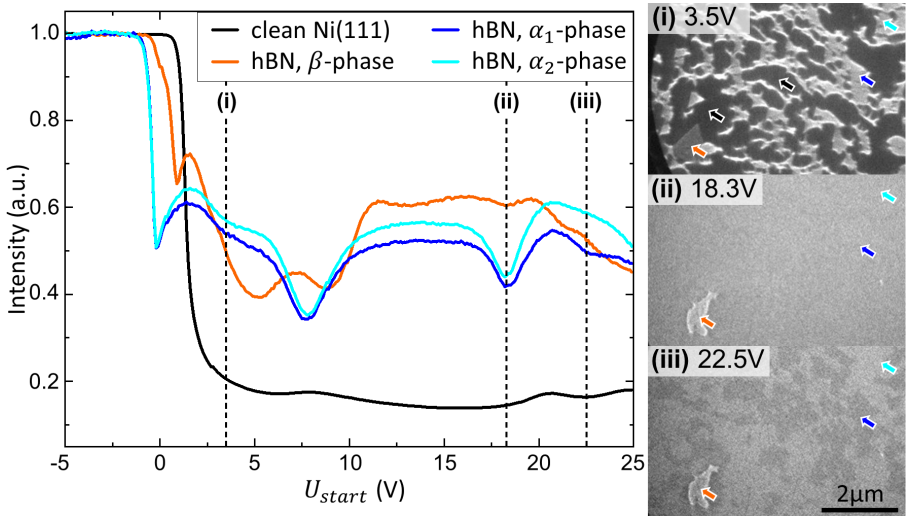


**Figure 2.7: Energy dependency of contrast in LEEM: LEEM-I(V) characterization of hBN grown on Ni(111).** Intensity vs. voltage curves evaluated from different surface areas, as indicated with colored arrows in the LEEM images (i-iii). **(i)** Growth of hBN islands (bright) on the Ni(111) surface (dark), imaged at  $U_{start} = 3.5$  V. **(ii)** The same surface area as (i), but after the surface is covered completely with hBN and imaged at  $U_{start} = 18.3$  V. Compared to (i), the contrast of  $\alpha$ -phase and  $\beta$ -phase hBN is inverted. **(iii)** The same as (ii) but imaged at  $U_{start} = 22.5$  V. Additional contrast arises within the  $\alpha$ -phase. Fig. 2.7 adapted with permission from Ref. [MR1]. © 2021 by the American Physical Society (see License Notice).

The energy dependence of LEEM contrast is commonly characterized by recording image series of the same surface region with varying  $U_{start}$ . By extracting the local intensity of selected areas and plotting it versus  $U_{start}$ , area-specific reflectivity spectra are obtained. These are also called LEEM-intensity-vs-start-voltage [LEEM-I(V)] spectra, in analogy to LEED-I(V). The general shape of LEEM-I(V) curves shows three characteristic features [cf. Fig. 2.7]. Firstly, at small and negative  $U_{start}$ , a plateau of maximum intensity occurs due to total reflection as the electrons have not enough energy to interact with the sample. With increasing  $U_{start}$ , the electrons eventually have enough energy to overcome the work function and interact with the surface. This results in the second feature, a drop of intensity at an energy directly related to the surface's work function. The third feature is the structure- and material-specific profile of the spectrum with increasing electron energy. With advanced approaches, LEEM-I(V) profiles have been used to extract detailed information on geometric and electronic structure as well as chemical composition of surfaces [94–97]. More directly, they can serve simply as a fingerprint to identify and differentiate surface structures. The LEEM-I(V) characterization of a surface is illustrated exemplary in Fig. 2.7 for the 2D-material hexagonal boron nitride (hBN) grown on a Ni(111) surface. The LEEM-I(V) curves of all observed surface structures are displayed, along with LEEM images for selected  $U_{start}$ . The contrast between Ni(111) and hBN in Fig. 2.7(i) is an example for material contrast, whereas the different hBN phases do not deviate from each other by their material composition but solely by their adsorption structure (for more details refer to Ref. [MR1]). Depending on the choice of  $U_{start}$ , the contrast in LEEM images can be inverted [cf. Fig. 2.7(i,ii)], canceled or enhanced [cf. Fig. 2.7(ii,iii)].

Another important contrast mechanism is phase contrast. It provides additional contrast when modifications of the phase of the imaging electron wave create intensity variations through interference [93]. In the following, its most prominent manifestations are introduced, namely step contrast and phase contrast. Here, the phenomena are illustrated using a simplified model. A more accurate and quantitative approach to phase contrast is derived in Ref. [93].

The phenomenon of step contrast is illustrated in Fig. 2.8(a). Electron waves which are reflected from the higher and lower terraces adjacent to an atomic step interfere with each other. The path length difference  $d$  is two times the step height  $a_0$  and corresponds to a relative phase shift of

$$\Delta\phi = kd = (2a_0/\hbar)\sqrt{2mE} \quad , \quad (2.10)$$

with  $k$ ,  $m$  and  $E$  being the free electron's wave vector, mass and energy, respectively [93]. For destructive interference, the step edges become visible as dark lines, as observed in Fig. 2.8(b) for a Ni(111) surface. The thinnest lines correspond to atomic steps, thicker lines to step bunches. In this way, imaging individual steps gives LEEM a sort of atomic resolution perpendicular to the surface. [76]

Note that three-dimensional surface structures such as hillocks, pits and step bunches produce gross features of contrast due to local field distortions which change the electron trajectory, an effect referred to as topographic contrast [71].

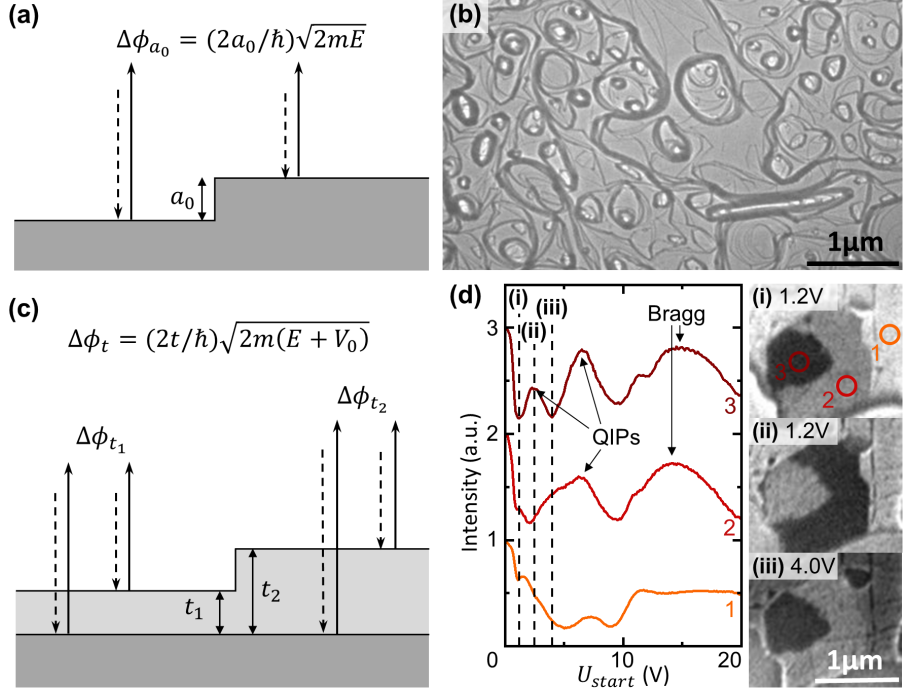


**Figure 2.8: Phase contrast in LEEM.** (a) Schematic of step contrast, based on Ref. [76]. Electron waves reflected from terraces on opposite sides of an atomic step interfere with each other. (b) Step contrast at a Ni(111) surface. The thinnest lines correspond to atomic steps, thicker lines to step bunches. (c) Schematic of quantum-size contrast, based on Ref. [76]. At a thin film, electron waves reflected from surface and buried interface interfere with each other. (d) LEEM-I(V) spectra for monolayer (orange), bilayer (red) and trilayer (brown) hBN on Ni(111), showing characteristic quantum interference peaks (QIPs). For clarity, the curves are shifted in intensity. The manifestation of quantum-size contrast is energy dependent, as illustrated by (i-iii) the corresponding LEEM images for different  $U_{start}$ . For more details on this sample system, refer to Ref. [MR2].

A second manifestation of phase contrast is quantum-size contrast. It is observed for thin adsorbate films of different thickness [93, 98]. Again using a simplified model as for step contrast, interference is considered between electron waves reflected from a thin film's surface and the interface of thin film and substrate in Fig. 2.8(c). Taking the inner potential  $V_0$  of the thin film into account and assuming free electron dispersion in the thin film, the resulting phase shift is

$$\Delta\phi = k'd = (2t/\hbar)\sqrt{2m(E + V_0)} \quad , \quad (2.11)$$

where  $k'$  is the wave vector in the thin film and  $d$  the path length difference of two

times the thin film thickness  $t$  [93]. Because the phase shift depends on film thickness  $t$  and energy  $E$ , the intensity is modulated periodically as a function of both film thickness and energy, such that, for an  $N$ -layer thick film,  $(N - 1)$  quantum interference peaks (QIPs) arise between consecutive Bragg peaks in LEEM-I(V) spectra [98]. This is illustrated by LEEM-I(V) measurements of differently thick hBN layers on a Ni(111) surface in Fig. 2.8(d). Due to the differences in reflectivity, energy-dependent contrast between films of different thickness is observed [cf. LEEM images (i-iii) in Fig. 2.8(d)]. It becomes apparent that the inelastic mean free path of electrons in solids increases significantly for very low electron energies. As a result, the probing depth may even extend up to tens of angstroms at the extreme low energy range below a few electron volts [76]. A more accurate and quantitative approach to phase contrast in Ref. [93].

Finally, the contrast in LEEM images can also be influenced by the focal condition of the objective lens. The focal length of the objective lens is varied by tuning its driving current  $I_{obj}$ . Depending on the focusing condition, the appearance of any surface structure might or might not change. This is illustrated in Fig. 2.9, where LEEM images of the hBN covered Ni(111) surface are shown, obtained in underfocus (a), focus (b) and overfocus (c). The majority of the surface is covered with  $\alpha$ -phase domains as introduced above. While these look similar in all pictures, the appearance of the  $\beta$ -phase domains changes strongly with the focal condition. While showing bright contrast and sharp edges in underfocus, they cannot be distinguished from the  $\alpha$ -phase in focus. In overfocus, they appear again, but oversized and showing inverted contrast. Note that focus in LEEM is (counterintuitively) identified by a minimum and/or change in contrast [99]. Therefore, many surface structures are often better visible in over- or underfocus. Throughout this work, different focal conditions were used to make the relevant objects better visible. While usually maintaining a realistic representation of object's sizes and shapes, sometimes small objects like nucleation sites are better visible when oversized [MR3].

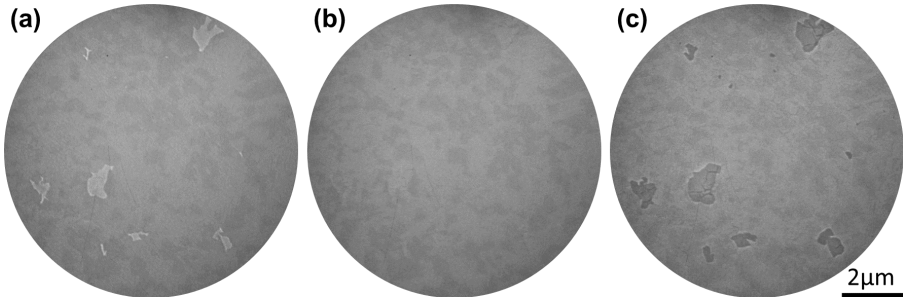


**Figure 2.9: Influence of the focusing condition on LEEM contrast.** The same surface area of hBN on Ni(111) is imaged for  $U_{start} = 20.0$  V in (a) underfocus ( $I_{obj} = 1884$  mA), (b) focus ( $I_{obj} = 1888$  mA) and (c) overfocus ( $I_{obj} = 1892$  mA).

### 2.3.3 Bright-field and dark-field LEEM

Specularly reflected electrons (00-beam) make up the largest component of the backscattered electrons [76]. In contrast to the diffracted electron beams, the 00-beam suffers the least from aberrations because it travels on the optical axis. Therefore, the resolution of LEEM images is improved when the diffracted beams are blocked by introducing the contrast aperture (CA) in the focal plane of the field lens (FL) [cf. Fig. 2.6] such that only the 00-beam contributes to imaging. A schematic of this so-called bright-field (BF-)LEEM imaging mode is shown in Fig. 2.10(a). Opposed to BF-LEEM, the use of non-specular diffracted electron beams for LEEM imaging is called dark-field (DF) imaging. This imaging mode is realized by simply changing the operation voltages of a set of deflectors in the incident beam path. In this way, the incident beam is tilted by the precise angle that places the desired non-specular diffracted beam (hk) along the optical axis [76], as shown in Fig. 2.10(b). In the resulting DF-LEEM image, any surface region that scatters strongly in the chosen diffraction condition will appear bright while regions that scatter weakly or for which the diffraction condition is forbidden will appear dark. This is illustrated in Fig. 2.11, where a full DF-LEEM characterization of hBN on Ni(111) is presented. Fig. 2.11(a) shows a BF-LEEM image of the area of interest.  $\alpha_1$ -,  $\alpha_2$ - and  $\beta$ -phases have been identified with LEEM-I(V), previously. The corresponding LEED pattern in Fig. 2.11(b) is composed of hexagonal groups of spots lying on a circle with similar radii but different azimuthal orientation. DF-LEEM imaging of spots A, B and C [cf. Fig. 2.11(c-e)] breaks the symmetry between the rotational equivalent  $\beta$ -phase domains [100], while  $\alpha_1$ - and  $\alpha_2$ -phase do not show any intensity. DF-LEEM imaging of spots 1 and 2 [cf. Fig. 2.11(f-g)] shows no intensity for the  $\beta$ -phase. The contrast of  $\alpha_1$ - and  $\alpha_2$ -phases is inverted but differently strong. The latter (and the remaining contrast in BF-LEEM) is an indication for nonequivalent adsorption configurations of  $\alpha_1$ - and  $\alpha_2$ -phase [MR1]. Finally, the surface composition can be summarized in a color composite image as shown in Fig. 2.11(g).

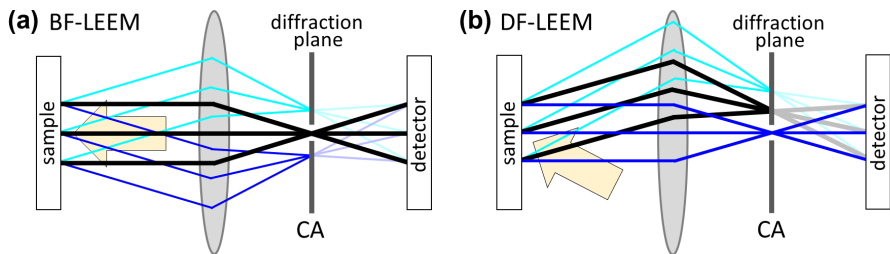


**Figure 2.10: Schematics of BF-LEEM and DF-LEEM imaging modes.** (a) BF-LEEM mode. The incident beam (yellow arrow) hits the sample's surface under normal incidence. Only the 00-beam passes the contrast aperture (CA) and is used for real-space imaging. (b) DF-LEEM mode. The incident beam is tilted such that a diffracted beam passes the contrast aperture. Based on Ref. [101].

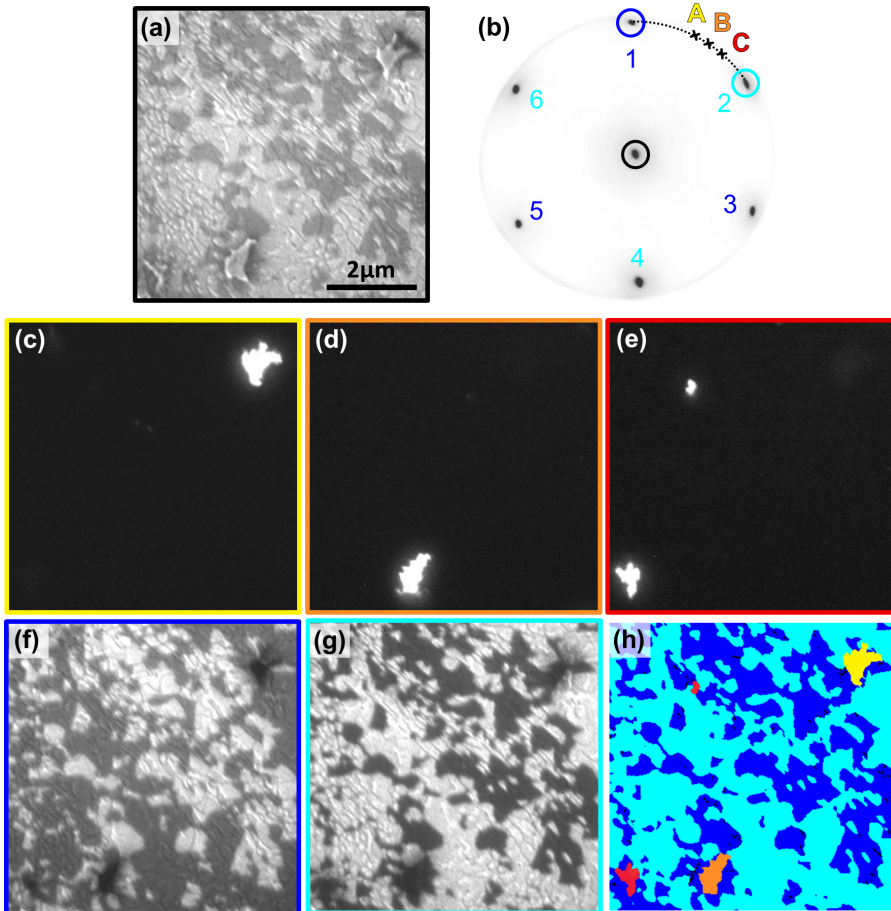


**Figure 2.11: DF-LEEM characterization of one layer hBN on Ni(111).** (a) BF-LEEM image taken at the same surface region as in Fig. 2.7. (b) LEED image of the corresponding surface area. The spots used for DF-LEEM characterization are highlighted. The LEED spots of the  $\alpha$ -phase (spots 1-6) superimpose with the hexagonal pattern of the Ni(111) surface. Spots of rotational equivalent  $\beta$ -phase domains A, B and C result into hexagonal patterns with similar lattice constant but rotated by  $27^\circ$ ,  $34^\circ$  and  $41^\circ$ , respectively. Their intensity is too low to be visible in the LEED pattern. (c-e) DF-LEEM images of the  $\beta$ -phase domains corresponding to the spots labeled A, B, and C in (b), respectively. (f,g) DF-LEEM images of spots 1 (symmetrically equivalent to 3 and 5) and 2 (symmetrically equivalent to 4 and 6), showing different contrasts for the two domains of the  $\alpha_1$ -phase and  $\alpha_2$ -phase. All images were taken with  $U_{start} = 60$  eV. (h) False-color composite image of all DF-LEEM images. Fig. 2.11 adapted with permission from Ref. [MR1]. © 2021 by the American Physical Society (see License Notice).

## 2.4 Probing surfaces with photoemission techniques

When a solid is illuminated with light of sufficiently high energy, electrons are emitted. This so-called photoelectric effect was first observed independently by Hertz [102] and Hallwachs [103] in the late 1880's. Shortly after, Einstein explained the effect by introducing the quantum nature of light, namely, the photon [104]. Today, experimental techniques based on the photoelectric effect are used routinely to probe the electronic structure of matter [105]. In photoelectron spectroscopy (PES), this is done by measuring the kinetic energy distribution of electrons emitted under exposure with monochromatic light and correlating it to the solid's electronic structure. Depending on the photon energy used in the experiment, it is differentiated between X-ray photoelectron spectroscopy (XPS), which probes deep core levels with photon energies in the range of 100 eV–10 keV, and ultraviolet photoelectron spectroscopy (UPS), which is used to study valence bands with photons in the ultraviolet (UV) spectral range of 10 eV–50 eV [80]. While the former allows access to electronic states of higher binding energy, the latter typically provides better energy resolution. In this work, UPS was performed with photons of 21.7 eV.

Fig. 2.12(a) illustrates the electronic structure of a metal surface, consisting of delocalized valence states and deeper lying, localized core levels. An electronic state's energy level is given by the so-called binding energy  $E_b$  relative to the Fermi energy  $E_F$ .<sup>1</sup> In the ground state, the electronic states are fully occupied up to the valence band edge at  $E_F$ . Commonly, the electronic structure is represented by the density of states  $N(E)$ , as shown in Fig. 2.12(b). In the simplified phenomenological three-step model [see Fig. 2.12(a)], the photoemission process is divided into three steps, the optical excitation of the electron within the bulk (1), its propagation to the surface (2), and the transition into vacuum (3). The photon is completely absorbed in the probabilistic excitation process. Therefore, energy conservation must be fulfilled:

$$E_{kin} = \hbar\omega - |E_b| - \Phi \quad , \quad (2.12)$$

where  $E_{kin}$  is the kinetic energy of the photoemitted electron,  $\hbar\omega$  the photon energy, and  $\Phi$  the work function, which is the energetic difference between  $E_F$  and the vacuum level  $E_{vac}$ . Photoemission is only possible if  $\hbar\omega$  exceeds the sum of  $|E_b|$  and  $\Phi$ . In the most simple approximation, the measured photoemission spectrum represents the density of states, as illustrated in Fig. 2.12(c). [105–107]

The propagation of the electron is considered in the second step of the three-step model. By inelastic scattering events, the photoelectrons lose energy and the information on their initial state. As discussed in Section 2.1, this effect scales with the energy-dependent inelastic mean free path, which is in the range of a few Å in UPS. On one hand, this makes UPS very surface-sensitive. On the other hand, the inelastically scattered electrons form a background of secondary electrons which increases towards the low  $E_{kin}$  cutoff in photoemission spectra [80, 107].

<sup>1</sup>Note that surface states might appear above  $E_F$ .

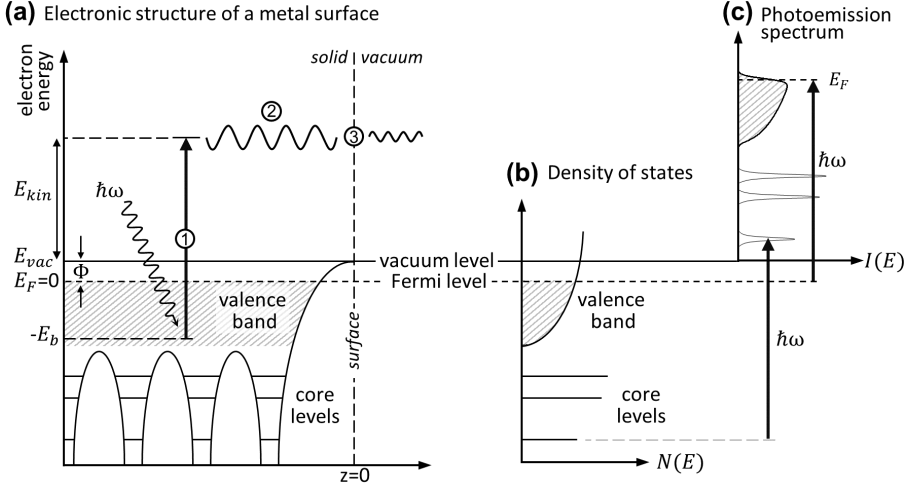


**Figure 2.12: The photoemission process.** (a) Schematic of the three-step model of photoemission: (1) optical excitation of an electron from the valence band, (2) propagation of the photoelectron to the surface, and (3) its transition into vacuum. Based on Ref. [107]. (b) The solid's density of states, which is directly reflected in (c) the photoelectron spectrum. Schematics (b,c) based on Ref. [108].

In the final step of the three-step model, the photoelectrons pass through the surface potential barrier into vacuum. Due to scattering at the surface potential, the photoelectron's wave vector in the crystal  $\mathbf{k}$  and in the vacuum  $\mathbf{K} = \mathbf{p}/\hbar$  are not equal [107]. Only the component parallel to the surface is conserved such that  $\mathbf{K}^{\parallel} = \mathbf{k}^{\parallel}$  [106] or

$$\mathbf{K}^{\parallel} = \mathbf{k}^{\parallel} + \mathbf{G}^{\parallel} \quad , \quad (2.13)$$

in the reduced zone scheme, where  $\mathbf{G}^{\parallel}$  is a two-dimensional reciprocal lattice vector [79, 107]. Note that in the excitation process itself, momentum conservation yields

$$\mathbf{k}_f - \mathbf{k}_i = \mathbf{k}_{\hbar\omega} \quad , \quad (2.14)$$

with the momentum of the photoelectron before transmission  $\mathbf{k}_f$ , the crystal momentum of the electron in its initial state  $\mathbf{k}_i$  and the photon momentum  $\mathbf{k}_{\hbar\omega}$ . However, the photon momentum is negligible small compared to the electron momenta in UPS [106]. Therefore, momentum-resolved photoemission experiments can directly access a solid's electronic band structure  $E(\mathbf{k})$  parallel to the surface.

Quantum-mechanically, the excitation process is correctly described by a one-step process in terms of an optical transition between the  $N$ -electron initial state  $\Psi_i^N$  and final state  $\Psi_f^N$ , each consisting of many-electron wave functions that obey appropriate boundary conditions at the surface of the solid. The photoemission intensity  $I(\mathbf{k}, E_{kin})$  is proportional to the transition probability  $w_{g \rightarrow f}$ , as given by Fermi's golden rule:

$$I(\mathbf{k}, E_{kin}) \propto w_{i \rightarrow f} = \frac{2\pi}{\hbar} |\langle \Psi_f^N | \hat{H}_{int} | \Psi_i^N \rangle|^2 \delta(E_f^N - E_i^N - \hbar\omega) \quad , \quad (2.15)$$

where the  $\delta$  function with initial and final-state energies of the  $N$ -electron system ( $E_i^N$  and  $E_f^N$ , respectively) ensures energy conservation [105, 107]. The interaction with the photon is treated as a perturbation, given by  $\hat{H}_{int}$  in its general form

$$\hat{H}_{int} = \frac{e}{2mc} (\mathbf{A} \cdot \hat{\mathbf{p}} + \hat{\mathbf{p}} \cdot \mathbf{A}) + \frac{e^2}{2mc^2} \mathbf{A}^2 \approx \frac{e}{mc} \mathbf{A} \cdot \hat{\mathbf{p}} \quad , \quad (2.16)$$

with  $\mathbf{A}$  being the electromagnetic vector potential of the incoming light, and  $\hat{\mathbf{p}}$  the electronic momentum operator [106]. The quadratic term in  $\mathbf{A}$  represents two photon processes. It becomes relevant only for high photon intensities and is therefore neglected [108]. Moreover, the commutator relation  $[\hat{\mathbf{p}}, \mathbf{A}] = -i\hbar(\nabla \cdot \mathbf{A})$  was used in equation 2.16. In the dipole approximation it is assumed that  $\mathbf{A}$  remains constant over atomic dimensions for photons in the UV range, therefore  $\nabla \cdot \mathbf{A} = 0$  applies [105, 106]. In the basic assumption (sudden approximation) of all photoemission theories, the transition process is considered instantaneous and interaction between the escaping photoelectron and the remaining system is neglected [105]. Hence, the  $N$ -electron final state  $\Psi_f^N$  can be expressed as a product of the one-electron wave function  $\psi_f^{\mathbf{k}}$  of the photoelectron with momentum  $\mathbf{k}$  and the final-state wave function  $\Psi_f^{N-1}$  of the remaining  $N - 1$  electrons. In analogy, the initial state  $\Psi_i^N$  is written as a product of the one electron wave function  $\psi_i^{\mathbf{k}}$  and the remaining  $(N - 1)$ -particle term  $\Psi_i^{N-1}$ . Consequently, the matrix elements in Eq. 2.15 can be written as

$$\langle \Psi_f^N | \hat{H}_{int} | \Psi_i^N \rangle = \frac{e}{mc} \langle \psi_f^{\mathbf{k}} | \mathbf{A} \cdot \hat{\mathbf{p}} | \psi_i^{\mathbf{k}} \rangle \langle \Psi_f^{N-1} | \Psi_i^{N-1} \rangle \quad , \quad (2.17)$$

where the first term contains the one-electron dipole matrix element and the second term is the  $(N - 1)$ -electron overlap integral [106]. In the frozen approximation, one assumes that the remaining  $(N - 1)$ -electron states do not change ( $\Psi_f^{N-1} = \Psi_i^{N-1}$ ), meaning that the overlap integral becomes unity. When Eq. 2.12 is included to reformulate the delta function of Eq. 2.15, the following expression results for the photoemission intensity:

$$I(\mathbf{k}, E_{kin}) \propto |\langle \psi_f^{\mathbf{k}} | \mathbf{A} \cdot \hat{\mathbf{p}} | \psi_i^{\mathbf{k}} \rangle|^2 \delta(E_b + \Phi + E_{kin} - \hbar\omega) \quad . \quad (2.18)$$

## 2.5 Angular-resolved photoemission spectroscopy

Fig. 2.13(a) displays a simplified schematic of a typical angular-resolved photoemission spectroscopy (ARPES) experiment. A beam of monochromatic light is generated, for example, by a gas discharge lamp, a synchrotron beamline or a laser, and directed on the sample [56, 109]. While the resulting photoelectrons escape in all directions, those which are emitted at an angle  $(\theta, \varphi)$  are collected by the energy analyzer. Here,  $\theta$  and  $\varphi$  are the polar and azimuthal emission angles as defined in Fig. 2.13(a). By tilting and rotating the sample with respect to its surface normal,  $\theta$  and  $\varphi$  are varied to obtain the angular-resolved three-dimensional spectral function  $I(\theta, \varphi, E_{kin})$ . The angle  $(\theta, \varphi)$  can easily be converted into the parallel momentum components  $\mathbf{k}^{\parallel} = \mathbf{k}_x + \mathbf{k}_y$  via the geometric relations [106]:

$$k_x = k \cdot \sin \theta \cos \varphi \quad \text{and} \quad k_y = k \cdot \sin \theta \sin \varphi \quad , \quad (2.19)$$

where the modulus of  $\mathbf{k}$  results from the kinetic energy by  $k = \sqrt{2m_e E_{kin}}/\hbar$ . ARPES data are commonly presented and discussed by slicing up the photoemission data cube of the momentum-resolved spectral function  $I(E_{kin}, k_x, k_y)$  into so-called band maps ( $I(E, k)$ ) or momentum maps ( $I(k_x, k_y)$  at constant energy). Spectra, also known as energy dispersive curves (EDCs), are often obtained by integration over certain angular ranges. As illustrated in Fig. 2.13(b), the accessible data cube is limited by the so-called photoemission horizon [106, 110, 111], given by

$$k^{\parallel}(E_{kin}) = k \cdot \sin \theta \quad \Rightarrow \quad k_{max}^{\parallel}[\text{\AA}^{-1}] = 0.511\sqrt{E_{kin}[\text{eV}]} \quad . \quad (2.20)$$

The ARPES measurements presented in Fig. 2.14 and Section 4.2 were done with the AC-SPELEEM III instrument introduced in Section 2.3.1. To this purpose, the illuminating electron beam is blocked completely with the illumination aperture (IA) [cf. Fig. 2.6]. Then, a photon source is employed to perform ARPES or

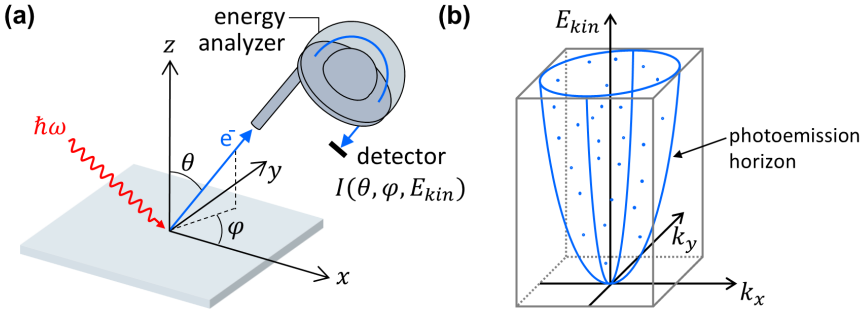


**Figure 2.13: Angular-resolved photoemission spectroscopy.** (a) Schematic illustration of ARPES. Under exposure of photons with energy  $\hbar\omega$ , electrons are ejected from the sample's surface. An energy analyzer collects photoelectrons at an angle  $(\theta, \varphi)$ . Based on Ref. [109]. (b) The photoemission data cube  $I(E_{kin}, k_x, k_y)$  is limited by the photoemission horizon. Based on Ref. [110].

photoemission electron microscopy (PEEM). The instrument is equipped with two photon sources: A mercury lamp provides a continuous spectrum and is mainly used for instrument alignment in PEEM mode, while a helium lamp provides monochromatic photons of 21.7 eV for spectroscopic surface characterization. In the electron optical system displayed in Fig. 2.6, the photoemitted electrons follow basically the same beam path as the diffracted electrons in LEEM. The investigated surface area is determined by the selected area aperture (SAA). It allows to perform spectroscopic measurements on surface regions with a minimum diameter of  $\sim 1.3 \mu\text{m}$ . By introducing the smallest energy slit (ES) at the energy analyzer's exit, an energy resolution of 0.2 eV is achieved. Finally, the photoelectron distribution in the  $k_x k_y$  plane is imaged in one shot by projecting the back focal plane onto the detector. Thus, unlike the conventional ARPES setup displayed in Fig. 2.13(a), this imaging technique does not require scanning in  $\theta$  and  $\varphi$  or rotating the sample. It is commonly referred to as momentum microscopy.

As an example, Fig. 2.14(a) shows a momentum map of graphene on SiC(0001), measured with the LEEM setup for  $U_{start} = 15.8 \text{ eV}$ . The first Brillouin zone (primitive unit cell in reciprocal space) of graphene is displayed schematically in the upper right. Its high symmetry points,  $\Gamma$ , K, and M, are indicated in both the schematic and the momentum map. To obtain the 3D spectral function  $I(E_{kin}, k_x, k_y)$ , an image series of momentum maps is recorded for varying  $U_{start}$  with a step size of 0.1 eV. Extracting the intensity along the  $\overline{\Gamma K}$  and  $\overline{KM}$  directions from each momentum map yields the band maps displayed in Fig. 2.14(b). The energy scale on the left is converted from  $U_{start}$  to  $E_{kin}$  using the energetic photoemission onset at the  $\Gamma$  point as reference for  $E_{kin} = 0 \text{ eV}$ . However, it is more common to use  $E_F$  as reference to express the energy in terms of the binding energy  $E_b$  (right).

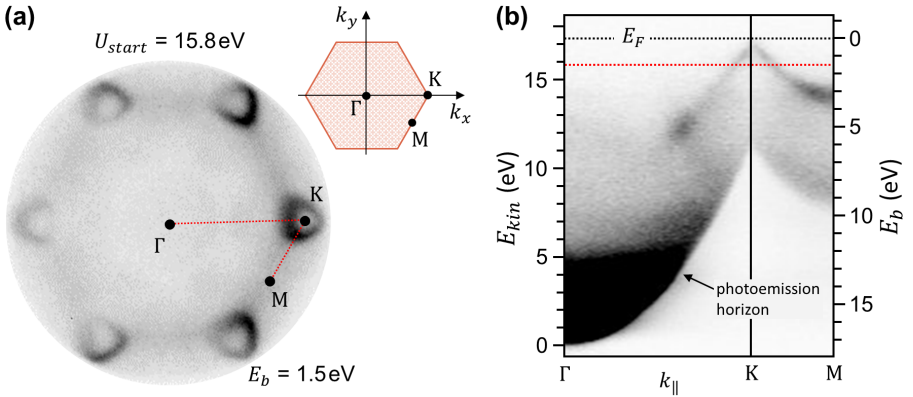


**Figure 2.14: ARPES data of graphene on SiC(0001) measured with the LEEM instrument.** (a) Momentum map, recorded for  $U_{start}=15.8 \text{ eV}$ . High symmetry points of the Brillouin zone (schematic in the upper right) are indicated. (b) Band maps in  $\overline{\Gamma K}$  and  $\overline{KM}$  directions.

## 2.6 Photoemission orbital tomography (POT)

POT is a combined theoretical and experimental approach based on ARPES, which investigates the electronic structure of surface-adsorbed molecules. While the electron density of extended periodic systems is described by a bandstructure with dispersion  $E(k)$ , molecules are finite systems which exhibit electronic states at discrete energies but with a specific spatial distribution, which is represented by single electron wave functions - the molecular orbitals [57]. The molecule's chemical, electronic and optical properties are primarily determined by its frontier orbitals, the highest occupied and the lowest unoccupied molecular orbital (HOMO and LUMO, respectively) [57, 112]. By measuring the orbital structure with ARPES and comparing the results with theoretical predictions from density functional theory (DFT), POT is used for example to determine molecular geometries, to identify unambiguously the orbital energy ordering, and to gain insight into the nature of the surface chemical bond [60].

Conceptually, POT is using the plane wave approximation for the final state of the photoemission process. This simplifies the transition matrix element introduced in Section 2.4, such that

$$I(\mathbf{k}, E_{kin}) \propto |\mathbf{A} \cdot \mathbf{k}|^2 |\tilde{\psi}_g(\mathbf{k})|^2, \quad (2.21)$$

where  $|\mathbf{A} \cdot \mathbf{k}|^2$  is the so-called geometry factor and  $\tilde{\psi}_g(\mathbf{k})$  is the Fourier transform of the initial state's wave function, i.e., a particular molecular orbital. Although being a strong simplification, the plane wave final state approximation is suited well to describe emissions from  $\pi$ -orbitals of planar organic molecules. [57, 59]

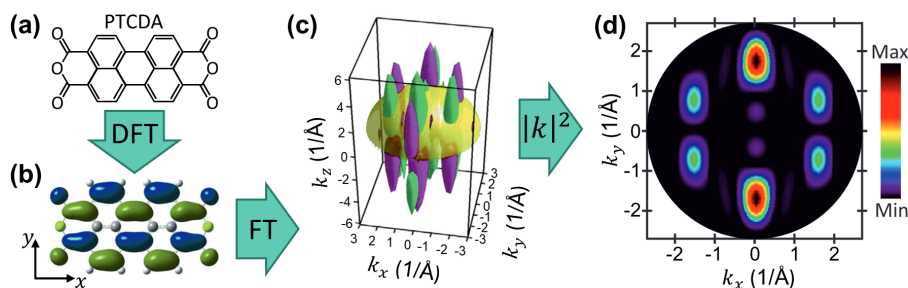


**Figure 2.15: Theoretical calculation of orbital tomography maps.** (a) Chemical structure model of PTCDA. (b) DFT-calculated real-space wave function of the LUMO of a gas phase PTCDA molecule. (c) Reciprocal-space representation of the LUMO, obtained by Fourier transforming (b). The colors in (b) and (c) represent the sign and phase of the wave function, respectively. The evaluation of the absolute square of (c) on the yellow hemisphere with radius  $k = \sqrt{2mE_{kin}}/\hbar$  and  $E_{kin} = 35$  eV results into (d) the simulated momentum map of the PTCDA LUMO. Fig. 2.15(b-d) adapted with permission from Ref. [112]. © IOP Publishing. All rights reserved. See License Notice.

The relationship described by Eq. 2.21 is of great advantage in the calculation of the theoretical photoemission signal, as illustrated for the LUMO of PTCDA in Fig. 2.15. First, the real-space representation of a free molecule's wave function is calculated by DFT (b). By Fourier transforming this wave function, its orbital representation in reciprocal (momentum) space is obtained (c). Here, the yellow hemisphere illustrates that the photoelectrons with a certain  $E_{kin}$  are detected in the experiment. Finally, evaluating the absolute square of the Fourier transform on this hemisphere yields the prediction for the intensity distribution in the experimental momentum map (d). [60, 112]

As an example, Fig. 2.16 presents experimental ARPES data of the model system PTCDA on Ag(110) [113]. In the band map and EDC displayed in Fig. 2.16(a), features of the metallic substrate (d-bands) and the molecule (M1-3) are distinguishable. The latter are located at discrete energy levels. By comparing experimental and theoretical momentum maps in Figs. 2.16(b,c), the molecular feature M1 is identified as the former LUMO (f-LUMO) of PTCDA. It became partially filled due to charge transfer across the metal-organic interface and hence visible in the photoemission experiment. By projecting the ARPES momentum maps on free-molecule orbitals, one can learn how close the true eigenstates of the coupled system are to those of the free molecule and can interpret energy shifts and broadenings in terms of molecule-substrate interactions [113].

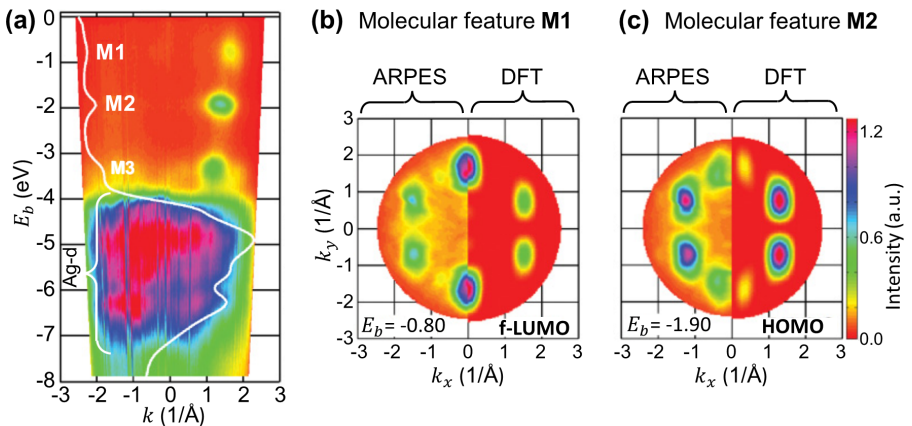


**Figure 2.16: Orbital tomography of PTCDA on Ag(110).** (a) Experimental band map of PTCDA on Ag(110), for an emission plane rotated by  $32^\circ$  with respect to the Ag[001] direction. The white line represents the  $k$ -integrated EDC. Molecular features (M1, M2 and M3) and the Ag  $d$ -bands are indicated. (b) Momentum map of the molecular feature M1, identified to be the partially filled f-LUMO of PTCDA. The measurement (left) is compared to the theoretical result for a free PTCDA molecule (right). (c) Same as (b) but for M2, which is identified as the HOMO of PTCDA. Fig. 2.16 adapted from Ref. [113], licensed under CC-BY 3.0.

## 2.7 Time-resolved photoemission experiments

In the photoemission experiments described so far, only the occupied and stationary electronic structure of surface structures can be probed. Beyond that, electronic excitation and relaxation dynamics are of high interest in today's research, as they play a crucial role for example in chemical reactions, electron transport through interfaces and surface recombination in semiconductor and optoelectronic devices. Such processes can be investigated with time-resolved photoemission experiments, which use two-photon photoemission. In the following, the basic principle is introduced based on Refs. [111, 114, 115].

### 2.7.1 Two-photon photoemission processes

With two-photon photoemission (2PPE), a pump-probe experiment can be performed as illustrated in Fig. 2.17. In the most simple picture, a first laser pulse (pump pulse) with photon energy  $\hbar\omega_a$  excites an electron from ground state  $|g\rangle$  below the Fermi level  $E_F$  into the formerly unoccupied intermediate state  $|e\rangle$  between  $E_F$  and the vacuum level  $E_{vac}$ . A second laser pulse (probe pulse) with photon energy  $\hbar\omega_b$  arrives at the surface with a time delay  $t_p$ . It lifts the electron to the final state  $|f\rangle$  above  $E_{vac}$ . This transiently excited photoelectron is then detected. Thereby, the usually unoccupied electronic structure of solid surfaces becomes accessible. In the following, it is assumed that the lifetime of the excited states significantly exceeds the pulse duration.

The energies of pump and probe pulse need to be chosen adequately. Considering the pump pulse,  $|e\rangle$  can only be transiently occupied if there exists an occupied state  $|g\rangle$  at  $\varepsilon_g = \varepsilon_e - \hbar\omega_a$ . A metallic substrate provides a continuum of possible initial states below  $E_F$ , therefore  $\hbar\omega_a > \varepsilon_e - E_F$  applies. In the special case of excitation from an isolated, narrow state  $|g\rangle$ , a pronounced resonance is observed [114]. At the same time, one-photon photoemission (1PPE) by the pump pulse needs to be suppressed as it would obscure the 2PPE signal. This is achieved by a pump energy  $\hbar\omega_a$  that does not exceed the surface's work function ( $\hbar\omega_a < E_{vac} - E_F$ ). Considering the probe pulse, its photon energy must be large enough to lift the electron from the excited state above the vacuum level ( $\hbar\omega_b > E_{vac} - \varepsilon_e$ ). Depending on the experiment, it is advantageous to avoid the 1PPE signal also from the probe pulse ( $\hbar\omega_b < E_{vac} - E_F$ ) or to use higher energies in order to access larger parallel momenta in angle resolved measurements [MR4, 66]. Note that the transition from initial state to final state can occur via two different pathways, namely via population of a real intermediate state (incoherent 2PPE) or via a direct two-photon transition involving a virtual intermediate state (coherent 2PPE) [116]. The latter is only observed during temporal overlap of pump and probe pulse.

Under these energetical considerations, 2PPE experiments combine the state selectivity of conventional photoemission with the time resolution of pump-probe laser experiments [111]. In Fig. 2.17(b), two data acquisition modes are illustrated. Energy-resolved 2PPE spectra (i) are recorded at a certain delay  $t_p$  between pump and probe pulse. In equivalence to 1PPE experiments, the energetic positions of

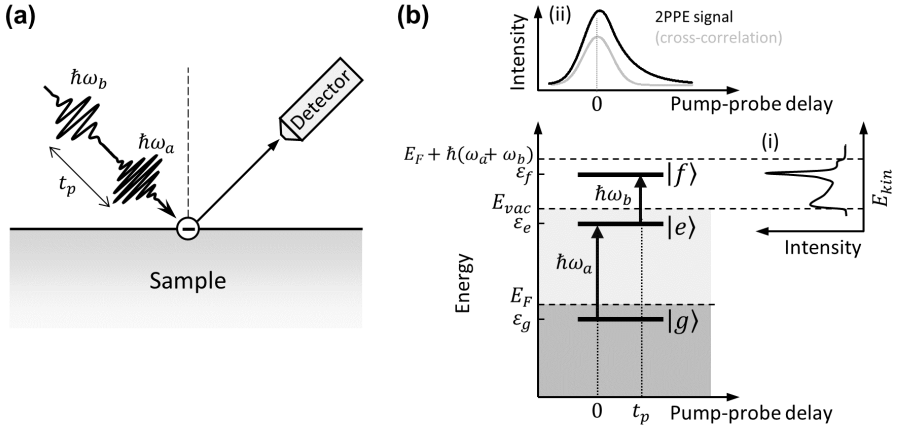


**Figure 2.17: The two-photon photoemission experiment.** (a) Simplified schematic of the measurement principle. A pump pulse of energy  $\hbar\omega_a$  and a probe pulse of energy  $\hbar\omega_b$  hit the sample with a temporal delay of  $t_p$ . The photoemitted electrons are detected. (b) Energetic three-level system of 2PPE. An electron is excited from the ground state  $|g\rangle$  to the excited state  $|e\rangle$  and final state  $|f\rangle$  by the pump and probe pulses, respectively. (i) Energy resolved 2PPE. An EDC is measured for a fixed delay time  $t_p$ . (ii) Time-resolved 2PPE. A delay curve (black) is measured for a fixed kinetic energy  $E_{kin}$ . The temporal overlap of pump and probe pulse is resembled by the cross-correlation curve (grey). Based on Ref. [111].

the photoemission features of interest are determined. With angular resolution, the latter can also be mapped in momentum space. The second acquisition mode is time-resolved 2PPE (ii). For a fixed kinetic energy, the 2PPE intensity is measured as a function of the pump-probe delay with femtosecond resolution [115]. In order to determine the delay, note that pump- and probe-pulse envelopes may be estimated as gaussian profiles with finite widths [111]. The temporal overlap is given by their symmetrical cross-correlation trace [gray profile in (ii)]. Its maximum denotes the optimum overlap between the laser pulses and is defined as zero delay ( $t_p = 0$ ). Per definition, the signal of a coherent 2PPE process is proportional to the cross-correlation of pump and probe pulse. Therefore, it is used to obtain the cross-correlation trace and to determine  $t_p = 0$  in the experiment [111].

Incoherent 2PPE processes involve a true intermediate level. The pump pulse does not immediately result into a population of the intermediate state. It rather creates a coherent superposition of initial and intermediate state, i.e., the electric field induces a polarization, which then leads to an incoherent change of the population of initial and intermediate state [117]. This dynamic process suffers from inelastic and elastic interaction with the environment. Thus, the dependence of the incoherent 2PPE signal on the pump-probe delay [black profile in (ii)] is more complex. Only after the pump pulse (or equivalently the cross-correlation) has

vanished completely, the excited state's lifetime can be extracted directly from the exponential decay [114]. In order to model time-resolved 2PPE spectra during temporal overlap, the density matrix formalism has been established [118, 119]. It is used to analyze time-resolved 2PPE spectra quantitatively over all pump-probe delays and thereby allows to separate inelastic and elastic scattering contributions to the excitation process.

### 2.7.2 Density matrix formalism for a three-level system

The theoretical model introduced in the following was used to model the time-resolved 2PPE spectra presented in Section 5.3.3. It is based on the well-known density matrix formalism for the phenomenological model of two-photon photoemission [111, 118–120].

**The equation of motion** Starting point is the Hamilton operator of the unperturbed and time independent three-level system

$$\hat{H}_0 = \sum_{i=g,e,f} \varepsilon_i |\varphi_i\rangle \langle \varphi_i| \quad \text{with} \quad \hat{H}_0 |\varphi_i\rangle = \varepsilon_i |\varphi_i\rangle \quad , \quad (2.22)$$

where  $\varepsilon_g$ ,  $\varepsilon_e$  and  $\varepsilon_f$  are the energy levels of ground state  $|\varphi_g\rangle$ , excited state  $|\varphi_e\rangle$  and final state  $|\varphi_f\rangle$ , respectively. When the optical excitation by the laser beams is turned on, the system couples via dipole interactions to the time dependent electric fields

$$\mathbf{E}_a(t) = \mathcal{E}_a(t) \mathbf{e}_a e^{i\omega_a t} + c.c. \quad \text{and} \quad \mathbf{E}_b(t - t_p) = \mathcal{E}_b(t - t_p) \mathbf{e}_b e^{i\omega_b(t - t_p)} + c.c. \quad (2.23)$$

of the pump and probe pulses [118]. They are characterized by the pulse envelopes  $\mathcal{E}_a(t)$  and  $\mathcal{E}_b(t - t_p)$ , the polarization vectors  $\mathbf{e}_a$  and  $\mathbf{e}_b$ , and the carrier frequencies  $\omega_a$  and  $\omega_b$ , respectively. Note that, the probe pulse arrives at delay time  $t_p$  with respect to the pump pulse. The Hamiltonian is now given by

$$\hat{H} = \hat{H}_0 + \hat{H}_{int} \quad \text{with} \quad \hat{H}_{int}(t) = -\hat{\boldsymbol{\mu}} \cdot \mathbf{E}(t) \quad , \quad (2.24)$$

where the interaction term  $\hat{H}_{int}(t)$  includes the transition matrix (or dipole operator)  $\hat{\boldsymbol{\mu}}$  with matrix elements  $\boldsymbol{\mu}_{ij}$  [119]. Furthermore, the energetic difference between the monochromatic pump and probe pulses is assumed significantly large, such that optical transitions only occur from  $|\varphi_g\rangle$  to  $|\varphi_e\rangle$  by the pump pulse and from  $|\varphi_e\rangle$  to  $|\varphi_f\rangle$  by the probe pulse [118]. Therefore,  $\hat{H}_{int}(t)$  is given by

$$\hat{H}_{int} = -|\varphi_g\rangle \langle \varphi_e| \boldsymbol{\mu}_{ge} \mathbf{E}_a(t) - |\varphi_e\rangle \langle \varphi_f| \boldsymbol{\mu}_{ef} \mathbf{E}_b(t - t_p) + h.c. \quad , \quad (2.25)$$

where  $h.c.$  is the hermitian conjugated of the preceding expressions. Relaxation was treated by considering an ensemble average of states  $|\varphi_i\rangle$  coupled to a bath. The time evolution of the optically excited system is then described by the Liouville-von-Neumann equation with density operator  $\hat{\rho}$  [119]:

$$\partial_t \hat{\rho} = \frac{1}{i\hbar} [\hat{H}, \hat{\rho}] + \partial_t \hat{\rho}^{relax} \quad . \quad (2.26)$$

In the matrix representation of the density operator  $\hat{\rho}$ , the diagonal elements  $\rho_{ii}(t)$  are the time-dependent populations  $n_i(t)$  of the states  $|\varphi_i\rangle$ . Off-diagonal elements  $\rho_{ij}(t)$  ( $i \neq j$ ) describe the optically induced coherent polarizations  $p_{ij}(t)$  between states  $|\varphi_i\rangle$  and  $|\varphi_j\rangle$ . The relaxation of the excited system is included phenomenologically with the dissipative part  $\hat{\rho}^{relax}$ . [118, 119]

**Phenomenological incorporation of relaxation processes** The diagonal relaxation terms  $\rho_{ii}^{relax}$  describe the energy relaxation of populations  $n_i(t)$  due to inelastic scattering [118]. This process is assumed to follow an exponential decay

$$\partial_t \rho_{ii}^{relax} = -\Gamma_i \rho_{ii} = -\frac{1}{T_i} n_i(t) \quad , \quad (2.27)$$

with relaxation rate  $\Gamma_i$  being the inverse inelastic lifetime  $T_i$  of state  $|\varphi_i\rangle$  [118]. Equivalently, the off-diagonal terms  $\hat{\rho}_{ij}^{relax}$  ( $i \neq j$ ) describe the loss (dephasing) of the polarization  $p_{ij}(t)$  by

$$\partial_t \rho_{ij}^{relax} = -\Gamma_{ij} \rho_{ij} = -\frac{1}{T_{ij}} p_{ij}(t) \quad . \quad (2.28)$$

Here, the decoherence rate  $\Gamma_{ij}$  (or total dephasing rate) is the inverse decoherence time  $T_{ij}$ . It has contributions due to both the inelastic decay of the population of the involved states and elastic scattering, so-called pure dephasing [119]. It can be written as

$$\Gamma_{ij} = \frac{1}{T_{ij}} = \frac{1}{2} \left( \frac{1}{T_i} + \frac{1}{T_j} \right) + \frac{1}{T_{ij}^*} \quad , \quad (2.29)$$

where  $1/T_{ij}^*$  is the pure dephasing rate of the polarization  $p_{ij}(t)$  [118, 119]. It is further decomposed into

$$\frac{1}{T_{ij}^*} = \frac{1}{T_i^*} + \frac{1}{T_j^*} \quad , \quad (2.30)$$

with  $T_i^*$  and  $T_j^*$  being the pure dephasing times of states  $|\varphi_i\rangle$  and  $|\varphi_j\rangle$  [117, 118].

In the 2PPE experiment, electrons in the ground state  $|\varphi_g\rangle$  do not suffer from relaxation per definition. Therefore, the inelastic lifetime  $T_g$  is considered infinite. Moreover, electrons that are excited into the final state above the vacuum level are captured by the detector. Consequently, both the inelastic lifetime  $T_f$  and the pure dephasing time  $T_f^*$  are also considered as infinite. Summarizing, the relaxation term in Eq. 2.26 is given by

$$\partial_t \hat{\rho}_{ij}^{relax} = -\Gamma_{ij} \hat{\rho}_{ij} \quad \text{with} \quad \Gamma = \begin{pmatrix} 0 & \frac{1}{2T_e} + \frac{1}{T_g^*} + \frac{1}{T_e^*} & \frac{1}{T_g^*} \\ \frac{1}{2T_e} + \frac{1}{T_g^*} + \frac{1}{T_e^*} & \frac{1}{T_e} & \frac{1}{2T_e} + \frac{1}{T_e^*} \\ \frac{1}{T_g^*} & \frac{1}{2T_e} + \frac{1}{T_e^*} & 0 \end{pmatrix} \quad , \quad (2.31)$$

where the damping matrix  $\Gamma$  is expressed in terms of the lifetime  $T_e$  of the excited state and the pure dephasing times  $T_g^*$  and  $T_e^*$  of ground state and excited state [111, 120].

**Applying perturbation theory** In order to solve the Liouville-von-Neumann equation, Ueba and coworkers [118] apply the perturbation expansion as illustrated in the following. The density operator  $\hat{\rho}$  is expanded into powers of  $\mathbf{E}(t)$ :

$$\hat{\rho} = \hat{\rho}^{(0)} + \hat{\rho}^{(1)} + \hat{\rho}^{(2)} + \hat{\rho}^{(3)} + \dots \quad \text{with} \quad \hat{\rho}^{(n)} \propto (\mathbf{E}(t))^n \quad . \quad (2.32)$$

This expansion is entered in the Liouville-von-Neumann equation (Eq. 2.26). Considering that  $\hat{H} = \hat{H}_0 + \hat{H}_{int}$  with  $\hat{H}_{int} \propto \mathbf{E}(t)$  and  $\partial_t \hat{\rho}^{relax} = -\hat{\Gamma} \hat{\rho}$ , the terms of the Liouville-von-Neumann equation can be sorted by their power  $n$  in  $\mathbf{E}(t)$  and are solved iteratively:

$$1^{st} \text{ order} : \quad \partial_t \hat{\rho}^{(1)} = \frac{1}{i\hbar} ([\hat{H}_0, \hat{\rho}^{(1)}] + [\hat{H}_{int}, \hat{\rho}^{(0)}]) - \hat{\Gamma} \hat{\rho}^{(1)} \quad \propto \mathbf{E}(t) \quad , \quad (2.33)$$

$$2^{nd} \text{ order} : \quad \partial_t \hat{\rho}^{(2)} = \frac{1}{i\hbar} ([\hat{H}_0, \hat{\rho}^{(2)}] + [\hat{H}_{int}, \hat{\rho}^{(1)}]) - \hat{\Gamma} \hat{\rho}^{(2)} \quad \propto (\mathbf{E}(t))^2 \quad , \quad (2.34)$$

...

$$n^{th} \text{ order} : \quad \partial_t \hat{\rho}^{(n)} = \frac{1}{i\hbar} ([\hat{H}_0, \hat{\rho}^{(n)}] + [\hat{H}_{int}, \hat{\rho}^{(n-1)}]) - \hat{\Gamma} \hat{\rho}^{(n)} \quad \propto (\mathbf{E}(t))^n \quad . \quad (2.35)$$

As initial condition, the density matrix  $\hat{\rho}^{(0)}$  describes the unperturbed system where the ground state is fully populated and no excitation into the higher energy levels has occurred, yet:

$$\hat{\rho}^{(0)} = |\varphi_g\rangle \langle \varphi_g| \quad . \quad (2.36)$$

Starting with Eq. 2.33,  $\hat{H}_0$  [cf. Eq. 2.22],  $\hat{H}_{int}$  [cf. Eq. 2.25] and  $\hat{\rho}^{(0)}$  [cf. Eq. 2.36] are applied as introduced above. This yields a differential equation for  $\rho_{ge}^{(1)}(t) = p_{ge}^{(1)}(t)$ :

$$\partial_t p_{ge}^{(1)}(t) = i(\varepsilon_g - \varepsilon_e) p_{ge}^{(1)}(t) - \frac{i}{\hbar} \boldsymbol{\mu}_{ge} \mathbf{E}_a(t) - \Gamma_{ge} p_{ge}^{(1)}(t) \quad , \quad (2.37)$$

which represents an optically induced polarization between ground state and excited state in the first order of the electric field of the pump laser, as illustrated in Fig. 2.18(a). In second-order perturbation theory, Eq. 2.34 yields a differential equation for  $\rho_{ee}^{(2)}(t) = n_e^{(2)}(t)$ :

$$\partial_t n_e^{(2)}(t) = \frac{i}{\hbar} \left( (\boldsymbol{\mu}_{ge} \mathbf{E}_a(t))^* p_{ge}^{(1)}(t) - \boldsymbol{\mu}_{ge} \mathbf{E}_a(t) (p_{ge}^{(1)}(t))^* \right) - \Gamma_e n_e^{(2)}(t) \quad . \quad (2.38)$$

Phenomenologically, this means that the polarization  $p_{ge}^{(1)}(t)$  is converted into an excited state population  $n_e^{(2)}(t)$  in the second order of the electric field of the pump laser.

Up to fourth-order perturbation theory, differential equations are derived for polarization and population terms as illustrated in Fig. 2.18(a-d). With  $n_f^{(4)}$ , an expression for the population of the final state is obtained. Perturbation expansion up to fourth order results into a set of nine coupled differential equations. These so-called Optical Bloch equations were solved numerically by applying the rotating wave approximation that eliminates fast variations of  $\mathbf{E}(t)$  with the carrier frequencies  $\omega_a$  and  $\omega_b$ . In order to model 2PPE spectra, note that the measured photon intensity is described by the population of the finite state in the limit of  $t \rightarrow \infty$ .

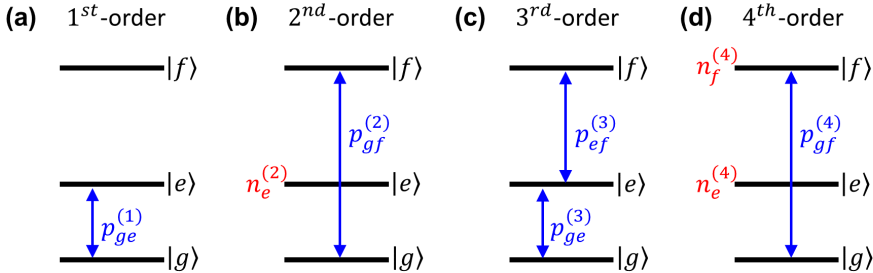


**Figure 2.18: Polarization and population terms derived by perturbation theory (PT) up to 4<sup>th</sup> order.** (a) 1<sup>st</sup>-order PT results into a polarization between  $|g\rangle$  and  $|e\rangle$ . (b) 2<sup>nd</sup>-order PT results into a population of  $|e\rangle$  and a polarization between  $|g\rangle$  and  $|f\rangle$ . (c) 3<sup>rd</sup>-order PT results into a population of  $|e\rangle$  and polarizations between  $|g\rangle$  and  $|e\rangle$ , and  $|e\rangle$  and  $|f\rangle$ , respectively. (d) 4<sup>th</sup>-order PT results into populations of  $|e\rangle$  and  $|f\rangle$ , and a polarization between  $|g\rangle$  and  $|f\rangle$ .

### 2.7.3 Experimental setup

The setup of the time-resolved momentum microscope is introduced, as used for the time-resolved POT (tr-POT) measurements presented in Section 5.3. It was build and operated by the Surface & Interface Science Department at the Philipps-Universität Marburg. The laser setup is based on the work of Heyl et al. [121].

On the illumination side, two pulsed photon beams with a well defined and controllable temporal delay are required for time-resolved measurements. Energetically, the pump beam needs to be tunable in the visible range to match the HOMO-LUMO transition of the investigated molecules and the probe beam needs to be of sufficiently high energy to probe the photoemission features characteristic for the molecular orbitals of interest. This is realized with the optical setup displayed in Fig. 2.19(a). A Ti:sapphire regenerative amplifier, operated at 200 kHz, provides pulsed laser light of 800 nm wavelength, 40 fs pulse duration and 8  $\mu$ J pulse energy. This laser beam is split into pump and probe branch with an intensity ratio of 7:3. The wavelength of the pump beam can be adjusted in the range of 480-700 nm, using an optical parametric amplifier (OPA). For the HOMO-LUMO transition of the PTCDA molecule, a wavelength of 540 nm and a pulse duration of 50 fs is used. Before entering the vacuum chamber through a glass window and being directed onto the sample, the temporal delay of the pump pulses with respect to the probe pulses is controlled by a linear delay stage. It basically tunes the delay time  $t_p$  by changing the optical path length. On the probe branch, after further amplification and frequency doubling, the probe beam is focused into a krypton gas jet inside the vacuum chamber. By high-harmonic generation (HHG), the 7<sup>th</sup> harmonic with a wavelength of 57 nm is obtained [122]. This corresponds to a photon energy of 21.7 eV, which makes it possible to access high parallel momenta in reciprocal space up to  $\sim 2 \text{ \AA}^{-1}$ . The residual adjacent harmonics are suppressed using multilayer mirrors and the residual 400 nm beam is blocked with

an Al-filter. The probe pulses have a temporal width of 20 fs. Both pump and probe beams enter the momentum microscope on the same trajectory and hit the sample under an angle of  $70^\circ$  from the surface normal.

On the detection side [see Fig. 2.19(b)], a PEEM lens system is used to project the photoemitted electrons onto a time- and position-sensitive delay-line detector [123]. Instead of using a hemispherical analyzer, the energy resolution is obtained by a time-of-flight measurement. To this end, a drift tube of 1 m length is implemented between lens system and detector. The time of flight is then converted to  $E_{kin}$ . Very low-energy electrons are suppressed by a biased mesh in front of the detector. Overall, this setup allows to measure the 3D data set  $I(E_{kin}, k_x, k_y)$  for each pump-probe delay time  $t_p$  in one shot, with an energy resolution of 150 meV and a momentum resolution better than  $0.01 \text{ \AA}^{-1}$ .

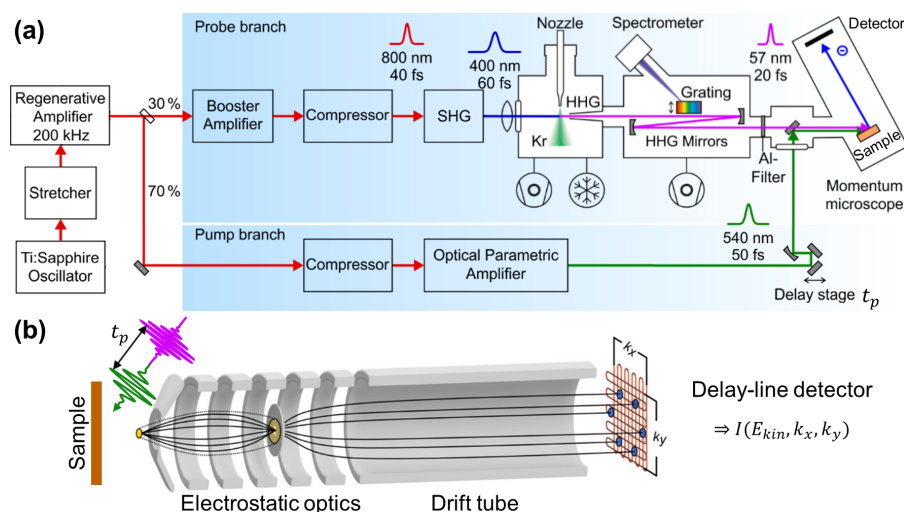


**Figure 2.19: Experimental setup of the time-resolved momentum microscope.** (a) Schematic of the light-optical illumination setup. A pulsed laser beam of 800 nm wavelength is split into a pump and a probe branch. After compression, visible pump pulses are provided by an optical parametric amplifier operated at 540 nm. The probe beam is further amplified, compressed and frequency-doubled (by second harmonic generation, SHG) before obtaining a laser beam of 57 nm wavelength through high-harmonic generation (HHG). The delay between pump and probe pulses is controlled with the delay stage. Fig. 2.19(a) adapted from the Supplementary Material of Ref. [MR4]. Reprinted with permission from AAAS (see License Notice). (b) Schematic of the electron-optical detection setup. The photoelectrons are imaged onto the time- and position-sensitive delay-line detector by electrostatic optics. In combination with the drift tube, time-of-flight measurements allow for spectroscopic analysis. Fig. 2.19(b) courtesy of Robert Wallauer from Philipps-Universität Marburg.



# Chapter 3

## Boron Nitride on 6H-SiC(0001)

In the field of van der Waals heterostructures, twisted bilayer graphene (TBLG) has been found to exhibit intriguing electronic properties that strongly depend on the exact twist angle[33]. Usually, the latter can only be controlled by manually stacking monolayers of exfoliated graphene. Recently, however, a promising way has been found to obtain TBLG with a twist angle of exactly  $30^\circ$  by epitaxy and intercalation, offering advantages in quality and scaling [41, 53, 54]. It is based on the sublimation growth of graphene on SiC, which produces multilayers of graphene without twist. Under the influence of borazine, a precursor commonly used in hBN growth, the topmost graphene layer is twisted by  $30^\circ$  with respect to conventionally oriented graphene layers below. A pre-step in understanding this process is to investigate the formation of boron nitride (BN) on SiC when exposed to borazine at temperatures below  $1150^\circ\text{C}$  [MR5]. In the present work, LEEM is used to observe BN formation on SiC in-situ and in real-time. New insights into the growth process, domain structure and temperature dependence of different BN phases are achieved.

In the first section of this chapter, the growth experiment of BN on 6H-SiC(0001) is introduced. The experimental procedure used in this work is based on the work of Lin et al. [MR5], which is briefly summarized. Prior to BN growth, a Si-rich (3x3) reconstruction is prepared. Its structure and terrace configuration are characterized by LEEM and LEED. In Section 3.2, LEEM and LEED observations during the in-situ growth experiment of BN on SiC are presented. In the following section, the composition of BN on SiC is analyzed. A complex lateral domain structure is found, consisting of five surface phases, which are identified by their LEEM and LEED characteristics. Finally, the temperature dependence of BN formation is discussed in Section 3.4. By increasing the heating rate during BN preparation, all but one of the surface phases could be suppressed. However, observations during the in-situ growth experiments suggest that temperature alone is not the critical parameter in this process.

Please note that the data presented in this chapter were collected under my guidance as a project for the master thesis of Hao Yin [124].

### 3.1 Introduction to the experiment

Borazine ( $B_3H_6N_3$ ) is the most commonly used precursor gas for epitaxial growth of hBN by chemical vapor deposition (CVD) [125]. Due to the high interest in hBN as the insulating counterpart of graphene in vdW heterostructures, the epitaxial growth of hBN on various transition metal surfaces has been frequently studied ([MR1, MR3, MR6, 126–129] and references in [125]). Throughout the CVD growth process, borazine is adsorbed and catalytically decomposed on the hot metal surface, followed by diffusion and nucleation or incorporation of the mobile surface species into the growing film [127]. For sufficiently low borazine pressure, the growth rate is found to be proportional to the uncovered metal surface area, so the growth self-terminates at one atomic layer thickness [MR3, MR6, 126–129]. This is attributed to the inertness of the already grown hBN to borazine adsorption and decomposition in contrast to an uncovered hot metal surface [125, 127]. Furthermore, the BN growth rate was found to increase with temperature [130].

The desire to implement hBN in electronic devices has sparked interest in growing it directly on SiC, a substrate commonly used in the semiconductor industry [52]. Note that the temperatures required for CVD growth of hBN from borazine are high enough to cause sublimation of the substrate species. This process does not hinder the growth of hBN on metal surfaces, as was observed *in situ* during hBN growth on Cu(111) [MR3]. In the case of a SiC substrate, the carbon vapor pressure is insignificant compared to that of silicon [13]. Consequently, when SiC is annealed in vacuum, the silicon atoms sublime, leaving an excess of carbon atoms on the surface that form graphitic layers. This mechanism is commonly used to grow epitaxial graphene on SiC in the conventional orientation of  $30^\circ$  with respect to the SiC substrate lattice (Refs. [50, 51] and references therein). Therefore, it is of interest to suppress graphitization when growing BN on SiC. However, BN on SiC can also be replaced by graphene when the annealing temperature is exceeded. This has been reported under vacuum conditions [41, 52] and during borazine exposure [MR5, 53]. Interestingly, B and N atoms are replaced by excess C within their original structure, which is aligned with the SiC substrate. The resulting graphene layer is therefore referred to as Gr- $R0^\circ$ , while the conventionally oriented epitaxial graphene is referred to as Gr- $R30^\circ$ .

The present work is based on that of Lin et al. [MR5], where BN was grown on a 6H-SiC(0001) surface by CVD with the precursor gas borazine. To prevent graphitization of the surface prior to BN growth, the SiC surface was exposed to a Si flux at  $880^\circ\text{C}$  for 30 min to create a Si-rich ( $3 \times 3$ ) reconstruction on the SiC surface. At a temperature below  $880^\circ\text{C}$ , the Si exposure was stopped and borazine was introduced into the experimental chamber. The Si flux was stopped at a temperature below  $880^\circ\text{C}$ , and a borazine partial pressure of  $1.5 \times 10^{-6}$  mbar was applied. The sample temperature was then immediately raised to the desired value and held stable for 30 min. It is assumed that upon Si depletion, the ( $3 \times 3$ ) reconstruction quickly evolves into a less Si-rich and very reactive Si-rich ( $\sqrt{3} \times \sqrt{3}$ )- $R30^\circ$  reconstruction on which the BN layer forms. After cooling to

room temperature, the samples were characterized using LEED, ARPES, and the normal incidence X-ray standing wave (NIXSW) technique (a method for probing vertical distances with chemical sensitivity). It was found, that a  $B_xN_y-R0^\circ$  layer forms in the range of 1100-1150°C. While it is composed of B and N atoms (of unclear stoichiometry  $x : y$ ) and has a hexagonal structure that is aligned with the substrate (rotated by  $0^\circ$ ), it does not exhibit the typical band structure, bonding distance, and stability in air, as would be expected for a 2D hBN layer. At the interface of  $B_xN_y-R0^\circ$  and SiC, a boron buffer layer resides. This buffer layer has no long-range order and is therefore undetectable by LEED. It was also found that a  $\begin{pmatrix} 3 & 1 \\ -1 & 2 \end{pmatrix}$  superstructure coexists with  $B_xN_y-R0^\circ$  at temperatures below 1150°C. However, it vanished with increasing preparation temperature and disappeared completely at 1150°C, which is before the replacement of  $B_xN_y-R0^\circ$  by graphene.

With the sublimation of Si at elevated temperatures and the coexistence of two surface phases ( $B_xN_y-R0^\circ$  and the commensurate surface reconstruction), BN growth on SiC is a complex experiment attractive for LEEM studies. LEEM enables in-situ observation of the growth experiment, while switching between LEEM and LEED modes within a short time. Furthermore, the domain structure and electronic properties can be probed locally by  $\mu$ LEED, DF-LEEM and LEEM-I(V) on areas of less than 1  $\mu\text{m}$  up to tens of  $\mu\text{m}$ . This allows a more detailed insight into the structure and formation process of the two BN phases and their temperature dependence.

While the experimental procedure of Lin et al. [MR5] is generally followed in this work, adjustments are required to adapt to the different experimental conditions at the LEEM instrument. Hence, the  $(3 \times 3)$  reconstruction is prepared in a separate preparation chamber and allowed to cool to room temperature. The SiC(0001) surface is then characterized prior to the BN growth experiment. To correctly interpret the LEEM features of BN on SiC, the structure of the Si-rich  $(3 \times 3)$  reconstructed SiC substrate and the associated LEEM features are discussed in the following.

#### 3.1.1 The Si-rich $(3 \times 3)$ surface reconstruction of 6H-SiC(0001)

SiC surfaces which have been exposed to air need cleaning before they can be used for the preparation of the Si-rich  $(3 \times 3)$  surface reconstruction. By annealing in vacuum, contamination and surface oxides can easily be removed. However, Si atoms do also desorb from the surface at elevated temperatures. From literature it is well known that upon increasing Si depletion, the SiC surface evolves through different carbon rich surface reconstructions depending on the Si:C ratio on the surface. Prolonged annealing leads to graphite formation. For producing the Si-rich  $(3 \times 3)$  reconstruction, this process must be prohibited and turned into a Si enrichment by supplying extra Si atoms during the annealing process. The most Si-rich surface reconstruction is the  $(3 \times 3)$ -Si reconstruction [131].

In this work, the as-purchased SiC wafer was mounted onto the LEEM sample

holder without further treatment and transferred into the preparation chamber of the LEEM setup. For cleaning and outgasing, the sample was then annealed at 600°C for 30 min. Subsequently, the (3×3)-Si reconstruction was prepared. To this end, the sample was annealed at a temperature of 900°C for 30 min, using combined filament and e-beam heating. During the annealing process, extra Si is supplied by operating a self-built Si evaporator. The latter consists of a Si wafer piece heated by direct current up to ~1200°C that is mounted ~8 cm above the sample. After cool down, the sample is transferred to the main chamber and characterized with LEEM and LEED.

In Fig. 3.1(a), a representative LEEM image of the (3×3)-Si reconstructed SiC surface is shown. It is dominated by terraces, which appear as stripes of varying intensity (discussed below) that run straight and parallel across the whole sample. Additionally, a number of small bright objects is distributed randomly across the surface. They are compact and of similar size, some showing a triangular shape (e.g. those marked with yellow and orange ellipses) or a cross-like imaging artifact (bottom-right from the orange ellipse) stemming from astigmatism.

The structure of the surface was characterized with  $\mu$ LEED. Illumination apertures of different size were used to select areas of interest, as indicated by colored ellipses in Fig. 3.1(a). First, the surface region marked by the black ellipse is considered. It encloses only terraces free from bright objects. The corresponding LEED image in Fig. 3.1(b) shows the characteristic pattern of a (3×3) reconstruction with the SiC first-order diffraction spots indicated by black dotted circles. With a smaller aperture, areas were selected that enclose single bright objects. The diffraction pattern which corresponds to the yellow ellipse is displayed in Fig. 3.1(c). In addition to the (3×3) pattern, other diffraction spots appear. The brightest are highlighted with red circles and form a hexagonal pattern. Compared to SiC, its reciprocal translation vectors are shorter by a factor of ~0.8 and rotated by +2.5°. Moreover, a set of weaker diffraction spots forms a (7×7) reconstruction. A similar LEED pattern is found for the surface area marked with an orange ellipse in Fig. 3.1(a) and shown in Fig. 3.1(d), where the additional pattern is rotated by -2.5° with respect to SiC. In total, ten of the bright objects have been studied with  $\mu$ LEED, the majority of them showing similar or less intense versions of the LEED characteristics described above. The (7×7) reconstruction is well known for Si(111) surfaces. Also, the ratio of SiC(0001) and Si(111) lattice parameters is 0.81 (calculated from  $a_{\text{SiC}(0001)}=3.08\text{\AA}$ [132] and  $a_{\text{Si}(111)}=3.81\text{\AA}$ [133]), which agrees well with the ratio given above. Therefore, the bright objects are identified as silicon agglomerations. Similar results were reported by Kulakov et al. [134], when exposing the (3×3)-Si reconstruction to a surplus of silicon.

Note that this chapter presents measurements from two different samples, identified as Sample 1 and Sample 2. The SiC substrates of these samples have different terrace configurations. No evidence was found that the terrace configuration has a significant effect on BN growth. However, it is relevant to the discussion of the BN domain structure. Therefore, the terrace configuration and its related LEEM features are analyzed in the following section.

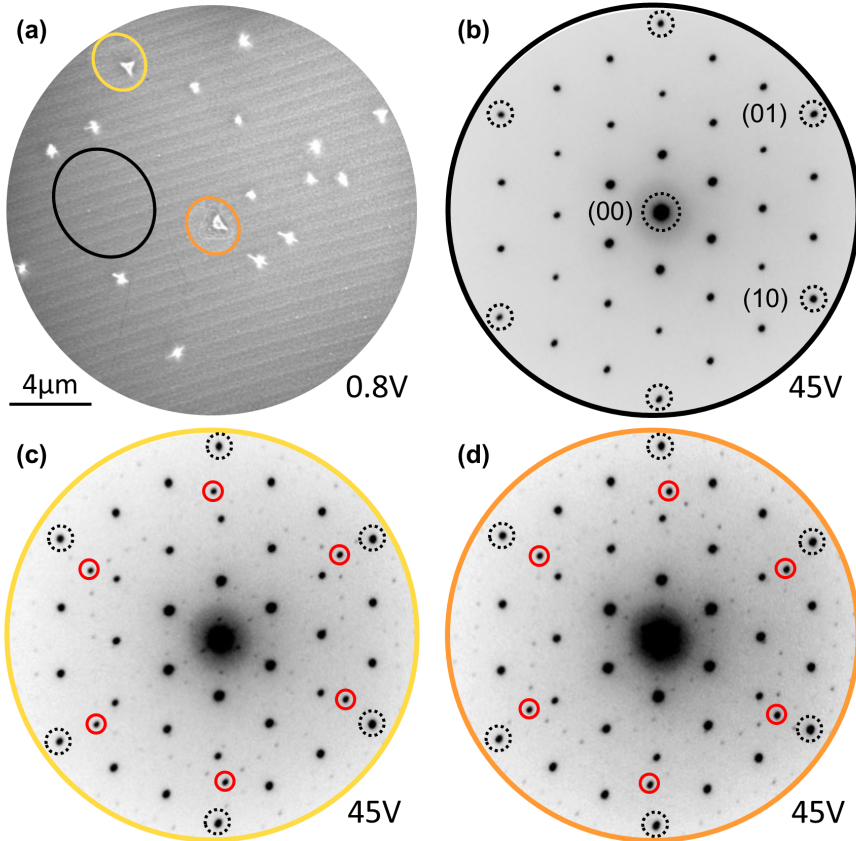


**Figure 3.1: The Si-rich  $(3 \times 3)$  surface reconstruction.** (a) LEEM image in under-focus conditions. Terraces appear as horizontal stripes and Si agglomerations as bright objects. The colored ellipses indicate areas which were characterized with  $\mu$ LEED in (b-d). (b)  $\mu$ LEED pattern showing the characteristic pattern of the  $(3 \times 3)$  surface reconstruction. The first order SiC spots are indicated. (c,d)  $\mu$ LEED patterns of areas including single Si agglomerations. The main spots of the additional  $(7 \times 7)$  patterns are indicated in red. Data measured on Sample 2.

### 3.1.2 Terrace configuration and step bunching on 6H-SiC(0001)

Further characterization of the  $(3 \times 3)$  reconstructed surface in Fig. 3.1(a) at different start voltages reveals contrast between neighboring terraces. This is exemplarily shown for  $U_{start} = 4.1$  V and  $U_{start} = 5.2$  V in Fig. 3.2(a) and (b), respectively. Terraces of three different brightness levels are identified, following a constant sequence across the surface. A group of three terraces is highlighted with black (3), red (2) and blue (1) boxes in Fig. 3.2(a) and (b). When the start voltage is varied, the contrast between the different terraces changes: While at 4.1 V terrace 2 appears brightest and terrace 1 darkest, at 5.2 V terrace 3 is brightest and terrace 2 darkest. The evolution of the contrast between the three terraces with  $U_{start}$  is illustrated by the LEEM-I(V) measurements in Fig. 3.2(c). The difference in contrast shows that the terraces are not equivalent in their crystalline structure and electronic properties.

In the following, the structure of the 6H-SiC polytype is reviewed based on Ref. [131] and used to explain the observed terrace configuration on the  $(3 \times 3)$ -Si reconstructed surface. As shown in Fig. 3.3(a), the atomic bonding in crystalline SiC is tetrahedral, whereby every Si atom has only C atoms as direct neighbors (and vice versa). In Fig. 3.3(b), several of these tetrahedra are assembled laterally, forming a (0001)-oriented SiC bilayer with three-fold rotational symmetry (and C atoms of the next layer on top). In the vertical direction, two stacking configura-

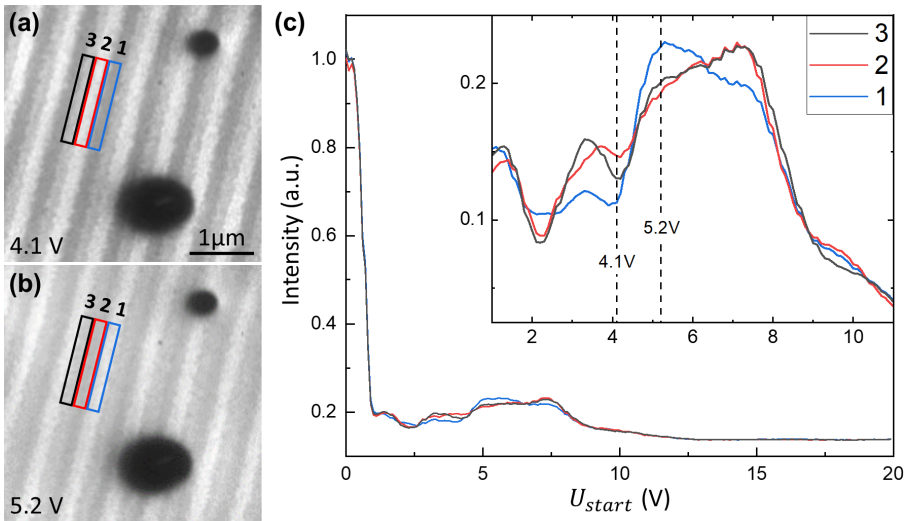


**Figure 3.2: LEEM-I(V) characterization of the Si-rich  $(3 \times 3)$  surface reconstruction.** (a) and (b) BF-LEEM images at  $U_{start} = 4.1$  V and  $5.2$  V, respectively. (c) BF-LEEM-I(V) curves measured on the three types of terraces 3, 2 and 1.  $U_{start}$  for (a) and (b) are indicated with dashed lines. Data measured on Sample 2.

tions are possible, either continued or switched stacking. Fig. 3.3(c) depicts the tetrahedron from panel (a) with a top layer in the continued stacking mode. Here, the orientation of the tetrahedra is the same in both layers. This configuration where the bonds between C and Si atoms of the bottom and top SiC bilayer have the same orientation is referred to as cubic ( $k$ ) configuration. The hexagonal ( $h$ ) configuration in Fig. 3.3(d) emerges from the switched stacking mode, where the tetrahedra in the top layer are rotated by  $60^\circ$ .

The freedom with respect to stacking results into a multitude of different SiC polytypes. Out of these, the 6H-SiC polytype (with a six-bilayer-high unit cell and hexagonal symmetry) follows the stacking sequence ABCACB in the  $[0001]$ -direction, as illustrated in Fig. 3.3(e). Going from bottom to top, a SiC bilayer that is stacked onto the layer underneath in hexagonal configuration is always followed by two bilayers stacked in cubic configuration. The next bilayer is again stacked in hexagonal configuration. In this way, consecutive groups of three equally oriented SiC bilayers are laterally rotated by  $60^\circ$ . Towards the right side of Fig. 3.3(e), the model is cut diagonally such that terraces with a step height of one SiC

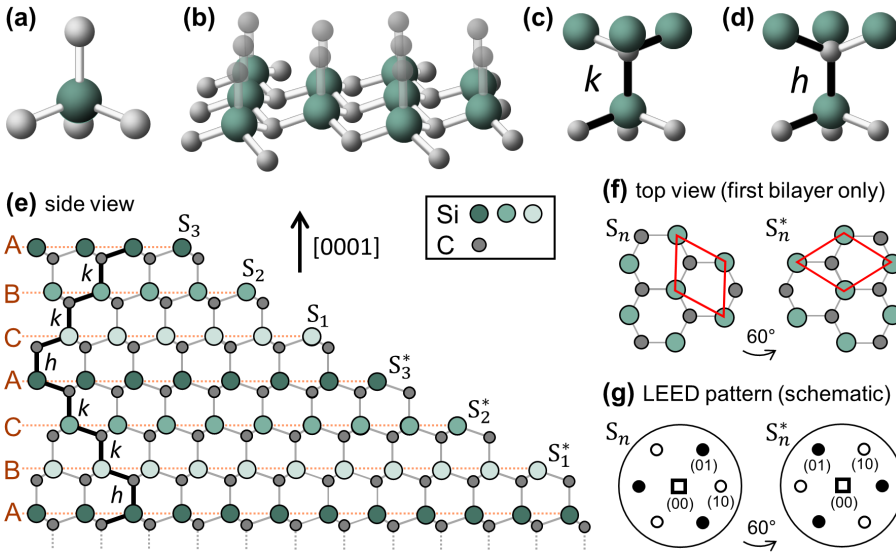


**Figure 3.3: Structure of 6H-SiC.** (a) The Si-C<sub>4</sub> tetrahedron as building block of the (b) planar SiC bilayer. The orientation of the tetrahedra in the next layer on top can be identical, as shown in (c) for the continued stacking mode (cubic ( $k$ ) configuration) or rotated by  $60^\circ$ , as shown in (d) for the switched stacking mode (hexagonal ( $h$ ) configuration). (e) Side view of 6H-SiC. For more information, see main text. (f) The topmost surface layers of a  $S_n$  and a  $S_n^*$  terrace and (g) their diffraction patterns are equivalent by  $60^\circ$  rotation. Hollow and full circles indicate a difference in intensity. Schematics in (a-g) based on Ref. [131].

bilayer emerge at the surface. Due to the above introduced stacking, six different domains can exist on the terraces, differing by their termination and stacking sequence below the surface. They are identified by  $S_n$  and  $S_n^*$ , where  $n \in \{1, 2, 3\}$  indicates that there is a switch in stacking ( $60^\circ$  rotation)  $n$  layers below the surface.  $S_n$  and  $S_n^*$  terraces have three-fold symmetry and are identical in their structure despite a rotation by  $60^\circ$  around the surface normal, as illustrated in Fig. 3.3(f). The presented structure model with step height of one SiC bilayer and the terrace sequence  $S_3$ - $S_2$ - $S_1$ - $S_3^*$ - $S_2^*$ - $S_1^*$  is consistent with the three different contrast levels seen in Fig. 3.2, when it is assumed that the  $S_n$  and  $S_n^*$  terraces show identical (or very similar) intensity, while a clear contrast is seen between  $S_1$ ,  $S_2$  and  $S_3$  terminations.

In LEED [see Fig. 3.3(g)], the symmetry of the  $S_n$  and  $S_n^*$  terminations manifests in the different spot intensities of the two three-fold symmetric patterns which are rotated  $60^\circ$  with respect to each other. This relationship was used to identify  $S_n$  and  $S_n^*$  domains on the surface area from Fig. 3.2 with DF-LEEM. Fig. 3.4(a) shows the LEED measurement of the  $(3 \times 3)$ -Si reconstructed 6H-SiC(0001) surface. The pattern exhibits six-fold symmetric spot intensities due to equal contributions of  $S_n$  and  $S_n^*$  terminated domains. While BF-LEEM images show no contrast between  $S_n$

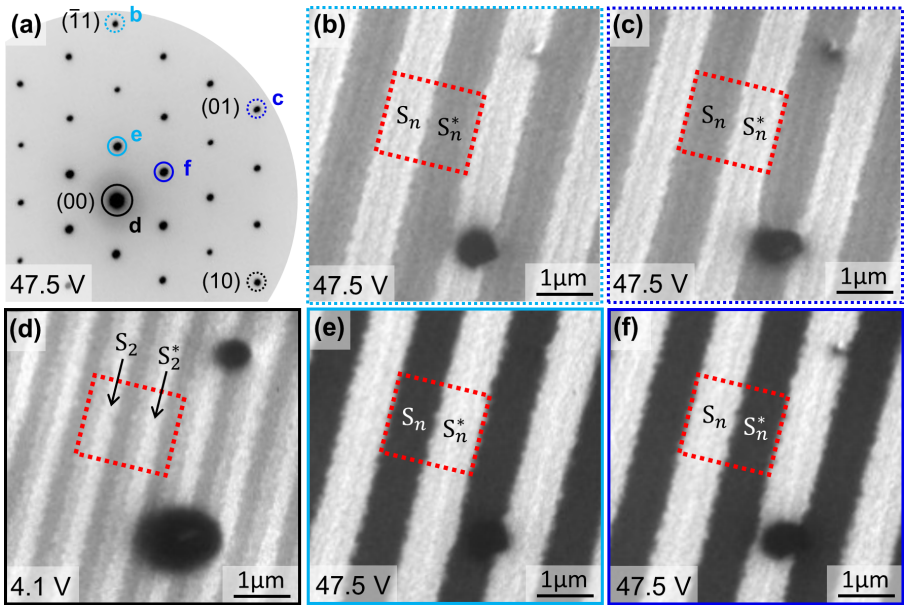


**Figure 3.4: Terrace configuration of  $(3 \times 3)$ -Si reconstructed 6H-SiC in DF-LEEM.** (a) LEED measurement. The highlighted spots have been used for BF-LEEM image (d) and DF-LEEM images (b,c) and (e,f). All LEEM images show the same surface region. A red dotted rectangle highlights a specific group of six terraces. Shape and size of the two defects vary due to slight differences in the focus condition and aperture position. Data measured on Sample 2.

and  $S_n^*$ , this equivalence is lifted by selecting the first-order SiC diffraction spots b and c for DF imaging: In Fig. 3.4(b,c), the corresponding DF-LEEM images reveal successive groups of three terraces with similar brightness that alternate in their contrast. A red dashed rectangle highlights the same surface area in both images. Out of the six terraces included, two groups of three consecutive terraces each are found to be  $S_n$  and  $S_n^*$  terminated, respectively. The contrast of the terraces is inverted when comparing the DF-LEEM images, which proves their  $60^\circ$  symmetry relation. Furthermore, by comparison with the BF-LEEM image in Fig. 3.4(d), the terraces that show the brightest contrast in BF-LEEM at 4.1 V can be identified as  $S_2$  or  $S_2^*$ . It has to be considered that actually, the SiC first order diffraction spots are superimposed by the third order diffraction spots of the  $(3 \times 3)$  reconstruction. Therefore, DF-LEEM was also performed on spots e and f [cf. Fig. 3.4(a)], which originate exclusively from the  $(3 \times 3)$  reconstruction. The corresponding DF-LEEM images in Fig. 3.4(e,f) exhibit a similar contrast between the  $S_n$  and  $S_n^*$  terraces, but with inverted and stronger contrast compared to Fig. 3.4(b,c). Therefore, it can be concluded that the  $(3 \times 3)$ -Si reconstruction adapts the three-fold rotational symmetry of the SiC surface, with one rotational domain occurring exclusively on  $S_n$  and the other exclusively on  $S_n^*$  terminated terraces. This observation agrees well with the atomic structure model of the  $(3 \times 3)$ -Si reconstruction by Schardt et al. [135].

An important effect related to the terrace configuration of 6H-SiC(0001) is step bunching due to non-uniform step movement. This effect was observed for example during hydrogen etching [137, 138] and graphene growth [51, 136] on 4H- and 6H-SiC polytypes. These processes have in common that they take place at elevated temperatures, where the sublimation of Si causes a decomposition of the terraces at their edges. However, the decomposition energies of  $S_1$ ,  $S_2$  and  $S_3$  terraces are different (while  $S_n$  and  $S_n^*$  can be considered identical in this context) [51, 136–138]. As a result, the retraction velocities of the individual terraces differ and depending on the initial state, the terrace configuration will change with prolonged

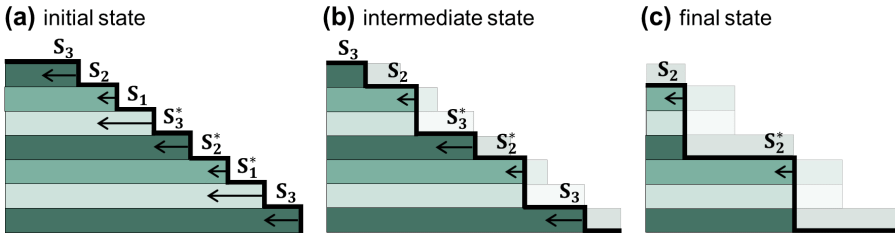


**Figure 3.5: Step retraction model at the 6H-SiC(0001) surface.** (a) Initial state. All terraces have the same width. Upon decomposition, the step edges of the terraces retract with the retraction velocities  $v_1 > v_3 > v_2$  (and  $v_n^* = v_n$ ), as indicated by arrows. (b) Intermediate state.  $S_1$  and  $S_1^*$  terraces have vanished. (c) Final state.  $S_3$  and  $S_3^*$  terraces have vanished. Only  $S_2$  and  $S_2^*$  terraces remain. Schematics in (a-c) based on Ref. [136].

decomposition. In the following, the so-called step retraction model is introduced based on the work of Momeni Pakdehi et al. [136]. The change of the 6H-SiC(0001) terraces upon decomposition is illustrated in Fig. 3.5. Starting point is a terrace configuration with equally wide terraces, constant step height of one SiC bilayer and a sequence  $S_3$ - $S_2$ - $S_1$ - $S_3^*$ - $S_2^*$ - $S_1^*$  [cf. Fig. 3.5(a)]. The retraction velocities of the terraces differ as  $v_1 > v_3 > v_2$  (and  $v_n^* = v_n$ ) [51, 136]. Upon decomposition, the  $S_1$  step edges retract fastest and catch up with those of the  $S_2$  terraces as shown in the intermediate state of the retraction model in Fig. 3.5(b), where the  $S_1$  terraces have already vanished. In the same way, the  $S_3$  step edges with their intermediate retraction velocity bunch together with those of the  $S_2$  terraces under prolonged decomposition. In the final state [cf. Fig. 3.5(c)], only  $S_2$  and  $S_2^*$  terraces with a step height of three SiC bilayers remain.

In this work, step retraction was observed during BN growth on the 6H-SiC(0001) surface. This is illustrated in Fig. 3.6 by comparing the same surface area before and after BN growth. Fig. 3.6(a) shows a composite image that summarizes the DF-LEEM results presented in Fig. 3.4 by superimposing the BF-LEEM image (d) with a false color composite of (e) and (f) in cyan and blue, respectively. Additionally, the step edges of the BF-LEEM image have been emphasized. The terrace configuration which becomes now obvious in Fig. 3.6(a) is similar to the initial state of the step retraction model in Fig. 3.5(a), only the terrace widths are slightly increasing within each group of three terraces with  $S_n$  or  $S_n^*$  termination from left to right. From the atomic structure model it was deduced that the middle terrace of each group has  $S_2$  or  $S_2^*$  character. Fig. 3.6(b) shows a BF-LEEM image of the same area after BN growth. Three kinds of terraces can still be identified, whereas the terrace widths have changed significantly. For better comparison, another composite image is presented in Fig. 3.6(c). It shows that the thinnest terrace is located on the right side of each

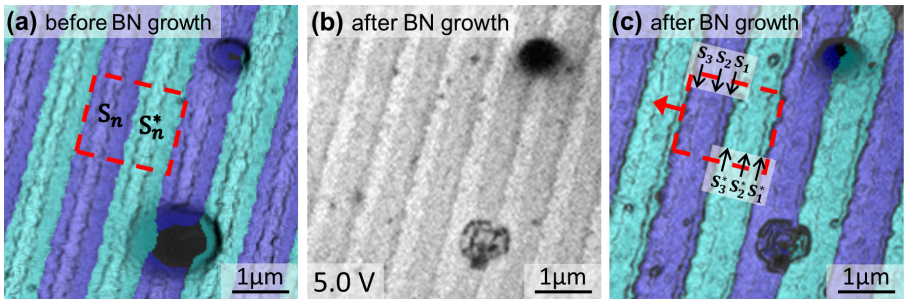


**Figure 3.6: Step retraction during BN growth.** (a) Terrace configuration before BN growth. (b) BF-LEEM image and (c) terrace configuration after BN growth. All images show the same surface area, determined by the position of the defect in the upper right corner. (a,c) are composite images. See main text for further information. The red dotted rectangle indicates a particular group of terraces. See text for terrace assignment. Data measured on Sample 2.

$S_n$  and  $S_n^*$  group, while the widest terrace resides in the middle. Considering the step-retraction model, this terrace configuration fits well with a stage in between the initial and intermediate state, shortly before the  $S_1$  terraces have vanished completely. Assigning the terraces by their widths, the terrace sequence  $S_3$ - $S_2$ - $S_1$ - $S_3^*$ - $S_2^*$ - $S_1^*$  is found to run from left to right. This assignment matches with the retraction direction, which was deduced from the step movement direction relative to the defect in the upper right corner and is illustrated by the red arrow in Fig. 3.6(c).

Note that in this chapter, the presented data was obtained from two samples with different terrace configurations. So far, the data shown was exclusively measured on Sample 2. The terrace configuration of Sample 1 was investigated by the same procedure as presented above and found to fit the final state of the retraction model already before and also after BN growth, i.e., only  $S_2$  and  $S_2^*$  terraces exist. It was not possible to deduce the direction of retraction. The terrace configuration as revealed by DF-LEEM can be easily used to determine the misscut angles of both samples. In Fig. 3.7, DF-LEEM composite images of both samples are displayed. The alternating  $S_n$  and  $S_n^*$  domains appear in blue and cyan, respectively. From these images, the lateral distance across which the total height of the surface steps sums up to one unit cell height is measured as  $\Delta_1 = 0.6 \mu\text{m}$  for Sample 1 and  $\Delta_1 = 1.7 \mu\text{m}$  for Sample 2. With the unit cell height of 1.5 nm [139], the misscut angles of  $\theta_1 = 0.14^\circ$  for Sample 1 and  $\theta_2 = 0.05^\circ$  for Sample 2 result from simple trigonometry.

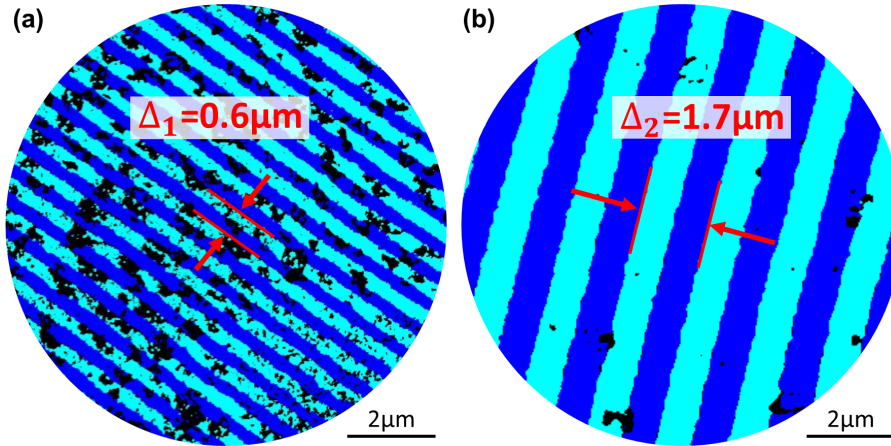


**Figure 3.7: Terrace and domain configuration of Sample 1 and Sample 2.** (a) False color composite DF-LEEM image depicting the alternating  $S_n$  and  $S_n^*$  domains on Sample 1 in blue and cyan, respectively. The lateral distance across which the total height of the surface steps sums up to one unit cell height is indicated. (b) Same as (a) but for Sample 2.

## 3.2 In-situ study of BN growth

BN was grown by CVD using the precursor borazine. The latter is stored in a small glass tube and cooled below 0°C to prevent it from thermal decomposition. The glass tube is connected with the experimental chamber by a gas line with a dosing valve. The growth process was followed in-situ and in real time with LEEM and LEED. Selected images are shown in Fig. 3.8.

Starting point is the (3×3)-Si reconstructed 6H-SiC(0001) surface as introduced previously. First, it is gassed out at temperatures up to ~500° without borazine. Then, a borazine partial pressure of  $2.0 \cdot 10^{-7}$  mbar is adjusted. After stabilizing the gas flow, the temperature is further increased with combined filament and e-beam heating. Under borazine exposure, no change of the surface is observed while the temperature is below 740°C. A LEED measurement at 740°C shows that the (3×3)-Si reconstruction is still present. The corresponding LEEM and LEED images are shown in panel (a) of Fig. 3.8 and its inset. The LEEM image was taken at underfocus conditions in order to make the step edges visible. The Si agglomerations appear as bright objects (for better comparison, one of them is highlighted by a black square in all panels). Up to 845°C [cf. panel (b)], only the appearance of small point-like objects on the terraces changes slightly, so that they now appear dark and slightly larger. The first significant change on the surface is observed when the temperature exceeds 850°C. Some of the Si agglomerations that appear as bright spots in panel (b) turn suddenly into dark spots of increased size in panel (c). Starting with the smaller sized ones, the Si agglomerations change their appearance one by one, until all but the two largest have transformed in panel (e). At 900°, the microscope was switched to LEED mode briefly, revealing that the superstructure spots of the (3×3)-Si reconstruction have vanished. Back in LEEM mode, at 915°C [cf. panel (f)] it is found that the largest Si agglomerations have now transformed as well. It is concluded that, in the range of 740 – 915°C, Si-depletion of the surface takes place (as expected for elevated temperatures), presumably independent from the presence of the precursor gas borazine.

Shortly after the last Si agglomerations transformed, another change of the surface is observed. Simultaneously, a large number of small dark spots appears and grows in size, as illustrated by the LEEM images in panels (g) and (h). This indicates the nucleation and growth of islands. The size of the islands is not realistic but over-sized due to imaging in underfocus. Beyond 950°, the growth seems to be terminated and no significant change on the surface is observed while the temperature is further increased up to 1000°C. The LEEM image in panel (i) was obtained after going to slight underfocus imaging conditions, where the remains of the Si agglomerations are almost unrecognizable and the islands appear in a more realistic size. The inset in panel (i) shows a LEED measurement of this surface, proving that a new crystalline structure is present. The annealing process was continued at 1000°C for ~20 min. No further changes on the surface were observed and the experiment was terminated by cooling down and stopping the borazine flow.

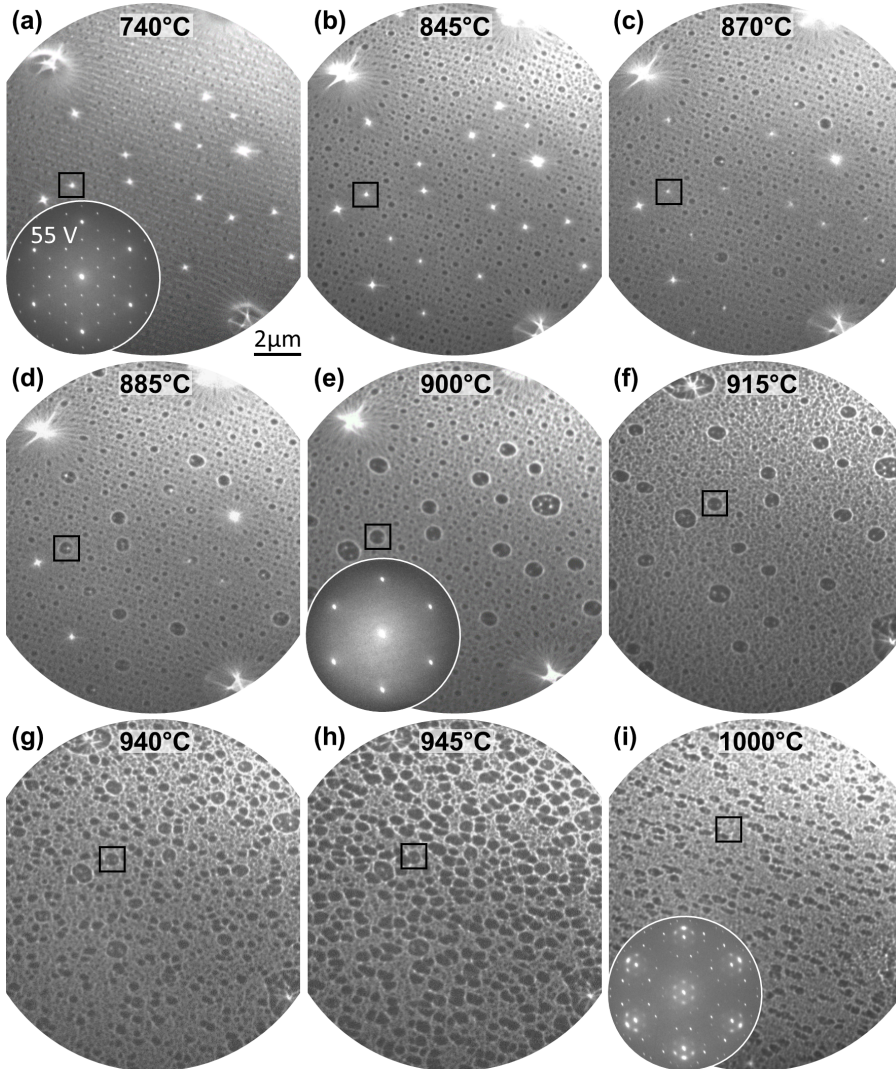


**Figure 3.8: BN Growth on SiC(0001).** LEEM images taken while heating the  $(3\times 3)$ -Si reconstructed surface of Sample 1 in borazine atmosphere. All LEEM images show the same surface area, as indicated by the black square which highlights the same object in all images (a slight shift in position appears due to thermal drift). The images were obtained at a start voltage of 0.2V and in (a-h) underfocus or (i) slight underfocus conditions. In panels (a,e,i), the inset shows LEED images taken from a representative surface area at 55 V, immediately before or after the respective LEEM image.

### 3.3 Structure of BN on SiC(0001)

This section presents the crystalline structure and lateral domain configuration of BN on SiC(0001) for Sample 1, the preparation of which was presented in the previous section. A first overview of the sample surface is provided through LEEM, and LEED is employed to investigate its structural composition. Three distinct structures were identified based on their LEED features and Ref. [MR5]:  $B_xN_y-R0^\circ$ ,  $(\sqrt{7} \times \sqrt{7})-R19.1^\circ$ , and a misoriented minority phase (note that these are not necessarily thermodynamic phases). Bright-field LEEM-I(V) measurements reveal a complex domain structure. Each surface phase is then characterized separately by DF-LEEM, LEEM-I(V), and  $\mu$ LEED.

#### 3.3.1 Structural overview

Fig. 3.9(a) shows a LEEM image of Sample 1 after BN growth and cooling to room temperature. Note that a different surface area is shown than before. Two different regions can be identified. The majority of the image shows terraces with islands similar to Fig. 3.8(i). These regions cover more than 99% of the surface. In the center-right of Fig. 3.9(a), there is an oval-shaped region that has a different appearance compared to the surrounding terraces and is free of islands. These

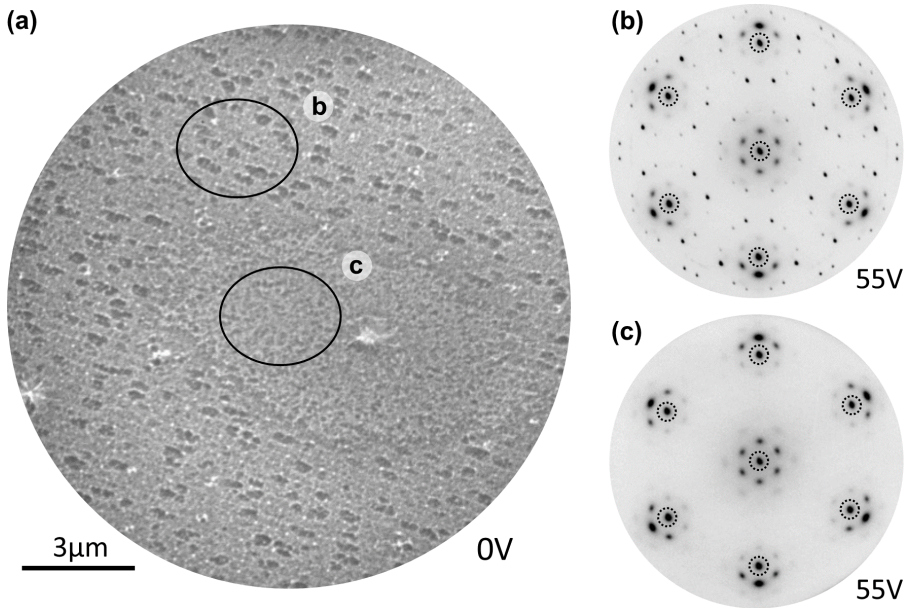


**Figure 3.9: Overview of BN on Sample 1.** (a) LEEM image of a representative surface area. (b,c)  $\mu$ LEED images of region b and region c as marked in (a), respectively.

types of regions comprise less than 1% of the surface. As observed in Fig. 3.9(a), the vast majority of them exhibit a bright defect in their center. Both types of surface regions were examined separately with  $\mu$ LEED. The positions of the aperture are indicated by black ovals in Fig. 3.9(a). The corresponding LEED images are shown in panels (b) and (c). While one set of LEED spots is present in both measurements, another set is exclusive to the measurement of the region with islands.

The LEED image in Fig. 3.9(b) is comprised of different LEED features. For a closer look, Fig. 3.10(a) depicts a larger version of this image. The first order diffraction spots of SiC are marked with black dotted circles and the main features of other patterns are indicated in different colors. In the following, the different structures are identified by their LEED characteristics.

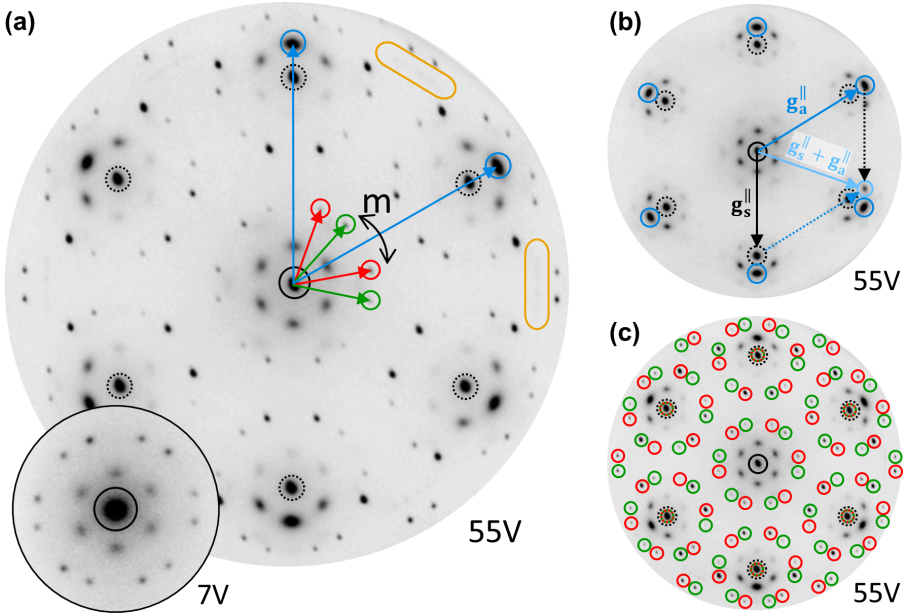


**Figure 3.10: LEED of BN on SiC(0001).** (a) LEED image containing all the LEED patterns of the structures present on the surface, the main features of which are indicated by different colors. The inset shows a LEED image taken on the same surface area but with  $U_{start} = 7$  V. (b) The LEED pattern obtained from the island-free region can be fully explained by a single hexagonal pattern (blue) and multiple scattering, as exemplified for the light blue highlighted 1<sup>st</sup>-order multiple scattering spot. (c) LEED pattern from (a), all spots of the  $(\sqrt{7} \times \sqrt{7})$ - $R19.1^\circ$  reconstruction are highlighted with red and green spots, originating from two mirror symmetric domains.

**$B_xN_y$ - $R0^\circ$**  The blue highlighted LEED spots in Fig. 3.10(a) form a hexagonal pattern with reciprocal unit cell vectors larger by a factor of  $\sim 1.17$  compared to SiC (corresponding to a real space lattice constant of 2.6 Å). While aligned with the substrate, the spots are elongated azimuthally, indicating a slight rotational misalignment of different domains. Considering multiple scattering events between the substrate and this adsorbate structure, all additional spots in the LEED measurement of Fig. 3.9(c) can be explained. This is demonstrated by the example of the light blue highlighted 1<sup>st</sup>-order multiple scattering spot in Fig. 3.10(b) [analogous to Fig. 2.4]. As expected for an MS spot, it is not elongated azimuthally, but in the same direction as the adsorbate first-order diffraction spot involved in the multiple scattering process. Note that in LEED, all MS spots are expected to disappear when  $U_{start}$  is reduced so that the first-order diffraction spots are no longer inside the Ewald's sphere. As shown in the inset of Fig. 3.10(a), this is not the case for the satellite spots surrounding the (00)-spot at  $U_{start}=7$  V. The existence of first-order diffraction spots that combine the periodicity of both the adsorbate and the substrate indicates that the substrate significantly alters the structure of the adsorbate and thus directly imposes its periodicity on it. The described LEED features correspond well with those of the  $B_xN_y$ - $R0^\circ$  structure reported by Lin et al. [MR5]. Lin et al. reported a lattice constant of 2.60 Å for  $B_xN_y$ - $R0^\circ$ , which is in agreement with the present work and significantly less densely packed than expected for 2D hBN (compared to literature values for hBN of 2.51 Å [140]).

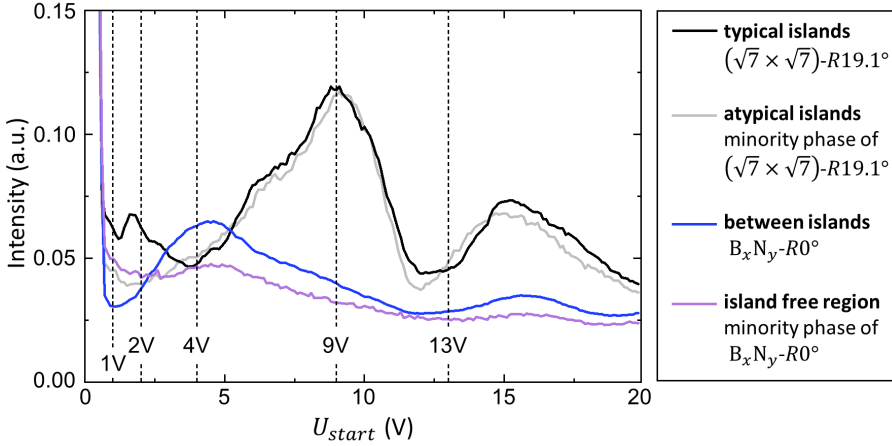
**$(\sqrt{7} \times \sqrt{7})$ - $R19.1^\circ$  reconstruction** The main features of the pattern that appears in LEED when islands contribute are highlighted in red and green in Fig. 3.10(a). For clarity, Fig. 3.10(c) shows the same LEED image with all spots highlighted that arise from translation of the corresponding red and green unit cell vectors. Note that the resulting patterns are mirror symmetric with respect to the substrate and that the first-order diffraction spots of the substrate coincide with both the red and green patterns. Therefore, they are described by a commensurate superstructure with the two matrices  $\begin{pmatrix} 2 & -1 \\ 1 & 3 \end{pmatrix}$  (red) and  $\begin{pmatrix} 3 & 1 \\ -1 & 2 \end{pmatrix}$  (green). In the following, the equivalent Wood notation  $(\sqrt{7} \times \sqrt{7})$ - $R19.1^\circ$  is used.

**Misoriented minority phase** Finally, the LEED features highlighted in orange in Fig. 3.10(a) are considered. Faint spots form hexagonal patterns of different orientations. All these spots are located on a circle with a radius that is slightly larger than that of the  $B_xN_y$ - $R0^\circ$  spots. The corresponding lattice constant of 2.5 Å may correspond to either hBN ( $a_{hBN}=2.51$  Å, as reported in Ref. [140]) or graphene ( $a_{gr}=2.46$  Å, as reported in Ref. [141]). Azimuthally, the spots are centered around an axis  $30^\circ$  from the main directions of SiC(0001) with a wide angular distribution of  $\pm 7^\circ$ . Note that no similar structure was reported by Lin et al. [MR5] or other literature on BN and graphene growth on SiC(0001) [51, 52, 142]. While thermal decomposition of SiC results in growth of Gr- $R0^\circ$ , this is usually found to be well oriented [50, 51].

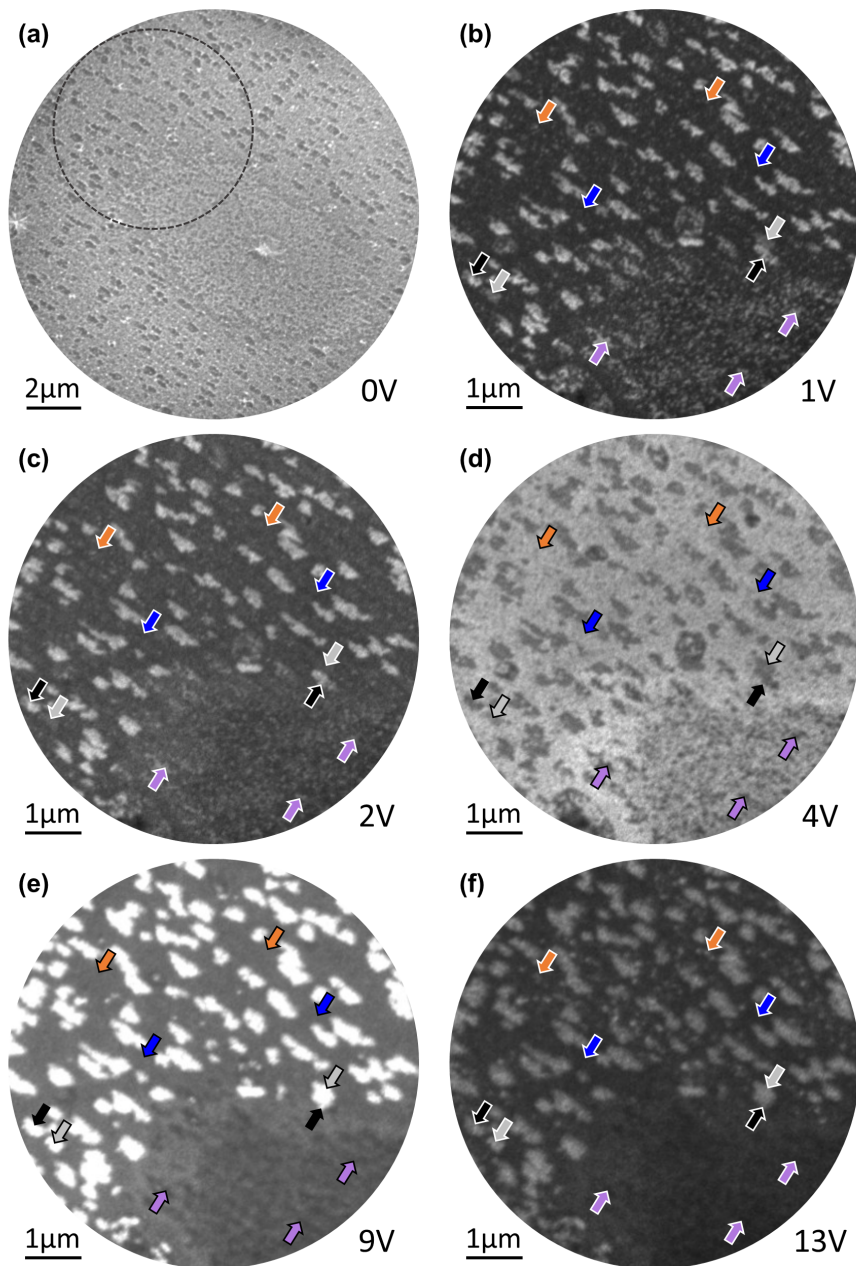
### 3.3.2 Domain structure

Fig. 3.12(a), depicts again the LEEM image of Fig. 3.9(a). The encircled surface region is selected as representative for the domain structure analysis of BN on SiC(0001). Different surface regions are identified by their change in contrast with varying  $U_{start}$ . To this end, Fig. 3.12(b-f) presents BF-LEEM images of the selected surface region for designated  $U_{start}$  as specified in the panels. Additionally, LEEM-I(V) profiles of selected areas are plotted in the range of  $U_{start} = 0-20$  V in Fig. 3.11.

Most islands are easily recognizable in all panels of Fig. 3.12(b-f). Note that some of the islands show a different contrast at low  $U_{start}$ . This is evident when comparing the black-marked typical islands with the gray-marked atypical islands in Fig. 3.12(b,c). For  $U_{start} = 1$  V, the gray islands appear slightly darker than the black islands, while for  $U_{start} = 2$  V, the gray islands have a similar contrast to their surroundings, thus becoming almost invisible. At higher values of  $U_{start}$ , there is no significant difference in contrast between the two types of islands. This observation is also corroborated by the LEEM-I(V) profiles of the typical and atypical islands depicted in Fig. 3.11. The region between and in the immediate vicinity of the islands appears relatively uniform. Some areas are marked with blue arrows in Fig. 3.12. Their LEEM-I(V) characteristics (blue profile in Fig. 3.11) differ strongly from those of the islands. The island-free region in the lower right of each panel in Fig. 3.12(b-f) appears slightly different and less uniform than the areas directly between the islands. Small objects in this region are found



**Figure 3.11: LEEM-I(V) spectra of BN on SiC(0001), in correspondence to Fig. 3.12.** The profiles shown belong to different surface regions as marked with colored arrows in Fig. 3.12. Dashed lines indicate the  $U_{start}$  for which BF-LEEM images are shown in Fig. 3.12(b-f). The structural composition of the different surface areas as provided in the legend is identified in the same section below.



**Figure 3.12: Identification of different surface regions with LEEM-I(V).** (a) LEEM image from Fig. 3.9(a), the region of interest is marked with a circle. (b-f) BF-LEEM images of this region taken at different  $U_{start}$  as indicated in the panels. Areas of different contrast are marked with colored arrows. The color code corresponds to the LEEM-I(V) spectra of Fig. 3.11.

to have different LEEM-I(V) characteristics than those described so far. Some of them are marked with purple arrows. While in Fig. 3.12(b-d), they appear to have similar contrast to the islands, at higher  $U_{start}$  [cf. panels (e) and (f)], they are darker than both the islands and the dark blue highlighted areas. Finally, in panel (f) of Fig. 3.12 some additional nm-sized bright objects (marked in orange) appear between the islands, which are not visible in panel (e). These objects are too small to reliably extract a LEEM-I(V) profile for Fig. 3.11.

In the following, the structural composition and the domain structure are related to each other by DF-LEEM and  $\mu$ LEED. For that purpose, the crystalline structure and domain configuration of each surface phase are analyzed and discussed in more detail separately.

### $B_xN_y-R0^\circ$

Fig. 3.13 presents DF-LEEM data measured on the area that is depicted in the BF-LEEM image in panel (b). First-order SiC(0001) and  $B_xN_y-R0^\circ$  diffraction spots were used for DF-LEEM imaging, as indicated in the LEED image in panel (a). The DF-LEEM images of the first-order SiC(0001) spots in panels (c) and (e) reveal the terrace configuration of the substrate, as discussed in Section 3.1.2. Adjacent SiC terraces are identical in their structure despite a  $60^\circ$  rotation. Note that the islands show non-vanishing intensity in these images. This is because, in LEED, the first-order SiC(0001) spots overlap with spots of the island structure, as illustrated in Fig. 3.10(c).

Panels (d) and (f) show the DF-LEEM images of the first-order  $B_xN_y-R0^\circ$  spots, revealing a terrace configuration consistent with that of the DF-LEEM images of the first-order SiC(0001) spots. Furthermore, all islands appear dark, as can be seen by comparing panels (d) and (f) with the BF-LEEM image in (b). It can be concluded that  $B_xN_y-R0^\circ$  grows between the islands and in two domains that are equivalent to each other by  $60^\circ$  rotation. A notable finding is the fixed relationship between these domains and the terrace configuration of SiC.

In the island-free region (lower right of each image), the aforementioned terrace configuration continues. Here, the terraces have a less uniform texture, as if scattered with nm-sized objects. Given the absence of any other structure than  $B_xN_y-R0^\circ$  in the LEED measurement of this region, it is characterized in more detail with LEEM-I(V) in Fig. 3.14. Panels (b) and (c) show an enlarged image section of the island-free region for different  $U_{start}$ . Two distinct phases can be distinguished, referred to as island-free type A and type B, some regions of which are highlighted in light blue and purple, respectively. For  $U_{start} = 1$  V, type A appears bright and type B dark. The contrast is inverted for  $U_{start} = 4$  V. The LEEM-I(V) profiles of both regions are extracted and plotted in panel (a) along with the LEEM-I(V) profile of  $B_xN_y-R0^\circ$  between the islands (dark blue). It is found that the profile of the island-free region type A is almost identical with  $B_xN_y-R0^\circ$  between the islands. Small deviations can be assigned to difficulties to separate the small areas properly from each other. Therefore, island free region type A is identified as  $B_xN_y-R0^\circ$ .

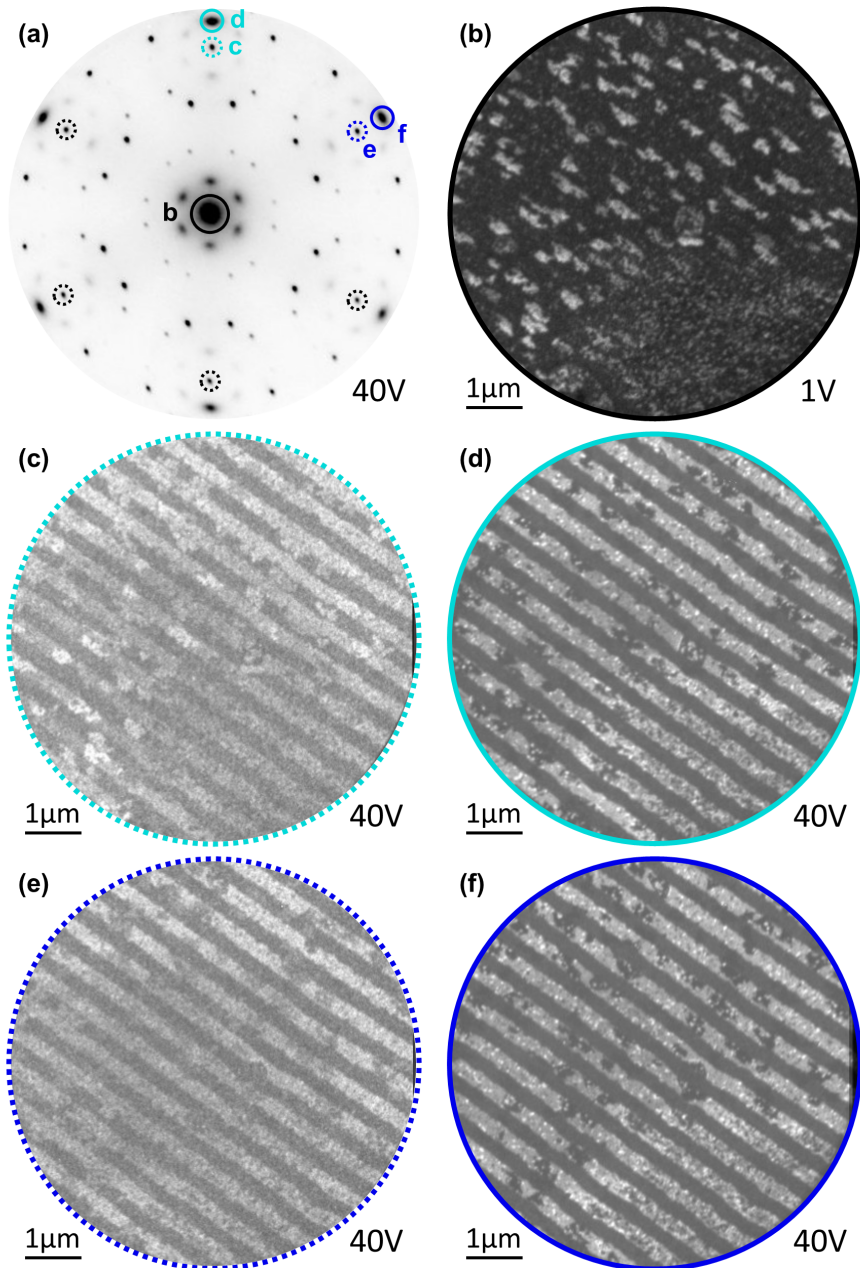


**Figure 3.13: DF-LEEM on  $B_xN_y-R0^\circ$ .** (a) LEED image of the investigated surface area. (b) BF-LEEM image at  $U_{start} = 1$  V. (c,e) DF-LEEM images of the SiC(0001) first-order diffraction spots and (d,f) DF-LEEM images of the  $B_xN_y-R0^\circ$  first-order diffraction spots at  $U_{start} = 40$  V. The spots selected for imaging are marked in (a) and named according to the respective panels.

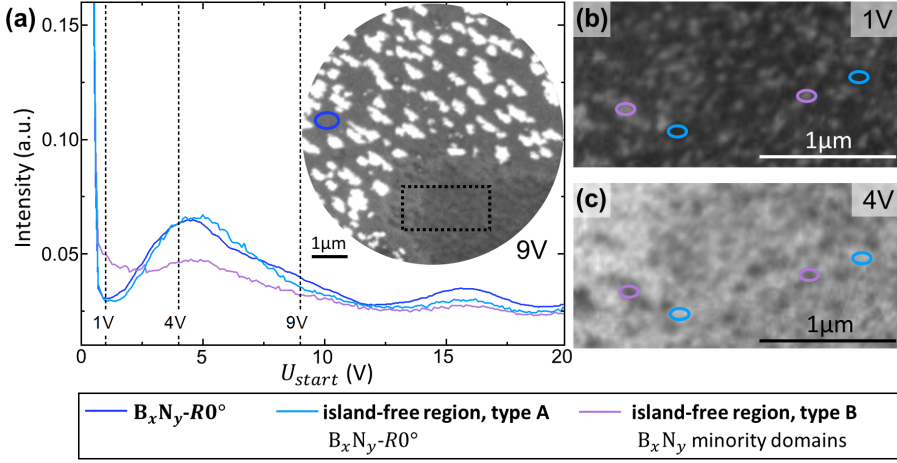


**Figure 3.14: LEEM-I(V) profiles of different  $B_xN_y-R0^\circ$  regions in the island free area.** (a) LEEM-I(V) profiles of regions as highlighted in respective colors in the inset and panels (b) and (c). (b,c) Enlarged BF-LEEM image sections of the island free region at different  $U_{start}$ . The image section corresponds to the black dotted rectangle in the inset of panel (a).

Next, domains of type B are considered more closely. These are found exclusively in the island-free region, which is best recognizable in the BF-LEEM image at  $U_{start} = 9$  V [see inset of Fig. 3.14(a) or Fig. 3.12(e) for a larger version]. Note that due to their small size and proximity to  $B_xN_y-R0^\circ$ , the structural characterization of type B domains is complicated. From the LEED measurement of the island-free region in Fig. 3.10, it can be concluded that type B domains either do not exhibit a crystalline structure, or their LEED spot positions coincide with those of the  $B_xN_y-R0^\circ$  LEED spots. However, comparing the LEEM-I(V) profiles of the island-free region type B (purple) and  $B_xN_y-R0^\circ$  (dark blue) in Fig. 3.14(a) suggests a certain degree of structural similarity. While the profile of the island-free region type B flattens out more quickly and reaches its first minimum at a significantly higher start voltage of  $U_{start} = 2$  V, both LEEM-I(V) curves have a similar work function and shape with equivalent numbers of minima and maxima in the investigated range. LEEM-I(V) curves are qualitatively representative of the local binding geometry and structure [76], so it is reasonable to assume that despite minor structural differences, the island-free region type B and  $B_xN_y-R0^\circ$  are similar. Structural differences that could result in minor alterations to LEEM-I(V) profiles could be, for example, different adsorption configurations [MR1]. Defects, the incorporation of other atoms, and differences in the B:N ratio are also plausible considerations. In this context, different configurations of the boron buffer layer that was found by Lin et al. [MR5] to reside at the interface of  $B_xN_y-R0^\circ$  and SiC should also be considered, as it exhibits no LEED pattern.

**$(\sqrt{7} \times \sqrt{7})$ -R19.1° reconstruction**

The domain configuration of the  $(\sqrt{7} \times \sqrt{7})$ -R19.1° surface reconstruction is characterized by DF-LEEM in Fig. 3.15. Four diffraction spots were selected for DF-LEEM imaging, as highlighted in panel (a). Note that spots c (magenta) and e (red) are described by the same superstructure matrix of the  $(\sqrt{7} \times \sqrt{7})$ -R19.1° surface reconstruction [cf. Fig. 3.10(c)] and are rotated to each other by 60°. Spots d (dark green) and f (light green) have been selected to represent the structurally equivalent mirror symmetric domains. Panels (c-f) display the corresponding DF-LEEM images. In all images, intensity is only provided by islands. Note that each image is distinct and shows two sets of islands with different brightness levels. A comparison of DF-LEEM images (c) and (e) (or (d) and (f), respectively) reveals that both images depict the same islands, but with inverted contrast. This finding is consistent with the symmetry relation of the selected LEED spots, if the two sets of island domains with different contrast in a DF-LEEM image are structurally identical despite an in-plane rotation of 60°. Images (d) and (f) show different islands than images (c) and (e), since the corresponding LEED spots are attributed to the mirror domain. Overall, DF-LEEM reveals the presence of four symmetry-equivalent rotational and mirror domains of the  $(\sqrt{7} \times \sqrt{7})$ -R19.1° surface reconstruction. In the following, the domain that appears brightest in each image of Fig. 3.15(c-f) is designated by the corresponding color.

The aforementioned symmetry relations of the four  $(\sqrt{7} \times \sqrt{7})$ -R19.1° domains can be readily verified by  $\mu$ LEED measurements of selected islands. In each DF-LEEM image of Fig. 3.15(c-f) one of the brighter islands is highlighted and chosen for  $\mu$ LEED characterization. The corresponding measurements are displayed in Fig. 3.16. As expected, the red and magenta islands (or the light green and dark green islands, respectively) produce LEED spots at the same positions. However, the intensity of the spots varies, such that a rotation of the magenta (light green) pattern by 60° reproduces the spot intensities of the red (dark green) pattern. A comparison of the intensity of specific spots in the magenta and red patterns implies which domain will appear brighter in DF-LEEM imaging at the same  $U_{start}$ . For instance, the first-order diffraction spot c exhibits higher intensity in the magenta pattern and spot e in the red pattern. For confirmation, see the DF-LEEM characterization in Fig. 3.17. It should be noted that here, the contrast of the images has been enhanced to such an extent that the less bright rotational domain in each DF-LEEM image is not visible anymore. Finally, the red and dark green patterns are found to be mirror-symmetric to each other, as well as the magenta and the light green. This observation is in agreement with the symmetry relations of the LEED spots that were chosen for DF-LEEM imaging.

To relate the domain configuration of the  $(\sqrt{7} \times \sqrt{7})$ -R19.1° islands to that of  $B_xN_y$ -R0° and the underlying SiC terraces, the DF-LEEM images of the LEED spots indicated in Fig. 3.18(a) are superimposed in the composite image in panel (b). It is evident that the majority of the islands are located on single terraces. Furthermore, it is found that the red and dark green islands grew preferably on the same terrace as the dark blue  $B_xN_y$ -R0° domain, and the magenta and light

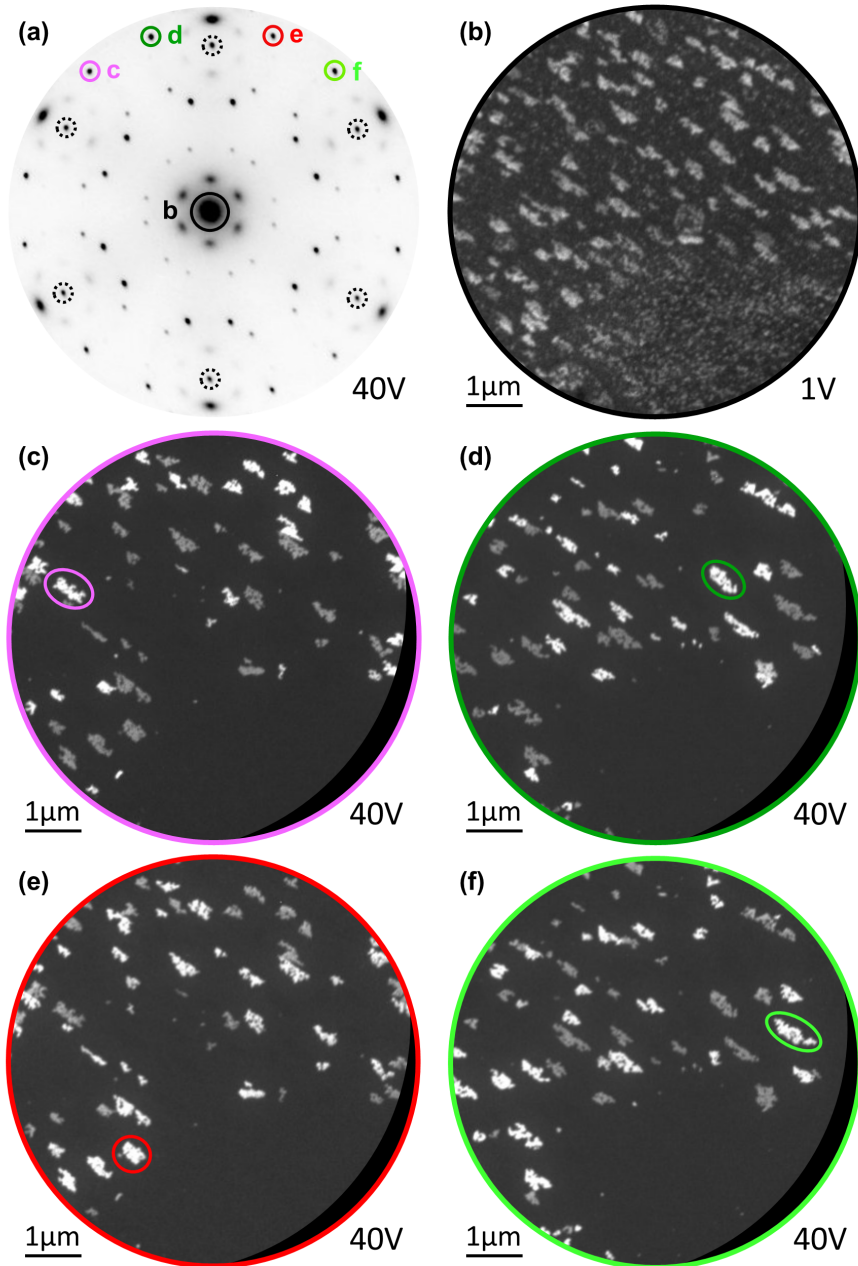


**Figure 3.15: DF-LEEM on the  $(\sqrt{7} \times \sqrt{7})$ -R19.1° reconstruction.** (a) LEED measurement of the investigated surface area. (b) BF-LEEM image at  $U_{start} = 1$  V. (c-f) DF-LEEM images of selected higher-order  $(\sqrt{7} \times \sqrt{7})$ -R19.1° diffraction spots at  $U_{start} = 40$  V. The spots selected for imaging are marked in (a) and named according to the respective LEEM images.

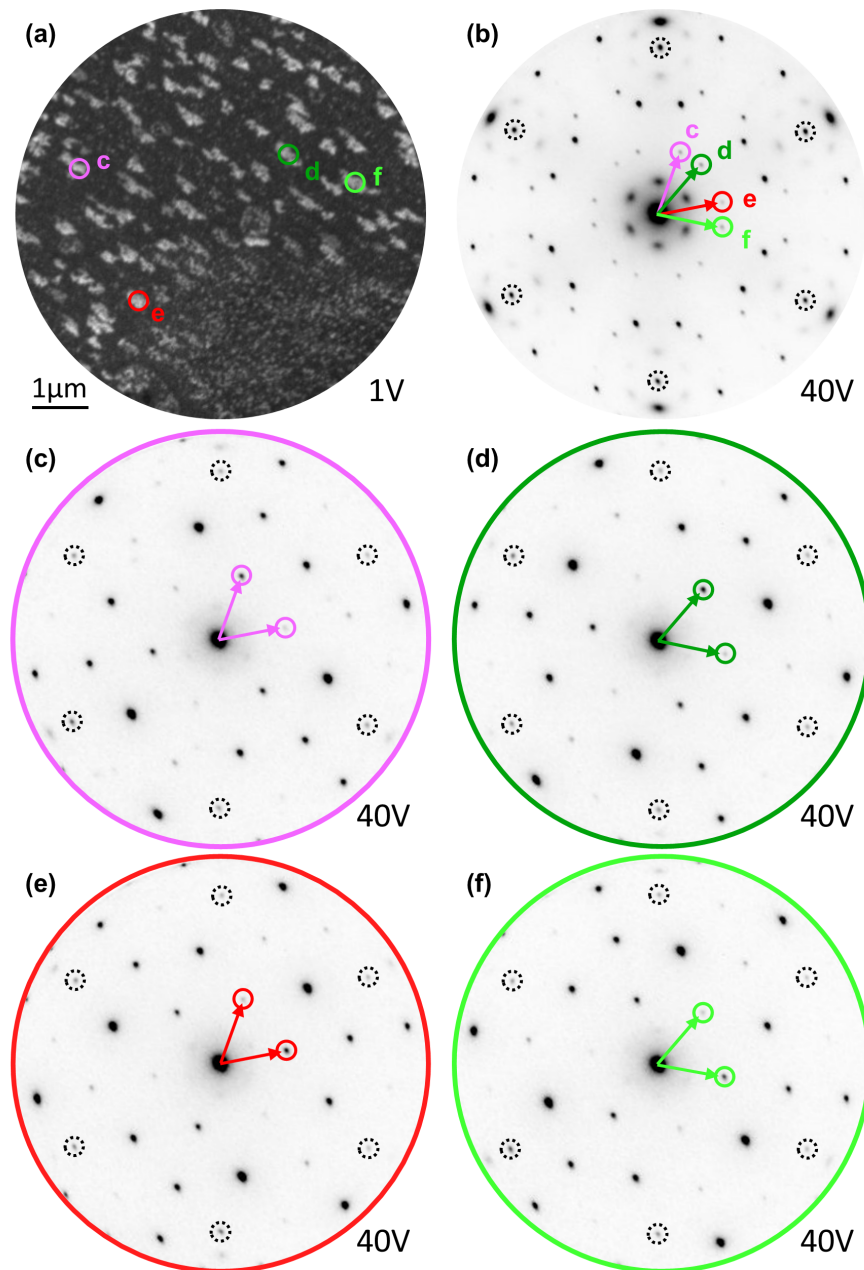


**Figure 3.16:  $\mu$ LEED on the  $(\sqrt{7} \times \sqrt{7})$ - $R19.1^\circ$  reconstruction.** (a) BF-LEEM image, the examined islands are highlighted. (b) LEED image with all LEED features. (c-f)  $\mu$ LEED images that represent each of the four  $(\sqrt{7} \times \sqrt{7})$ - $R19.1^\circ$  domains, as indicated by the color code.

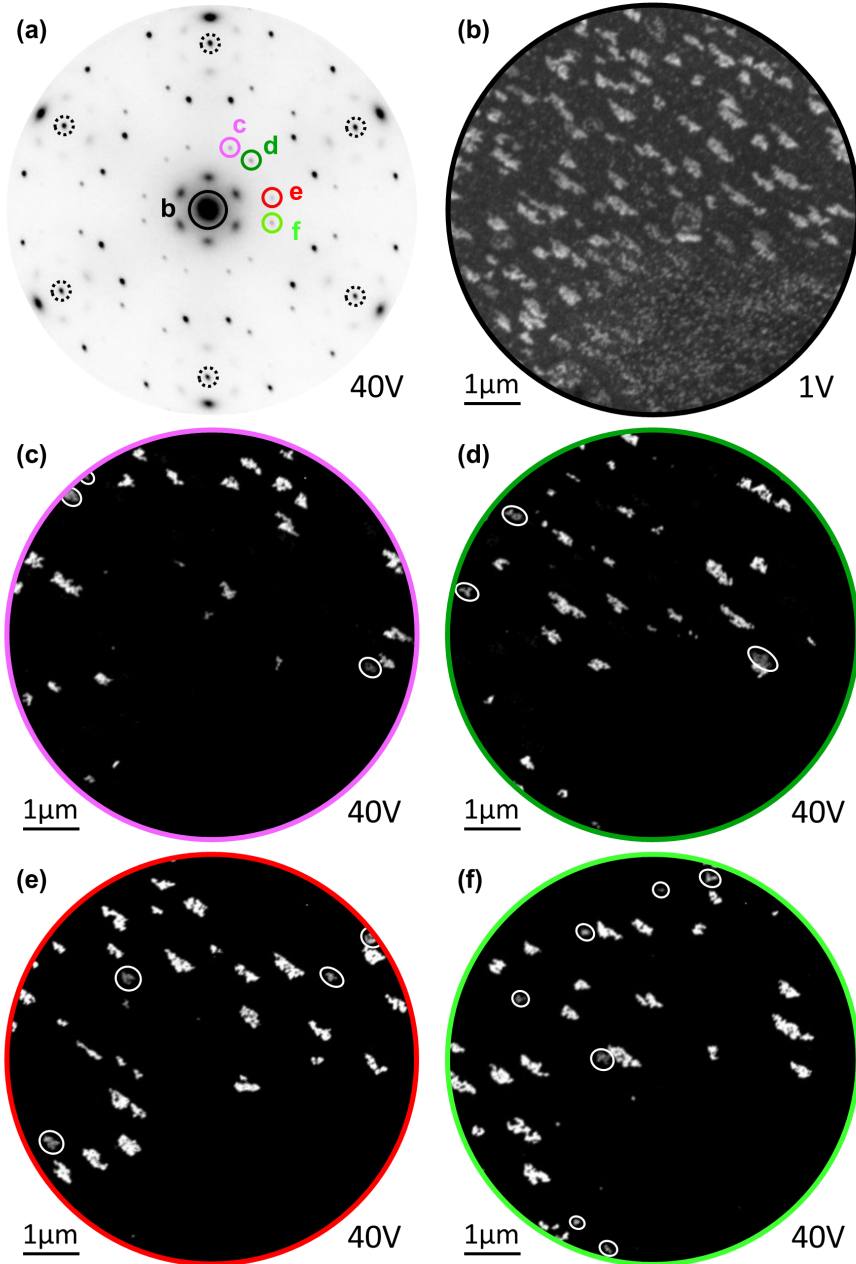


**Figure 3.17: DF-LEEM on the  $(\sqrt{7} \times \sqrt{7})$ - $R19.1^\circ$  reconstruction.** (a) LEED measurement of the investigated surface area. (b) BF-LEEM image at  $U_{start} = 1$  V. (c-f) DF-LEEM images of the  $(\sqrt{7} \times \sqrt{7})$ - $R19.1^\circ$  first-order diffraction spots at  $U_{start} = 40$  V. The spots selected for imaging are highlighted in (a) and named in accordance to the respective LEEM images.

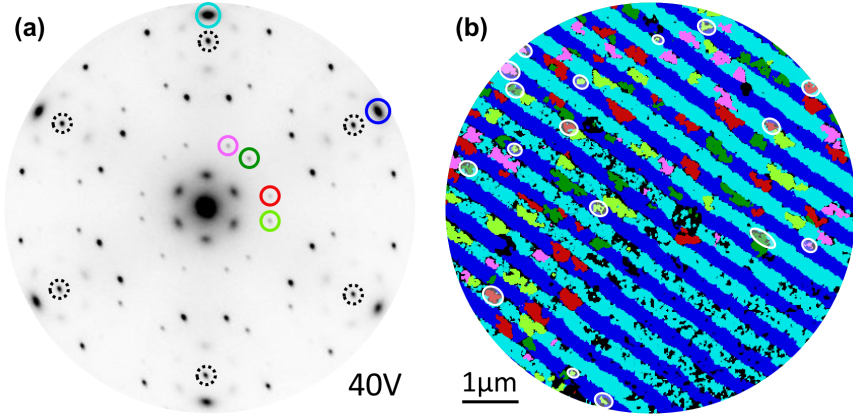


**Figure 3.18: DF-LEEM composite of  $B_xN_y-R0^\circ$  and  $(\sqrt{7} \times \sqrt{7})-R19.1^\circ$ .** (a) LEED spots used for DF-LEEM. (b) Composite of the two  $B_xN_y-R0^\circ$  domains from Fig. 3.13(d,f) and the four  $(\sqrt{7} \times \sqrt{7})-R19.1^\circ$  domains from Fig. 3.17(c-f).

green islands grew preferably on the same terrace as the light blue  $B_xN_y-R0^\circ$  domain. Given that the  $B_xN_y-R0^\circ$  rotational domains share a fixed adsorption configuration with the underlying substrate, it can be deduced that this also applies to the  $(\sqrt{7} \times \sqrt{7})-R19.1^\circ$  reconstructed islands.

However, not all  $(\sqrt{7} \times \sqrt{7})-R19.1^\circ$  islands exhibit the same adsorption configuration. As highlighted in white in Fig. 3.18(b), some of the dark green and red islands grew on light blue terraces and some of the magenta or light green islands grew on dark blue terraces. These are identical with the previously introduced atypical islands. Based on the symmetry relations of the different domains, it can be concluded that the atypical islands are characterized by a rotation of  $60^\circ$  with respect to the majority of the  $(\sqrt{7} \times \sqrt{7})-R19.1^\circ$  reconstructed islands on the same three-fold rotationally symmetric SiC terrace. It stands to reason that another adsorption configuration goes along with a difference in electrical properties, resulting in different LEEM intensities as reported in previous works, e.g. [MR1]. Therefore, typical and atypical islands can be distinguished by their LEEM-I(V) profiles shown in Fig. 3.11 and also in the DF-LEEM images of Fig. 3.17, where the atypical islands (white circles) show a reduced intensity compared to other islands. The small number and size of the atypical islands indicate that the adsorption configuration of this minority domains is energetically less favorable.

### Misoriented minority phase

In order to characterize the domain structure of the misoriented minority phase, the contrast aperture was positioned on the faint ring,  $30^\circ$  off from the SiC main axes, as indicated by the yellow and brown arrows in Fig. 3.19(a). The corresponding DF-LEEM images in Fig. 3.19(c,d) show that the minority phase manifests as small point-like objects. Their distribution across the surface is reminiscent

of the orange-marked nm-sized objects in Fig. 3.12(f). For better comparison, the composite image of the  $(\sqrt{7} \times \sqrt{7})\text{-}R19.1^\circ$  structure has been superimposed on a BF-LEEM image at  $U_{start} = 15\text{ V}$  in Fig. 3.19(b). The small bright objects near the islands exhibit different LEEM-I(V) characteristics than any other surface phase discussed so far. They are identified to belong to the misoriented minority phase. Because of its small contribution, small size, and orientational range, further characterization of this phase would be disproportionately elaborate.

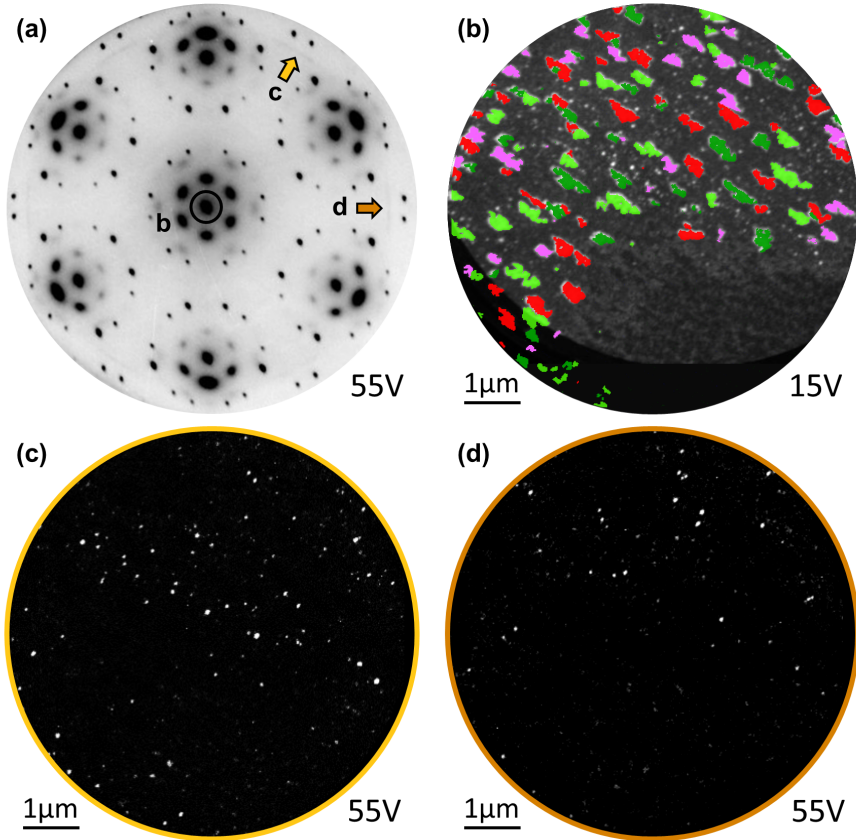


**Figure 3.19: DF-LEEM characterization of the misoriented minority phase.** (a) LEED measurement and (b) BF-LEEM image of the investigated surface area. The composite of the  $(\sqrt{7} \times \sqrt{7})\text{-}R19.1^\circ$  domains is superimposed. (c,d) DF-LEEM images of the misoriented minority phase. The contrast aperture positions selected for imaging are marked in (a).

### 3.4 Temperature dependence

To investigate the influence of temperature on the growth of BN, Sample 2 was annealed at a higher heating rate than Sample 1 while keeping the other preparation parameters constant. In the following, the surface structure of BN on Sample 2 is presented and compared with that of Sample 1. Then, the growth characteristics of BN on SiC(0001) and their temperature dependence are discussed in more detail and in the context of the literature.

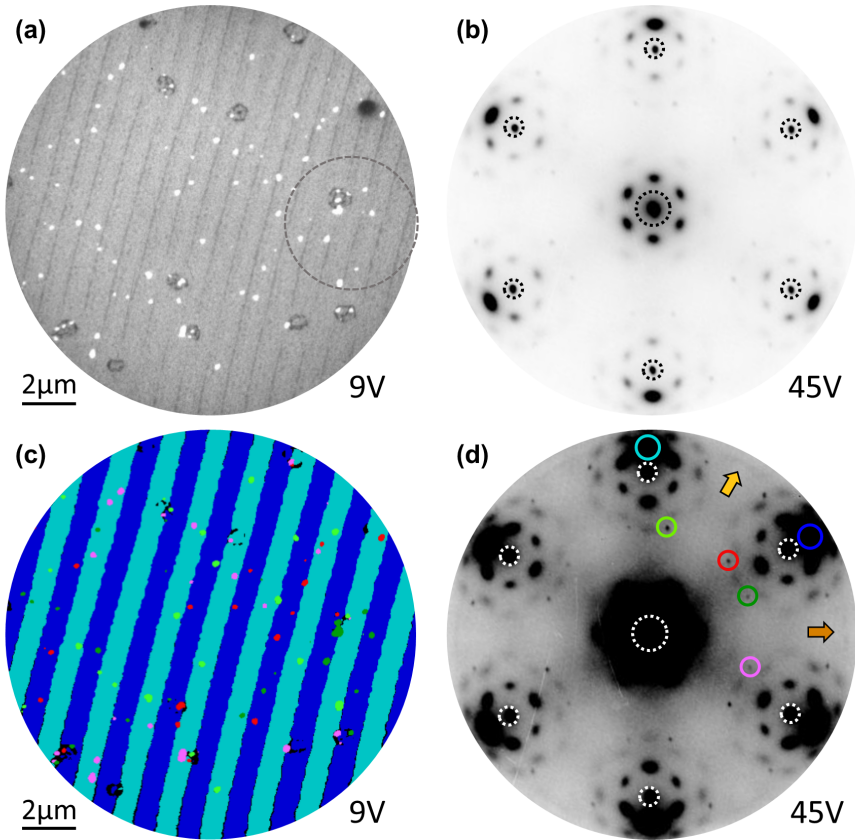
#### 3.4.1 BN on Sample 2 after fast annealing in Borazine

Fig. 3.20(a) shows a BF-LEEM image of Sample 2 after BN growth. The area shown is representative of Sample 2 and  $U_{start} = 9\text{ V}$  was chosen to provide optimal contrast between the bright  $(\sqrt{7} \times \sqrt{7})\text{-}R19.1^\circ$  reconstructed islands and the darker  $\text{B}_x\text{N}_y\text{-}R0^\circ$  terraces. Note that regions analogous to the island-free regions on Sample 1 were not found on Sample 2. Also, the number and size of the islands has strongly decreased compared to Sample 1. This is further substantiated by the LEED measurement in Fig. 3.20(b), which is dominated by the  $\text{B}_x\text{N}_y\text{-}R0^\circ$  pattern. With different brightness and contrast [see Fig. 3.20(d)], spots of the  $(\sqrt{7} \times \sqrt{7})\text{-}R19.1^\circ$  structure are better recognized (green and red). Additionally, traces of the misoriented minority phase are present, as indicated by the orange and brown arrows. Fig. 3.20(c) shows a DF-LEEM composite image of  $\text{B}_x\text{N}_y\text{-}R0^\circ$  and  $(\sqrt{7} \times \sqrt{7})\text{-}R19.1^\circ$  domains of the surface area from panel (a), analogous to that of Sample 1 [see. Fig. 3.18]. Apart from their reduced occurrence, the  $(\sqrt{7} \times \sqrt{7})\text{-}R19.1^\circ$  reconstructed islands are found in a similar domain configuration as on Sample 1.

Additional and more detailed information on the domain structure was obtained at a higher lateral resolution. To this end, the region marked with a dashed circle in Fig. 3.20(a) is characterized at a smaller field of view in Fig. 3.21. Panel (a) shows a BF-LEEM image at  $U_{start}=5.5\text{ V}$ . Three types of terraces can be distinguished by their width and contrast. The terrace marked in light blue is very thin and exhibits the darkest contrast. The terraces marked in medium and dark blue are nearly the same width and show bright contrast, however, the dark blue terrace is slightly thinner and darker. The LEEM-I(V) profiles of these three terraces are shown in panel (b). As discussed in Section 3.1.2, the different LEEM-I(V) profiles of these terraces are due to the varying SiC terminations underneath the  $\text{B}_x\text{N}_y\text{-}R0^\circ$  layer, and the different widths of the terraces result from the non-uniform step retraction of differently terminated SiC terraces during BN growth.

As in Section 3.1.2, the stacking configurations of the different terraces are identified by considering the stacking sequence of 6H-SiC(0001) and the step retraction model. Fig. 3.21(e) shows a BF-LEEM image at  $U_{start}=47.5\text{ V}$ . In this image, all three terrace types can easily be distinguished by their contrast. In panel (f), this BF-LEEM image is superimposed on a DF-LEEM composite of the  $\text{B}_x\text{N}_y\text{-}R0^\circ$  and  $(\sqrt{7} \times \sqrt{7})\text{-}R19.1^\circ$  domains, allowing identification of the  $S_n$  and  $S_n^*$  groups. According to the step retraction model, the terrace edge of  $S_1$  terraces retracts the

fastest during SiC decomposition at elevated temperatures. Thus, the stacking configuration of the thinnest terrace type (light blue) is identified as  $B_xN_y-R0^\circ$  on  $S_1$ . From the stacking sequence of 6H-SiC(0001), it follows that the medium blue and dark blue marked terraces have  $B_xN_y-R0^\circ$  on  $S_2$  and  $B_xN_y-R0^\circ$  on  $S_3$  stacking configurations, respectively. In agreement with Section 3.1.2, it is concluded that the surface slopes from left to right with step heights of one SiC bilayer and a terrace sequence  $S_3-S_2-S_1-S_3^*-S_2^*-S_1^*$  underneath  $B_xN_y-R0^\circ$ . Note that observations during the growth process indicate that step retraction terminates as soon as the terraces are covered with  $B_xN_y-R0^\circ$ .



**Figure 3.20: Overview of BN on Sample 2.** (a) LEEM image of a representative surface area and (b) corresponding LEED measurement. (c) DF-LEEM composite of  $B_xN_y-R0^\circ$  (light blue, dark blue) and  $(\sqrt{7} \times \sqrt{7})-R19.1^\circ$  (red, magenta, dark green, light green) domains, in analogy to the DF-LEEM composite of Sample 1 in Fig. 3.18(b). (d) LEED image from (b) but with different brightness and contrast. The spots used for DF-LEEM are colored in agreement with (c).

Now that the stacking configuration of the three different terrace types has been identified, the LEEM-I(V) data in Fig. 3.21(b) is considered again. As expected, the LEEM-I(V) profile of  $B_xN_y-R0^\circ$  on  $S_2$  terraces agrees well with that of  $B_xN_y-R0^\circ$  on Sample 1, as shown in Fig. 3.14(a). This is because the terrace configuration on Sample 1 corresponds to the final state of the step retraction model [see Fig. 3.5(c)], exhibiting only  $S_2$  terraces underneath  $B_xN_y-R0^\circ$ . Notably, the LEEM-I(V) profile of  $B_xN_y-R0^\circ$  on  $S_3$  is almost identical to that of  $B_xN_y-R0^\circ$  on  $S_2$ , while the LEEM-I(V) profile of  $B_xN_y-R0^\circ$  on  $S_1$  differs more strongly. This is in good agreement with the short penetration depth of electrons in LEEM. From top to bottom, the stacking of the first three layers of all terraces is identical, namely  $B_xN_y-R0^\circ$  on a boron buffer layer on a SiC bilayer. For  $B_xN_y-R0^\circ$  on  $S_2$  and  $B_xN_y-R0^\circ$  on  $S_3$ , the fourth layer is a SiC bilayer in cubic stacking. However, for  $B_xN_y-R0^\circ$  on  $S_1$ , the fourth layer is a SiC bilayer in hexagonal stacking.  $B_xN_y-R0^\circ$  on  $S_2$  and  $B_xN_y-R0^\circ$  on  $S_3$  only differ in stacking from each other in the fifth. As the contribution of deeper layers to the LEEM signal decreases, it is in agreement with the stacking sequences that the LEEM-I(V) profiles of  $B_xN_y-R0^\circ$  on  $S_2$  and  $B_xN_y-R0^\circ$  on  $S_3$  differ less from each other than from that of  $B_xN_y-R0^\circ$  on  $S_1$ .

The  $(\sqrt{7} \times \sqrt{7})-R19.1^\circ$  reconstruction and the misoriented minority phase in the investigated surface region in Fig. 3.21 are identified by imaging at higher  $U_{start}$  in panels (c) and (d). As presented in Section 3.3.2, the  $(\sqrt{7} \times \sqrt{7})-R19.1^\circ$  reconstruction exhibits bright contrast at  $U_{start} = 9\text{ V}$  and  $13\text{ V}$ , whereas the misoriented minority phase exhibits bright contrast only at  $U_{start} = 13\text{ V}$ . The latter manifests as nm-sized, point-like objects. The domains of the  $(\sqrt{7} \times \sqrt{7})-R19.1^\circ$  reconstruction and the misoriented minority phase appear to be randomly distributed.

While the contrast between  $B_xN_y-R0^\circ$  terraces of different SiC terminations almost vanishes in Fig. 3.20(c,d), a contrast between two domains of  $B_xN_y-R0^\circ$  becomes apparent. For better visibility, the contrast of the images was enhanced and a selected surface area is enlarged by a factor of 2 in the insets of both panels. Note that the two domains cannot be distinguished in DF-LEEM of the  $B_xN_y-R0^\circ$  main spots at  $U_{start} = 47.5\text{ V}$ . Furthermore, compared to  $B_xN_y-R0^\circ$  and its minority domain as found on Sample 1, the contrast between both domains is less strong and shows different LEEM-I(V) characteristics. Consequently, structure and electronic properties of the two domains largely match. Observations by Shin et al. [52] may provide a direction to explain the appearance of these domains. Upon the transition from BN to Gr- $R0^\circ$  under annealing in vacuum, the two structures were found to coexist in domains of similar size and shape. However, Sample 2 is not expected to show a transformation from BN to graphene already at the applied annealing temperatures. Thus, the difference between the domains is more likely due to differences in the stoichiometry of  $B_xN_y-R0^\circ$  as reported by Lin et al. [MR5].

Furthermore, the large number of dark spots scattered across all terraces in panels (a) and (e) is addressed. They do not correspond to the misoriented minority phase, as can be seen by comparing the surface region marked with a white ellipse in the lower left of panels (d) and (e). Given their similarity in contrast to the step edges, these dark spots are interpreted as point-like defects.

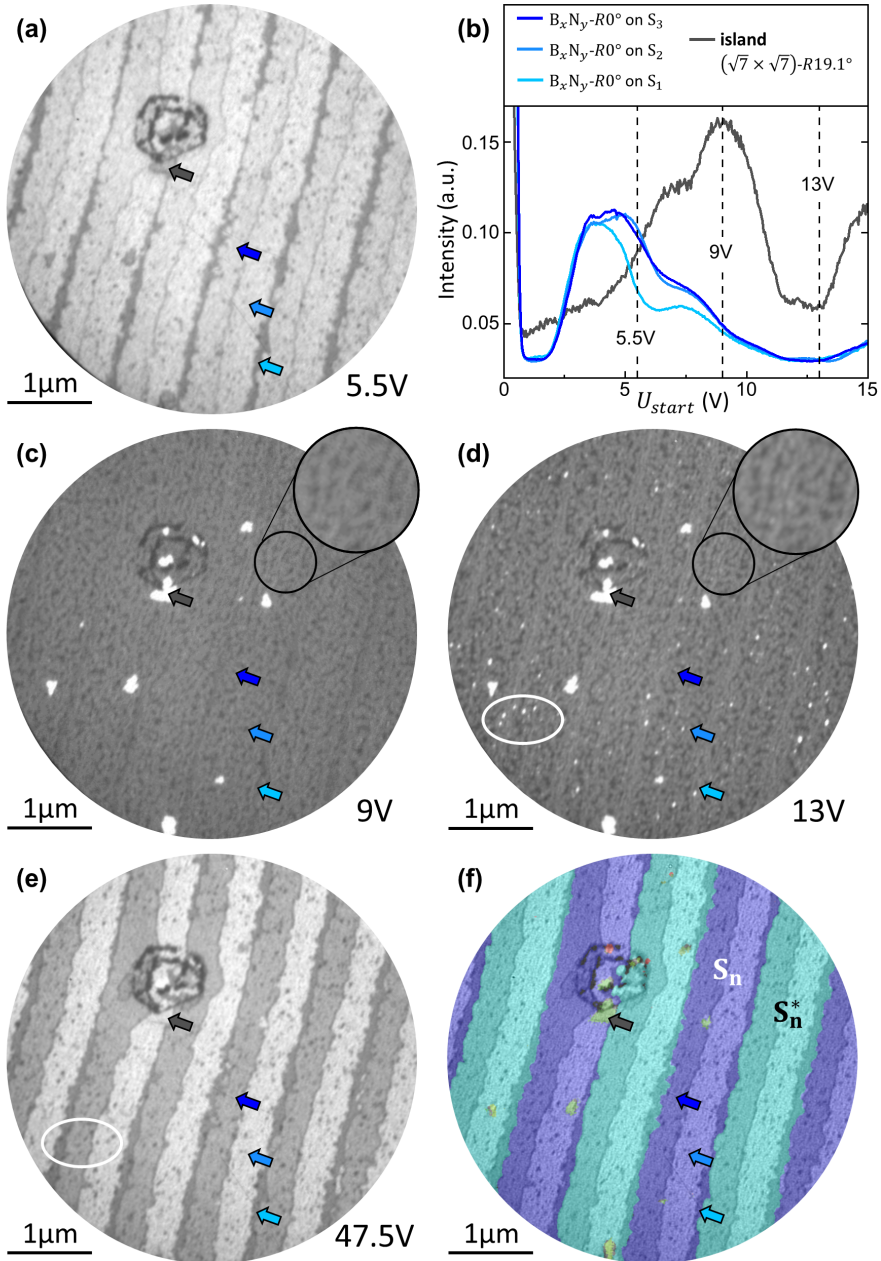


**Figure 3.21: Domain structure of Sample 2.** (a,c,d,e) BF-LEEM images of the same surface area that is marked with a dashed circle in Fig. 3.20(a). Imaging at selected  $U_{start}$  reveals further details on the domain structure, as discussed in the main text. (b) LEEM-I(V) profiles of the  $B_xN_y$ - $R0^\circ$  terraces and  $(\sqrt{7} \times \sqrt{7})$ - $R19.1^\circ$  reconstruction. (f) DF-LEEM composite image in analogy to Fig. 3.20.

In summary, the structural characterization of BN on Sample 2 shows that annealing at a higher heating rate during BN growth yields a more homogeneous  $B_xN_y$ - $R0^\circ$  layer. The  $(\sqrt{7} \times \sqrt{7})$ - $R19.1^\circ$  reconstruction and the misoriented minority phase remain present, exhibiting a domain structure consistent with that of Sample 1. However, their overall contribution has decreased significantly in favor of  $B_xN_y$ - $R0^\circ$ . This finding is consistent with the work of Lin et al. [MR5], who completely suppressed the growth of the  $(\sqrt{7} \times \sqrt{7})$ - $R19.1^\circ$  reconstruction by applying an even higher heating rate during BN growth.

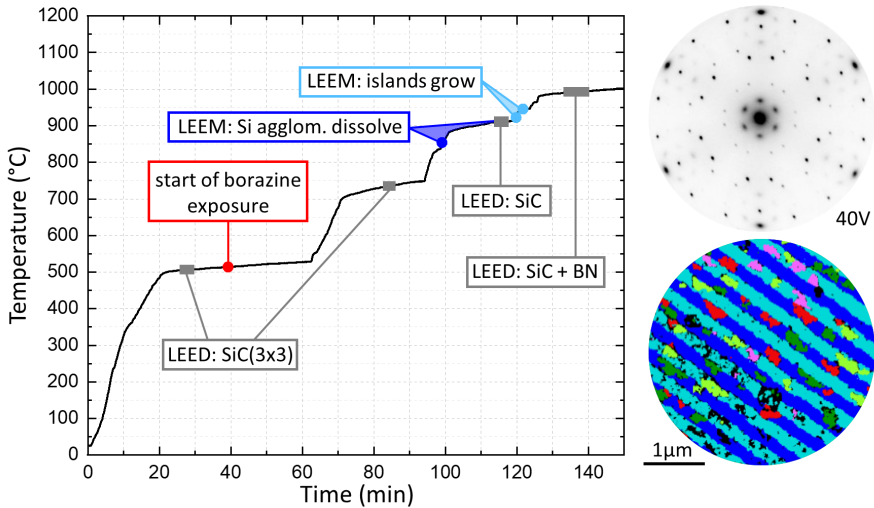
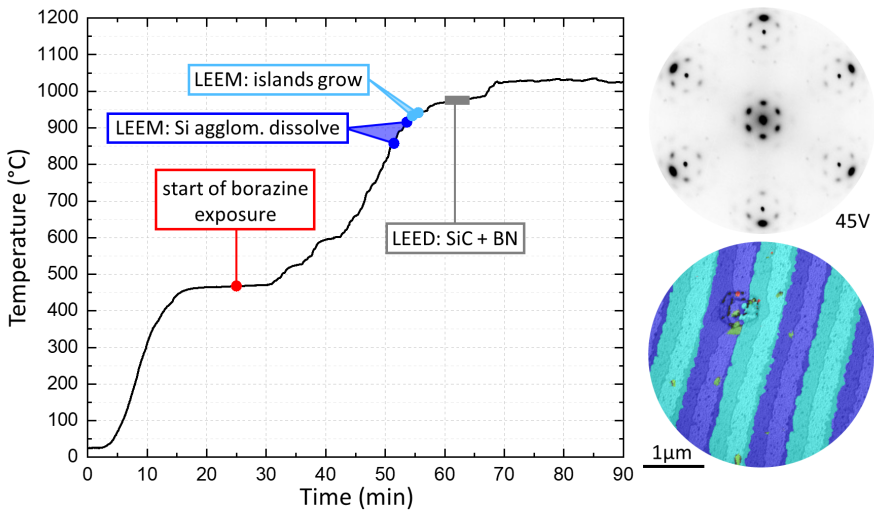
### 3.4.2 Discussion of BN growth characteristics

Finally, this section is devoted to the growth process of BN on SiC. New insights into the BN growth characteristics can be derived from observations during the growth experiments on Sample 1 and Sample 2 and are discussed in the following.

For both samples, the growth of  $B_xN_y$ - $R0^\circ$  could not be observed directly in LEEM mode. One possible reason could be that for the chosen  $U_{start}$ , there is no contrast between  $B_xN_y$ - $R0^\circ$  and the uncovered surface. Another possibility is that  $B_xN_y$ - $R0^\circ$  grows on a size scale too small to resolve and evolves by a uniform and continuous transformation of the surface. For example, a dendritic growth mode was found for NTCDA growth on Cu(001), which showed only a continuous change of intensity in LEEM mode [130]. Note that the boron buffer layer that was found to reside at the interface of  $B_xN_y$ - $R0^\circ$  and SiC in the work of Lin et al. [MR5] was not detected in this work, owing to its non-existing LEED signal.

To better understand the temperature dependence of the BN growth process, the temperature of both samples was recorded over time during BN growth, as shown in Fig. 3.22. Important observations in LEEM mode and LEED measurements are indicated, as well as the start of borazine exposure. The resulting surface composition is illustrated by the LEED and DF-LEEM composite images to the right of each panel. Throughout the experiment, emphasis was placed on correcting thermal drift, maintaining a constant borazine partial pressure, and applying appropriate imaging parameters. As the heating power was adjusted manually, the temperature-versus-time plot cannot be described by a simple function.

During the BN growth experiment, the temperature was measured using a thermocouple (W/Re 95:5 and 74:26) spot welded to the sample holder near the sample. However, in the case of the LEEM instrument the temperature measurement is complicated by the fact that the sample is floating at 20 keV, as well as a large part of the electronics, which includes the thermocouple readout. This results in a temperature offset that changes with the temperature inside the HV rack [130]. For this reason, the temperature scale has been corrected by an offset, assuming that the sample is at room temperature at the start of the experiment. By careful calibration, the uncertainty is estimated to be between 5°C and 15°C [130]. However, it should be noted that Samples 1 and 2 were mounted on two different sample holders. Furthermore, the thermocouple contacts are spot welded to the sample holder several millimeters away from the sample area observed with LEEM.

**(a) BN growth at slow annealing speed (Sample 1)****(b) BN growth at increased annealing speed (Sample 2)**

**Figure 3.22:** (a) Temperature-versus-time plot of Sample 1 during BN preparation. Events of interest (LEED measurements, borazine injection and observations in LEEM) are indicated. LEED measurement and false color composite image represent the surface composition after BN growth. (b) Temperature-versus-time plot of Sample 2, in analogy to (a).

Thus, systematic errors cannot be excluded. Estimating all these errors, the temperatures at which Si agglomerations dissolve ( $\sim 850 - 910^\circ\text{C}$ ) and islands grow ( $\sim 920 - 950^\circ\text{C}$ ) were similar in both experiments.

The experimental course and the final composition of the two samples offer valuable insights into the growth mechanism of BN on SiC. For Sample 1, a LEED measurement towards the end of the Si agglomerations dissolving and immediately before the island growth showed only the LEED pattern of SiC. Consequently, the  $(3 \times 3)$  reconstruction has vanished and no other stable surface reconstruction of SiC is present on the surface just before BN growth starts. Furthermore, a LEED measurement on Sample 2, less than 10 min after the  $(\sqrt{7} \times \sqrt{7})\text{-}R19.1^\circ$  islands began to grow, already showed a strong signal of the  $\text{B}_x\text{N}_y\text{-}R0^\circ$  structure. This suggests that  $\text{B}_x\text{N}_y\text{-}R0^\circ$  begins growing almost simultaneously with the  $(\sqrt{7} \times \sqrt{7})\text{-}R19.1^\circ$  structure, and proceeds at a considerable rate. Presumably, the  $(\sqrt{7} \times \sqrt{7})\text{-}R19.1^\circ$  reconstruction stops to grow at an early stage, because the surrounding area is already covered by  $\text{B}_x\text{N}_y\text{-}R0^\circ$  or other growth conditions are no longer met. In this context, note that Lin et al. [MR5] suggest that Si atoms are incorporated into the  $(\sqrt{7} \times \sqrt{7})\text{-}R19.1^\circ$  reconstruction. Under this hypothesis, an early termination of the growth of the  $(\sqrt{7} \times \sqrt{7})\text{-}R19.1^\circ$  reconstructed islands is plausible, since the Si-rich reconstruction is gone and Si atoms desorb faster with increasing temperature. Subsequent to the LEED measurement on Sample 2, the growth conditions were sustained for an additional 20 min. Since no evidence of second layer formation was found on either sample, it is concluded that BN growth on SiC is self-terminating, as it is also the case on metal surfaces.

Summarizing, the discussed BN growth characteristics imply that BN growth follows the typical scheme of CVD growth. However, when growing hBN on metal surfaces using CVD, the standard approach is to expose the metal to borazine only once the desired growth temperature is reached. This will initiate the growth immediately. The situation in the present experiment is more complicated because the composition of the SiC surface changes due to the ongoing Si sublimation during annealing. Previous studies have reported that the presence of a Si-rich reconstruction prior to borazine exposure at elevated temperatures is a necessary prerequisite for the growth of BN on SiC [MR5, 52]. Without the possibility to follow the growth process *in situ*, it was assumed that BN grows on the highly reactive Si-rich  $(\sqrt{3} \times \sqrt{3})\text{-}R30^\circ$  reconstruction, which is less Si-rich than the  $(3 \times 3)$  reconstruction. However, the *in situ* study presented here indicates that BN growth begins only once the excess of silicon has vanished due to sublimation at elevated temperatures. This results in a narrow regime of temperature and annealing duration where the Si loss has a specific grade and BN growth starts. It can be concluded that the reactivity necessary for CVD growth of BN on SiC is produced not only by the elevated temperature, but also by the Si depletion of the surface.

### 3.5 Conclusion

The study of BN growth on SiC is an important step in understanding the formation of unconventionally oriented Gr- $R0^\circ$  on SiC. In this chapter, BN growth was performed analogously to the work of Lin et al. [MR5]. New insights into the growth and domain structure of BN on SiC are obtained by LEEM, which allows BN growth to be observed *in situ* and in real time, and its structure and domain configuration to be characterized with lateral resolution.

Prior to BN growth, the SiC surface is enriched with Si by preparing a Si-rich ( $3 \times 3$ ) surface reconstruction. In this process, an excess of Si is found to form three-dimensional crystalline agglomerations. The structure of the 6H-SiC(0001) polytype and step retraction upon Si sublimation are discussed in context of literature and the LEEM-I(V) and DF-LEEM data of the two samples investigated in this chapter. The terrace configurations of Sample 1 and Sample 2 correspond to different stages of step bunching.

After BN growth, three structures were identified by LEED, namely  $B_xN_y-R0^\circ$ , a  $(\sqrt{7} \times \sqrt{7})-R19.1^\circ$  surface reconstruction, and a misoriented minority phase. A detailed discussion of their domain structure is presented for Sample 1. The most dominant surface phase is  $B_xN_y-R0^\circ$ . It covers the SiC terraces uniformly and with one fixed adsorption configuration. The  $(\sqrt{7} \times \sqrt{7})-R19.1^\circ$  reconstruction forms compact islands that are randomly distributed on the SiC terraces and do not cross step edges. Two adsorption configurations with SiC are possible, one of them being less energetically favored. Each configuration manifests in two mirror-symmetric domains. The misoriented minority phase (presumably BN or graphene) appears as nm-sized, point-like objects that are randomly distributed on the  $B_xN_y-R0^\circ$  covered islands. Sample 2 was prepared in the same way as Sample 1, but the heating rate during BN growth was increased. This resulted in a more homogeneous BN layer and shifted the ratio of  $(\sqrt{7} \times \sqrt{7})-R19.1^\circ$  reconstruction, misoriented minority phase, and  $B_xN_y-R0^\circ$  in favor of the latter, which is in good agreement with the work of Lin et al. [MR5].

The BN growth process is studied by LEEM and LEED *in situ* and in real time on both samples. Thereby, the formation of the  $(\sqrt{7} \times \sqrt{7})-R19.1^\circ$  reconstruction by nucleation and island growth is directly observed in LEEM mode. The formation of  $B_xN_y-R0^\circ$  can not be directly observed, suggesting growth by a uniform and continuous transformation of the surface on a size scale too small to resolve. From LEED measurements it is concluded that  $B_xN_y-R0^\circ$  begins to grow almost simultaneously with the  $(\sqrt{7} \times \sqrt{7})-R19.1^\circ$  reconstruction and shortly after the Si agglomerations dissolve. During the growth experiment, step retraction occurs due to thermal decomposition of SiC. This process as well as BN growth are found self-terminating once the surface is completely covered by one layer.

With a high initial growth rate and self-termination, the growth of BN on SiC fits the characteristics of CVD growth on metal surfaces. Yet, BN growth only begins at elevated temperatures when a specific level of Si depletion is reached. Therefore, it can be concluded that the necessary reactivity for CVD growth is produced not

only by elevated temperatures directly, but also indirectly due to the surface's structural change upon the temperature-induced Si sublimation. Note that this observation revises the assumption of Lin et al. [MR5] and Shin et al. [52] that BN grows on the highly reactive Si-rich  $(\sqrt{3} \times \sqrt{3})$ - $R30^\circ$  reconstruction. Nevertheless, it highlights the importance they attributed to silicon-rich starting conditions. These allow the necessary Si depletion for BN growth to be reached at higher temperatures, which results in higher-quality  $B_xN_y$ - $R0^\circ$  layers.

# Chapter 4

## Graphene on 6H-SiC(0001)

As previously outlined, the borazine-induced growth of Gr- $R0^\circ$  on SiC(0001) offers a promising way of producing large-scale, high-quality,  $30^\circ$ -twisted bilayer graphene ( $30^\circ$ -tBLG) [41, 53, 54]. The first step in understanding this process was to investigate the growth of BN under borazine exposure at temperatures up to  $1050^\circ\text{C}$ , as discussed in the previous chapter. To replace BN with graphene, the temperature must be increased significantly for a sufficiently long time. Thereby, silicon sublimates, leaving behind an excess of carbon atoms. This graphitization process is commonly used to grow conventional Gr- $R30^\circ$  on SiC(0001). However, when  $B_xN_y$ - $R0^\circ$  covers the SiC(0001) surface prior to graphitization, it is gradually replaced by Gr- $R0^\circ$ , while the  $0^\circ$ -orientation is conserved [MR5, 41, 52]. For the study reported in this chapter, the well-characterized BN layers from the previous chapter serve as templates for graphene growth on SiC(0001). This process and the resulting surface structures are investigated with LEEM. Thus, the graphitization processes of  $B_xN_y$ - $R0^\circ$  and the  $(\sqrt{7} \times \sqrt{7})$ - $R19.1^\circ$  reconstruction can be characterized separately. Furthermore, evidence was found that the surface morphology influences the graphitization process.

The first section of this chapter briefly summarizes the relevant details on the structures and the growth processes of Gr- $R30^\circ$  and Gr- $R0^\circ$  as reported in literature. Next, the experimental procedure is discussed that was applied to observe the replacement of BN by graphene in the in-situ LEEM experiment. During the experiment, the lateral domain configuration of the BN surface phases was found to remain unaltered. However, the graphitization of the surface becomes apparent through a structural analysis presented in Section 4.2. First, a structural overview of Sample 1 and Sample 2 (as presented in Chapter 3) after graphitization is given. Then, the structural change of three different surface domains is demonstrated for Sample 2:  $B_xN_y$ - $R0^\circ$  transforms continuously into Gr- $R0^\circ$ . Conventional Gr- $R30^\circ$  emerges in a small and clearly distinct area surrounding a defect. Strikingly, the  $(\sqrt{7} \times \sqrt{7})$ - $R19.1^\circ$  reconstruction is found to vanish in favor of a structure that shows characteristics of both Gr- $R0^\circ$  and Gr- $R30^\circ$ . Finally, different manifestations of bilayer graphene, possibly being  $30^\circ$ -tBLG, are identified on Sample 1 and Sample 2. In this context, it is discussed how the morphology of the samples affected the growth of graphene.

Please note that parts of the LEEM and LEED data presented in this chapter were collected under my guidance as a project for Hao Yin's master's thesis [124].

## 4.1 Introduction to the experiment

To motivate the experimental procedure of choice and interpret the LEED and LEEM features of different graphene configurations, an introduction to epitaxial graphene growth on SiC(0001) is provided first.

### 4.1.1 Gr- $R30^\circ$ and Gr- $R0^\circ$ on SiC(0001) in literature

In the context of this work, two methods of epitaxial graphene growth on SiC(0001) are relevant and were briefly introduced in the previous chapter. The first is the conventional growth of Gr- $R30^\circ$  by thermal decomposition in vacuum [50, 51, 143–145]. The second is the growth of Gr- $R0^\circ$  by using borazine as precursor gas [MR5, 41, 52–54]. This section provides more details on these graphene structures and their preparation, based on literature and selected by their relevance to the present work.

#### Gr- $R30^\circ$ grown by sublimation

As introduced in Section 3.1.2, SiC(0001) consists of SiC bilayers that are stacked on one another. In each bilayer, the silicon atoms on top form bonds with three carbon atoms below, resulting in a hexagonal lattice. When SiC(0001) is annealed at sufficiently high temperatures, Si atoms sublime, leaving behind an excess of C atoms at the surface. Thereby, the decomposition of about three SiC bilayers is required to form a carbon layer with a graphene-like atomic density. When SiC decomposition continues, a second carbon layer emerges underneath the first. [50]

Fig. 4.1(a) illustrates the vertical stacking of this layer system. The carbon layer directly atop SiC(0001) is the so-called carbon buffer layer or zeroth layer graphene (ZLG- $R30^\circ$ ) [145]. This layer has a hexagonal lattice and forms a commensurate  $(6\sqrt{3} \times 6\sqrt{3})$ - $R30^\circ$  superstructure on SiC(0001). Although it is geometrically very similar to graphene, it does not exhibit its characteristic electronic properties [143]. This can be attributed to the covalent interaction of about every third carbon atom with the Si dangling bonds at the interface of the SiC bulk and ZLG- $R30^\circ$  [143]. The second carbon layer on top is a former ZLG- $R30^\circ$ . Separated from the SiC bulk by the new ZLG- $R30^\circ$ , it does not share covalent interlayer bonds [145]. Therefore, it is found to exhibit the electronic characteristics of graphene. Note that the sublimation growth of graphene on SiC(0001) in UHV is a process far from equilibrium, resulting in inhomogeneous graphene layer thickness [51]. In LEEM, the layer thickness can easily be determined by LEEM-I(V) spectra due to the quantum size contrast [146, 147]. Thus, the number of minima in the  $\sim 0$ -8 eV range corresponds to the number of graphene layers (with ZLG- $R30^\circ$  not included), as demonstrated in Section 4.2.3 below.

Fig. 4.1(b) shows the characteristic LEED pattern of a monolayer Gr- $R30^\circ$  on ZLG- $R30^\circ$ /SiC(0001) obtained by thermal decomposition [144]. The unit cell vectors of SiC and graphene are indicated by black and brown arrows, respectively. The latter show the typical  $30^\circ$  rotation with respect to the SiC lattice. Other

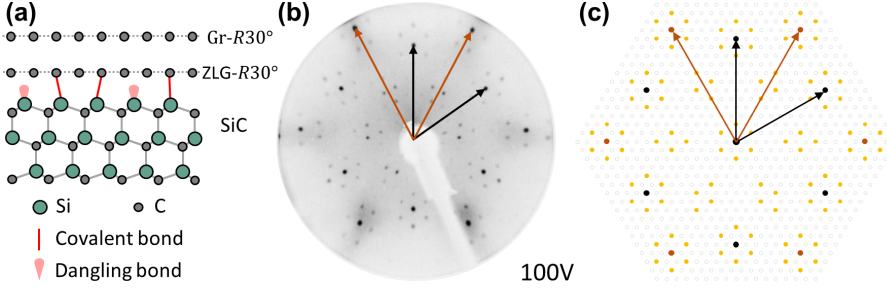


**Figure 4.1: Gr- $R30^\circ$  on SiC(0001), grown by thermal decomposition.** (a) Structure model of a monolayer graphene on ZLG- $R30^\circ$ /SiC(0001). Schematic based on Ref. [145]. (b) LEED measurement of Gr- $R30^\circ$ /ZLG- $R30^\circ$ /SiC(0001). The unit cell vectors of SiC (black) and graphene (brown) are indicated. The shown LEED data is courtesy of Hao Yin from PGI-3, Forschungszentrum Jülich. (c) Simulated LEED pattern. The  $(6\sqrt{3} \times 6\sqrt{3})$ - $R30^\circ$  lattice points are drawn in gray. The  $6\sqrt{3} \times 6\sqrt{3}$ -spots that are visible in the experiment are drawn in yellow.

spots lie on the  $(6\sqrt{3} \times 6\sqrt{3})$ - $R30^\circ$  grid of the superstructure pattern, as illustrated by the simulated LEED pattern in Fig. 4.1(c). The most intense spots on the  $(6\sqrt{3} \times 6\sqrt{3})$ - $R30^\circ$  grid are colored in yellow.

### Gr- $R0^\circ$ grown by borazine exposure

Annealing SiC(0001) in the presence of the precursor gas borazine opens up a route to obtain Gr- $R0^\circ$ , an unconventionally orientated graphene layer aligned with the SiC substrate [MR5, 41, 52–54]. Two preparation techniques have been established to grow Gr- $R0^\circ$  on SiC(0001), applying either a template-induced or a surfactant-mediated growth mode.

The template-induced growth mode was introduced by Shin et al. [52]. First, they prepared a BN layer on SiC(0001) by annealing a Si-enriched surface under borazine exposure. Then, they gradually converted the BN layer into graphene by performing annealing sequences at higher temperatures in UHV. The resulting stacking configuration is Gr- $R0^\circ$ /ZLG- $R30^\circ$ /SiC(0001). Based on this work, it was demonstrated that  $30^\circ$ -tBLG can be obtained by either further annealing of Gr- $R0^\circ$ /ZLG- $R30^\circ$ /SiC(0001) in UHV or by hydrogen intercalation of the ZLG- $R30^\circ$  underneath Gr- $R0^\circ$  [41]. However, it is evident that the quality of the final  $30^\circ$ -tBLG is constrained by the quality of the BN layer used as a template. Bocquet et al. [53] addressed this issue by introducing the surfactant-mediated growth method. Thereby, Gr- $R0^\circ$ /ZLG- $R30^\circ$ /SiC(0001) is obtained by directly annealing the Si-enriched SiC(0001) surface to the final temperature in borazine.

Following the surfactant-mediated growth mode, Bocquet et al. [53], Lin et al. [MR5] and Yin et al. [54] investigated the structural properties of layer systems obtained at different temperatures in more detail. Based on those works, Fig. 4.2 summarizes structural information of four different layer systems resulting from

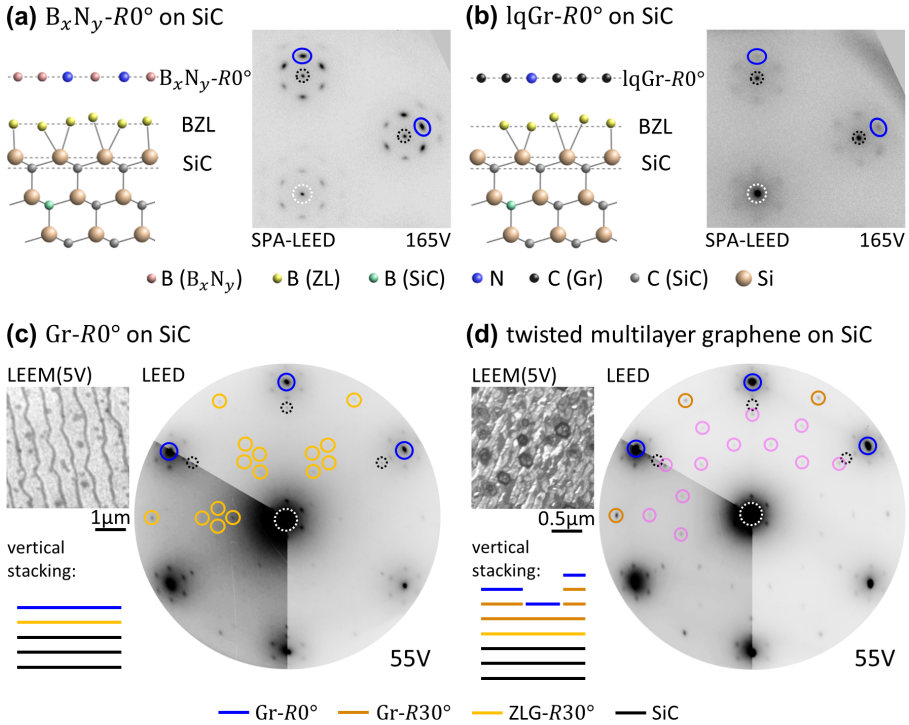


**Figure 4.2: Surface structures obtained by annealing a  $(3 \times 3)$ -Si reconstructed SiC(0001) surface in borazine at increasingly higher temperatures.** (a,b) Vertical structure models and SPA-LEED patterns of  $B_xN_y$ - $R0^\circ$  on SiC, obtained by annealing at 1100-1150°C and  $lqGr$ - $R0^\circ$  on SiC, obtained by annealing at 1225-1250°C. Ball-and-stick models of the vertical structures in (a) and (b) are based on NIXSW data and adapted with permission from Ref. [MR5], © 2022 by the American Physical Society (see License Notice). SPA-LEED data in (a) and (b) are taken from [148], licensed under CC-BY 4.0, see also Supplemental Material of Ref. [53]. (c,d) LEEM and LEED data of  $Gr$ - $R0^\circ$  on SiC, obtained by annealing at 1330° and twisted multilayer graphene on SiC, obtained by annealing at 1380°. The respective layer configuration is illustrated in the bottom left of each panel. LEEM and LEED data in (c) and (d) taken from [149], licensed under CC-BY 4.0, see also Ref. [54]. Note that all samples were produced in the same experimental setup, applying a borazine partial pressure of  $1.5 \times 10^{-6}$  mbar [MR5, 53, 54]. The sample temperature was increased rapidly to the respective preparation temperature and kept constant for 30 min.

annealing a  $(3 \times 3)$ -Si reconstructed SiC(0001) surface in borazine at increasingly higher temperatures.

Fig. 4.2(a) shows the structure of  $B_xN_y-R0^\circ$ , as previously introduced. A boron zeroth layer (BZL) is located between  $B_xN_y-R0^\circ$  and SiC [MR5]. The BZL does not exhibit long-range order. Consequently, the LEED pattern only exhibits features of SiC (black) and  $B_xN_y-R0^\circ$  (blue), along with satellite spots that can be explained by multiple scattering [see Section 3.3]. Note that boron also diffuses into the bulk, thereby possibly replacing C atoms in the SiC lattice (see Ref. [MR5]).

When the preparation temperature of  $B_xN_y-R0^\circ$  is exceeded, a carbon layer is found on the BZL instead, as shown in Fig. 4.2(b). In LEED, the first-order diffraction spots of this carbon layer form a hexagonal pattern (blue), which is aligned with SiC but has slightly larger reciprocal lattice vectors than  $B_xN_y-R0^\circ$ . This graphene layer exhibits a significant N doping and shows only faint, broad Dirac cones in ARPES [MR5]. Therefore, it is referred to as low-quality  $Gr-R0^\circ$  ( $lqGr-R0^\circ$ ) [MR5].

At high enough annealing temperatures,  $ZLG-R30^\circ$  evolves between  $Gr-R0^\circ$  and SiC. This is evident in the LEED pattern shown in Fig. 4.2(c). The satellite spots surrounding the 00-spot and the spots marked yellow are characteristic of  $ZLG-R30^\circ$ , as shown in Fig. 4.1. Furthermore, the satellite spots surrounding the blue-marked  $Gr-R0^\circ$  spots can be explained only by multiple scattering involving  $Gr-R0^\circ$  and  $ZLG-R30^\circ$  [53]. In LEEM, this layer system showed uniform terraces with LEEM-I(V) characteristics of a graphene monolayer, as well as indications of  $30^\circ$ -tBLG at the step edges [54].

Further increasing the temperature or extending the annealing time both results in the growth of  $Gr-R30^\circ$  multilayers underneath  $Gr-R0^\circ$ . As illustrated by the LEEM image and the schematic drawing to the left of Fig. 4.2(d), this manifests as small domains of various layer thicknesses [54]. In the corresponding LEED pattern,  $Gr-R0^\circ$  and  $Gr-R30^\circ$  (or  $ZLG-R30^\circ$ ) spots are marked in blue and brown, respectively. Besides the satellite spots surrounding the 00-spot and the  $Gr-R0^\circ$  spot (discussed above), two rings of additional twelve spots each (marked pink) are present. These LEED spots were found to be characteristic of  $30^\circ$ -tBLG [41, 54] and can be attributed to its quasicrystalline properties (see Ref. [41]).

### 4.1.2 The in-situ LEEM experiment

As described above, two pathways may be considered to obtain  $Gr-R0^\circ$  on SiC(0001). By first impression, it appears more attractive to aim for the surfactant-mediated growth mode, as it has proven to produce samples of higher quality [53]. Yet, the template-induced growth method was chosen for several technical reasons.

One of the major advantages of LEEM is the ability to observe the sample surface *in situ* during an experiment. However, fast annealing while operating the LEEM instrument is problematic. As the sample and sample holder heat up, material outgases, causing the pressure in the experimental chamber to rise.

The increased pressure in the mm-sized gap between sample and objective lens, where the electric potential drops by  $\sim 20$  kV, encourages sparks. The faster the annealing process, the greater the pressure increase and risk of sparks. These sparks contaminate sample surfaces with large amounts of defects and can destroy the surface structures that shall be investigated. Furthermore, maintaining proper imaging conditions and correcting thermal drift while monitoring temperature and pressure control is challenging, even at an annealing rate far below that used in the surfactant-mediated growth method. Finally, the well-characterized BN samples from the previous chapter are an optimal starting point for applying the template-induced growth method.

Accordingly, the BN layers prepared on Sample 1 and Sample 2, which were analyzed in the previous chapter, were observed with LEEM *in situ* while annealing in UHV. Note that two effects were encountered during annealing at high temperatures that significantly impacted the *in situ* LEEM measurement. The first effect is the increased emission of thermally excited electrons from the sample's surface. The second is a warming up (and hence a slight deformation) of the objective lens due to its short distance of  $\sim 2$  mm to the hot sample. Strategies to address the related imaging issues were successfully tested throughout this work and can be implemented in future experiments. For more details, refer to Appendix A.

The aforementioned effects can sometimes make *in situ* measurements during high-temperature annealing impossible. In the present work, however, this was a minor drawback because no visible changes occurred in the morphology or lateral domain distribution of BN on SiC. This can be seen, for example, in Fig. 4.3, which shows the same surface area of Sample 2 after BN preparation in panel (a) and after subsequent annealing in UHV at  $\sim 1200^\circ\text{C}$  for 20 min in panel (b). In both images, the contrast between the different terraces is dominant. Furthermore, the terrace contours remain unchanged, proving that no step retraction took place. The same applied to Sample 1 and Sample 2 when annealed in UHV up to  $\sim 1250^\circ\text{C}$ , as can be seen from the measurements presented in the following section.

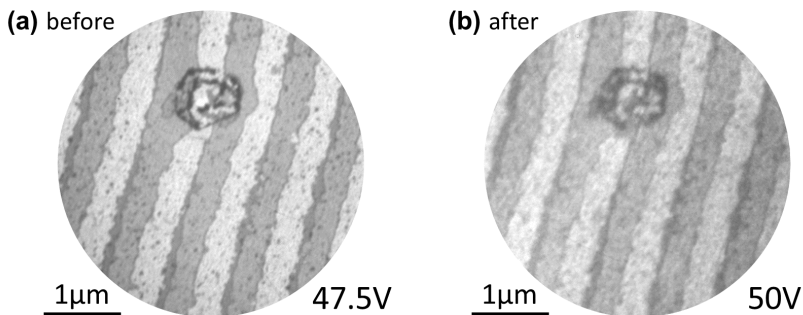


**Figure 4.3: BN on Sample 2 before and after annealing in UHV.** LEEM images taken of the same surface region (a) before and (b) after annealing at  $\sim 1200^\circ\text{C}$ . The blurring of (b) is mainly attributed to different imaging settings.

## 4.2 Graphitization of BN on SiC(0001) upon annealing in UHV

While the lateral domain distribution did not change upon annealing in UHV, BN was replaced by graphene. In this section, the structural composition of Sample 1 and Sample 2 is investigated at different stages of graphitization. The resulting graphene configurations vary, depending on the BN template, the sample morphology, temperature, and duration of the heat treatment. First, an overview of the structural composition of the examined surface regions after replacement by graphene is presented. Then, the evolution of different graphene configurations from the BN template is discussed in detail. Their structure and electronic properties are investigated using LEED, LEEM-I(V), DF-LEEM, and ARPES. Finally, hints for 30°-tBLG formation are discussed.

### 4.2.1 Structural overview

The following discussion of the template-grown graphene on SiC focuses on two surface regions. The first region is on Sample 2 and produced large, uniform areas of Gr- $R0^\circ$ . However, a different region is chosen to that observed during BN formation. The second region is on Sample 1, for which a detailed analysis of the BN domain structure prior to graphitization was presented in Section 3.3.2. Here, a first structural overview of these two regions after graphitization is given by LEEM and  $\mu$ LEED.

#### Graphene on Sample 2

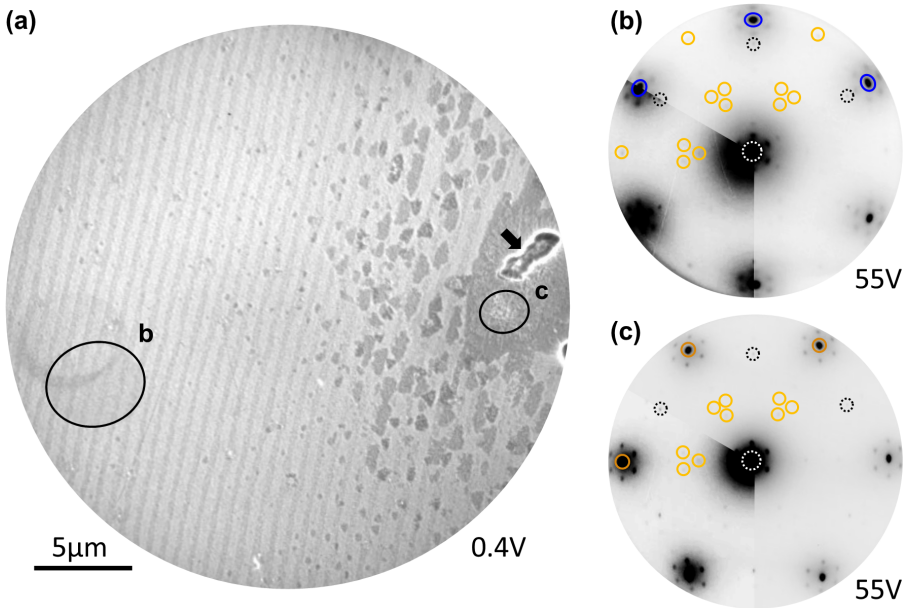
To obtain Gr- $R0^\circ$ , the BN on SiC(0001) prepared on Sample 2 was annealed in UHV by several runs. A first annealing was performed at  $\sim 1200^\circ\text{C}$  for 20 min. This yielded characteristics of lqGr- $R0^\circ$ . Subsequently, a temperature of  $\sim 1250^\circ\text{C}$  was applied for a total duration of  $>60$  min (second annealing). Note that characteristics of Gr- $R0^\circ$  were evident after only 20 min of this process. However, further annealing did not significantly alter the structural composition of Sample 2.

Fig. 4.4(a) shows a LEEM image of a particular surface area of Sample 2 taken after the second annealing. The left side of the LEEM image is representative of almost the entire investigated sample surface. It shows uniform terraces scattered with a few small, point-like objects. Some of these objects are defects with no crystalline structure that remained from the silicon agglomerations. Others originate from  $(\sqrt{7} \times \sqrt{7})$ - $R19.1^\circ$  reconstructed islands. These did not change shape during annealing but were replaced by graphene, as discussed below. A  $\mu$ LEED measurement of this surface area is shown in panel (b), confirming that it is largely dominated by Gr- $R0^\circ$  which replaced  $B_xN_y$ - $R0^\circ$ . The characteristic pattern of ZLG- $R30^\circ$  is recognizable by the satellite spots surrounding the 00-spot and the Gr- $R0^\circ$  spots, as well as the fainter spots in between.

In the right of Fig. 4.4(a), there is an area with a different domain structure. This

region is the only one with this particular domain structure on Sample 2. A defect located in its center is marked with a black arrow. This three-dimensional defect shows no LEED structure. Within a radius of several  $\mu\text{m}$ , it is surrounded by a compact domain with darker contrast than Gr- $R0^\circ$ . A  $\mu\text{LEED}$  measurement of this domain is shown in panel (c). It shows only the pattern characteristic of conventional Gr- $R30^\circ$  on SiC(0001). In the vicinity of the Gr- $R30^\circ$  domain, the surface is scattered with objects that can be identified as former  $(\sqrt{7} \times \sqrt{7})$ - $R19.1^\circ$  reconstructed islands, by their shape and similar contrast to the small islands found in other regions of the surface. With increasing distance from the large defect, they decrease in size and number.

Note that the BN configuration of this region was not characterized prior to graphitization. Presumably, the defect served as a nucleation center for a large silicon agglomeration when the  $(3 \times 3)$ -Si reconstruction was prepared but did not dissolve completely during BN growth. Once annealed in UHV, the silicon agglomeration likely dissolved completely, resulting in the formation of conventionally oriented Gr- $R30^\circ$  from the bare SiC surface. Furthermore, the large Si agglomeration may have served as a Si reservoir during BN growth, altering the growth conditions in its surroundings. This could explain the increased number and size of former  $(\sqrt{7} \times \sqrt{7})$ - $R19.1^\circ$  reconstructed islands found near the defect.



**Figure 4.4: Graphene on Sample 2.** (a) LEEM overview image of a particular surface region on Sample 2 after the second annealing. (b,c) LEED measurements of selected surface areas, as indicated in panel (a).

### Graphene on Sample 1

Sample 1 exhibited graphene-like features after just one annealing at  $\sim 1200^\circ\text{C}$  for 20 min. The surface area shown in Fig. 4.5 is the same as that characterized after BN growth and before graphitization. Under the chosen imaging conditions, the islands appear bright on the darker terraces. Direct comparison with LEEM images of BN on Sample 1 in Fig. 3.12(a,b) and the DF-LEEM composite image in Fig. 3.18(b) confirms that the shapes of the islands and step edges have not changed.

LEED measurements of a surface region that encloses islands, and of the region that is free of islands, are depicted in panels (b) and (c), respectively. Both patterns exhibit characteristics of Gr- $R0^\circ$  and Gr- $R30^\circ$ . Additionally, a faint ring indicates the presence of misoriented graphene with various rotational angles, but centered azimuthally around the Gr- $R30^\circ$  spots. The two patterns differ significantly only in the intensity of the Gr- $R30^\circ$  spots, which are more intense in the pattern of the surface region enclosing islands. Note that the carbon buffer layer spots are present in both LEED patterns, however less well pronounced than for Sample 2.

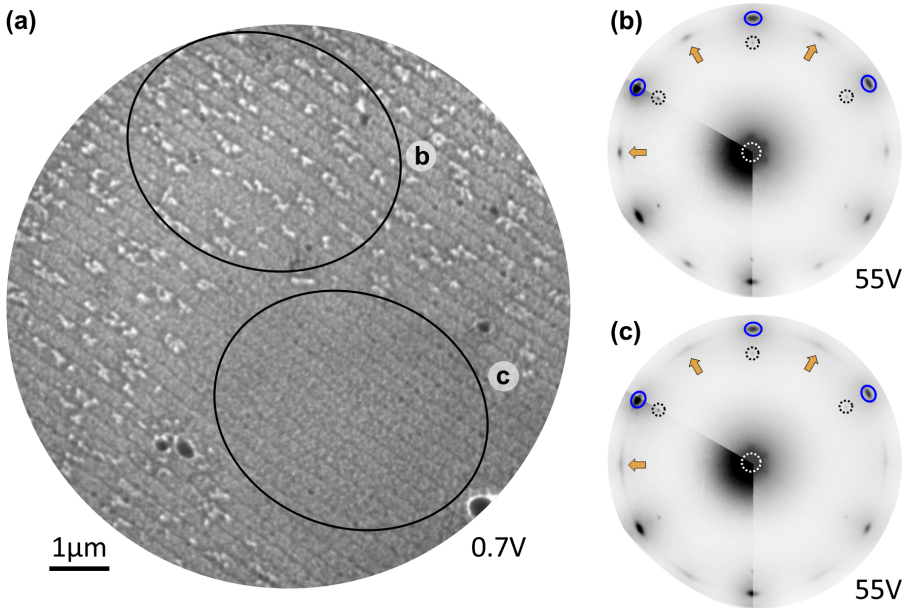


**Figure 4.5: Graphene on Sample 1.** (a) LEEM overview image of the same surface region that was characterized after BN growth in Section 3.3.2. (b,c) LEED measurements of selected surface areas, as indicated in panel (a).

## 4.2.2 Replacement of $B_xN_y-R0^\circ$ by $Gr-R0^\circ$

In the following, the structure and electronic properties of  $B_xN_y-R0^\circ$  upon annealing in vacuum is presented for Sample 2. As previously discussed, Sample 2 exhibits large, uniform areas of  $B_xN_y-R0^\circ$  after BN growth, which can be easily characterized with LEED and LEEM-I(V). Equivalent measurements were performed after the first and second annealing in UHV and are displayed in Fig. 4.6. Note that only the LEEM-I(V) profiles of terraces with SiC terminations of type  $S_2$  and  $S_3$  are shown. Those with  $S_1$  SiC termination vanished in the evaluated surface region displayed in Fig. 4.4. Panel (a) once again illustrates the LEED characteristics of  $B_xN_y-R0^\circ$ . The first-order diffraction spots of  $B_xN_y-R0^\circ$  are marked in blue. Most of the remaining spots are the result of multiple scattering including the SiC substrate and  $B_xN_y-R0^\circ$ . Some faint but sharp spots from the  $(\sqrt{7} \times \sqrt{7})-R19.1^\circ$  reconstruction are also present.

After the first annealing in UHV, the LEED pattern changed, as shown in panel (b). The reciprocal lattice vectors of the first-order diffraction spots became longer, corresponding to a shorter lattice vector in real space compared to  $B_xN_y-R0^\circ$ . This is also evident in the change of the multiple scattering pattern. Additionally, the traces of the island reconstruction have vanished. The LEED pattern described here agrees well with that of  $lqGr-R0^\circ$  reported by Bocquet et al. [53] upon annealing  $B_xN_y-R0^\circ$  in vacuum at 1225°C, and by Lin et al. [MR5] upon annealing to similar temperatures during borazine exposure. At this stage, the surface of Sample 2 was characterized by DF-LEEM, as presented in Fig. 4.7. Here, only the DF-LEEM images of the  $lqGr-R0^\circ$  main spots in panels (c) and (d) are considered. The terraces between the islands still exhibit inverted contrast, proving the three-fold symmetry of  $lqGr-R0^\circ$ . If all the boron and nitrogen atoms had already been replaced by carbon atoms, the inverted contrast of these DF-LEEM images would disappear. The LEEM-I(V) measurements of  $lqGr-R0^\circ$  on the right side of panel (b) differ significantly from those of  $B_xN_y-R0^\circ$  in panel (a). However, they also do not correspond to those of graphene monolayers on SiC reported in literature. This is another indication that the replacement by  $Gr-R0^\circ$  is incomplete. Therefore, the LEEM-I(V) profiles shown here may serve as a fingerprint to identify similar surface structures.

Panel (c) shows a LEED measurement taken after the second annealing in UHV. The first-order diffraction spots of  $lqGr-R0^\circ$  shifted slightly to larger  $|\mathbf{k}^\parallel|$ . These spots, as well as the 00-spot, are now surrounded by satellite spots that cannot be explained by multiple scattering at the graphene layer and the substrate. However, these spots, as well as other faint spots indicated in yellow, can be explained by the emerging carbon buffer layer at the interface of  $Gr-R0^\circ$  and SiC(0001), as previously discussed. The described LEED features are consistent with those expected for  $Gr-R0^\circ$ , as measured by Yin et al. [54] for a monolayer of  $Gr-R0^\circ$  on SiC obtained by surfactant-mediated growth [cf. Fig. 4.2(c)].

At this stage, the surface of Sample 2 was investigated again with DF-LEEM,

## 4.2 Graphitization of BN on SiC(0001) upon annealing in UHV

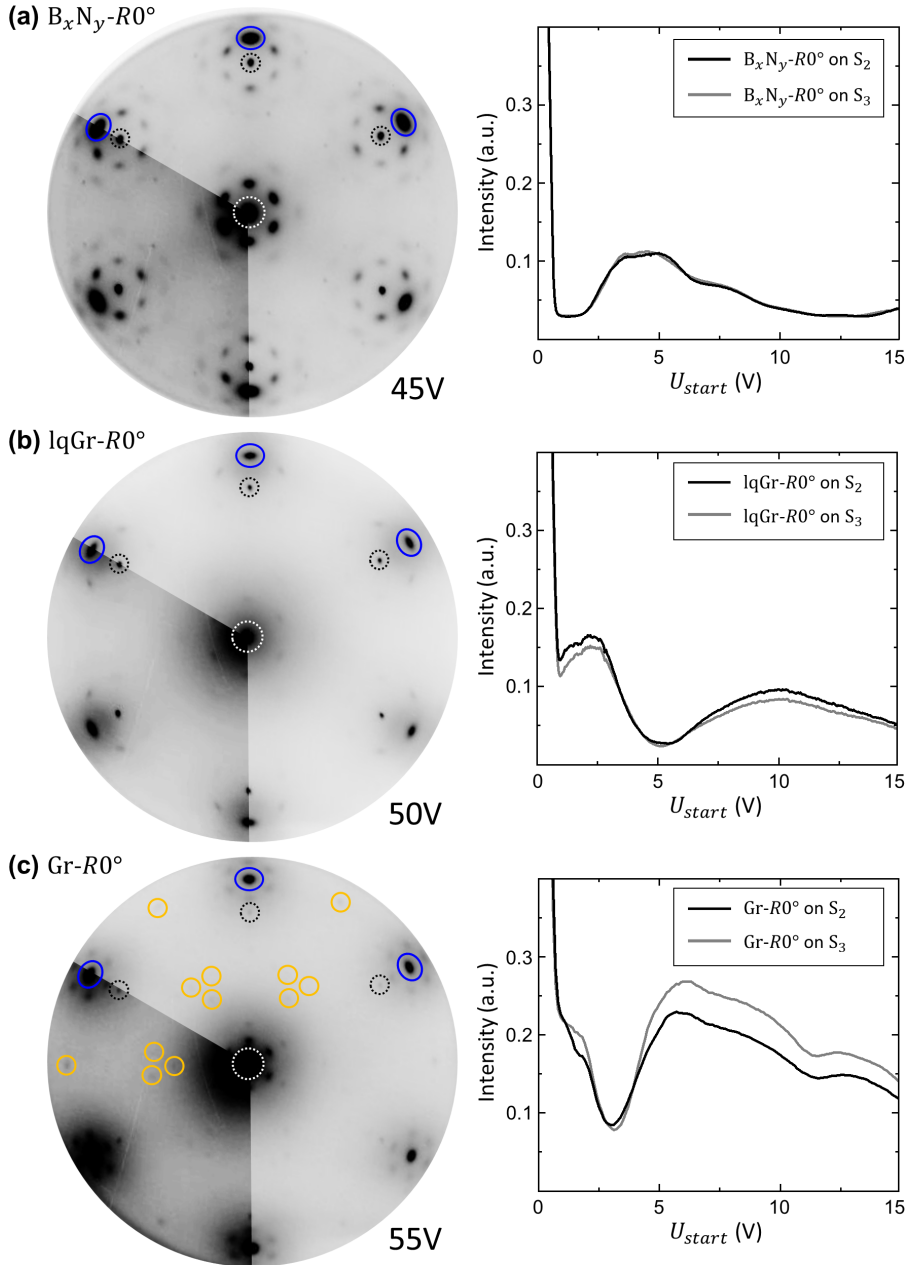


**Figure 4.6: Replacement of  $B_xN_y-R0^\circ$  by Gr- $R0^\circ$ .** (a) LEED measurement and LEEM-I(V) profiles of  $B_xN_y-R0^\circ$  on SiC. (b,c) Same as (a), after the first and second annealing in UHV, respectively. The structures are identified as (b) lqGr- $R0^\circ$  and (c) Gr- $R0^\circ$ . In the LEED images, the first-order diffraction spots of the adlayer are highlighted in blue and some characteristic spots of the carbon buffer layer are highlighted in yellow. Data measured on Sample 2.

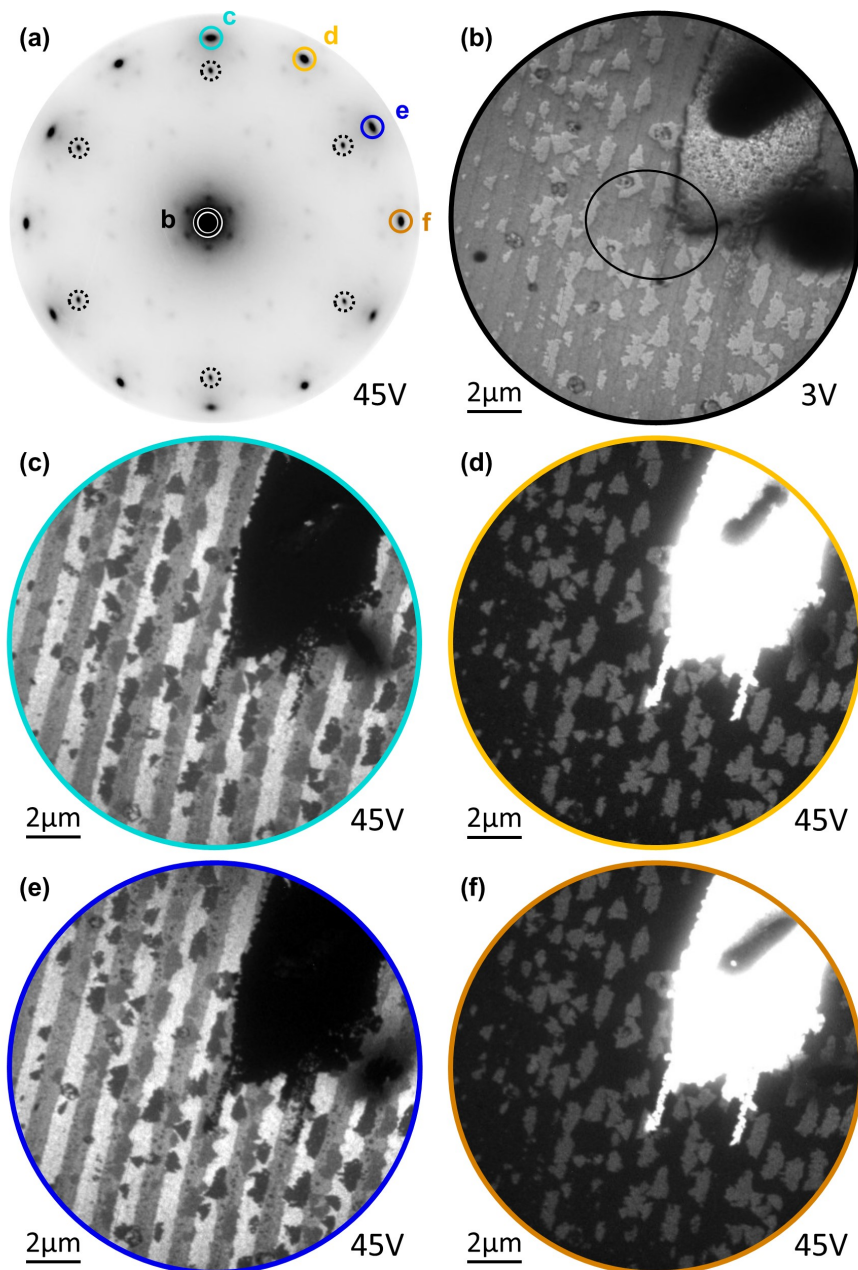


**Figure 4.7: DF-LEEM data recorded from Sample 2 after the first annealing in UHV.** (a) LEED measurement of the area marked in the (b) BF-LEEM image, which shows a section of Fig. 4.4(a) with a field of view of  $\sim 15 \mu\text{m}$ . (c-f) DF-LEEM images of the same area at  $U_{\text{start}} = 45 \text{ V}$ . The spots selected for imaging are marked in (a) and named according to the respective LEEM images.

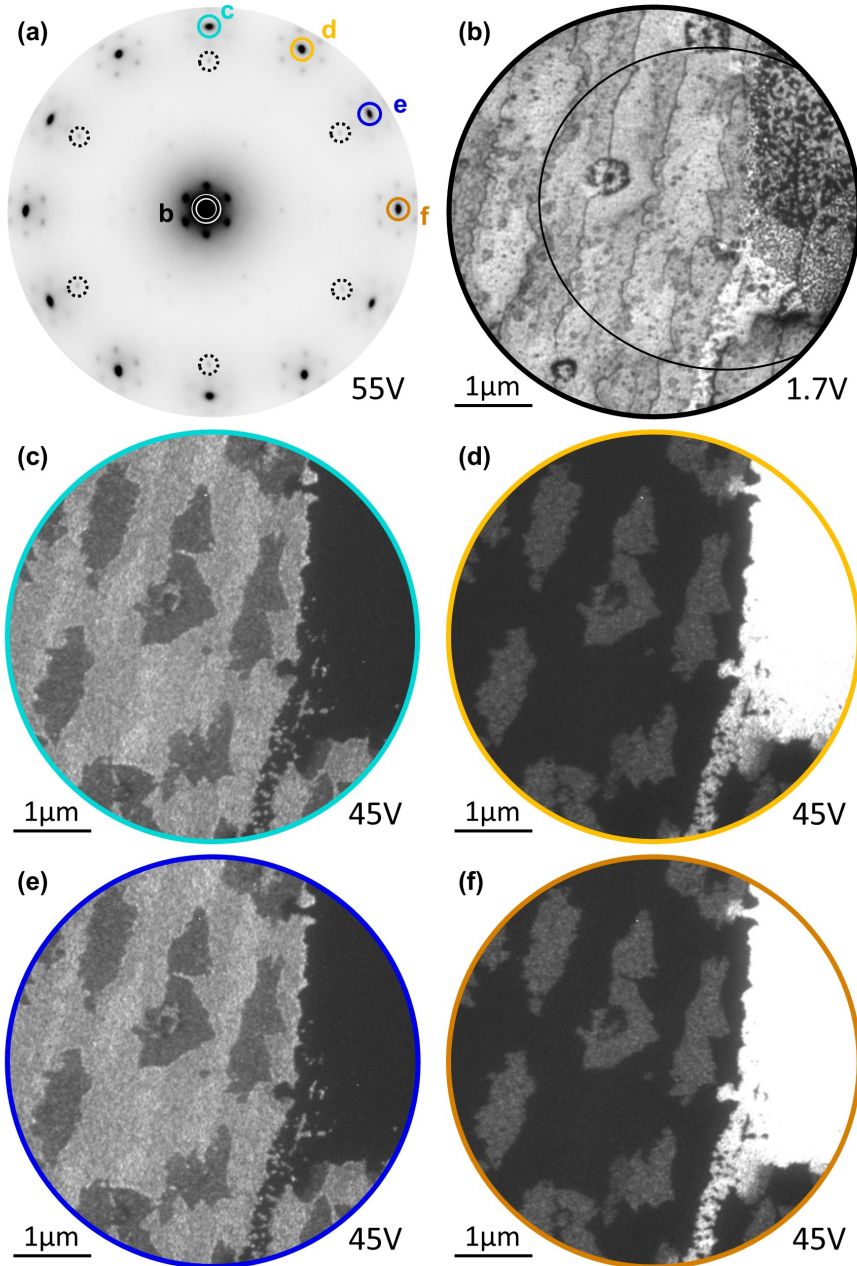


**Figure 4.8:** DF-LEEM data recorded from Sample 2 after the second annealing in UHV. (a) LEED measurement of the area marked in the (b) BF-LEEM image. The latter shows a section of Fig. 4.4 with a field of view of  $\sim 5 \mu\text{m}$ . (c-f) DF-LEEM images of the same area at  $U_{start} = 45 \text{ V}$ . The spots selected for imaging are marked in (a) and named according to the respective LEEM images.

as shown in Fig. 4.8. Once more, only the terraces between the islands in the DF-LEEM images of the Gr- $R0^\circ$  main spots in panels (c) and (d) are discussed. The different SiC terminations of the underlying substrate result in slightly different contrast of alternating terraces. However, there is no contrast inversion between panel (c) and (d). This confirms that the three-fold symmetry of  $B_xN_y$ - $R0^\circ$  and lqGr- $R0^\circ$  has vanished, indicating that the replacement of boron and nitrogen atoms is largely complete. However, note that considerable doping by substitutional B and N atoms is likely to remain present [MR5, 53].

Next, the LEEM-I(V) characteristics of Gr- $R0^\circ$  are addressed. It is well known from previous studies that for graphene layers grown on SiC with a carbon buffer layer at the interface, the number of dips in the 0-7 V range of LEEM-I(V) spectra corresponds directly to the number of graphene layers (see Ref. [147] and references therein). The LEEM-I(V) spectra of Gr- $R0^\circ$  to the right of Fig. 4.6(c) show one well pronounced dip close to  $U_{start} = 3$  V. The overall shape of the profiles also corresponds well with measurements of epitaxial graphene on SiC as reported in literature [54, 96, 145, 146, 150]. This confirms that Gr- $R0^\circ$  exhibits the electronic characteristics of monolayer graphene on SiC with ZLG- $R30^\circ$  at the interface.

In addition to LEEM, ARPES was applied to study the band structure of lqGr- $R0^\circ$  and Gr- $R0^\circ$ . Fig. 4.9 shows the momentum maps of both structures taken at  $E_b = 1.5$  eV. The inset in each panel shows a band map along the  $\overline{\Gamma K}$  direction, however with low statistical significance. Data on both surface struc-

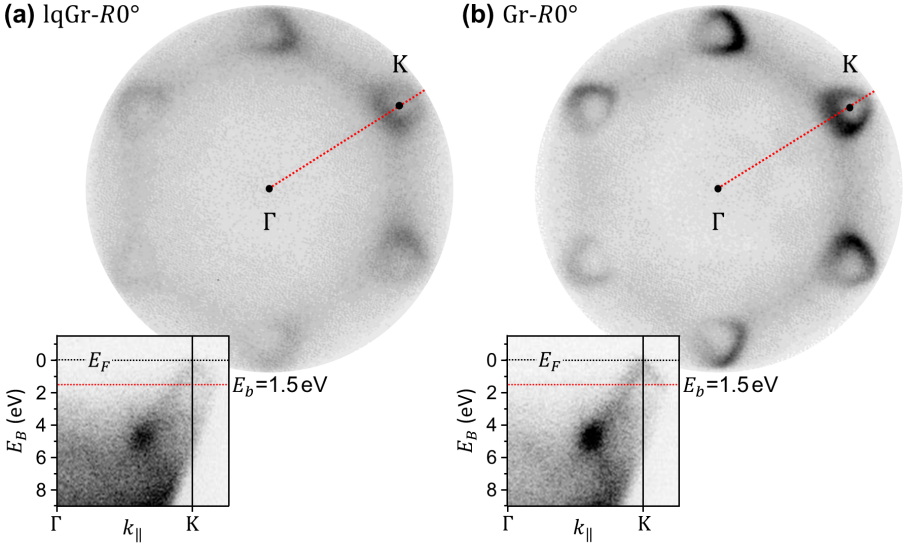


**Figure 4.9: ARPES data, recorded on Sample 2.** Momentum maps of (a) lqGr- $R0^\circ$  and (b) Gr- $R0^\circ$  at a binding energy of  $E_b = 1.5$  eV. The inset of each panel shows a band map along  $\overline{\Gamma K}$ , as indicated in the momentum map.

tures were taken with the same imaging parameters, allowing direct comparison of intensities. The ARPES data show the characteristic features of graphene's Dirac cones for both lqGr- $R0^\circ$  and Gr- $R0^\circ$ . However, the latter yields a significantly stronger signal and sharper features. This further supports the improvement of the electronic structure of Gr- $R0^\circ$  upon the second annealing in UHV.

### 4.2.3 Emergence of conventional Gr- $R30^\circ$

Next, the area close to the defect in Fig. 4.4 is investigated. As mentioned above, it exhibits LEED features solely of Gr- $R30^\circ$ . Since Gr- $R30^\circ$  naturally grows by SiC decomposition during annealing in UHV, it is concluded, that the surface area covered by Gr- $R30^\circ$  at this stage has not been covered by  $B_xN_y$ - $R0^\circ$  during BN growth. Presumably, this is due to the large defect that may have served as a nucleation center for an exceptionally large Si agglomeration. In this case, the Si agglomeration would have dissolved completely during the first annealing in UHV, thereby enabling the growth of conventional Gr- $R30$ .

Fig. 4.7 shows DF-LEEM images of the area of interest obtained from Gr- $R30^\circ$  first-order diffraction spots after the first annealing in panels (d) and (f). Areas of three different intensities can be distinguished. The darkest intensity is found on the lqGr- $R0^\circ$  terraces. The islands exhibit an intermediate intensity, which is discussed below. The region surrounding the defect provides the brightest intensity. In the DF-LEEM images obtained from the lqGr- $R0^\circ$  spots in Fig. 4.7(c,e), this region exhibits no intensity. Investigating this surface region with DF-LEEM after the second annealing in UHV [cf. Fig. 4.8] shows an equivalent structural composition. Consequently, this region is covered exclusively by conventional Gr- $R30^\circ$  after the first and second annealing in UHV.

After the second annealing, the area covered by Gr- $R30^\circ$  was examined more closely using LEEM-I(V), as presented in Fig. 4.10. Panel (a) shows the same surface area that was previously investigated with DF-LEEM. This image was captured in BF-LEEM mode at  $U_{start} = 5.2$  V. The area highlighted in yellow is covered exclusively by Gr- $R30^\circ$ , as identified by DF-LEEM. Within this area, some of the terrace contours are visible. However, the terraces are not uniform; rather, they show small domains of varying intensity. For a closer view, the surface region within the black rectangle is shown again in panels (i-iv) for varying  $U_{start}$ . Four domains are identified by their different LEEM-I(V) characteristics and marked with colored arrows. Panels (b) and (c) display the extracted LEEM-I(V) profiles of these domains in two different diagrams. In the latter, the profiles are shifted in intensity and sorted by the number of dips in the range of 0-7 V. This number corresponds directly to the number of graphene layers on top of the carbon buffer layer [147], which is indicated for each profile. By comparing the unmodified LEEM-I(V) profiles in panel (b), areas can be assigned to specific film thicknesses. Following the contours of the terraces from bottom to top in the LEEM images, it is evident that the area adjacent to Gr- $R0^\circ$  is dominated by one-layer thick Gr- $R30^\circ$ . At the top of panels (i-iv) and farther away from

Gr- $R0^\circ$  on the same terrace, the coverage of one-layer thick domains decreases and three-layer and four-layer thick domains appear more frequently. Overall, it is concluded that the observed domain structure of Gr- $R30^\circ$  is consistent with the results of previous LEEM studies on the growth of Gr- $R30^\circ$  on SiC by thermal decomposition in UHV (e. g. Refs. [144, 145]).

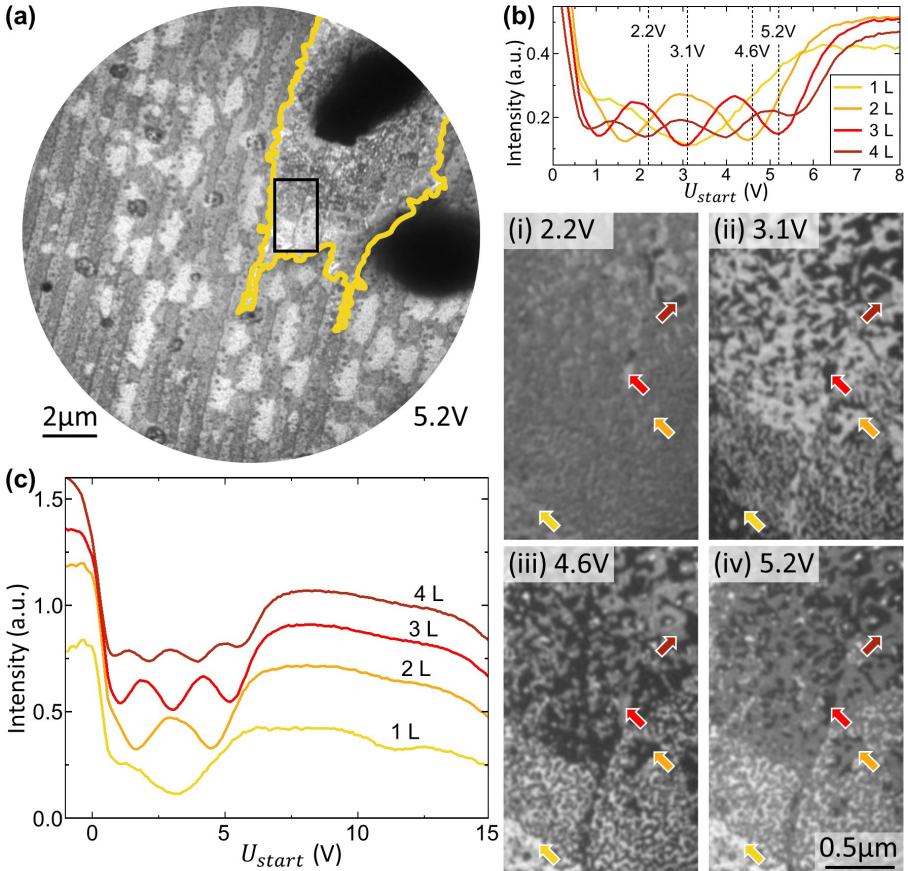


**Figure 4.10: Determination of the multilayer thickness of Gr- $R30^\circ$  on Sample 2.** (a) BF-LEEM image. The yellow line marks the Gr- $R30^\circ$  region [c.f. DF-LEEM characterization in Fig. 4.7]. The area marked with a black rectangle is shown in the BF-LEEM images (i-iv) for different  $U_{start}$  and at a smaller field of view. (b) LEEM-I(V) profiles of different surface areas, as marked in panels (i-iv). (c) LEEM-I(V) profiles as shown in (b), shifted vertically by applying an offset. Data measured after the second annealing in UHV.

#### 4.2.4 Replacement of the $(\sqrt{7} \times \sqrt{7})$ - $R19.1^\circ$ reconstruction by mixed Gr- $R0^\circ$ /Gr- $R30^\circ$

As previously mentioned, the spots originating from the  $(\sqrt{7} \times \sqrt{7})$ - $R19.1^\circ$  reconstruction disappeared in LEED after the first annealing of Sample 2. Nevertheless, the island-shaped domains of the  $(\sqrt{7} \times \sqrt{7})$ - $R19.1^\circ$  reconstruction remain visible in LEEM, even after the second annealing in UHV. Their structural change upon graphitization is analyzed by  $\mu$ LEED, DF-LEEM, LEEM-I(V) and ARPES.

The DF-LEEM measurements presented in Fig. 4.7 and 4.8 gave a first idea of the structural composition of the islands on Sample 2. Fig. 4.7(c,e) shows the DF-LEEM images obtained from the lqGr- $R0^\circ$  first-order diffraction spots. The islands appear darker than the lqGr- $R0^\circ$  covered terraces. However, they still exhibit a non-vanishing intensity, unlike the Gr- $R30^\circ$  region. Moreover, the islands can be divided into two groups of slightly different intensities. The islands on the brighter lqGr- $R0^\circ$  terraces exhibit lower intensity than the islands on the less bright lqGr- $R0^\circ$  terraces. Similar to the lqGr- $R0^\circ$  terraces, the contrast is inverted between panels (c) and (e). This contrast inversion disappeared after the second annealing, as shown in Fig. 4.8(c,e). Again, the intensity of the islands is lower than that of the surrounding terraces. Strikingly, the islands also exhibit intensity in the DF-LEEM images obtained from the Gr- $R30^\circ$  spots after the first and the second annealing in UHV [cf. Figs. 4.7(d,f) and 4.8(d,f)], respectively. However, their intensity is significantly lower than that of the area covered exclusively by Gr- $R30^\circ$ .

In addition to DF-LEEM,  $\mu$ LEED was applied to the islands. Fig. 4.11 depicts  $\mu$ LEED measurements of an individual island after the first and second annealing in panels (a) and (b), respectively. After the first annealing in UHV, the LEED pattern characteristic of lqGr- $R0^\circ$  [cf. Fig. 4.6(b)] is clearly visible. Additional

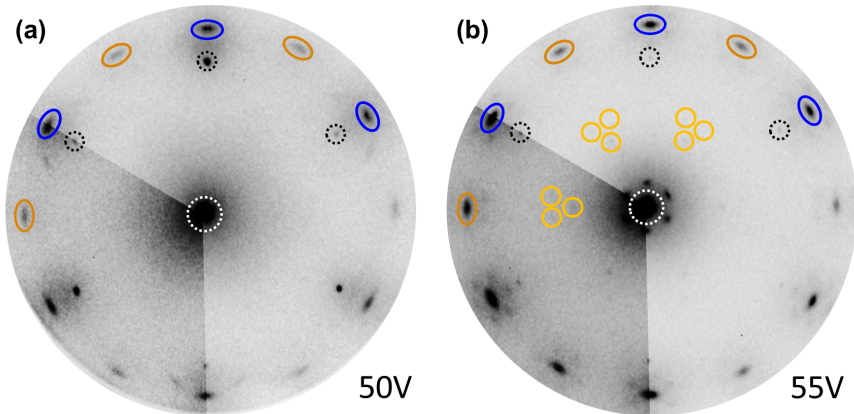


**Figure 4.11:**  $\mu$ LEED measurements on an island on a  $S_2$  terminated terrace of Sample 2, recorded (a) after the first and (b) after the second annealing.

spots are found at the Gr- $R30^\circ$  positions. After the second annealing, the  $\mu$ LEED image in panel (b) shows a superposition of the Gr- $R0^\circ$  and Gr- $R30^\circ$  patterns. The spots of the carbon buffer layer are also present. Note that these images were obtained with different settings and statistics. Therefore, the intensities and sharpness of the spots cannot be compared. However, the spots of Gr- $R0^\circ$  and Gr- $R30^\circ$  are azimuthally broadened compared to the patterns of exclusively Gr- $R0^\circ$  and Gr- $R30^\circ$  areas discussed previously [cf. Fig. 4.4(b,c)].

The coexistence of Gr- $R0^\circ$  and Gr- $R30^\circ$  LEED characteristics on the areas previously covered by the  $(\sqrt{7} \times \sqrt{7})$ - $R19.1^\circ$  reconstruction is an interesting finding. Of particular note, the islands are laterally homogeneous in their intensity in the DF-LEEM images for both graphene orientations [cf. Figs. 4.7 and 4.8]. This naturally evokes associations with  $30^\circ$ -tBLG. Therefore, the next step is to consider LEEM-I(V), as it has proven to be an effective tool for layer thickness determination.

In the vicinity of the defect, islands grew on SiC of different termination. Therefore, slight variations in their LEEM-I(V) characteristics were observed. This is illustrated in Fig. 4.12 for Sample 2 after the first annealing. Panels (i-iii) show the surface at different  $U_{start}$ . In each image, a distinct group of islands exhibits the brightest contrast. These groups differ considerably in the number and size of islands, which relates to the different terrace widths resulting from step bunching

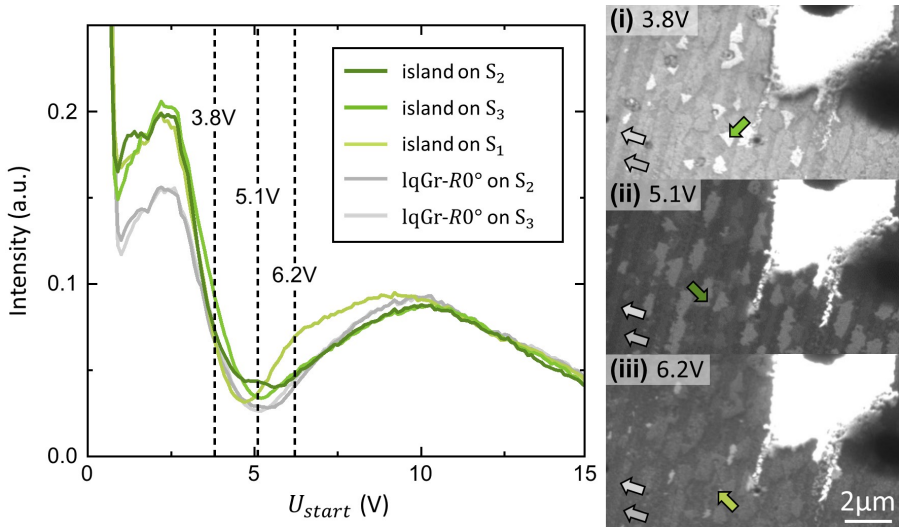


**Figure 4.12: LEEM-I(V) profiles of islands on Sample 2 after the first annealing in UHV**, recorded from different surface regions as shown in the BF-LEEM images (i-iii). Different sets of islands show the brightest intensity depending on  $U_{start}$ . The different areas in the BF-LEEM images and their respective LEEM-I(V) profiles are color-coded.

during BN growth. Note that the SiC termination underneath the BN layer is likely to change upon graphitization, as SiC is decomposed. However, the actual termination cannot be measured. Therefore, it is always referred to the termination that was assigned in Chapter 3, after BN growth.

The islands on the  $S_2$  termination are the largest and most numerous. They stand out from the other islands in panel (ii) of Fig. 4.12. Fewer and smaller islands are found on the thinner  $S_3$  termination in panel (i). Lastly, some of the smallest islands exhibit the brightest intensity in panel (iii). These islands are located next to  $S_2$  terraces on the left and  $S_3$  terraces on the right. This is

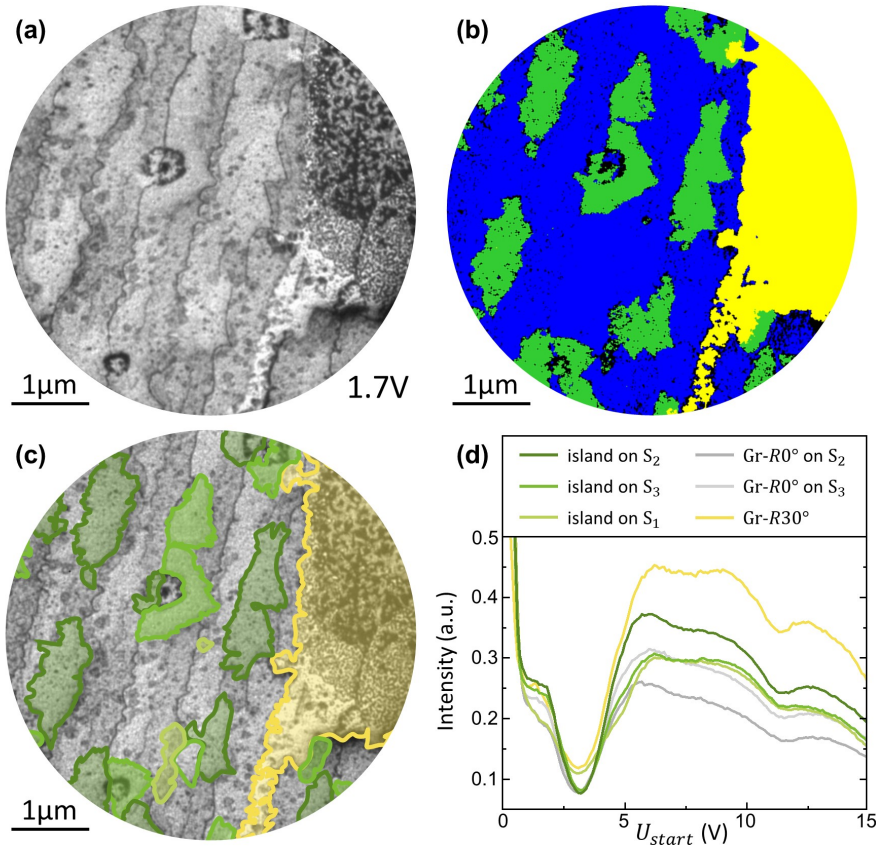


**Figure 4.13: Different graphene monolayer configurations on Sample 2 after the second annealing in UHV.** (a) BF-LEEM image. (b) DF-LEEM composite image of the same surface area, created from the data shown in Fig. 4.8 with Gr- $R0^\circ$  in blue, conventional Gr- $R30^\circ$  in yellow, and the islands in green. (c) Same as (a), but with contours. (d) LEEM-I(V) profiles of different surface regions, color-coded. See the main text for more details.

where the  $S_1$  termination is expected, as discussed in the previous chapter [see Fig. 3.5 and related text]. However, it vanished almost completely due to step bunching. LEEM-I(V) profiles were extracted from these three types of islands and are shown alongside the profiles of neighboring  $\text{lqGr-}R0^\circ$  regions in Fig. 4.12. Interestingly, the profiles extracted from the islands resemble those of  $\text{lqGr-}R0^\circ$ , exhibiting maxima at  $\sim 2.5$  V and  $\sim 10$  V, and a minimum at  $\sim 5$  V. It is concluded that the electronic properties of the islands are highly comparable to those of  $\text{lqGr-}R0^\circ$ . However, it is noteworthy that within the 1-3 V range, all types of islands exhibit significantly higher intensity compared to the  $\text{lqGr-}R0^\circ$  covered terraces.

Next, the LEEM-I(V) measurements on the islands after the second annealing in UHV are discussed. It is important to note that in this instance, differentiating the islands from the terraces in BF-LEEM became increasingly difficult. Therefore, the respective surface areas are first identified in Fig. 4.13(a-c) by considering previous measurements. Panel (a) shows a BF-LEEM image of Sample 2 with a field of view of  $5 \mu\text{m}$ . The surface area shown has previously been characterized by DF-LEEM, as presented in Fig. 4.8. These DF-LEEM results were used to create the composite image in Fig. 4.13(b), thereby differentiating the areas of  $\text{Gr-}R0^\circ$  (blue),  $\text{Gr-}R30^\circ$  (yellow) and the islands (green). The latter show a mixed  $\text{Gr-}R0^\circ$  and  $\text{Gr-}R30^\circ$  LEED signal, as discussed above. The composite image is used to trace the island's and  $\text{Gr-}R30^\circ$  contours onto the BF-LEEM image in Fig. 4.13(c). Thereby, different shades of green indicate the termination of the SiC terraces of each island, as identified in Fig. 4.12. In addition, the  $\text{Gr-}R0^\circ$  covered  $S_2$  and  $S_3$  terraces in Fig. 4.13(a,b) can be distinguished by their slight intensity difference, with  $S_2$  appearing slightly darker. Eventually, Fig. 4.13(d) shows the LEEM-I(V) profiles of all these regions, along with that of one layer  $\text{Gr-}R30^\circ$ . Overall, they all exhibit the signature of monolayer graphene on a carbon buffer layer on SiC. Therefore, it can be concluded that the islands are not  $30^\circ$ -tBLG.

Finally, the electronic structure of the islands is investigated with ARPES. However, the islands are too small to measure them exclusively. Therefore, ARPES is applied on two regions, as illustrated in Fig. 4.14(a). The ARPES measurement on the uniform  $\text{Gr-}R0^\circ$  region (i) has been discussed previously [cf. Fig. 4.9(b) and related text]. In Fig. 4.14(b), it is now compared to the ARPES measurement on region (ii), which includes a considerable amount of islands in addition to  $\text{Gr-}R0^\circ$ . As highlighted by the arrows, the latter exhibits additional faint features of Dirac cones  $30^\circ$  rotated with respect to those of  $\text{Gr-}R0^\circ$ . Thereby, the presence of  $\text{Gr-}R30^\circ$  on the islands is proofed. In conclusion, the islands consist of monolayer graphene with  $\text{Gr-}R0^\circ$  and  $\text{Gr-}R30^\circ$  fragments below resolution limit.

In the interest of comprehensive analysis, it should be noted that in particular the islands, but also the terraces, are not as uniform in their structure as the data presented so far suggests. As illustrated in Fig. 4.15, this becomes apparent in BF-LEEM, when different values for  $U_{start}$  are applied. Panel (a) shows a section of the BF-LEEM image at  $U_{start} = 1.7$  V shown previously. The different domains appear rather uniform except for what appears like point-size defects. However, BF-LEEM images at  $U_{start} = 3.5$  V in panel (b) and  $U_{start} = 5.0$  V in panel (c)

#### 4.2 Graphitization of BN on SiC(0001) upon annealing in UHV

give the impression of a much more complex lateral structure within the domains so far identified. These local variations may correspond to slight differences in the stage of graphitization, which in general is a continuous process.

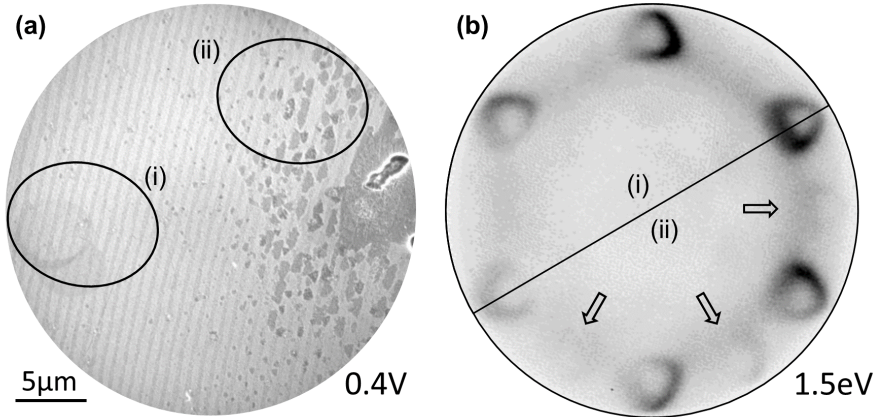


**Figure 4.14:** ARPES data recorded on the islands on Sample 2 after the second annealing in UHV. (a) LEEM image. The black ellipses mark the areas investigated with ARPES. (b) ARPES measurement of (i) Gr- $R0^\circ$  and (ii) Gr- $R0^\circ$  with islands, taken at a binding energy of 1.5 eV. The signal of Gr- $R30^\circ$  is indicated by arrows.

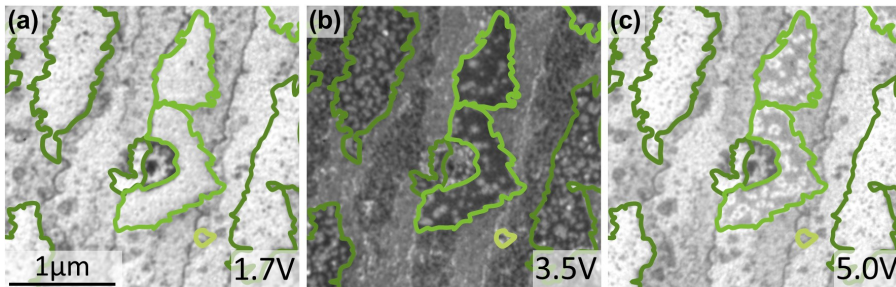


**Figure 4.15:** Inhomogeneity of the domains revealed by LEEM-I(V). BF-LEEM images of Sample 2 after the second annealing in UHV, taken at different  $U_{start}$  as indicated in the panels. The contours of the islands are drawn and colored in equivalence to Fig. 4.13.

### 4.2.5 Formation of 30°-tBLG

In both surfactant-mediated and template-induced growth modes, Gr- $R0^\circ$  growth is limited to one layer [41, 53, 54]. Sufficiently high temperatures and long annealing times can lead to the formation of 30°-tBLG, when Gr- $R30^\circ$  emerges underneath Gr- $R0^\circ$  [41, 54]. 30°-tBLG on SiC can be identified by combining LEEM-I(V) and DF-LEEM since areas covered with 30°-tBLG exhibit LEEM-I(V) profiles that are characteristic of two graphene layers and show a signal in DF-LEEM when Gr- $R0^\circ$  spots are used for imaging. As discussed in the following, indications for beginning 30°-tBLG formation on Sample 2 were found at defects and terrace edges. On Sample 1, large areas of 30°-tBLG were identified. However, it appears to be of low structural quality. These different 30°-tBLG configurations are discussed in the context of the samples' morphologies and differences in their preparation procedure.

#### Indications for starting 30°-tBLG formation on Sample 2

As shown above, Sample 2 is mostly covered by monolayer graphene after the second annealing in UHV. To search specifically for signs of 30°-tBLG, the LEEM-I(V) data are considered again. As known from previous measurements on conventionally grown graphene multilayers [see Fig. 4.10] and on 30°-tBLG in the work of Yin et al. [54], the LEEM-I(V) spectrum of bilayer graphene on SiC exhibits a maximum at  $U_{start} \sim 3\text{V}$ , where the LEEM-I(V) spectrum of monolayer graphene exhibits a minimum. Therefore, 30°-tBLG is expected to show bright contrast at  $\sim 3\text{V}$  and dark contrast at slightly smaller and larger  $U_{start}$ .

Fig. 4.16(a,b) shows BF-LEEM measurements of the same surface area that was previously characterized. The images were taken at  $U_{start} = 2.2\text{V}$  and  $3.2\text{V}$  and after the second annealing. The majority of the surface appears bright at  $2.2\text{V}$  and dark at  $3.2\text{V}$ , which agrees well with the LEEM-I(V) signature of monolayer graphene. However, many small objects and step edges that show dark contrast at  $U_{start} = 2.2\text{V}$  exhibit bright contrast at  $3.2\text{V}$ . Out of these, three areas at step edges (A-C) and three of the brightest point-like objects (D-F) are marked by colored arrows in panel (b) and further investigated.

To confirm that these surface areas are covered with graphene bilayers, LEEM-I(V) spectra were extracted and plotted in Fig. 4.16(i,ii). The general shape of curves A-F indicates the presence of two minima at  $\sim 2.4\text{V}$  and  $\sim 4.5\text{V}$  (dashed lines) and differs significantly from the spectrum of monolayer graphene, which is drawn in black in panel (i). Considering each curve individually in panel (ii), curves A, C, and D show two distinct minima. Curves E and F are relatively flat, and curve B has a strong maximum at  $\sim 2.4\text{V}$  but only a weak one at  $\sim 4.5\text{V}$ .

The shapes of curves B, E and F may be explained by a superposition of two differently weighted spectra, one with a single minimum at  $\sim 3\text{V}$  and one with two minima to the left and right. Note that many other bright objects that appear bright in Fig. 4.16(b) show either similar or less well-pronounced LEEM-I(V) signatures of bilayer graphene. This finding is consistent with the work of Yin et

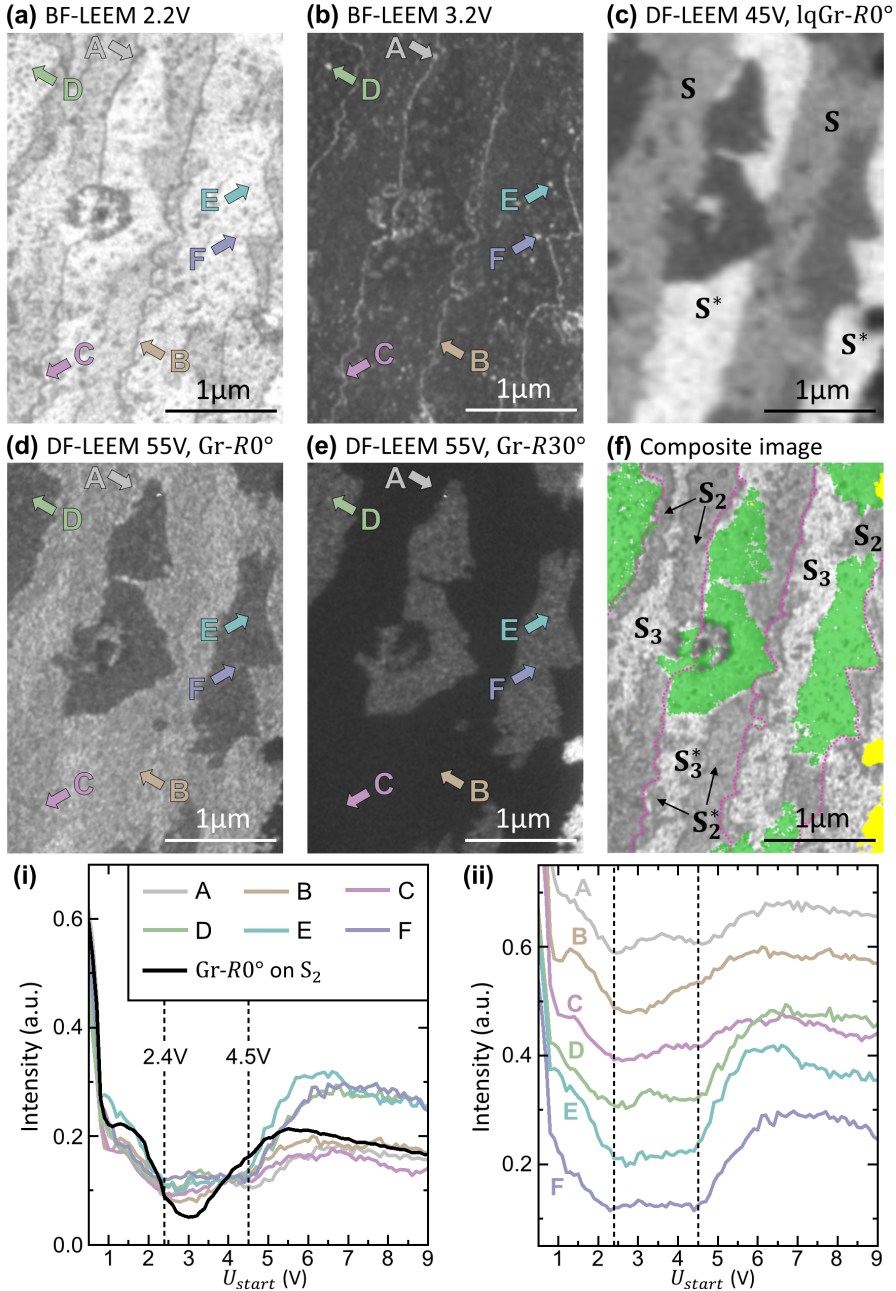


**Figure 4.16: Bilayer graphene, domains and terrace configuration on Sample 2.** (a,b) BF-LEEM and (c,d,e) DF-LEEM images. (f) Composite image. A BF-LEEM image taken at  $U_{start} = 9$  V is superimposed with island (green) and Gr-R30° (yellow) domains as identified by DF-LEEM. The magenta dotted lines correspond to step edges that appear bright in panel (b). (i,ii) LEEM-I(V) spectra of different surface areas as indicated. See main text for more details.

al. [54], who found that the transformation of the buffer layer underneath Gr- $R0^\circ$  into Gr- $R30^\circ$  is a continuous process, evident in a steady change of LEEM-I(V) spectra.

To verify the presence of Gr- $R0^\circ$  on the marked surface areas, DF-LEEM measurements are shown in Fig. 4.16(d,e). Areas A-C show intensity in the DF-LEEM image of the Gr- $R0^\circ$  spots in panel (d) but not in the DF-LEEM image of the Gr- $R30^\circ$  spots. This indicates that the Gr- $R0^\circ$  layer strongly attenuates the signal of Gr- $R30^\circ$  underneath. It is concluded that  $30^\circ$ -tBLG has started to form at the step edges that appear bright in Fig. 4.16(b). Additionally,  $30^\circ$ -tBLG is assumed to start forming at the bright, point-like surface areas that are scattered across the terraces in Fig. 4.16(b). Areas D-F are located on the islands. These show DF-LEEM intensity for both Gr- $R0^\circ$  and Gr- $R30^\circ$  because they consist of monolayer graphene with Gr- $R0^\circ$  and Gr- $R30^\circ$  fragments below the resolution limit, as discussed above.

Given that the graphene formation underneath Gr- $R0^\circ$  requires the evaporation of Si atoms from the SiC bulk, the described domain distribution of  $30^\circ$ -tBLG is plausible and in agreement with observations by Yin et al. [54]. In locations where SiC is most directly exposed to vacuum, the sublimation process proceeds fastest. Therefore, Si evaporation and graphene bilayer formation are favored at step edges and on defective surface areas rather than on flat terraces. However, indications for  $30^\circ$ -tBLG are not equally present at all step edges on Sample 2. To illustrate this, the terrace configuration on the investigated surface area is analyzed more closely in the composite image in Fig. 4.16(f). The underlying BF-LEEM image was recorded at  $U_{start} = 9.0$  V and shows good contrast between Gr- $R0^\circ$  on neighboring terraces. Areas covered with islands and Gr- $R30^\circ$  are colored in green and yellow, respectively, and the contours of the step edges showing indications of beginning  $30^\circ$ -tBLG formation are drawn as magenta dashed lines. Notably, several step edges between neighboring terraces are recognizable that did not appear bright in Fig. 4.16(b) and therefore do not show indications of beginning  $30^\circ$ -tBLG formation.

A plausible explanation for this finding could be different step heights at the terrace edges. As discussed before, Sample 2 was found to slope down from left to right in the sequence  $S_3$ - $S_2$ - $S_1$ - $S_3^*$ - $S_2^*$ - $S_1^*$ , with step heights of one SiC bilayer [as discussed in Section 3.1.2]. During BN growth, step bunching took place as a result of unevenly fast step retraction of the differently terminated terraces. In this process,  $S_1$ -type terraces have mostly vanished in the examined surface area. Only small islands which grew on  $S_1$ -type terraces remain present (see above). As a result, the step edges of the former  $S_1$ -type terraces have merged with the step edges of the higher  $S_2$ -type terraces to the left to form two-bilayer-high step edges. This step configuration corresponds to the intermediate state of step bunching that was illustrated in Fig. 3.5(b).

In Fig. 4.16(f), the SiC termination underneath Gr- $R0^\circ$  is indicated for each terrace. At  $U_{start} = 9$  V, the  $S_3$ -type terraces show a bright contrast against the darker  $S_2$ -type terraces [cf. LEEM-I(V) spectra in Fig. 4.6(c)]. The  $S_n$  and  $S_n^*$

groups were identified from the DF-LEEM image of  $lqGr-R0^\circ$  spots after the first annealing, as displayed in Fig. 4.16(c). Comparing panels (c) and (f), the step edges that show beginning  $30^\circ$ -tBLG formation are found to be those where  $S_n$  and  $S_n^*$  groups meet. This is where  $S_1$ -type terraces merged with  $S_2$ -type terraces to form two-bilayer-high step edges. Note that in Fig. 4.16(f), it sometimes appears that the terrace edges bordering  $S_n$  and  $S_n^*$  groups have  $S_2$ -type terraces on both sides. This indicates an irregularity in step retraction at this surface area, resulting in local step heights of three SiC bilayers.

In summary, the SiC bilayers beneath  $Gr-R0^\circ$  on  $S_2$ -type terraces and to the left of the magenta dotted lines are directly exposed to vacuum at the step edge. This promotes Si evaporation and sublimation growth of  $Gr-R30^\circ$  at the step edge. Other step edges between  $S_2$  and  $S_3$  (or  $S_2^*$  and  $S_3^*$ , respectively) are only one SiC bilayer high. These seem to have been well enough protected by  $Gr-R0^\circ$  during the second annealing to prohibit Si sublimation and graphene growth underneath.

### Large areas of low-quality $30^\circ$ -tBLG on Sample 1

So far, only the graphitization of Sample 2 has been addressed. This is because, for Sample 1, bilayer graphene was already formed after a single annealing at  $\sim 1250^\circ\text{C}$  for only 20 min.

Fig. 4.17(a) shows a BF-LEEM image of the same surface area that was characterized after BN growth in Chapter 3. At  $U_{start} = 10\text{ V}$ , the islands are clearly visible on the dark terraces. On the island-free area, domains of even darker intensity are present. Their lateral domain distribution corresponds well to that of the  $B_xN_y$  minority domains discussed in Section 3.3. LEEM-I(V) profiles were extracted from these three surface areas and are displayed in panel (b). The LEEM-

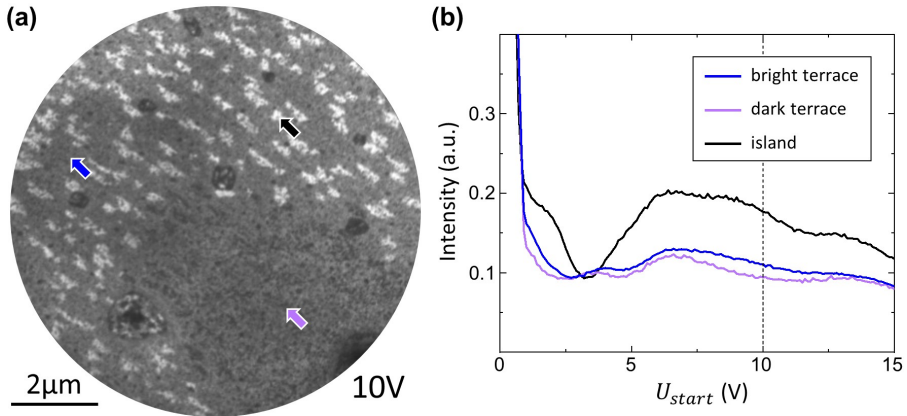


**Figure 4.17: LEEM-I(V) data of Graphene on Sample 1.** (a) BF-LEEM at  $U_{start} = 10\text{ V}$ . (b) LEEM-I(V) profiles extracted from the highlighted surface areas in (a).

I(V) profile of the islands on Sample 1 shows the signature of monolayer graphene and agrees well with the LEEM-I(V) data for islands on Sample 2 that were presented above [cf. 4.13(d)]. The profile extracted from the surrounding terraces is rather flat, but it clearly exhibits two minima in the range of 0-7 V, matching the expected features of bilayer graphene. For the slightly darker domains in the island free region, the LEEM-I(V) profile is almost identical, despite the overall lower intensity. Except for the contrast observed between these two domains, no other variations in LEEM-I(V) were observed across the terraces.

The DF-LEEM measurements performed on Sample 1 after graphitization are presented in Fig. 4.18. The data obtained by selecting the Gr- $R0^\circ$  spots for imaging are shown in panels (c) and (e). Both images appear identical and no contrast is observed between consecutive terraces. As discussed above regarding Sample 2, this result proves that the transformation of  $B_xN_y-R0^\circ$  into graphene is also complete for Sample 1. While the terraces exhibit strong intensity in these images, the islands and minority domains in the island-free surface area exhibit lower intensity. The DF-LEEM images of the Gr- $R30^\circ$  spots are shown in panels (d) and (f). In these images, the islands appear bright on the dark terraces. Some bright, nm-sized objects are found between the islands. These are likely corresponding to the misoriented minority phase observed already prior to graphitization [cf. Section 3.3]. In addition, a large number of bright, nm-sized objects are found in the island-free region. Their locations appear to roughly coincide with the domains that show darker contrast in the BF-LEEM image [cf. Fig. 4.18(b)] and the DF-LEEM images of the Gr- $R0^\circ$  spots [cf. Fig. 4.18(c,e)].

The presented measurements imply that, except for the islands, Sample 1 is covered with  $30^\circ$ -tBLG. However, several experimental findings suggest that its structural quality differs significantly from that of  $30^\circ$ -tBLG described in literature [41, 54]. The most obvious difference is that the  $30^\circ$ -tBLG layer in this work is interspersed with nm-sized Gr- $R30^\circ$  domains and the mixed Gr- $R0^\circ$ /Gr- $R30^\circ$  structure at the islands. Furthermore, the oscillations in the LEEM-I(V) spectra of  $30^\circ$ -tBLG on Sample 1 have a rather low amplitude compared to literature [54]. Note that, in general, differences in absolute LEEM-I(V) intensities cannot be considered meaningful across different studies. In this case, however, the LEEM-I(V) spectra of monolayer graphene serve as a reference in both studies. Finally, the LEED patterns of Sample 1 [cf. Fig. 4.5(b,c) and Fig. 4.18(a)] do not exhibit the additional spots that were found to be characteristic of  $30^\circ$ -tBLG in literature [41, 54], as presented in Fig. 4.2(d). It is concluded that the  $30^\circ$ -tBLG on Sample 1 is of rather low structural quality. A possible reason for this could be an incomplete transformation of the underlying ZLG- $R30^\circ$  into Gr- $R30^\circ$ .

In this context, the different speed at which the graphitization of Sample 1 progressed compared to Sample 2 is discussed. After annealing Sample 1 at  $\sim 1250^\circ\text{C}$  for 20 min, bilayer graphene was found to cover the terraces rather homogeneously. For comparison, Sample 2 was annealed at  $\sim 1200^\circ\text{C}$  for 20 min and at  $\sim 1250^\circ\text{C}$  for  $> 60$  min. Even then, the terraces previously covered by  $B_xN_y-R0^\circ$  showed the LEEM-I(V) signature of monolayer graphene. Based on the discussion of bilayer

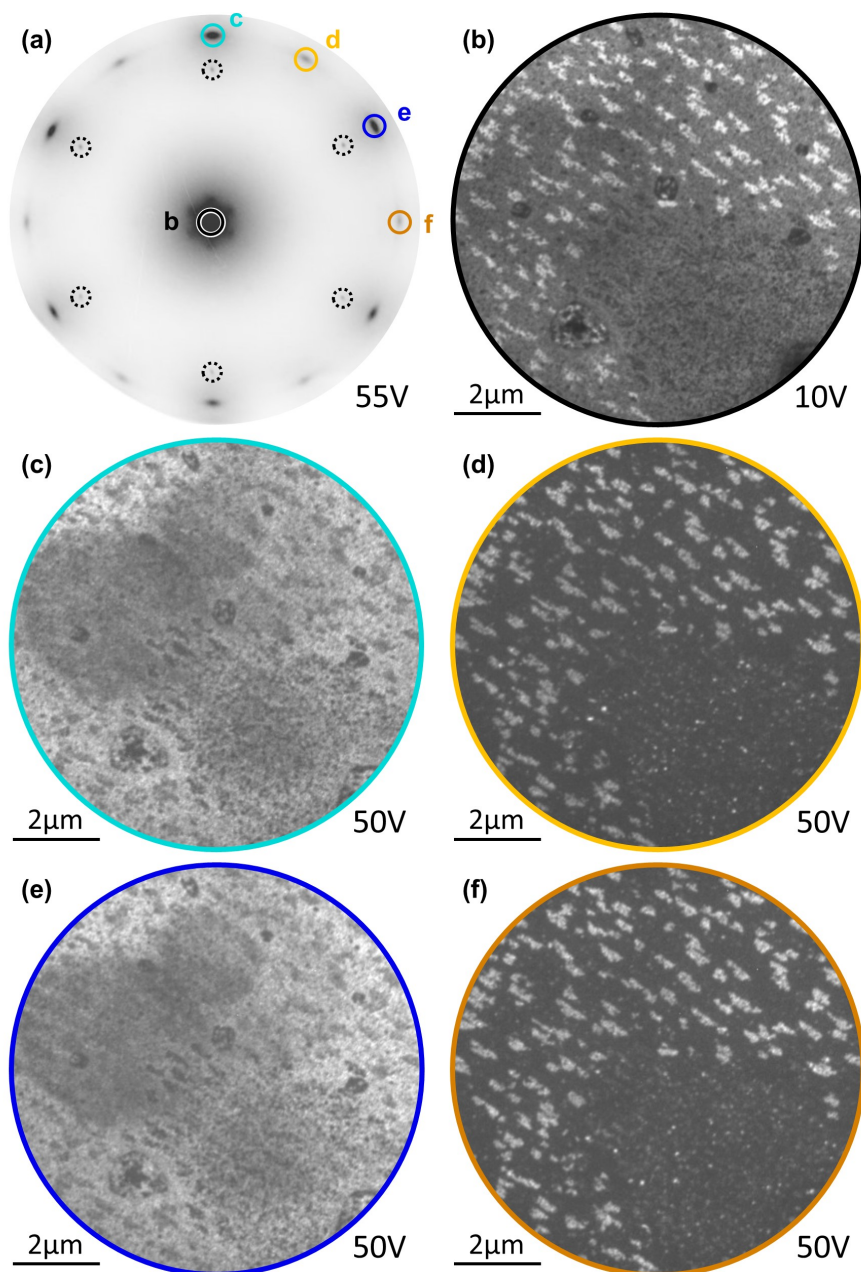


**Figure 4.18: DF-LEEM data recorded from Sample 1 after graphitization.** (a) LEED measurement and (b) BF-LEEM image of the investigated surface area. (c-f) DF-LEEM images taken at  $U_{start} = 50$  V. The spots selected for imaging are highlighted in (a) and named according to the respective DF-LEEM images.

graphene on Sample 2, one might suspect that this difference is due to the two sample's different terrace configurations. As discussed above, the graphitization progresses faster at higher step edges, likely due to easier diffusion and sublimation of Si atoms. The terrace configuration of Sample 1 corresponds to the final state of the step retraction model [cf. Fig. 3.5], meaning all of its terraces are separated by step edges that are three SiC bilayers high. This appears to be a good prerequisite for uniform and fast graphitization. However, Sample 2 exhibited three-bilayer-high step edges locally and showed indications of  $30^\circ$ -tBLG only on  $\sim 20$ nm wide stripes along these terrace edges, despite much longer annealing.

Note also that a homogeneous graphene thickness of two layers all over the terraces is an unexpected outcome when growing graphene on SiC by Si sublimation in UHV. Typically, multilayer growth occurs such that the growth of the third and higher layers starts before a homogeneous bilayer can be found [51, 54]. Therefore, it can be concluded that Si sublimation on the terraces beneath Gr- $R0^\circ$  is favored over sublimation at step edges on Sample 1. Considering that Gr- $R0^\circ$  on Sample 1 is also interspersed with nm-sized Gr- $R30^\circ$  domains, this indicates that the Gr- $R0^\circ$  layer on Sample 1 is defective in a way that makes it more permeable for Si sublimation. This conclusion may be further supported by the finding that the islands still exhibit a LEEM-I(V) profile associated with monolayer graphene. This proves that graphitization is inhibited in these areas, but not in areas covered by Gr- $R0^\circ$ .

Overall, Gr- $R0^\circ$  on Sample 1 appears to be of lower structural quality than Gr- $R0^\circ$  on Sample 2. In the template-induced growth mode, the quality of Gr- $R0^\circ$  is strongly influenced by the quality of the  $B_xN_y$ - $R0^\circ$  template. Thus, this finding corresponds well with the data presented on the BN templates of Sample 1 and Sample 2, as discussed in Chapter 3.

## 4.3 Conclusion

A comprehensive understanding of the growth process is essential for producing large-area, high-quality Gr- $R0^\circ$  monolayers on SiC(0001), which are known to offer a promising way of producing  $30^\circ$ -tBLG. This chapter reports on the growth of Gr- $R0^\circ$  on SiC(0001) by annealing BN on SiC(0001) in UHV. With LEEM, the graphitization process is analyzed at different stages and with lateral resolution. Thus, information is provided on how the configuration and quality of the BN templates, as well as the sample morphology, influence the graphitization process.

Gr- $R0^\circ$  on SiC can be obtained either via a template-induced or a surfactant-mediated growth mode. While the latter has the potential to yield higher-quality samples [53], the experimental procedure for the template-induced growth mode allows for detailed analysis of the intermediate stages. This includes the growth of BN on SiC(0001), discussed in Chapter 3, and the stages of graphitization presented in this chapter.

Following the template-induced growth technique, the BN covered samples are annealed in UHV up to  $1250^\circ\text{C}$ . During the experiment, the lateral domain con-

figuration of the BN surface phases remains unchanged. However, the structural analysis at different stages of graphitization reveals a continuous transformation of different surface structures into graphene. For Sample 2, this transformation is seen in areas that are initially covered by  $B_xN_y$ - $R0^\circ$ , in areas initially covered by  $(\sqrt{7} \times \sqrt{7})$ - $R19.1^\circ$  reconstruction, and also in one area initially uncovered by a BN template. These are located in close proximity to each other and are examined at two stages of graphitization, after a first and a second annealing in UHV:

- $B_xN_y$ - $R0^\circ$  transforms via  $lqGr$ - $R0^\circ$  (first stage) into  $Gr$ - $R0^\circ$  (second stage), which agrees well with previous studies [MR5, 41, 52].
- The  $(\sqrt{7} \times \sqrt{7})$ - $R19.1^\circ$  reconstruction is replaced by a structure that shows similar LEEM-I(V) characteristics as  $lqGr$ - $R0^\circ$  in the first stage and monolayer graphene in the second stage. However, this monolayer graphene consists of both  $Gr$ - $R0^\circ$  and  $Gr$ - $R30^\circ$ , which are found laterally next to each other in fragments below resolution limit.
- On areas of bare SiC that have not been covered by BN in the first preparation step, conventional  $Gr$ - $R30^\circ$  emerges. It produces small domains of different multilayer thicknesses, as known from previous LEEM studies on the growth of  $Gr$ - $R30^\circ$  on SiC by thermal decomposition in UHV (e.g., Refs. [144, 145]).

Upon annealing at sufficiently high temperatures and for a sufficiently long time,  $Gr$ - $R30^\circ$  is known to also emerge below  $Gr$ - $R0^\circ$ , thereby producing the desired  $30^\circ$ -tBLG [41, 54]. Indications of this were found on Sample 2 after extend annealing in UHV at  $1250^\circ\text{C}$  for more than 60 min, but only in areas about  $\sim 20$  nm wide at step edges higher than one SiC bilayer. This demonstrates the  $Gr$ - $R0^\circ$  layer's potential to protect the underlying SiC substrate from further Si sublimation and illustrates the importance of morphology in this process. On Sample 1, however,  $B_xN_y$ - $R0^\circ$  was found to be replaced uniformly by  $30^\circ$ -tBLG already after annealing in UHV at  $1250^\circ\text{C}$  for only 20 min. Several findings suggest that the faster graphitization of Sample 1 compared to Sample 2 is due to the inferior structural quality of its  $B_xN_y$ - $R0^\circ$  layer that is inherited during replacement by  $Gr$ - $R0^\circ$ .

Consequently, the data on graphitization of BN on SiC(0001), presented in this chapter, reinforce the conclusion from Chapter 3 that an increased heating rate during BN growth improves the quality of the BN layer. The quality of the BN template limits the quality of  $Gr$ - $R0^\circ$  and, in turn, the quality of the final  $30^\circ$ -tBLG.



## Chapter 5

# Electron Dynamics of Molecular Orbitals in Time and Space

Frontier orbitals determine fundamental molecular properties such as chemical reactivities. Although the electron distribution of occupied orbitals can be imaged in momentum space by photoemission tomography, it has so far been impossible to follow the momentum-space dynamics of a molecular orbital in time, for example during an excitation process or a chemical reaction. In the present experiment, time-resolved photoemission is combined with a momentum microscope to establish a tomographic, femtosecond pump-probe experiment to probe a transiently occupied molecular orbital. Thereby, the full momentum-space distribution of transiently excited electrons was measured successfully, connecting their excited-state dynamics to real-space excitation pathways. Since in molecules this distribution is closely linked to orbital shapes, the presented proof of principle experiment may in the future offer the possibility to observe ultrafast electron motion in time and space: A new window is opened to investigate the ultrafast electron transfer dynamics in such processes as chemical reactions on surfaces and intermolecular charge transfers.

The data and results presented in this chapter have been published in R. Wallauer, M. Raths, K. Stallberg, L. Münster, D. Brandstetter, X. Yang, J. Gütde, P. Puschnig, S. Soubatch, C. Kumpf, F. C. Bocquet, F. S. Tautz, and U. Höfer, “Tracing orbital images on ultrafast time scales”, *Science* **371**, 1056 (2021)[MR4]. This work was part of the collaborative research center SFB 1083 “Structure and Dynamics of Internal Interfaces”. While R. Wallauer and U. Höfer’s group from Philipps-Universität Marburg built the measurement setup and contributed their expertise in pump-probe experiments, the co-authors from Forschungszentrum Jülich (PGI-3) selected and provided the sample system, and contributed their expertise in POT of molecular orbitals. This collaboration was supported by P. Puschnig and his group at the University of Graz, who conducted simulations of molecular orbitals and momentum maps. As a PhD student at PGI-3, I contributed to this work by preparing and pre-characterising the samples, with support from F. C. Bocquet and C. Kumpf. I also organized and carried out the transport of the samples under UHV conditions to Marburg, where I joined R. Wallauer, K. Stallberg, L. Münster and J. Gütde in performing the experiment. A more detailed description of all author contributions is provided in Ref. [MR4].

In the first section of this chapter, the proof of principle tr-POT experiment on transiently occupied molecular orbitals is introduced. The requirements on the sample are discussed and a suitable sample system is chosen: PTCDA on the missing-row oxygen reconstructed Cu(001) surface. In Section 5.2, detailed information on the preparation process is provided. A well understood and controlled preparation process was established to provide reproducible samples of high quality for the tr-POT experiment. The sample's structure is characterized with LEED and a real-space structure model is presented. Finally, the results of the tr-POT experiment are presented and discussed in Section 5.3.

## 5.1 Introduction to the experiment

The basis for a quantum-mechanical description of matter is the many-electron wave function. At various levels of approximation, up to the exact configuration interaction wave function, this can be written in terms of single-electron wave functions: the orbitals. Orbitals provide a link between spectral properties and spatial electron distributions, which is of obvious benefit in chemistry [151, 152]. Consequently, there has been a lot of interest in measuring orbitals [153–156]. With photoemission tomography, a powerful technique has recently been introduced by which the electron distribution in orbitals of molecules adsorbed on surfaces can be imaged in momentum space [57, 157–159]. Addressing molecular orbitals of excited states in pump-probe experiments brings photoemission tomography to its culmination, because it empowers it to provide access to molecular excitation and electron transfer processes at surfaces not only in time but also in space: Instead of just recording the photoemission intensity from the corresponding energy level, the evolution of the electron wave function after excitation is traced by monitoring the orbitals in momentum space. This new technique is called time-resolved photoemission orbital tomography (tr-POT).

Photoemission by conventional lasers with photon energies of a few electron volts can access only small electron momenta parallel to the surface. The prominent features in frontier orbital photoemission from organic molecules, as determined by the periodicity of the molecular C–C bond network, are therefore out of reach [57]. Recently, however, probe photon energies that are high enough have become available through high-harmonic generation (HHG) and have enabled time-resolved photoemission experiments to record band structure movies of solids, i.e., to trace the temporal evolution of the electron system over the complete Brillouin zone [65, 67–69]. In their investigation of the laser-induced phase transition of In nanowires on Si(111), Nicholson *et al.* [68] related this information to real-space chemical bond formation in a lattice. However, photoemission tomography of unoccupied states of molecules, the missing element to following molecular electron dynamics in time and space, has not yet been accomplished.

In gas-phase photochemistry, it has long been recognized that femtosecond time-resolved photoelectron spectroscopy is a powerful method to investigate the coupled electron and nuclear dynamics [160–162]. There, it is difficult to align

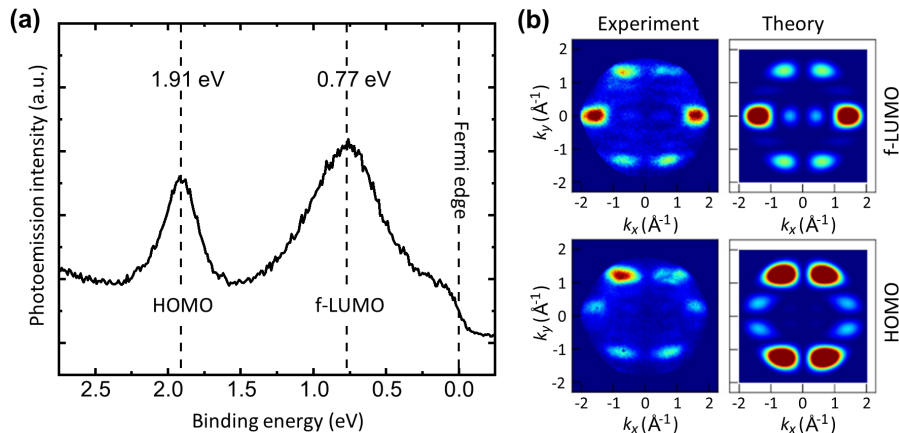


**Figure 5.1: 1PPE Results for PTCDA on Ag(110).** (a) Energy dispersive curves integrated along the  $[1\bar{1}0]$  direction, measured with the ARPES setup at Jülich. (b) Experimental and theoretical constant binding energy maps of PTCDA on Ag(110), measured on the same sample with 1PPE at the tr-POT setup in Marburg. The asymmetric intensity distribution in the experimental maps stems from the off-normal incident photons and irregularities stem from gain inhomogeneities of the detector. Fig. 5.1(b) is courtesy of Robert Wallauer from Philipps-Universität Marburg.

molecules in all three dimensions [162–164]. As in photoemission experiments the signal from all molecular orientations is superimposed, the interpretation of tomographic data is complicated.

For conventional POT, the situation is reversed. Single crystalline metal surfaces are used as substrates for molecular layers, since both a conductive and a sufficiently corrugated substrate is required. The latter promotes a small number of well-defined azimuthal orientations of the molecular adsorbate on the substrates surface. Ideally, only one molecular orientation occurs. This simplifies the interpretation of tomographic data as momentum maps are directly obtained in the molecular frame [57, 157–159]. However, interaction between the organic molecules and metallic substrates inhibits excitation dynamics within the molecule, as they are observed for gas phase molecules.

In the following, this issue is addressed by looking more closely at the example of PTCDA on the Ag(110) surface. At room temperature, the PTCDA molecules arrange in a well-ordered structure with only one molecular orientation [165]. As this leads to well differentiable molecular features in POT [cf. Sec. 2.6], this sample system has been already object of several conventional POT studies [59, 113, 158, 166, 167]. Therefore, it also serves as a convenient test sample to confirm that the molecular orbitals can be imaged in good quality with the tr-POT setup in this work. Fig. 5.1(a) shows the photoemission spectrum of one layer PTCDA

on Ag(110) with two distinct maxima right below the Fermi edge, measured with ARPES. For the corresponding peak binding energies, the momentum maps in Fig. 5.1(b) were measured with the tr-POT experimental setup in Marburg. The data were obtained by direct photoemission (1PPE). This corresponds to turning off the pump beam and using only the probe beam at the tr-POT setup, which makes it a conventional POT experiment. The momentum in Fig. 5.1(b) are identified as the HOMO and the f-LUMO of the gas phase PTCDA molecule, which is consistent with literature [59, 113, 158, 166, 167]. From various experimental studies, the strong interaction between the PTCDA molecules and the Ag(110) surface is well known [166, 168–171]: The oxygen atoms of the PTCDA molecules are covalently bound to the Ag surface atoms. Hybridization of the metal states with the molecular orbitals occurs, going along with a negative charge transfer into the f-LUMO. This makes the latter a well known indication for the strong electronic coupling of molecules and metallic surfaces.

Due to the charge transfer into the PTCDA molecules, the HOMO-LUMO transition cannot be excited in 2PPE experiments and in general, no exciton states are supported [172, 173]. Therefore, an additional requirement on the sample system arises: Sufficient electronic decoupling of the organic molecules from the substrate.

### 5.1.1 On decoupling organic adsorbates from metal supports

While various model systems of organic semiconducting molecules on metal surfaces have been studied intensively in the past decades, the general interest in decoupling strategies is growing recently. As previously exemplified for PTCDA on Ag(110), many sample systems with organic molecules on metal surfaces show strong adsorbate-substrate interactions. These often result in an altering of the electronic properties, sometimes strong enough to turn off the desired functionality of the organic molecules. Decoupling mechanisms open a possibility to reduce the strong interactions and therefore, preserve the molecules' intrinsic properties. Consequently, decoupling mechanisms are of high interest for the development of electronic and optoelectronic devices as well as for fundamental research. [174]

For metal substrates, the most common decoupling method is to introduce ultrathin semiconducting or insulating spacer layers. These hinder direct chemical bonding between metal and molecule and therefore physically decouple them from each other. Ideally, the spacer materials also prevent wavefunction hybridization of the spacer layer with the molecular states as well as with the metallic substrate. In this way, not only physical but also electronic decoupling is realized. [174, 175] Promising candidates for decoupling spacer layers are:

- Ultrathin dielectric layers of either alkali halides (NaCl [154]), metal oxides (MgO [176], Al<sub>2</sub>O<sub>3</sub> [177], CuO [175]) or nitrides (CuN [178])
- Van der Waals 2D materials such as hBN [179, 180], graphene [181–183], and MoS<sub>2</sub> [184]
- Ultrathin organic spacer layers [185–187]

- Post-deposition intercalation of atomic species, allowing retrospective decoupling of on-surface-synthesized organic nanostructures [188]

None of the above mentioned approaches is universal. How well the decoupling mechanism works depends also on the choice of substrate and molecule, provided that the preparation of the sample system is actually possible. In addition, it should be remembered that the tr-POT experiment requires well-aligned molecules with only few well-distinguishable molecular orientations.

### 5.1.2 Choosing a suitable sample system

Considering recent publications on decoupling approaches for organic adsorbates on metal surfaces, two sample systems appear as promising candidates, both using the prototype organic molecule PTCDA as probing molecule: PTCDA decoupled from a Cu(111) surface by a monoatomic layer of the 2D material hBN [180], and PTCDA decoupled from a Cu(001) surface by oxygen atoms that induce the well known  $(\sqrt{2} \times 2\sqrt{2})R45^\circ$ -2O missing-row reconstruction [175]. For both sample systems, the probed adsorption heights of PTCDA above the supports indicate good physical decoupling. Moreover, no charge transfer into the molecular LUMO was observed, indicating also a good electronic decoupling [175, 180].

The number of molecular orientations arises as the decisive criterion. While the PTCDA molecules on the oxygen missing-row reconstructed Cu(001) surface form a structure with only two molecular orientations, it appears in twelve orientations on hBN/Cu(111) [180]. Therefore, the sample system PTCDA on Cu(001)- $(\sqrt{2} \times 2\sqrt{2})R45^\circ$ -2O is chosen for the proof of principle tr-POT experiment. In the following section, the preparation procedure and the structural properties of this sample system are discussed.

## 5.2 The sample preparation in Jülich

In the previous section, it was explained how crucial the sample is for the success of the tr-POT experiment. Moreover, the time expenditure which goes along with time-resolved orbital mapping and the coordination of sample preparation and experiment taking place at spatially separated laboratories has to be taken into account. Consequently, it is important to establish a preparation procedure which provides well defined samples of high and reproducible quality on demand. Therefore, the preparation process needs to be well understood and controlled. This is a non-trivial task, although the sample system PTCDA on Cu(001)- $(\sqrt{2} \times 2\sqrt{2})R45^\circ$ -2O has already been produced and measured in other experiments [175, 189].

As the sample preparation was my main contribution to the project, it is explained in detail here. After starting with an overview of the experimental setup, detailed information on the different steps of the preparation process is provided: Cleaning of metal substrates, calibration of the PTCDA evaporator, oxidation

of the Cu(001) surface and deposition of PTCDA on the oxygen reconstructed Cu(001) surface. To fully understand the preparation process, the results of recent publications are included into the discussion. Moreover, the problems that needed to be understood and solved in order to optimize the preparation procedure for high sample quality and reproducibility are illustrated. Finally, a detailed characterization of the real-space structure of the sample system is presented and the photoemission features which are expected to be observed in the tr-POT experiment are discussed.

### 5.2.1 Experimental setup

The samples for the tr-POT experiment have been prepared under UHV conditions in a preparation setup in Jülich, as shown schematically in Fig. 5.2(a). The sample holder with the metal crystal [Fig. 5.2(b)] is introduced via the load lock and transferred onto the manipulator heads sample stage in the preparation chamber. The manipulator head [Fig. 5.2(c)] is equipped with a filament [Fig. 5.2(d)]. Filament and electron bombardment heating were used for sample heating up to 860 K. Furthermore, the preparation chamber has a sputter gun for sample cleaning. Its gas line was also used to expose the sample to oxygen. Moreover, the chamber is equipped with an evaporator for PTCDA deposition and an ion gauge for pressure control. Outside the vacuum, a pyrometer is directed through a glass window onto the sample to measure its temperature. Between the preparation steps, the sample can be transferred to the measuring stages for LEED and ARPES. Finally, the sample can be transferred through the load lock into the transportable vacuum suitcase.

### 5.2.2 The metal substrate - Cleaning and sample handling

In this work, the metal substrates Cu(001) and Ag(110) have been used. The crystals have a cylindrical shape with a height of 2 mm and a diameter of 7-10 mm. They are fixed on the commercial sample holders (ScientaOmicron PN07177-S) by spot-welding stripes of tantalum foil onto the sample holder and around the base of the metal crystal as shown in Fig. 5.2(b). When introducing new samples into the preparation chamber, and between different sample preparations, the metal substrates are cleaned by repeated cycles of sputtering with argon ions (with a partial pressure of  $p_{Ar^+} = 1 \times 10^{-5}$  mbar in the preparation chamber, a kinetic Energy of 1 keV, an incident angle of  $45^\circ$ , and for a duration of 30 min per cycle) and annealing (at a temperature of 860 K, and for the duration of 30 min per cycle). The cleanliness is controlled with LEED measurements: The substrate's LEED pattern of a clean sample surface exhibits sharp and bright substrate spots which don't show significant changes in intensity in between consecutive cleaning cycles. After the last cleaning process and before subsequent preparation processes, the metal substrates are allowed to cool down for at least 1 hour.

As the manipulator at the setup in Marburg is not able to rotate the sample

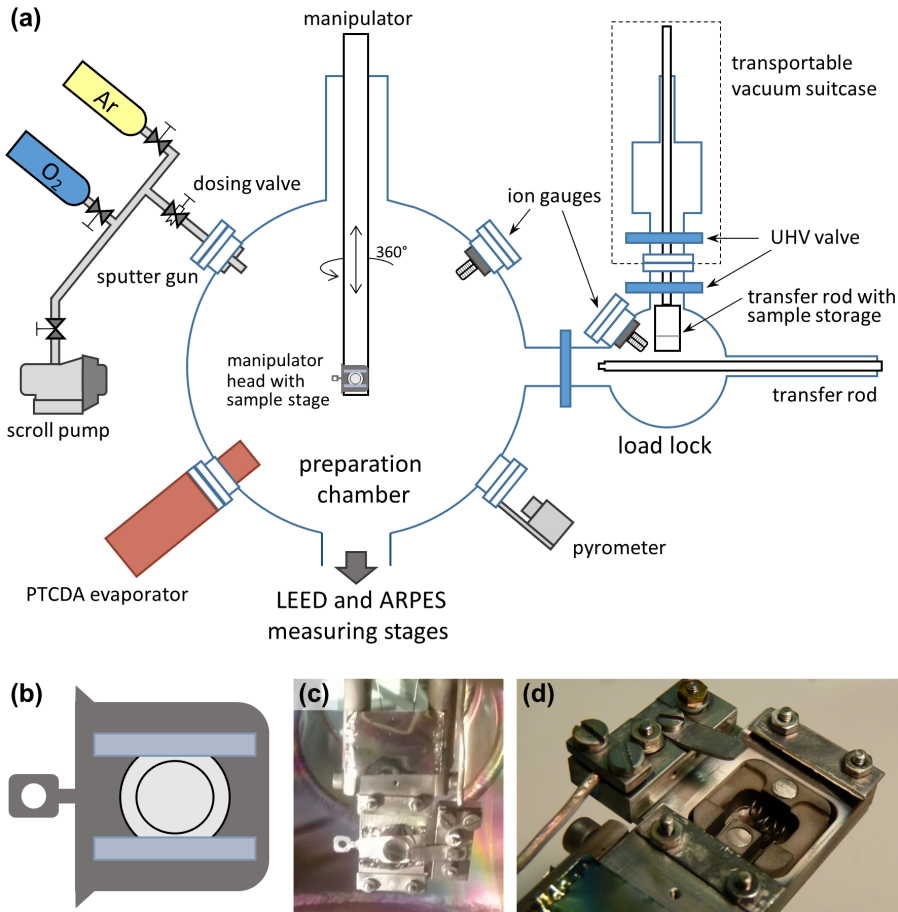


**Figure 5.2: Experimental setup for sample preparation in Jülich.**

(a) The sample is introduced via the load lock and transferred into the preparation chamber, which is equipped with a sputter gun, a PTCDA evaporator and a pyrometer for temperature control. In all chambers, ion gauges are used to control the pressure. After the preparation, the sample is transferred through the load lock into the transportable vacuum suitcase. (b) Schematic of the sample holder (ScientaOmicron PN07177-S). The metal crystal is fixed with spot welded tantalum stripes. (c) Photo of the sample holder fixed on the manipulator head. (d) Photo of the manipulator head without sample, showing the filament used for sample annealing.

with respect to the direction of the incoming photons, the metal crystals had to be oriented in the desired direction upon mounting on the sample holder. Therefore, the crystal's orientation was determined with LEED and the crystal was remounted in the desired direction.

### 5.2.3 Calibration of the PTCDA evaporator

For the planned tr-POT experiment, a homogeneous layer with a thickness of one molecular layer of PTCDA is desired to be grown on the oxygen-reconstructed Cu(001) surface. This requires a well calibrated growth rate. But in the preparation chamber used in this work, neither the deposition rate nor the coverage can be tracked during PTCDA deposition. Although the intensity of LEED spots is a relative reference for the coverage, it is not precise enough for the determination of the absolute coverage. Therefore, the growth rate is calibrated by a growth series of PTCDA on the Ag(110) surface at room temperature, taking advantage of the fact that PTCDA exhibits different structures in the first and second layer, which are well distinguishable in LEED.

The sample system PTCDA on Ag(110) has been frequently discussed in literature [113, 165, 167, 169, 170, 190–195]. Its structure, growth behavior and optoelectronic properties are well understood. When PTCDA is deposited on a Ag(110) surface at room temperature, it forms a so-called brickwall (BW) structure in the first layer. The corresponding structure model and LEED pattern are illustrated in Figs. 5.3(a-c). From literature it is also known that the first layer of PTCDA closes completely before molecules start to form a second layer on top [169]. In the second layer, the PTCDA molecules arrange in a different configuration, the so-called herringbone (HB) structure. The corresponding structure model is presented in Fig. 5.3(d). Note that in the simulated and measured LEED images of the bilayer structure, both patterns superimpose as shown in Figs. 5.3(e,f).

In order to deposit PTCDA, the molecules were evaporated from a commercial Knudsen cell evaporator. In several runs, the position of the sample relative to the evaporator was optimized to achieve a homogeneous coverage on the whole sample. A constant deposition rate was achieved by applying a preheating procedure. For a rough calibration of the growth rate, PTCDA was deposited in sequences of 2 min. The approximate deposition time required for a closed layer was derived by the time when the spots of the second layer structure appear [cf. Fig. 5.3(f)].<sup>1</sup> It had to be considered that a growth rate estimated by sequential deposition always suffers a systematical error, as with every interruption of the deposition (by closing the shutter in front of the Knudsen cell) the evaporated molecules do not vanish from the chamber immediately and can still adsorb on the sample surface. Therefore, the calibration was refined by depositing the full amount of PTCDA in one run.

The deposition rate depends mainly on the evaporation temperature of the

---

<sup>1</sup>The obvious disagreement of the LEED patterns measured in this work [cf. Fig. 5.3(f)] and the structure proposed by Willenbockel et al. [167] [cf. Fig. 5.3(e)] is not relevant here. For a detailed discussion, see Appendix B.

Knudsen cell. It changes over time slightly, as e.g. the amount of molecules in the crucible decreases. Especially after dismantling and refilling of the evaporator, a new calibration is necessary. In this work, the evaporation temperature was always chosen such that it took 10-15 min to grow a closed layer. This allowed accuracy and efficiency at the same time. Close to the deposition time for one layer, the step size for calibration experiments was chosen to be 30 sec. Therefore, the statistical error on the coverage is estimated not to exceed  $\pm 2.5\%$  of a closed layer.

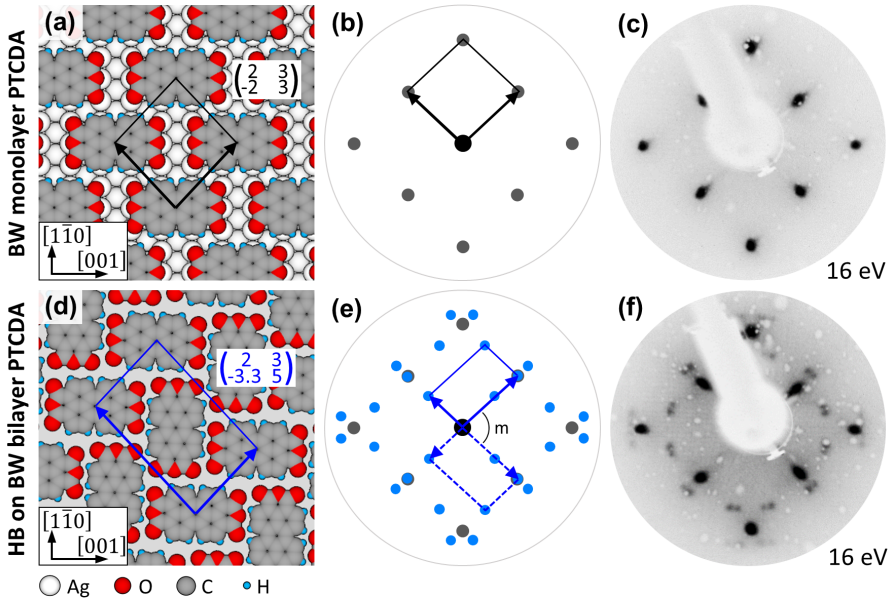


**Figure 5.3: Structure of PTCDA on the Ag(110) surface.** (a) Structure model and (b) simulated LEED pattern of the PTCDA brickwall (BW) monolayer as presented by Willenbockel et al. [167] and (c) LEED pattern as measured in this work, for  $t_{depos} = 6 \times 2$  min. (d) Structure model and (e) simulated LEED pattern of the PTCDA herringbone on brickwall (HB on BW) bilayer as proposed by Willenbockel et al. [167] and (f) LEED pattern as measured in this work for  $t_{depos} = 7 \times 2$  min.

### 5.2.4 Oxygen induced reconstruction of the Cu(001) surface

The oxygen reconstruction of the Cu(001) surface has been frequently studied and debated in literature [82, 196–223]. While the LEED pattern of the Cu(001)- $(\sqrt{2} \times 2\sqrt{2})R45^\circ$ -2O reconstruction [cf. Fig. 5.4(i)] was known already in 1965 [196], a satisfying structural model could not be found for a long time. Toward the end of the 1980s, a missing-row model was developed by Zeng et al. [207, 209] and verified through STM measurements by Jensen et al. [211] in 1990. By now, the Cu(001)- $(\sqrt{2} \times 2\sqrt{2})R45^\circ$ -2O missing-row reconstructed surface structure is well understood and has served as model system and substrate in different experiments [189, 224, 225]. This energetically most favored surface structure for an oxygen saturated Cu(001) surface [222] is introduced in this section.

The Cu(001) surface is saturated at an oxygen coverage of  $\theta_O = 0.5$ , forming the  $(\sqrt{2} \times 2\sqrt{2})R45^\circ$ -2O missing-row reconstruction [208, 211, 214]. To illustrate how this oxygen reconstruction is formed, atomic structure models of the clean Cu(001) surface and the missing row reconstructed Cu(001) surface are shown in Figs. 5.4(a,g). The latter is formed by oxygen atoms occupying every second hollow site at the surface (which alone would form a  $c(2 \times 2)$  structure, as illustrated in Fig. 5.4(d)), and ejection of one quarter of the Cu surface atoms in a way that missing Cu rows emerge [208, 209, 220]. Due to the four-fold rotational symmetry of the Cu(001) substrate, two missing row domains occur, as illustrated in Fig. 5.4(d), left vs. right side. The missing rows are aligned with the [100] and [010] direction, respectively [211, 215]. During the preparation process, surface oxygen and copper atoms are mobile [223]. The ejected Cu atoms diffuse across the surface and are re-incorporated into the surface structure elsewhere [211, 221, 223]. As a consequence, step edges move and both step edges and domain boundaries preferably align with the [100] and [010] direction, creating characteristic rectangular terraces [211, 215, 221, 224].

The presented structure is described by the superstructure matrices  $\begin{pmatrix} -2 & 2 \\ -1 & -1 \end{pmatrix}$  and  $\begin{pmatrix} 2 & 2 \\ -1 & 1 \end{pmatrix}$ . The corresponding unit cells are drawn with red lines in Fig. 5.4(g). Compared to the Cu(001) unit cell, which is depicted by black lines in Fig. 5.4(a), the unit cell of the missing row reconstruction is rotated by  $45^\circ$  and the vector lengths are multiplied with  $\sqrt{2}$  and  $2\sqrt{2}$ , respectively. One unit cell contains 2 oxygen atoms. Therefore, this missing-row reconstruction is called Cu(001)- $(\sqrt{2} \times 2\sqrt{2})R45^\circ$ -2O in Wood notation. In the following, the short name Cu(001)-MR-2O will be used. In this work, the surface structure is probed with LEED before and after the oxidation process. Simulated and measured LEED patterns for the clean Cu(001) surface, a  $c(2 \times 2)$  oxygen reconstructed surface and the Cu(001)-MR-2O surface are shown in Figs. 5.4(b,c), Figs. 5.4(e,f) and Figs. 5.4(h,i), respectively. Note that the  $\begin{pmatrix} 1 & 1 \\ 2 & 2 \end{pmatrix}$  spots of the  $c(2 \times 2)$  LEED pattern are common with the Cu(001)-MR-2O pattern, whereas the quarter-order spots, such as the highlighted  $\begin{pmatrix} 1 & 1 \\ 4 & 4 \end{pmatrix}$  spots in Figs. 5.4(h,i), are characteristic only for the Cu(001)-MR-2O pattern.

The Cu(001)-MR-2O reconstruction is obtained by exposing the clean Cu(001)

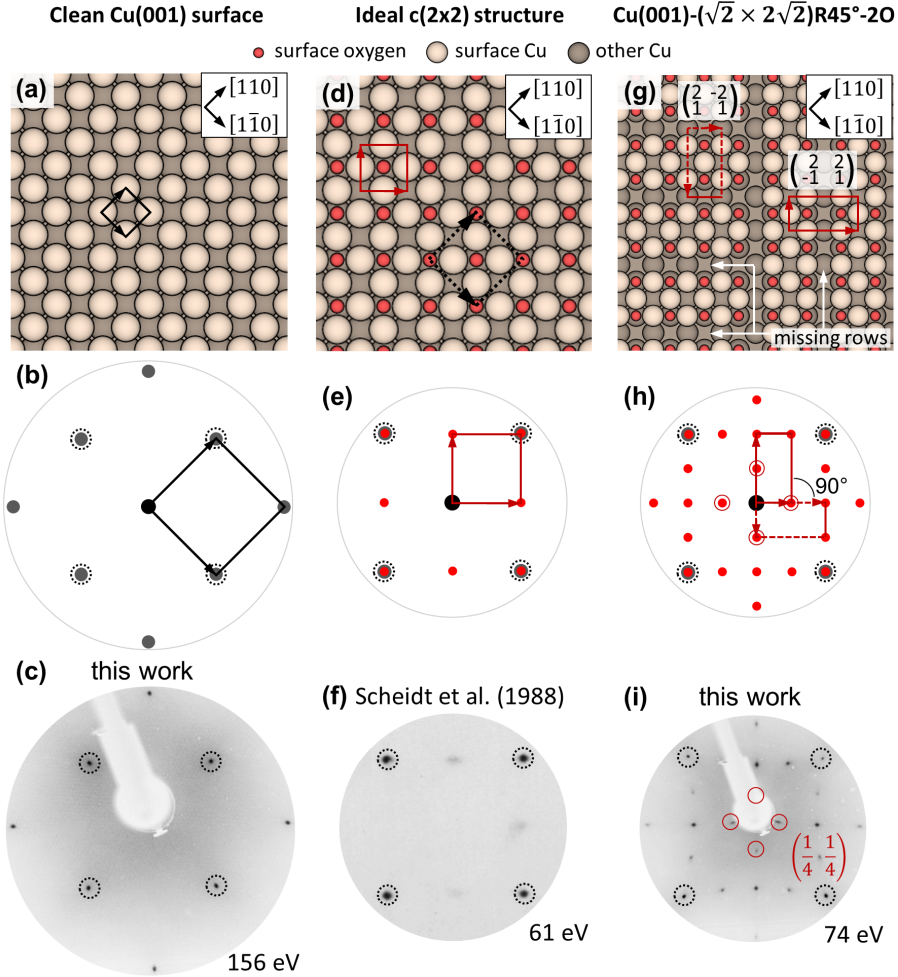


**Figure 5.4: Formation of the  $\text{Cu}(001)-(\sqrt{2} \times 2\sqrt{2})R45^\circ\text{-}2\text{O}$  surface reconstruction.** (a) Structure model of the  $\text{Cu}(001)$  surface and (b,c) the corresponding simulated and measured LEED patterns, respectively. The unit cell is drawn in black. (d) Idealized  $c(2 \times 2)$  oxygen reconstruction with oxygen atoms occupying every second hollow site. The  $c(2 \times 2)$  unit cell is highlighted with black dashed lines, the corresponding primitive unit cell in red. (e) Simulated LEED pattern of a  $c(2 \times 2)$  structure. In addition to the substrate spots,  $(\frac{1}{2}\frac{1}{2})$  spots appear. (f) LEED pattern with faint  $(\frac{1}{2}\frac{1}{2})$  spots, as measured by Scheidt et al. [82] for oxygen-reconstructed  $\text{Cu}(001)$  with  $\theta_o < 0.5$ . Panel (f) adapted from Ref. [82], © 1988, with permission from Elsevier. See License Notice. (g) The  $(\sqrt{2} \times 2\sqrt{2})R45^\circ\text{-}2\text{O}$  surface reconstruction derives from the idealized  $c(2 \times 2)$  structure by removing every fourth Cu row. Two mirror symmetric domains occur, with missing rows along the directions  $[100]$  (left) and  $[010]$  (right). (h,i) Simulated and measured LEED patterns of the  $\text{Cu}(001)-(\sqrt{2} \times 2\sqrt{2})R45^\circ\text{-}2\text{O}$  surface reconstruction. The first order diffraction spots in all LEED patterns are marked with black dotted circles.

surface to oxygen atmosphere. The relevant preparation parameters are: The sample temperature  $T_{O_2}^{sample}$  during oxygen exposure, the partial oxygen pressure  $P_{O_2}$ , and the duration of the oxygen exposure  $t_{O_2}$ . In literature, often only values for  $T_{O_2}^{sample}$  and a dosage are given [82, 205, 206, 208]. The dosage is defined as the product of  $P_{O_2}$  and  $t_{O_2}$  in units of Langmuir ( $1 \text{ L} = 10^{-6} \text{ Torr}\cdot\text{s}$ ) [82, 205]. Frequently, an additional post-annealing of the sample surface in absence of oxygen is applied to improve the lateral ordering of the missing-row reconstruction [189, 209, 211, 218].

It should be noted that, especially due to recurring reports on deviant oxygen adsorption structures at comparably low  $T_{O_2}^{sample}$  and/or very small oxygen exposure (which result into a low oxygen coverage of  $\theta_O \ll 0.5$ ), the oxygen reconstruction of the Cu(001) surface has been a much debated research topic in the 1980's and 1990's [82, 205, 208–212, 217, 218]. A frequently reported surface structure is a  $c(2 \times 2)$  reconstruction [82, 199–202, 204, 213] with its characteristic LEED pattern shown in Fig. 5.4(f). As all LEED spots of the  $c(2 \times 2)$  structure are also present in the LEED pattern of the Cu(001)-MR-2O structure [see Figs. 5.4(e,f,h and i)], a coexistence of both structures is difficult to exclude based on LEED measurements alone. By quantitative LEED studies or including other surface characterization techniques such as STM, a disordered phase [208, 211], later identified as clusters of nanometer size  $c(2 \times 2)$  domains [217], was reported to dominate for  $\theta_O < 0.3$ . In the range of  $0.3 \simeq \theta_O < 0.5$ , this phase coexists with but vanishes in favor of the Cu(001)-MR-2O structure with increasing  $\theta_O$  [208, 217, 221]. For more detailed information on the oxygen reconstruction for  $\theta_O < 0.5$ , refer to Appendix C.

In the first try to prepare a Cu(001)-MR-2O reconstructed surface, the preparation process was performed in analogy to Yang et al. [175, 226]: The Cu(001) crystal was heated up with the filament which sits behind the sample. Using the signal of a pyrometer as reference, a temperature of 470 K was kept stable during the exposure to an oxygen atmosphere of  $P_{O_2} = 5 \times 10^{-7} \text{ mbar}$  for 30 min. The exposure corresponds to a dosage of 675 L. At the end of the oxidation process, the filament heating and the oxygen flow were switched off at once. No post-annealing was applied. In Figs. 5.4(c,i), LEED measurements of the clean Cu(001) surface before and after oxidation are shown. Comparing Fig. 5.4(h) and Fig. 5.4(i), it is found that the measured LEED pattern after oxygen exposure exhibits the characteristic quarter-order spots of the Cu(001)-MR-2O reconstruction. For simplicity, the preparation process of the oxygen reconstruction on the Cu(001) surface will be called oxidation process in the following. Note that in this work, all preparation procedures used pressures and dosages far below the range where thicker oxide layers (growth of  $\text{Cu}_2\text{O}$ ) are expected [214, 221].

### 5.2.5 Structure of PTCDA on the oxidized Cu(001) surface

In the second preparation step, after a cool-down time of at least one hour, a monolayer of PTCDA is deposited on the Cu(001)-MR-2O surface. The deposition time is chosen according to the calibration process on the Ag(110) surface described in Section 5.2.3. In general, the growth rate cannot be considered equal for different surfaces. However, experimental results show that this assumption is adequate for PTCDA deposition on the Ag(110) surface and Cu(001)-MR-2O surface at room temperature.<sup>2</sup> In the following, the LEED results of the sample system PTCDA on Cu(001)-MR-2O are discussed.

#### Structural variations of PTCDA on Cu(001)-MR-2O

Subsequent to the growth of PTCDA on the oxidized Cu(001) surface, the surface structure of the sample was probed with LEED. The LEED pattern shown in Fig. 5.5(a) was obtained after the deposition of PTCDA on the oxide preparation according to the recipe provided at the end of Section 5.2.4. The  $\begin{pmatrix} 1 & 1 \\ 4 & 4 \end{pmatrix}$  spots of the Cu(100)-MR-2O LEED pattern are highlighted with red circles. All remaining spots appeared after PTCDA deposition. The LEED spots of PTCDA are sharp and intense, indicating a well ordered adsorption structure. Characteristic features of the PTCDA pattern are two rings of LEED spots. The spots on the outer ring can be subdivided into eight groups of three spots each (triplets). The spots in the middle of each triplet are more intense and located at the same azimuth as the  $\begin{pmatrix} 1 & 1 \\ 4 & 4 \end{pmatrix}$  spots of the Cu(100)-MR-2O reconstruction, or rotated by 45°. A close look at the inner ring shows that some spots are located at a slightly larger radius than the majority of the spots. They can be subdivided into eight groups of two spots each (doublets). These are centered around the same azimuth as the triplets on the outer ring.

In literature, the deposition of PTCDA on Cu(001)-MR-2O has been reported by Yang et al. [226] and Gärtner et al. [189]. Fig. 5.5(b) displays the measured and simulated LEED pattern by Yang et al. [226]. The  $\begin{pmatrix} 1 & 1 \\ 4 & 4 \end{pmatrix}$  spots of Cu(100)-MR-2O are indicated in analogy to Fig. 5.5(b). The LEED pattern of PTCDA is simulated by the incommensurate structure matrix  $\begin{pmatrix} 0.6 & 5.2 \\ -8.2 & 0.8 \end{pmatrix}$  with four symmetry-equivalent rotational and mirror domains. Characteristic LEED features are recognizable: The outermost LEED spots are located on a ring and grouped into four triplets, with the middle spot of each triplet being azimuthally aligned with the  $\begin{pmatrix} 1 & 1 \\ 4 & 4 \end{pmatrix}$  spots of Cu(100)-MR-2O and more intense than its side spots. On an inner ring, four doublets and four quadruplets are arranged in an alternating fashion. The doublets are located on a ring with slightly larger radius than the quadruplets. Azimuthally, the quadruplets are aligned with the  $\begin{pmatrix} 1 & 1 \\ 4 & 4 \end{pmatrix}$  spots and the doublets are rotated off by

<sup>2</sup>In the aftermath of the present work, a layer of PTCDA on Cu(001)-MR-2O was prepared with the same procedure (and covered with an additional submonolayer of the organic molecule Tetraphenylporphyrin) by M. Stettner. STM measurements of this sample by S. Wenzel showed a well ordered and closed layer of PTCDA molecules on the Cu(001)-MR-2O surface with no indication for PTCDA molecules forming a second layer. [227]

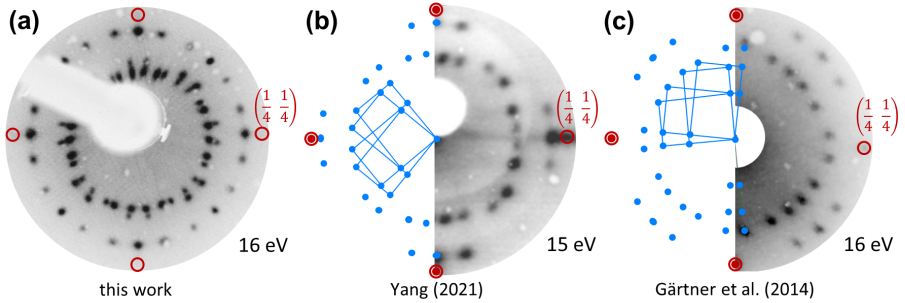


**Figure 5.5: LEED of PTCDA on Cu(001)-MR-2O, comparison with literature.** (a) LEED pattern measured in this work. (b) Measured and simulated LEED pattern with  $\begin{pmatrix} 0.6 & 5.2 \\ -8.2 & 0.8 \end{pmatrix}$  structure. Adapted from Ref. [226], licensed under CC BY 4.0. (c) Measured and simulated LEED pattern with  $\begin{pmatrix} -3.7 & 3.0 \\ 4.8 & 5.8 \end{pmatrix}$  structure. Adapted from Ref. [189], licensed under CC BY 2.0. In each panel, the simulated LEED spots of the PTCDA structure are shown in blue and the  $\begin{pmatrix} 1/4 & 1/4 \end{pmatrix}$  spots of the oxygen reconstruction are highlighted in red in analogy to Fig. 5.4(h,i).

45°. Strikingly, Gärtner et al. [189] presents a different LEED pattern for PTCDA on Cu(100)-MR-2O, which is displayed in Fig. 5.5(c). The PTCDA structure is simulated by the incommensurate structure matrix  $\begin{pmatrix} -3.7 & 3.0 \\ 4.8 & 5.8 \end{pmatrix}$ .

By comparing the simulated PTCDA LEED patterns presented by Yang et al. [226] [cf. Fig. 5.5(b)] and Gärtner et al. [189] [cf. Fig. 5.5(c)], both are found to exhibit four symmetry-equivalent rotational and mirror domains, with unit cells of similar dimensions. A rotation of the PTCDA LEED pattern by Gärtner et al. by 45° (while leaving the  $\begin{pmatrix} 1/4 & 1/4 \end{pmatrix}$  spots of the Cu(100)-MR-2O pattern unchanged) completely reproduces the LEED pattern presented by Yang et al. [226]. This structural similarity of the two PTCDA patterns despite the symmetrical non-equivalent orientation with respect to the substrate indicates that the PTCDA layer formation is mainly determined by the inter-molecular interaction and not by the molecule-substrate interaction. Consequently, the substrate-molecule interaction can be considered relatively small for both PTCDA structures. Despite these similarities, the structural difference of both preparations is still of scientific interest. Moreover, the reproduction of the PTCDA structure observed by Yang et al. [175] is the primary goal of this work. In the following, this desired structure will be called Yang structure, while the structure reported by Gärtner et al. [189] will be referred to as 45°-rotated PTCDA structure.

Next, the LEED patterns of the Yang structure [cf. Fig. 5.5(b)] and the 45°-rotated PTCDA structure [cf. Fig. 5.5(c)] are compared with the preparation of this work in Fig. 5.5(a): All LEED spots of the latter can be identified either with the Yang structure or the 45°-rotated PTCDA structure. Consequently, the Yang structure and the 45°-rotated PTCDA structure coexist. Due to the difference in spot intensities, it can be concluded that the Yang structure slightly dominates.

The fact that both the Yang structure and the 45°-rotated PTCDA structure coexist on the sample indicates that this preparation represents the transition between two structural phases of the same system. In order to control the phase transition, the relevant parameters during sample preparation need to be identified. As the preparation procedure is divided into two preparation steps, the structural variation may originate from the PTCDA deposition process or the oxidation process. While the structural difference between the phases becomes apparent in the LEED pattern of PTCDA, the process of PTCDA deposition itself is straight forward and does not leave much room for variation. Moreover, PTCDA has become a common model molecule within the class of organic semiconductors [228]. Its growth behavior in the submonolayer and monolayer level has been extensively studied and is considered as well understood, especially on metal and insulator substrates where the molecule-substrate interaction is relatively weak [229]. The preparation process of the Cu(100)-MR-2O reconstruction however, has been debated intensively in literature. The involved parameters interplay in a more complex way and need to be chosen careful. Especially the possibility of a  $c(2 \times 2)$  phase coexisting with the Cu(100)-MR-2O reconstruction has to be considered in this context, because it does not become apparent in LEED. Therefore, the different PTCDA structures result most likely from different configurations of the underlying oxygen reconstructed surface.

A comparison of the preparation procedure for the Cu(100)-MR-2O reconstruction by Yang et al. [175] (which was adapted in this work) and Gärtner et al. [189] gives a first hint on the origin of the structural variation. Considering that the preparation parameters at different setups are comparable only to a limited extent, two significant differences stand out: While the sample temperature during oxygen exposure appears comparable for both works (470 K for the Yang structure and  $T_{O_2}^{sample} = 500$  K for the 45°-rotated PTCDA structure), the first difference is an oxygen exposure larger by a factor of two for the Yang structure ( $\sim 740$  L compared to  $\sim 360$  L for the exclusively 45°-rotated PTCDA structure). The second difference is that for the 45°-rotated PTCDA structure an additional post-annealing at 700 K for 10 min was applied after the actual oxidation process.

In this work, the post-annealing or likewise the temperature  $T_{O_2}^{sample}$  during oxygen exposure was found to cause the variation of the PTCDA adsorption structure. By applying an additional post-annealing after the oxygen exposure and before PTCDA deposition, it was possible to significantly shift the intensity ratio of the two PTCDA structures towards higher contributions of the undesired 45°-rotated PTCDA structure. Without post-annealing and gradually reducing  $T_{O_2}^{sample}$ , the spots of the 45°-rotated PTCDA structure became fainter. The measurements displayed in Figs. 5.6(a-c) describe the structural transition with variation of  $T_{O_2}^{sample}$  based on the PTCDA LEED pattern. Compared to the LEED pattern in Fig. 5.5(a), the LEED pattern in Fig. 5.6(c) was obtained by using the same preparation procedure, only a lower  $T_{O_2}^{sample}$  was applied during oxygen exposure. The reduction of  $T_{O_2}^{sample}$  results into strong LEED spots of the Yang structure and significantly fainter spots of the 45°-rotated PTCDA structure. By further reducing

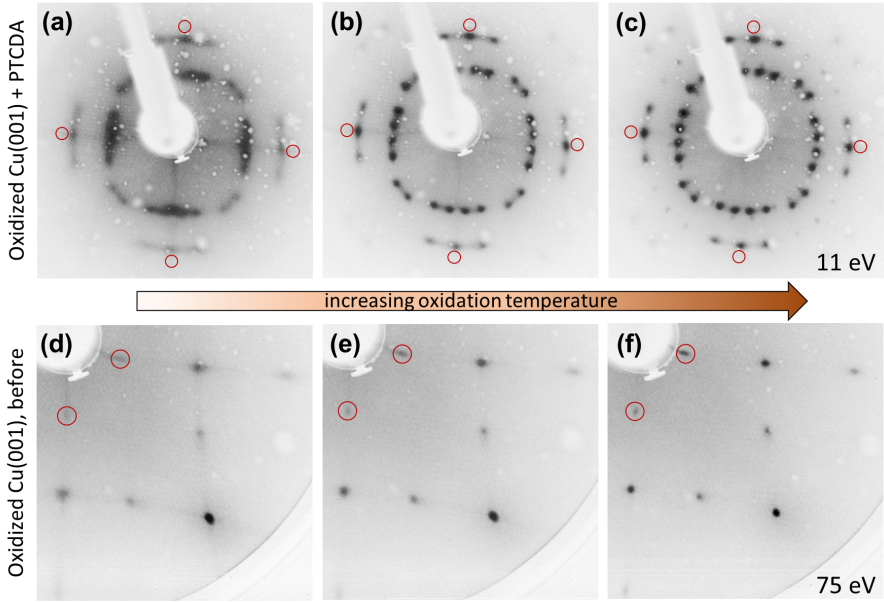


**Figure 5.6: LEED measurements for different preparations of PTCDA on oxygen reconstructed Cu(001).** The first row shows the patterns of the oxygen reconstructed Cu(001) after deposition of PTCDA at 11 eV, the second row before (75 eV): **(a,d)** The oxidation temperature was too cold, as the spots of the PTCDA structure are blurred in (a). **(b,e)** The oxidation temperature was optimal, as sharp spots of only the Yang structure are observed in (b). **(c) and (f)** The oxidation temperature was too hot, as additional spots from the 45°-rotated PTCDA structure are visible in (c). By further increasing  $T_{O_2}^{sample}$ , a LEED pattern similar to Fig. 5.5(a) is obtained.

$T_{O_2}^{sample}$ , the LEED spots of the 45°-rotated PTCDA structure vanish completely [cf. Fig. 5.6(b)]. For even lower  $T_{O_2}^{sample}$ , the LEED spots of the Yang structure become blurred [cf. Fig. 5.6(a)], which hints for a reduction of the structural quality of the oxygen reconstruction. In this way, the optimal  $T_{O_2}^{sample}$  to obtain the Yang structure is clearly delimited both to higher and lower  $T_{O_2}^{sample}$ .

Comparing Fig. 5.6(b) with the LEED pattern reported by Yang et al. [cf. Fig. 5.5(b)], some differences in the spot intensities are observed. Firstly, the PTCDA spots which are arranged on the inner ring in alternating doublets and quadruplets show all the same intensity for this work's preparation but not for the preparation by Yang: Half of the spots show reduced intensity compared to the others. This difference of the spot intensities can be explained easily by imbalanced contributions of the four PTCDA domains. The spots of low intensity can all be assigned to one of the PTCDA domains and its mirror-symmetric equivalent.

Secondly, the intensity ratio of the  $\left(\frac{1}{4}\frac{1}{4}\right)$  spots of the missing row reconstruction compared to the PTCDA spots differs for this work's preparation and for the preparation by Yang. On one hand, this can be simply a result of the different LEED energies. On the other hand, a reduced intensity of the substrate spots in this work can hint for an increased PTCDA coverage compared to Yang. Overall, the Yang structure was reproduced successfully.

In order to better understand the structural transition of the oxygen reconstructed Cu(001) surface with decreasing  $T_{O_2}^{sample}$ , the LEED measurements of the oxygen reconstructed surfaces themselves are discussed. Figs. 5.6(d-f) display the LEED patterns of the oxygen reconstructed surface before PTCDA deposition for the same preparation experiments which resulted in the previously discussed PTCDA patterns [cf. Figs. 5.6(a-c)]. With decreasing  $T_{O_2}^{sample}$ , the spots of the surface reconstruction lose intensity and undergo a slight blurring. In general, this development hints for a reduced structural long-range order of the oxygen reconstruction. However, from LEED alone it remains unclear how exactly this reduced structural order manifests. One possibility could be a reduction of the domain size. Another possibility could be the coexistence of the Cu(001)-MR-2O reconstruction with clusters of nanometer sized  $c(2 \times 2)$  domains, which was reported for oxygen coverage  $\theta_O < 0.5$  (see above). For the oxygen reconstruction which results in the well ordered Yang structure [cf. Figs. 5.6(b,e)], the latter can be considered unlikely: In the context of other experiments, the oxygen reconstructed Cu(001) surface (as prepared for exclusively  $0^\circ$ -rotated PTCDA) was covered with CuPc molecules instead and investigated with low-temperature STM [MR7]. The measurements revealed that, under the well-ordered and closed molecular layers, the terraces of the oxygen reconstructed surface exhibited well-defined rectangular shapes. The latter is characteristic to a Cu(001)-surface covered with large areas of missing-row reconstruction [221, 224]. However, a coexistence of the Cu(001)-MR-2O reconstruction with clusters of nanometer sized  $c(2 \times 2)$  domains with decreasing  $T_{O_2}^{sample}$  seems to agree well with the transition from the LEED pattern in Fig. 5.5(b) to the same but more diffuse pattern in Fig. 5.5(c).

The LEED measurements of the oxygen reconstructed surfaces in Figs. 5.6(d-f) reveal another structural trend: In addition to the intensity reduction and blurring, faint lines running through the quarter-order spots and along the [100] or the [010] direction gradually appear in Figs. 5.6(d-f) with decreasing  $T_{O_2}^{sample}$ . These lines hint for a Cu(001)-MR-2O structure which exhibits domains large and well defined in one direction (the direction in which the line in the LEED pattern is thin) and domains small and out of phase in the other direction (the direction in which the quarter-order spots are elongated). From the elongation directions, it can be deduced that both of the missing row domains are elongated in the direction of the missing rows [cf. Figs. 5.4(g-i)].<sup>3</sup> As no other structural difference could be revealed, the question arises if the size and shape of the domains and domain boundaries of the Cu(001)-MR-2O reconstruction can play a crucial role

---

<sup>3</sup>Note that the  $\left(\frac{1}{2}\frac{1}{2}\right)$  spots and the substrate spots are common with both missing row domains and therefore comprise the stripes of both domains.

in the formation of the Yang structure and the 45°-rotated PTCDA structure. Eventually, conventional LEED is an averaging technique and provides only limited information on the local surface structure.

Summarizing, the described changes in the LEED measurements of the oxygen reconstructed surface with varying  $T_{O_2}^{sample}$  agree well with literature on the formation process of the missing row-reconstruction, as summarized in Section 5.2.4. It should be mentioned that the occurrence of the 45°-rotated PTCDA structure was believed to result from a destruction of the long-range order of the missing rows at elevated  $T_{O_2}^{sample}$  [MR4, 226]. This conclusion is based on the order-disorder phase transition observed by Iddir et al. [220], which goes along with a decreasing intensity of the quarter-order spots [220] with increasing  $T_{O_2}^{sample}$ .<sup>4</sup> As the opposite trend is observed in the present work, a destruction of the long-range order of the missing rows can be excluded to be the origin of the structural transition of the oxygen reconstructed Cu(001) surface with increasing  $T_{O_2}^{sample}$  as described above. However, the exact structural configuration of the Cu(001)-MR-2O surface which results either in the Yang structure or the 45°-rotated PTCDA structure can not be identified with conventional LEED before PTCDA was deposited. This makes the deposition of PTCDA and subsequent LEED measurement a very sensitive and accurate probe for the desired structural configuration of the Cu(001)-MR-2O reconstruction.

### Optimization of the sample preparation procedure

In order to achieve a better reproducibility, a higher sample quality and a shorter preparation time, the oxidation temperature was optimized. As mentioned before, the sample was heated with a filament and the temperature of its surface was measured using a pyrometer. During the oxidation process, the filament current was adjusted to maintain a constant temperature  $T_{O_2}^{sample}$ . For this procedure, the preparation of the oxygen reconstruction was found to be not well reproducible: The range of  $T_{O_2}^{sample}$  for which a Yang structure of high quality could be obtained appeared to be very narrow and often PTCDA structures characteristic for higher or lower  $T_{O_2}^{sample}$  during the oxidation process [cf. Figs. 5.6(d,f)] were observed, although the nominal  $T_{O_2}^{sample}$  was constant. By recording the signal of the pyrometer during the whole preparation process, it was found that the pyrometer's signal does not resemble the sample temperature while the filament is operated. This becomes obvious in the right part of the temperature profile displayed in Fig. 5.7. For a duration of 30 min, the filament current was operated in a way to keep the pyrometer's signal [black curve in Fig. 5.7] stable at  $\sim 430$  K. After turning off the filament at  $t = 55$  min, the temperature dropped immediately by  $\sim 35$  K. This fast drop does not resemble a realistic cool-down process of the sample. The conclusion is that the pyrometer's signal is rather a measure for the heating power of the filament than the actual sample temperature. As a consequence, the actual temperature during the oxygen preparation process as described before is unknown

<sup>4</sup>For more information on the order-disorder phase transition, refer to Appendix C.

and cannot be assumed to be constant.

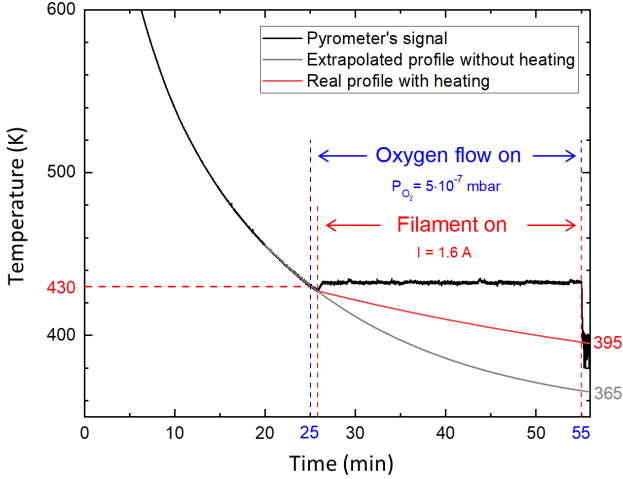


**Figure 5.7: Temperature profile during the optimized oxidation process.** The pyrometer’s temperature signal (black curve) is recorded from that point ( $t = 0$ ), where the annealing process of the preceding cleaning procedure is finished. Up to  $t = 25$  min, the profile describes a realistic exponential cool-down process. At  $t = 25$  min, oxygen is introduced into the preparation chamber and kept at a constant pressure of  $P_{O_2} = 5 \times 10^{-7}$  mbar. Immediately after, the filament is turned on. At  $t = 55$  min, the oxidation process is finished by turning off the oxygen flow and the filament current at once. The real temperature profile during heating and the temperature profile without filament heating are estimated by the red and grey curve, respectively. For more information, see main text.

In order to improve the temperature control, the residual heat of the sample after the cleaning procedure was used for the oxidation process. The following procedure was established: As displayed in Fig. 5.7, the sample temperature was tracked by the pyrometer, starting from the time when the filament was switched off at the end of the cleaning procedure ( $t = 0$  min). During the cool-down process of the sample, the ion gauge in the preparation chamber and all other sources of thermal radiation were switched off, such that the pyrometer’s signal did resemble the actual sample temperature. Up to  $t = 25$  min, the profile describes a realistic exponential cool-down process and the sample temperature dropped down to  $\sim 430$  K. At this point, oxygen was introduced into the chamber so that the temperature at the beginning of the oxidation process is well defined. As the ion gauge in the neighboring load lock was found to not affect the pyrometer’s signal, it was used to maintain a constant oxygen pressure of  $5 \times 10^{-7}$  mbar. Immediately after starting the oxygen flow, the filament was tuned up to a current of  $I = 1.6$  A and its power was kept stable by using the pyrometer’s signal as a reference. Thereby, the temperature

variation during the oxidation procedure was reduced such that  $T_{O_2}^{sample} = 395$  K at the end of the oxidation process (which can be measured after the filament is switched off). The real temperature profile during the oxidation process is estimated by the red curve in Fig. 5.7. Without heating, the temperature profile would have followed the exponential decay described by the grey curve, resulting in  $T_{O_2}^{sample} = 365$  K. It should be noted that a procedure without the additional heating during oxygen exposure was tried and discarded, as the LEED pattern of the subsequently deposited PTCDA was of lower quality.

The described procedure made it possible to fabricate reproducible samples of high quality, confirmed by LEED measurements after the subsequent deposition of PTCDA. Although the temperature measurement with a pyrometer did not work while operating the filament, the applied procedure guarantees a well defined temperature profile during the oxygen exposure. Moreover, starting the oxidation already during the cool-down process shortened the preparation time by 30 min.

### Structure and expected photoemission features of PTCDA on Cu(001)-MR-2O

Finally, detailed real- and reciprocal-space structure models of the Yang structure on the Cu(001)-MR-2O surface reconstruction are presented. For that, the results of this work and Yang et al. [175, 226] are combined. The section concludes with a discussion of the expected photoemission features in the tr-POT experiment.

The resulting PTCDA structure, as depicted in Fig. 5.8, was a well-ordered, incommensurate superstructure that is described by the matrix  $\begin{pmatrix} 0.6 & 5.2 \\ -8.2 & 0.8 \end{pmatrix}$ . The corresponding unit cell [dark blue colored solid rectangle in the upper right quadrant of Fig. 5.8(a)] is almost rectangular with  $a_1 = 13.38$  Å,  $a_2 = 21.06$  Å, and  $\gamma = 91.0^\circ$ . From the size and dimensions of this unit cell it was concluded that the molecules orient themselves in a herringbone-like pattern. The herringbone structure is stabilized by hydrogen bonding and is very often seen upon adsorption on weakly interacting surfaces, as well as in the bulk crystal [228]. The molecules adopt an angle of  $\sim 90.0^\circ$  with respect to each other, and they are rotated by  $\pm 45^\circ$  with respect to the fundamental Cu(001) crystallographic directions  $[\bar{1}10]$  and  $[110]$ , an orientation that is confirmed by Yang et al. [175] and the photoemission tomography results in the following section. In the work of Yang et al. [175] it was also found that the adsorption height of PTCDA above the oxide layer is  $\sim 3.49$  Å. This value is in the range of the sum of the van der Waals radii of copper and carbon/oxygen [see Fig. 5.8(b)], which indicates an efficient electronic decoupling of the molecules from the copper substrate [175].

The adsorption structure of PTCDA as such exhibits only two-fold rotational symmetry. Considering the two (by  $90^\circ$ -rotation equivalent and 2mm symmetric) Cu(001)-MR-2O domains that form on the 4mm symmetric Cu(001)-surface, the Cu(001)-MR-2O surface exhibits an effective 4mm symmetry. As a result, PTCDA crystallizes in four symmetry-equivalent rotational and mirror domains, the structures and unit cells of which are shown in Fig. 5.8(a). Fig. 5.8(c) shows the corresponding simulated LEED pattern, which has been presented already be-



fore [cf. Fig. 5.5(b)]. Here, the LEED spots and unit cells of the four domains are colored according to the color code used in Fig. 5.8(a). Although the presented sample system forms four domains with two molecular orientations per unit cell, overall only two orientations (labeled  $0^\circ$  and  $90^\circ$  with respect to the laboratory frame) exist for every single PTCDA molecule on the Cu(001)-MR-2O surface [cf. Fig. 5.8(a)]. All symmetry operations of the 4mm symmetric substrate reproduce these same two orientations.

Finally, the simulated momentum maps for the HOMO and LUMO signatures of PTCDA on Cu(001)-MR-2O are presented in Fig. 5.8(d). These have been generated with “kMap.py” (a Python program for simulation and data analysis in photoemission tomography [230]) and a database of DFT calculated gas phase molecular orbitals [231], both provided by the cooperation partners from the University of Graz. By Fourier transforming the calculated real-space HOMO and LUMO orbitals of PTCDA (left), theoretical momentum maps have been generated (middle). The experimentally expected photoemission features (right) result from the sum of the momentum maps for the  $0^\circ$  and  $90^\circ$  oriented molecule. It becomes clear that all four photoemission features of the HOMO and LUMO of both the  $0^\circ$  and  $90^\circ$  oriented molecules are expected to be well distinguishable in the experiment. This simplifies the interpretation of the experimental photoemission data significantly and therefore proves that the sample system PTCDA on Cu(001)-MR-2O is a good choice for the tr-POT experiment.

### 5.3 The tr-POT experiment in Marburg - Results and discussion

For the tr-POT experiments, the prepared samples were transported to Marburg under UHV conditions by using a vacuum suitcase. The suitcase kept a base pressure of  $1 \times 10^{-10}$  mbar stable during the transport. The sample transfer to the measuring chamber was completed within one day after sample preparation.

The cooperation partners from the Philipps-Universität Marburg designed the experimental setup especially for the tr-POT experiment [see Sec. 2.7.3]. It combines two recent developments: For illumination, a 2PPE laser setup with a tunable visible pump beam and a HHG probe beam of 21.7 eV photon energy were implemented [66, 121, 122]. This allows for resonant excitation of the molecules and makes it possible to access high parallel momenta up to  $\sim 2 \text{ \AA}^{-1}$ . For detection, a newly designed momentum microscope with a PEEM-like lense system, a drift tube and a time- and position-sensitive delay-line detector is implemented, which enables recording of the full momentum space in one shot [123].

Figure 5.9(a) displays the scheme of the experiment: A 2.3 eV pump pulse excites electrons resonantly from the molecules HOMO into the LUMO. With a 21.7 eV probe pulse, the electrons are photoemitted at variable delay times  $t_p$ . The parallel photoelectron momenta  $k_x$  and  $k_y$  were mapped onto the detector, and the energy  $E$  was retrieved simultaneously for every single photoelectron by

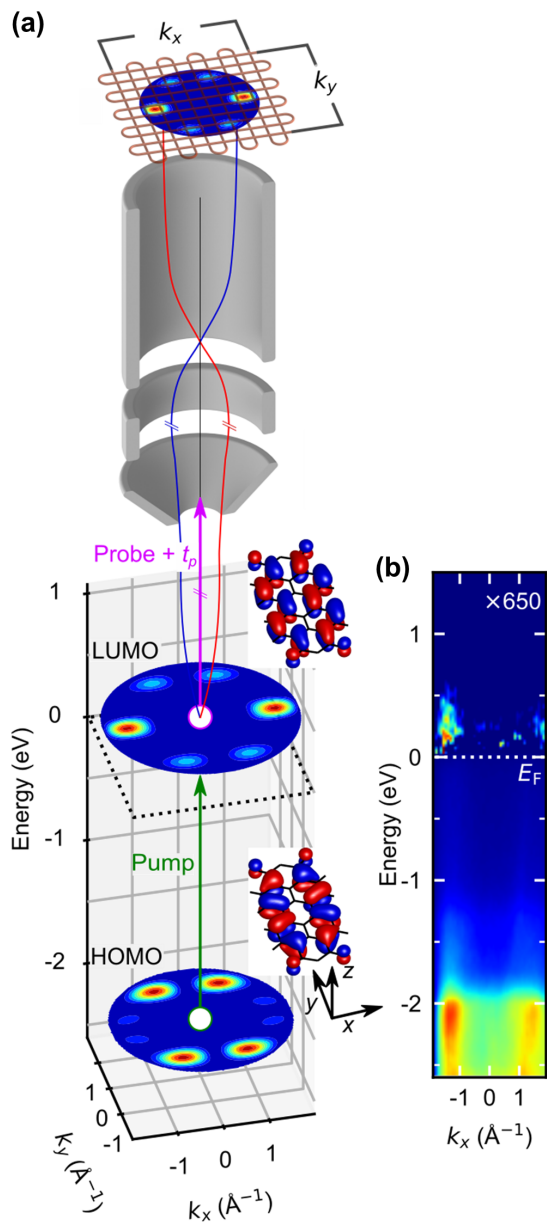


**Figure 5.9: Femtosecond time-resolved photo-emission tomography of molecular orbitals.** (a) Scheme of the experiment. Electrons from the PTCDA HOMO are excited into the LUMO by the pump pulse (green) and then photoemitted by the probe pulse (purple) after a variable delay time  $t_p$ . The photoemitted electrons are recorded in a TOF-PEEM setup. Theoretical  $I(k_x, k_y)$  maps indicate the distribution of photoelectrons in momentum space. Momentum maps and corresponding real-space orbitals of HOMO and LUMO have been calculated with density functional theory. (b) Experimental  $I(E, k_x)$  map, extracted from  $I(E, k_x, k_y, t_p)$ , for  $k_y \in [-0.2; 0.2] \text{\AA}^{-1}$  in temporal overlap ( $t_p = 0$ ).  $E = 0$  refers to the Fermi energy  $E_F$ . For  $E > 0$ , the experimental Fermi-Dirac distribution has been subtracted by using the most negative delay time  $t_p = -46$  fs and the signal has been scaled with a factor of 650. Fig. 5.9 adapted from Ref. [MR4]. Reprinted with permission from AAAS (see License Notice).

the time-of-flight (ToF) measurement. The recorded four-dimensional data cube  $I(E, k_x, k_y, t_p)$ , where  $I$  denotes the photoemission intensity, makes it possible to deduce the spatial electron distribution in terms of orbitals in momentum space, their energy position, and their time evolution. Figure 5.9(b) shows a cut through a data cube integrated in the interval  $k_y \in [-0.2; 0.2] \text{ \AA}^{-1}$ , displaying  $I(E, k_x)$  at zero delay time. As expected for  $\pi$ -orbitals of flat lying PTCDA molecules, photoemission occurred at parallel momenta of  $\sim 1.4$  to  $1.6 \text{ \AA}^{-1}$  [166]. The intensity in the range from 1.3 to 2.3 eV below the Fermi energy  $E_F$  (defined as  $E = 0$ ) derived from standard 1PPE (composed of the HOMO of the PTCDA molecule at  $E \sim 2.2$  eV sitting on top of the Cu d-band onset and the O 2p states of the oxide), whereas the weaker intensity at  $\sim 0.25$  eV above  $E_F$  originated from 2PPE of the LUMO, populated by the pump pulse before photoionization. These assignments are unambiguous, as the constant energy intensity maps, evaluated at orbital energies  $E$  as a function of  $k_x$  and  $k_y$ , are fingerprints of individual orbitals. Theoretical momentum maps of HOMO and LUMO of PTCDA are displayed in the excitation scheme in Fig. 5.9(a).

In the following, the results of the tr-POT experiment on the sample system PTCDA on Cu(001)-MR-2O are presented as published in [MR4]. The experiment was performed by R. Wallauer, myself and K. Stallberg, with support by L. Münster and J. Güdde. The resulting data was analyzed and interpreted by R. Wallauer, K. Stallberg, F. S. Tautz and U. Höfer. D.Brandstetter, P.Puschnig, and S.Soubatch simulated the momentum maps of the PTCDA molecule in the gas phase. In general, when molecules undergo excitation processes, electronic relaxations may result in alterations to the shapes of their orbitals. This issue is addressed by P. Puschnig in the supplemental material of Ref. [MR4]. It was found that only minor changes of the orbital's shape occur, which do not play any role for analyzing the tr-POT data of the present work.

### 5.3.1 Observing transiently occupied molecular states

In a first experiment, the in-plane rotation of the sample was chosen such that the plane of incidence of pump and probe pulses is oriented  $45^\circ$  to both the  $0^\circ$  and the  $90^\circ$  molecule. In this way, both molecules were illuminated under symmetrically equivalent conditions. The projected light incidence is illustrated in Fig. 5.10(a) with colored arrows. Figs. 5.10(a,b) display the theoretical momentum maps of LUMO and HOMO, respectively. These are obtained in analogy to Fig. 5.8(d), whereby it was taken into account that the angle of incidence is inclined by  $70^\circ$  from the surface normal. Hence, the maps show a gradient of intensity along the projected light incidence.

In Figs. 5.10(c,d), measured momentum maps at the energies of the LUMO and HOMO for three selected delay times are presented. The LUMO map was scaled by a factor of 1850. Each orbital shows a distinct momentum distribution that can be traced on the ultra-fast time scale of the experiment. The agreement between the theoretical and measured momentum maps is obvious, both for the LUMO

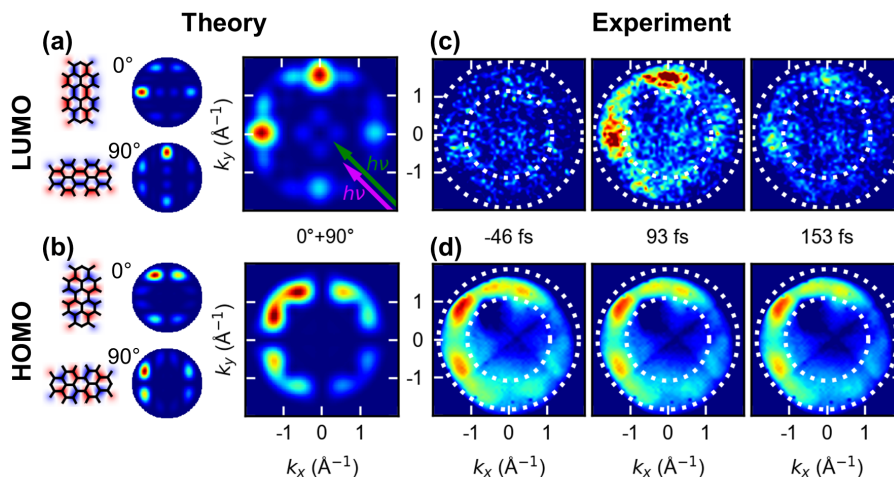


**Figure 5.10: Momentum maps of the frontier orbitals.** (a) Two-dimensional cuts through the real-space LUMO of gas-phase PTCDA (left) and corresponding theoretical momentum maps with polarization factor  $P(k)$  plotted for two orientations  $0^\circ$  and  $90^\circ$  (middle) and their sum (right). The colored arrows indicate projected light incidence ( $45^\circ$ ) with different photon energies  $h\nu$ . (b) Same as for (a) but for the HOMO. Both orbitals have been calculated for neutral, closed-shell PTCDA. However, an open-shell calculation of the highest occupied orbital for the PTCDA anion yields almost indistinguishable results from the LUMO of neutral PTCDA [refer to the supplement of Ref. [MR4]]. (c) Experimental momentum maps obtained at selected delay times  $t_p$  and  $E = +0.45$  eV. Both pump and probe pulses are p-polarized. The two dotted circles indicate the momentum integration range used for the determination of the lifetime [see Sec. 5.3.2 and Fig. 5.11]. (d) Same as for (c), but at  $E = -2.18$  eV (intensity reduced by a factor 1850). Note that the intensity of the experimental HOMO features for  $k_y > 1 \text{ \AA}^{-1}$  is reduced due to irregularities of the detector. Fig. 5.10 adapted from Ref. [MR4]. Reprinted with permission from AAAS (see License Notice).

[cf. Figs. 5.10(a,c)] and for the HOMO [cf. Figs. 5.10(b,d)]. As the single-photon photoemission pattern for the HOMO in Fig. 5.10(d) shows no dependence on the delay time, only a small fraction of the molecules was excited by the pump pulse. Saturation effects due to optical pumping as well as cross-talk between excited molecules can thus be neglected for the data analysis.

As can be seen in Fig. 5.10(c), the population of the LUMO shows a strong dependence on the delay time. For a delay time of  $-46$  fs, the measured momentum map shows no distinct features. As the delay time is negative, the probe pulse arrives before the pump pulse. The measuring condition corresponds to a 1PPE experiment. Therefore, no f-LUMO is observed, which proves that there is no static charge transfer from the Cu(001)-MR-2O surface to the PTCDA molecules [175]. For a positive delay just above temporal overlap of the pump and probe pulse ( $t_p = 93$  fs), the measured momentum map exhibits clear features, which agree well with the theoretical LUMO pattern. This already confirms that the excited molecular state's finite lifetime is sufficiently long enough to be probed in the presented tr-POT experiment. With increasing delay time, the intensity of LUMO features decreases [cf. Fig. 5.10 (c),  $t_p = 153$  fs]. It was found that at delay times far beyond temporal overlap the LUMO pattern is still detectable [cf. Fig. 5.11,  $t_p = 393$  fs]. This already indicates that the oxygen reconstruction of the Cu(001) surface decouples the PTCDA molecules very efficiently. Otherwise, the lifetime of the excited LUMO state was much shorter. For a quantitative analysis, the lifetime of the excited state is determined in the following section.

### 5.3.2 Determination of the inelastic lifetime $T_1$ of the LUMO

As introduced in Section 2.7.2, the inelastic lifetime  $T_1$  of the excited state describes its population relaxation due to inelastic scattering. This effect becomes dominant at significantly large delay times beyond the temporal overlap, when the optically induced coherence between ground state and excited state has decayed. In this regime, the population of the excited state is expected to describe an exponential decay with the decay rate  $\Gamma_1 = -1/T_1$ .

In order to determine the lifetime  $T_1$  of the excited electron in the PTCDA LUMO, the decay of the excited state's measured intensity with increasing delay time is analyzed. Importantly, the shape of the LUMO pattern in momentum space [as shown in Fig. 5.10(c)] remained constant for all delay times, proving that no changes in the excited orbital took place during its decay. Therefore, the measured intensity of the excited state is considered directly proportional to the population of the LUMO. For a fixed delay time, the photoemission intensity of the orbital features was determined separately for every constant energy plane. This was done by integrating the intensity over the momentum range as indicated by the area between the two white dotted circles in Figs. 5.10(c,d). By plotting the orbital feature's intensity versus the energy, an energy distribution curve (EDC) was obtained for every delay time. The EDC for the most negative delay ( $-46$  fs) is shown as black curve on the left side of Fig. 5.11(a). It corresponds to the 1PPE

signal from the PTCDA HOMO and the substrate. Above  $E_F$ , the green curves show the intensity differences between the EDC for  $t_p = -46$  fs and the EDCs for increasing delay time  $t_p$ . This signal corresponds to photoemission from the transiently occupied LUMO.

In a second step, the peak area of the LUMO signal in the energy dispersion curves is determined for every delay time. By plotting this intensities of the LUMO as a function of delay time, the decay curve is obtained as displayed in Fig. 5.11(b). For comparison, the dependence of the measured photoemission for the HOMO is also plotted as black data points with time average (black line) in Fig. 5.11(b). While the HOMO signal is constant for all delay times, the integrated LUMO intensity reveals that after about 100 fs, the LUMO population suffered a single-exponential decay with a lifetime of  $T_1 \simeq 250$  fs. For an excited molecule at a metal surface, this longevity is exceptional [115, 232].

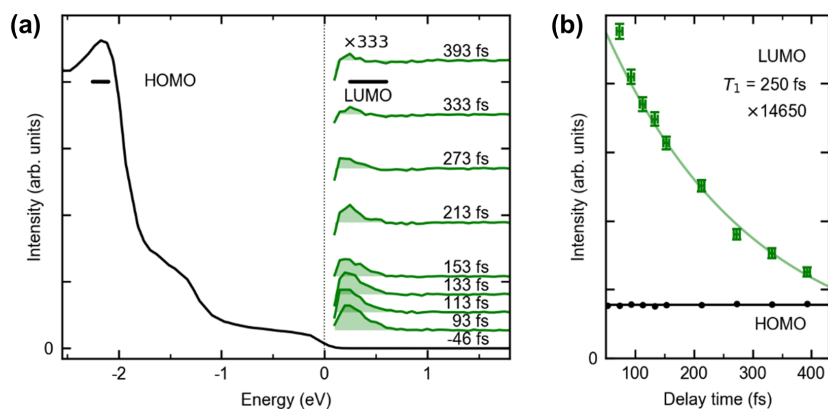


**Figure 5.11: Lifetime of the excited electron in the LUMO.** (a) Energy distribution curves (EDC) of the experiment in Fig. 5.10, with the intensity integrated between the two white dotted circles in Figs. 5.10(c,d). The black curve belongs to the data obtained for the most negative delay time (-46 fs), corresponding to 1PPE from the HOMO and the metal substrate. On the right side above  $E_F = 0$ , the 2PPE signal is displayed by green curves that were obtained by subtracting the EDC for  $t_p = -46$  fs from the EDCs for increasing delay time  $t_p$ . The area highlighted in a lighter green shade corresponds to photoemission from the transiently occupied LUMO. (b) LUMO intensity (green data points with error bars) with fit to a single exponential decay (green line) and HOMO intensity (black data points) with time average (black line). The curve for the LUMO is scaled by a factor of 14650 compared to the curve for the HOMO. The energy integration ranges used in (b), as well as in Figs. 5.10(c,d), are indicated by thick horizontal bars in (a). The integration range of the LUMO is between 0.3 and 0.6 eV. Fig. 5.11 adapted from the Supplemental Material of Ref. [MR4]. Reprinted with permission from AAAS (see License Notice).

### 5.3.3 Real-space excitation pathways

In a second experiment, the symmetry between the two differently oriented PTCDA molecules was broken by aligning the plane of light incidence with the long axis of the  $0^\circ$  molecule. As the orbital features of the  $0^\circ$  molecule and the  $90^\circ$  molecule do not overlap in the momentum-space patterns, both molecules can be tracked separately. Moreover, the 2PPE measurements were performed both for s- and p-polarized pump pulses.

First, the 2PPE measurement was done with s-polarized pump pulses. As illustrated in Fig. 5.12(a), this means that the polarization vector  $\mathbf{E}$  of the pump pulse is perpendicular to the plane of incidence. Consequently, it is parallel to the sample surface ( $\mathbf{E} = \mathbf{E}_{\parallel}$ ) and the long axis of the  $90^\circ$  molecule. The measured momentum map of the excited state is presented in Fig. 5.12(c), with white and orange contours highlighting the positions where signal from the  $0^\circ$  molecule and the  $90^\circ$  molecule is expected, respectively. The data of all delay times was summed up for this image, showing that s-polarized light only excited the  $90^\circ$  molecule but not the  $0^\circ$  molecule. Based on the HOMO-LUMO transition being a dipole transition, a group theory analysis confirmed that the transition is only allowed when the polarization vector is aligned along the long molecular axis, as it is the case for the  $90^\circ$  molecule, but not for the  $0^\circ$  molecule (for more details, see supplemental material of Ref. [MR4]).

Secondly, the experiment was repeated with p-polarized pump pulses [experimental geometry as depicted in Fig. 5.12(b)]. The p-polarized geometry is defined by the polarization vector  $\mathbf{E}$  lying in the plane of incidence. As the photon beam is tilted with respect to the surface normal,  $\mathbf{E}$  exhibits both a component  $\mathbf{E}_{\parallel}$  parallel and  $\mathbf{E}_{\perp}$  perpendicular to the surface. Now,  $\mathbf{E}_{\parallel}$  is aligned with the long axis of the  $0^\circ$  molecule. Measured momentum maps of the excited state for different delay times are presented in Fig. 5.12(d). These show, that p-polarized light was able to excite both molecules, albeit with surprisingly different excitation dynamics: The LUMO pattern of the  $0^\circ$  molecule lit up much earlier and much brighter than that of the  $90^\circ$  molecule.

In order to quantify the different excitation dynamics, the intensities of the two molecular orientations were integrated within the contours and plotted versus the delay time both for s- and p-polarized pump pulses in Fig. 5.12(e). Before the excitation dynamics are discussed in detail, it should be mentioned that excitation only happens during temporal overlap of the pump and probe pulses. The temporal overlap was quantified for each measured transient by integrating the photoelectron signal in the unoccupied part of the spectrum, far from intermediate states. The energy range of 1.5 to 2.0 eV above  $E_F$  was chosen, where the intensity is most likely caused by a direct two-photon transition out of substrate electronic states just below  $E_F$ . This resulted in the fully symmetric cross-correlation trace, as depicted by the grey triangles (cc) in Fig. 5.12(e). Its maximum defines the delay time  $t_p = 0$ . Note that, due to the finite pulse duration (50 fs for the pump and 20 fs for the probe pulse), temporal overlap exists not only at  $t_p = 0$  but also before and after, as described by the shape of the cross-correlation trace.

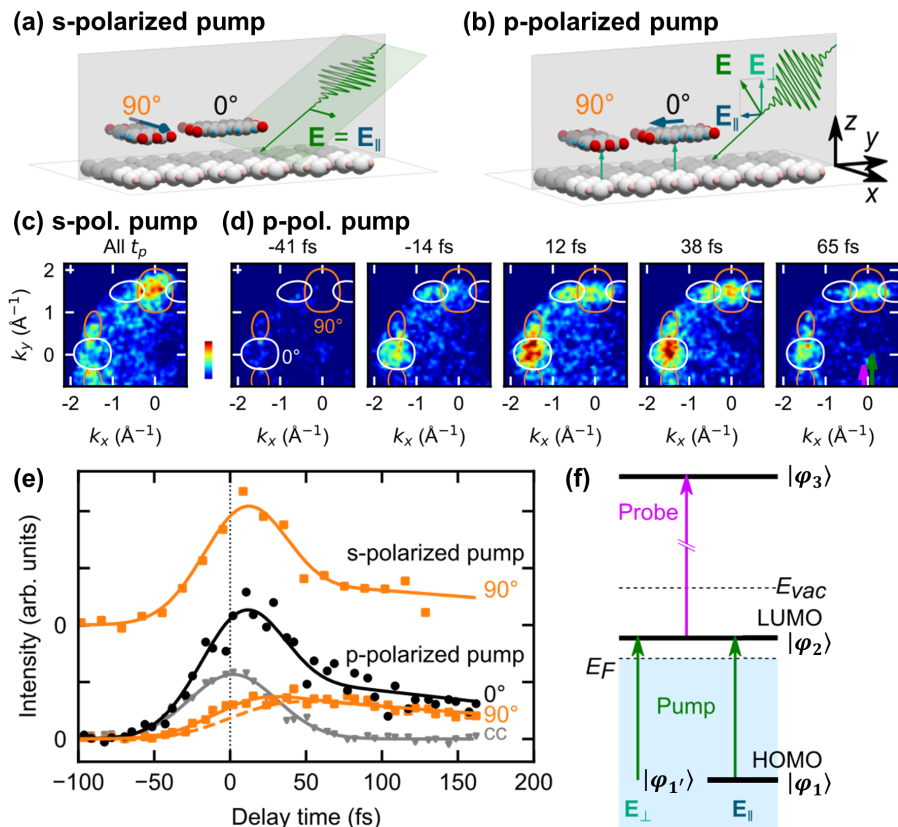


**Figure 5.12: Momentum-resolved LUMO dynamics for different excitation pathways.** (a) Schematic illustration of the experimental geometry for s- and (b) p-polarized pump pulse. (c) Momentum map integrated over all delay times  $t_p$  for an s-polarized pump pulse. The momentum map is overlaid by theoretical constant-intensity contours as expected for the  $0^\circ$  (white) and  $90^\circ$  molecules (orange). (d) Momentum maps for a p-polarized pump pulse at selected delay times. (e) Temporal evolution of the photoelectron intensity of the two LUMOs ( $0^\circ$ , black circles;  $90^\circ$ , orange squares) for s- and p-polarized pump pulses. Intensities are integrated within circular regions with a radius of  $0.2 \text{\AA}^{-1}$  centered within the main lobes of each molecular orientation. Solid lines indicate the best fit to the optical Bloch equations for the four-level system, see main text. The dashed orange line represents a completely incoherent excitation. It is obtained within the same model by setting the decoherence time to zero. Gray triangles show the cross-correlation (cc) of the pump and probe pulses. (f) Schematic representation of the four-level model used to fit the data in (e), with  $E_{vac}$  being the vacuum level. Fig. 5.12 adapted from Ref. [MR4]. Reprinted with permission from AAAS (see License Notice).

The different excitation dynamics for the two molecular orientations under s- and p-polarized excitation are illustrated by the orange (90° molecule) and black (0° molecule) data points in Fig. 5.12(e). Upon excitation with s-polarized light, the LUMO signal of the 90° molecule rose fast, reaching a pronounced maximum after  $\sim 15$  fs. At later times ( $t_p > \sim 75$  fs), it exhibits a slow decay with the time constant of  $T_1 \simeq 250$  fs (orange curve, top). As signal from the 0° molecule is absent in the momentum map for excitation with s-polarized light [see Fig. 5.12(c)], no data is displayed. For excitation with p-polarized light, the markedly different behavior for the two molecular orientations [see Fig. 5.12(e), bottom] is confirmed. Whereas the 0° molecule behaved similar to the 90° molecule under s-polarized excitation, the LUMO signal of the 90° molecule gradually built up over the duration of the pump pulse (compare with cc), reaching a less pronounced maximum at  $\sim 30$  fs. At later times, it exhibits the same slow decay with time constant  $T_1$  as for the 0° molecule.

Obviously, the question arises why these different excitation dynamics are observed. The possibility that a second excited state with different excitation dynamics than the LUMO is involved, can be excluded easily: The momentum maps of Fig. 5.12 show signal only from the LUMO and momentum maps at higher energies showed no involvement of another state for all delay times. Instead, the differences in the excitation dynamics indicate that there must be two distinct real-space excitation pathways of the electron in the sample before it is photoemitted: Electrons can be excited to the LUMO either from the HOMO or the metal substrate. As resulted from the measured excitation dynamics for the s-polarized pump pulse, excitation from the HOMO into the LUMO occurs only, when the polarization vector  $\mathbf{E}$  of the pump pulse exhibits a component  $\mathbf{E}_{\parallel}$  parallel to the long axis of the molecule. This is the case for 90° molecules under s-polarized pump and for 0° molecules under p-polarized pump, which show similar excitation dynamics in Fig. 5.12(e). As the 90° molecules under p-polarized pump do not meet this condition and show qualitatively different excitation dynamics, a second excitation pathway from the metal into the LUMO must be involved. The results for the p-polarized pump pulse indicate that this excitation pathway is only allowed if  $\mathbf{E}$  exhibits a component  $\mathbf{E}_{\perp}$  perpendicular to the sample surface.

Based on this picture, the present experiment is described by a four-level system as schematically illustrated in Fig. 5.12(f). It consists of the HOMO  $|\varphi_1\rangle$  and an occupied substrate state  $|\varphi_{1'}\rangle$  as initial states, the LUMO as intermediate state  $|\varphi_2\rangle$ , and the photoemission final state  $|\varphi_3\rangle$ . As the two different excitation channels are decoupled from each other, the problem can be reduced to solving two three-level systems with initial state  $|\varphi_g\rangle$  ( $= |\varphi_1\rangle$  or  $|\varphi_{1'}\rangle$ ), intermediate excited state  $|\varphi_e\rangle$  ( $= |\varphi_2\rangle$ ) and final photoelectron state  $|\varphi_f\rangle$  ( $= |\varphi_3\rangle$ ). In this way, the density matrix formalism and perturbation theory for a three-level system was applied to obtain the optical Bloch equations, as presented in Section 2.7.2. The parameters which are defined by the experimental pre-conditions were chosen adequately as provided in the supplement of Ref. [MR4]. This left the true dephasing time  $T_2^*$  of the molecular state (HOMO and LUMO are assumed to exhibit similar

dephasing) and the true dephasing time  $T_2^{*}$  of the metallic ground state as well as the overall intensity as free parameters. By solving the Bloch equations numerically and fitting the population  $n_3$  of the final state to the data points, the fitted curves in Fig. 5.12(e) were obtained.

### Interpretation of the fit results

In the perturbative description [cf. Sec. 2.7.2] of light-matter interaction, the pump pulse creates a coherent polarization between the ground state  $|\varphi_1\rangle$  or  $|\varphi_{1'}\rangle$  and excited state  $|\varphi_2\rangle$  in the first order of the electric field. In second order of the electric field, this polarization is converted into a population of the excited-state  $n_2$ . This conversion is governed by phase-destroying elastic scattering processes, which are quantified by the pure dephasing times  $T_2^*$  and  $T_2^{*}$ .

Fitting the intensity profile of the 90° molecule under p-polarized pump in Fig. 5.12(e), it was found that the data is described well with an extremely short true dephasing time  $T_2^{*} \simeq 3$  fs of the substrate state  $|\varphi_{1'}\rangle$ . In this limit, when dephasing is fast and the inelastic decay of the excited state's population is slow, the build-up of the intermediate state's population  $n_2$  follows the time-integrated intensity of the pump pulse. The field component  $\mathbf{E}_\perp$  drives a perpendicular electron motion between substrate and molecule. As the initial state  $|\varphi_{1'}\rangle$  is metallic and coupled to a bath, it dephases fast. Although this mechanism applies also to the 0° molecule under p-polarized pump, a competing process takes place (see below), such that the signature of the fast dephasing was only seen in the data for the 90° molecule.

Fitting the data of the 90° molecule under s-polarized pump in Fig. 5.12(e), a surprisingly long decoherence time  $T_2^{12}$  of more than 150 fs was found for the polarization between the molecular ground state  $|\varphi_1\rangle$  and the excited state  $|\varphi_2\rangle$ . This corresponds to a pure dephasing time  $T_2^* \simeq 490$  fs of the molecular state. As a consequence, dephasing is slow compared to the inelastic decay of the excited state's population. Therefore, the oscillating polarization between ground and excited state decays slowly. In this coherent regime, the interaction of the electric field of the probe pulse with the induced polarization between groundstate and excited state can contribute to the two-photon photoemission process for short delay times. In addition, if the driving pump laser is slightly detuned from the transition energy, the excited state can be populated and depopulated by the pump pulse. Both effects give rise to a pronounced peak in the photoemission signal, as observed in Fig. 5.12(e) for the 90° molecule excited with s-polarized light as well as for the 0° molecule excited with p-polarized light.

The existence of such a long-lived coherence in an electronic excitation at a metal surface is unexpected [232, 233]. It has previously only been observed for image-potential states with high quantum numbers where the electron is mainly located in the vacuum, tens of angstroms above the surface [232]. In the present experiment, this long coherence time can be rationalized by the fact that the pump pulse induced an in-plane oscillatory electron motion that is confined to the molecule: For both combinations, s-polarization-90° molecule and p-polarization-0° molecule, there is an electric field component along the long axis of the respective molecule [cf.

Fig. 5.12(e)], i.e., parallel to the HOMO-LUMO transition dipole, thus permitting an excitation directly from the HOMO  $|\varphi_1\rangle$  into the LUMO  $|\varphi_2\rangle$ . If the hybridization of the molecule with the metal beneath the oxide is negligible, which is also revealed by the long inelastic lifetime  $T_1$  measured for the LUMO, this spatial confinement of electron motion in the molecule explains the long coherence. The modeling thus suggests that for this excitation pathway, the emitted photoelectron can be traced back to the HOMO.<sup>5</sup>

## 5.4 Conclusion

Following molecular excitation and electron transfer processes in time and space within a single experiment is a long-standing goal of spectroscopy in the field of chemistry. In this chapter, a proof of principle tr-POT experiment was presented, which combines tomographic photoemission imaging with a femtosecond pump-probe scheme to trace the excited state molecular orbitals of surface-adsorbed molecules with both spatial and temporal resolution.

For the success of the experiment, the choice of a suitable sample system is of crucial importance. As few as possible molecular orientations with well distinguishable photoemission features are desired because only this makes it possible to unambiguously assign the orbital data directly to the molecular orientations. While the investigation of surface-adsorbed molecules (compared to gas phase molecules) allows a good alignment of the molecules, the strong interaction between the molecules and the metallic substrate results into excitation dynamics too fast to be observed in the tr-POT experiment. This problem was solved by introducing an ultrathin oxygen layer between the PTCDA molecules and the Cu(001) substrate which decouples them physically and electronically. Moreover, the submonolayer oxygen coverage provided a  $(\sqrt{2} \times 2\sqrt{2})R45^\circ\text{-}2\text{O}$  surface corrugation that imposed two clearly defined orthogonal orientations of PTCDA exhibiting well distinguishable HOMO and LUMO photoemission features.

Preliminary to the experiments, a preparation procedure for the described sample system was established to provide samples of high and reproducible quality on demand. Meanwhile, also the understanding of the formation process of the oxygen reconstruction and the different PTCDA adsorption structures reported in literature [189, 226] was deepened. Moreover, successful UHV transport of the prepared samples from the preparation setup in Jülich to the measurement setup in Marburg was demonstrated.

In a first tr-POT experiment, the measurement geometry was chosen to be symmetric, such that the two molecular orientations were excited under the same incident angle by the p-polarized pulse. Observing transiently occupied states of

---

<sup>5</sup>Note that for nonresonant excitation, the coherent interaction of pump and probe light can lead to the emission of photoelectrons from the HOMO in a true two-photon process without involving an intermediate state [232]. The observed momentum map, which in this experiment was that of the molecular LUMO  $|\varphi_2\rangle$  and not that of the HOMO  $|\varphi_1\rangle$ , however, provided clear experimental evidence that this was not the case here.

organic molecules for the first time, a surprisingly long lifetime  $T_1=250$  fs of these was found. This confirms the potency of the atomically thin oxide as a decoupling layer. Considering that chemical bonding and reaction dynamics at the molecular level are characterized by the fundamental molecular motions [234], a lifetime of 250 fs exceeds the time scale of typical vibrational motion and therefore, makes future time-resolved investigations of chemical bond breaking highly promising.

A different measurement geometry was chosen to exploit distinct real-space excitation pathways in a targeted manner. To describe the excitation dynamics of the system quantitatively, a quantum-mechanical four-level model was applied and its optical Bloch equations were solved. This made it possible to reveal surprisingly long-lived coherence in the electronic excitation of the molecules in contrast to extremely fast decoherence for the excitation from the metal into the molecule.

In conclusion, the present tr-POT experiment proves that the combination of photoemission tomography with laser pump-probe techniques is a highly promising tool for the future investigation of the ultrafast electron transfer dynamics in such processes as chemical reactions on surfaces and intermolecular charge transfers.



# Chapter 6

## Summary and Outlook

This work investigates the growth and excitation dynamics of 2D materials and molecular layers by means of electron and momentum microscopy. Chapters 3 and 4 focus on the first project, which studies the growth of BN on SiC(0001) under borazine exposure, and its replacement by graphene upon annealing in UHV at elevated temperatures. Building on the methodology of previous studies [MR5, 41, 52–54], this work aims to expand the understanding of the growth mechanisms involved. To this end, LEEM is employed to perform *in situ* growth experiments, and to study the different BN and graphene surface structures and their lateral domain configuration. The second project, discussed in Chapter 5, is dedicated to a proof-of-principle experiment that combines time-resolved 2PPE with photoemission orbital tomography. The realization of this experiment enables the observation of excitation dynamics of surface-adsorbed molecules in both time and momentum space for the first time.

### Growth of BN and graphene on SiC(0001)

The epitaxial growth of unconventionally oriented Gr- $R0^\circ$  on SiC(0001) presents a promising avenue for the large-scale, high-quality production of  $30^\circ$ -twisted bilayer graphene. The key to preparing unconventionally oriented Gr- $R0^\circ$  is the exposure of a  $(3\times 3)$ -Si reconstructed SiC(0001) surface to borazine at elevated temperatures. An important step in understanding the formation of Gr- $R0^\circ$  on SiC(0001) is BN growth at temperatures below  $1050^\circ$ , as discussed in Chapter 3.

The growth of BN on SiC(0001) is found to be more complex than expected. The necessary reactivity for CVD growth is produced not only by elevated temperatures directly, but also indirectly, by the surface's structural change upon Si sublimation. As a result, BN does not grow on a Si-rich surface reconstruction, contrary to previous hypotheses [MR5, 52]. Instead, it starts to grow only when the Si-rich surface reconstruction and crystalline Si agglomerations have vanished from the SiC(0001) surface. During BN growth, step retraction occurs due to thermal decomposition of SiC. This process, as well as BN growth, is self-terminating once the surface is completely covered by one BN layer.

Three different structures are found to form on the SiC(0001) surface during BN growth:  $B_xN_y$ - $R0^\circ$ , a  $(\sqrt{7}\times\sqrt{7})$ - $R19.1^\circ$  surface reconstruction, and a misoriented minority phase. However, only the growth of the  $(\sqrt{7}\times\sqrt{7})$ - $R19.1^\circ$  reconstruction

via nucleation and island growth has been directly observed in LEEM mode. It forms compact islands that are randomly distributed on the SiC terraces and do not cross step edges. The dominant surface phase is  $B_xN_y-R0^\circ$ . It starts growing almost simultaneously with the  $(\sqrt{7} \times \sqrt{7})-R19.1^\circ$  surface reconstruction; however, its formation could not be observed in LEEM mode. This suggests growth by a uniform and continuous transformation of the surface on a size scale that is too small to resolve. Eventually,  $B_xN_y-R0^\circ$  uniformly covers the SiC terraces with one fixed adsorption configuration. After BN growth, the misoriented minority phase is identified. Presumably consisting of either BN or graphene, it appears as nm-sized domains randomly distributed across the  $B_xN_y-R0^\circ$ -covered terraces.

It has been demonstrated that by increasing the heating rate during BN growth, the ratio of surface phases is shifted in favor of the desired surface phase  $B_xN_y-R0^\circ$ . This also enhances the structural quality of  $B_xN_y-R0^\circ$ .

Following the template-induced growth route, the replacement of BN by graphene upon annealing in UHV is studied in Chapter 4. During this process, the lateral domain configuration of the BN surface phases is found to remain unchanged.  $B_xN_y-R0^\circ$  transforms continuously into  $Gr-R0^\circ$ , supporting the assumption that B and N atoms are gradually replaced by C atoms that originate from the decomposing SiC surface. In a similar scheme, the  $(\sqrt{7} \times \sqrt{7})-R19.1^\circ$  reconstruction is replaced by monolayer graphene that consists of both  $Gr-R0^\circ$  and  $Gr-R30^\circ$ , which are found to reside laterally next to each other in fragments below the LEEM instrument's resolution limit. A region that had not been covered by BN during borazine exposure was found to give rise to conventional  $Gr-R30^\circ$  multilayer growth. The misoriented minority phase remains present as nm-sized point-like graphene domains. Consequently,  $B_xN_y-R0^\circ$  is the only template that produces  $Gr-R0^\circ$ . In this way, it is demonstrated how the inhomogeneity of the BN template affects the quality of the  $Gr-R0^\circ$  layer.

Sufficiently high and long annealing can result in conventional sublimation growth of  $Gr-R30^\circ$  at the interface of  $Gr-R0^\circ$  and SiC. This process depends not only on the annealing temperature and duration but also on the sample's morphology and the structural quality of the  $Gr-R0^\circ$  layer. A  $B_xN_y-R0^\circ$  template prepared at a higher heating rate evolves into a  $Gr-R0^\circ$  layer that effectively protects the underlying SiC terraces from further graphitization, even during prolonged annealing at 1250°C. First indications of bilayer formation are mainly found at step edges that are more than one SiC bilayer high. In contrast, a  $B_xN_y-R0^\circ$  template prepared at a lower heating rate evolves into a  $Gr-R0^\circ$  layer that appears to be highly permeable to Si sublimation. As a result,  $B_xN_y-R0^\circ$  is replaced by 30°-twisted bilayer graphene of uniform thickness, albeit low structural quality, already after short annealing at 1250°C.

In conclusion, this work demonstrates how the inhomogeneity and reduced structural quality of the  $B_xN_y-R0^\circ$  template are inherited by  $Gr-R0^\circ$ , thereby limiting its quality as well as that of the resulting 30-tBLG. It also emphasizes the importance of silicon-rich starting conditions and a fast heating rate during preparation of the BN layer for template-induced growth of  $Gr-R0^\circ$ .

While the graphitization process of the BN template in UHV is rather well understood, the same cannot be said for Gr- $R0^\circ$  growth on SiC via the surfactant-mediated growth method. This method is of particular interest, since it yields higher-quality, more homogeneous samples compared to the template-induced method [53]. In this dynamic approach, the  $(3 \times 3)$ -Si reconstructed SiC(0001) surface is prepared at  $880^\circ\text{C}$  and heated directly in borazine to temperatures at which Gr- $R0^\circ$  grows. Bocquet et al. [53] assume that the  $\text{B}_x\text{N}_y$ - $R0^\circ$  layer does not stabilize in this process, thereby eliminating the intermediate stage of template growth that limits quality. However, the question remains of how the unconventional Gr- $R0^\circ$  orientation would be induced in this scenario. One reasonable explanation could be the transient formation of a metastable  $\text{B}_x\text{N}_y$ - $R0^\circ$  phase that defines the orientation.

Thus far, surfactant-mediated growth has not been observed *in situ* and in real time. Therefore, it should first be clarified whether Gr- $R0^\circ$  really forms without the intermediate stage of  $\text{B}_x\text{N}_y$ - $R0^\circ$ . To this end, a  $(3 \times 3)$ -Si reconstructed SiC(0001) surface could be heated in borazine while the LEED signal is detected *in situ* and in real time. This experiment could also shed more light on the growth behavior of  $\text{B}_x\text{N}_y$ - $R0^\circ$ .

For the goal of producing  $30^\circ$ -tBLG on SiC(0001), the next step is to obtain a single layer of Gr- $R30^\circ$  underneath a high-quality Gr- $R0^\circ$  layer. Two approaches have been suggested, either further annealing of Gr- $R0^\circ$ /ZLG- $R30^\circ$ /SiC(0001) in UHV or hydrogen intercalation of the ZLG- $R30^\circ$  underneath Gr- $R0^\circ$  [41]. The present work shows that graphitization is strongly inhibited underneath a Gr- $R0^\circ$  layer of reasonable quality at temperatures below  $1250^\circ\text{C}$ . Furthermore, higher annealing temperatures promote multilayer growth before a bilayer can fully spread [54]. Therefore, intercalation of the ZLG- $R30^\circ$  layer at the interface of Gr- $R0^\circ$  and SiC is considered a more promising approach for obtaining large-scale, high-quality  $30^\circ$ -tBLG on SiC(0001). Work in this direction is further pursued by Hao Yin as part of his PhD thesis [235].

## Electron dynamics of molecular orbitals in time and space

Chapter 5 presents a proof-of-principle tr-POT experiment. It combines tomographic photoemission imaging at high parallel momenta with a femtosecond pump-probe scheme. Thereby, the full momentum-space distribution of transiently occupied molecular orbitals of surface-adsorbed molecules is traced for the first time with both spatial and temporal resolution. The proof-of-principle tr-POT experiment was realized through a fruitful collaboration of the research groups of U. Höfer from Philipps-Universität Marburg, F. S. Tautz from Forschungszentrum Jülich, and P. Puschnig from University of Graz. The primary contribution of this work, which was conducted at Forschungszentrum Jülich, was providing high-quality, reproducible samples on demand.

For the experiment to be successful, selecting a suitable sample system was crucial. Although growing molecular layers on metallic surfaces allows for good

molecular alignment, the strong interaction between the molecules and the metallic substrate results in excitation dynamics that are too fast to be observed in the tr-POT experiment. This problem was solved by passivating the Cu(001) surface with an ultrathin layer of oxygen prior to depositing the PTCDA molecules, which physically and electronically decoupled the molecules from the substrate. Additionally, the submonolayer oxygen coverage provides a  $(\sqrt{2} \times 2\sqrt{2})R45^\circ$ -2O surface corrugation, which imposes two clearly defined, orthogonal orientations of PTCDA. These orientations exhibit well distinguishable HOMO and LUMO photoemission features, which is a necessary prerequisite for unambiguously assigning orbital data to molecular orientations.

The samples were transported in UHV to the tr-POT setup, operated by the group of U. Höfer at the Philipps-Universität Marburg. In a first experiment, the transiently occupied LUMO of PTCDA was observed in both time and momentum space for the first time. With 250 fs the lifetime of the excited state was found to be unexpectedly long, thereby confirming the effectiveness of the atomically thin oxide as a decoupling layer. In a second tr-POT experiment, distinct real-space excitation pathways were exploited in a targeted manner. A quantum-mechanical four-level model was applied and its optical Bloch equations were solved to describe the excitation dynamics of the system quantitatively. This revealed surprisingly long-lived coherence in the electronic excitation of the molecules, contrasting the extremely fast decoherence found for excitation from the metal to the molecule.

The ability to investigate molecular excitation and electron transfer processes with both temporal and spatial resolution in a single experiment has long been a goal of spectroscopic research in chemistry. In this context, the successful realization of the proof-of-principle tr-POT experiment presented in this work is an important breakthrough with the potential to greatly enhance our understanding of the nanocosmos. In the future, tr-POT may provide unique insight into the inner structure of quantum leaps, strong-field control of electrons, charge transfer processes, and chemical reactions, as well as their control by electric fields and light [236]. A promising follow-up experiment to the present work is the investigation of charge transfer processes in more complex systems. An investigation that has been already started is the charge transfer across an organic heterointerface, consisting of two layers of different molecular species. With PTCDA being a well-characterized molecule, a potential candidate for the second molecular species is copper phthalocyanine (CuPc). From literature, it is known that an ordered layer of CuPc can be grown on PTCDA/Ag(111) [237]. In a first step, CuPc has already been prepared as an ordered monolayer on the Cu(001)-MR-2O surface and studied with tr-POT [MR7] in the aftermath of the presented work. The realization of this and other tr-POT experiments is being pursued by the groups of F. S. Tautz (Forschungszentrum Jülich), U. Höfer (Universität Regensburg), R. Huber (Universität Regensburg) and P. Puschnig (University of Graz). Their joint project “Photoemission Orbital Cinematography: An ultrafast wave function lab” (short: “Orbital Cinema” [236]) was awarded a major Synergy Grant by the European Research Council (ERC) in 2022 [238].





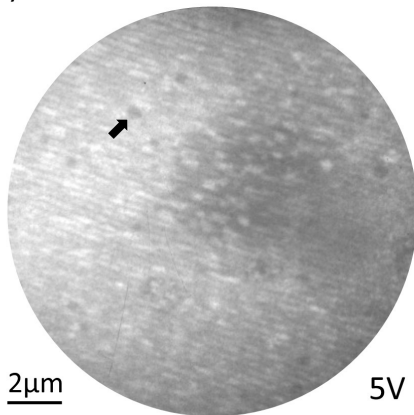
## Appendix A

# Challenges in LEEM Imaging at High Sample Temperatures

During annealing of SiC samples at high temperatures two effects were encountered, that lead to an impairment in LEEM imaging. In the following, these effects and countermeasures are discussed in more detail.

The first effect addressed is a blurring of the LEEM image, which is observed at temperatures above  $\sim 1100^\circ\text{C}$  and independent of the annealing time. Fig. A.1(a) illustrates this effect on the example of a LEEM image of BN on Sample 1 taken at an annealing temperature of  $1230^\circ\text{C}$ . Compared to LEEM images taken during BN growth at temperatures up to  $\sim 1000^\circ\text{C}$  [cf. Fig. 3.8], the image is blurred such that islands and terraces are barely recognizable. The described effect can be attributed to thermally emitted electrons. An easily applicable countermeasure to block these electrons is to introduce the energy slit (ES) into the electronic beam path (for details on the LEEM electron optics refer to Section 2.3.1). Fig. A.1(b) demonstrates the effect on the LEEM image when introducing the largest

(a) LEEM at  $1230^\circ\text{C}$  without ES



(b) LEEM at  $1230^\circ\text{C}$  with largest ES

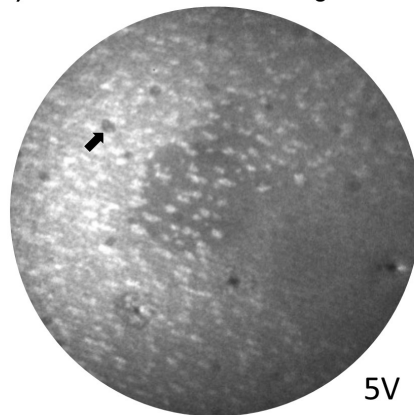


**Figure A.1: Thermal electrons.** LEEM images of Sample 1 at  $\sim 1230^\circ\text{C}$ , taken (a) without energy slit and (b) with energy slit. A black arrow marks a characteristic object in both images.

Contrast Aperture (diameter in $\mu\text{m}$ )	Energy Slit (width in $\mu\text{eV}$ )
1000	60 (1 eV)
70	25 (0.4 eV)
60	12.5 (0.2 eV)
50	
30	
25	
10	

**Table A.1: Available contrast apertures and energy slits at the AC-SPELEEM.** The apertures are sorted by their size from large to small. The energetic resolution of the respective energy slits is given in brackets.

ES into the beam path (see Table A.1 for technical details on the available energy slits). The contrast between islands and terraces has significantly improved, and the image is less blurred compared to Fig. A.1(a).

A second effect complicates in situ LEEM imaging when the annealing time is sufficiently long. Note that this effect may also be encountered at temperatures below those at which blurring due to the thermal emission of electrons becomes noticeable. This effect is illustrated in Fig. A.2(a), which shows a LEEM image of Sample 1 during BN growth. The sample was slowly heated to  $\sim 1000^\circ\text{C}$  and held at that temperature for  $\sim 20$  min before the image was recorded. At the bottom left, a segment of the LEEM image appears dark. As annealing continues, the border between bright and dark areas moves in the direction of the white arrow. Consequently, the dark segment gradually enlarges, obscuring more of the LEEM image.

It was found that the border between the bright and dark areas in Fig. A.2(a) is actually the edge of the electron beam spot on the surface. The LEEM images presented in this work thus far have been taken at a field of view (FoV) of  $30 \mu\text{m}$  or smaller, where the entire FoV is illuminated by the electron beam. At a larger FoV, the electron beam spot profile becomes visible, as illustrated in Fig. A.2(b). The image depicts an alignment sample illuminated by both the mercury lamp and the electron beam. The image was taken at a FoV of  $100 \mu\text{m}$ , in which the electron beam's profile is recognizable as an oval-shaped bright spot with a diameter of  $\sim 70\text{-}90 \mu\text{m}$ . For well-aligned LEEM optics, the electron beam is centered within the FoV. However, with prolonged annealing at sufficiently high temperatures, the electron spot slowly slides off center. This occurs because the thermal radiation from the sample heats up the objective lens, which is positioned only a few millimeters away. Due to thermal expansion, the objective lens's optical properties change, deflecting the electron beam away from the original alignment.

To maintain good imaging quality throughout the experiment, it is important to avoid shadowing the LEEM image due to the aforementioned effect. However, thermal expansion of the objective lens due to heating the sample is inevitable

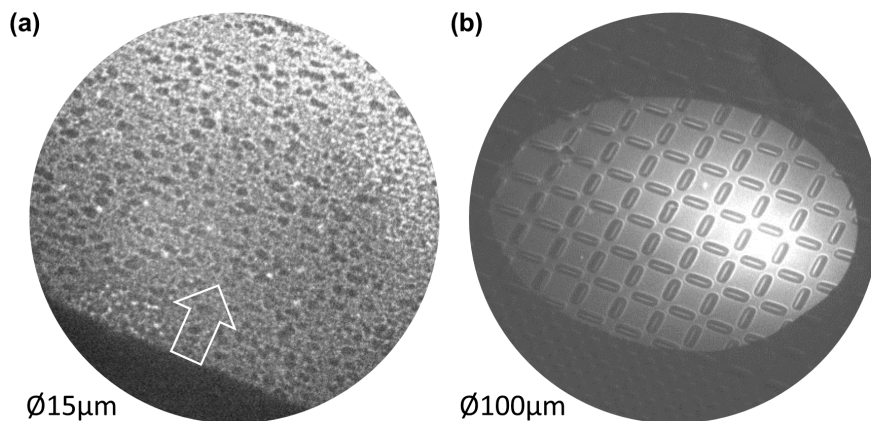


**Figure A.2: Spot profile of the electron beam.** (a) LEEM image of Sample 1 after prolonged annealing at  $\sim 1000^\circ\text{C}$ . The white arrow indicates the movement of the edge of the electron beam profile with increasing duration of annealing. (b) Image of an alignment sample, illuminated with electron beam and mercury lamp at a field of view of  $100\ \mu\text{m}$ .

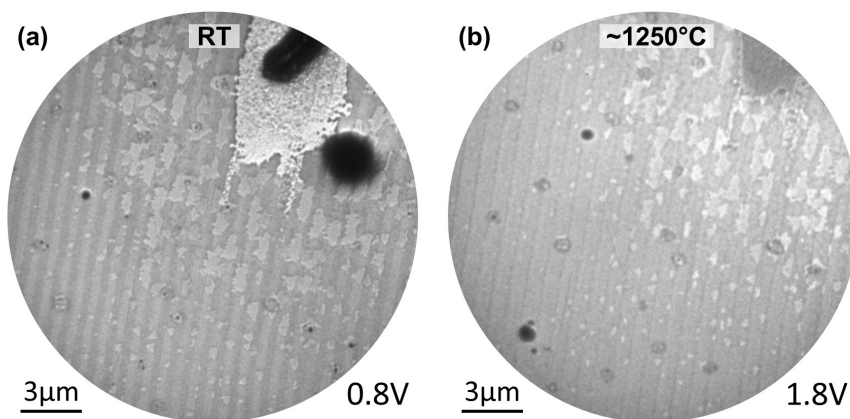


**Figure A.3: LEEM imaging at high T with optimized settings.** (a) Image of Sample 2 at room temperature, prior to annealing. (b) LEEM image of Sample 2 annealed at  $\sim 1250^\circ\text{C}$ .

during in situ LEEM studies. One option would be to adjust the alignment during the experiment, but this would significantly complicate the experimental procedure. Therefore, an intentional misalignment of the electron beam was introduced prior to the experiment. To this end, the deflectors in the imaging column were used to deflect the electron beam in the opposite direction from that in which it moves when the objective lens heats up. This significantly delayed the shadowing of the LEEM image during an annealing experiment.

In the course of the experiments conducted for this work, the countermeasures against the aforementioned effects were further refined. Good and still practical LEEM imaging was established by intentionally misaligning the electron beam before the experiment, using the medium-size energy slit to block thermally emitted electrons, and using the second smallest contrast aperture (CA) to enhance lateral resolution (see Table A.1 for technical details on the available energy slits and contrast apertures). Fig. A.3 illustrates the effect of these optimized settings. Panels (a) and (b) show images of the surface of Sample 2 taken at room temperature and at  $\sim 1250^\circ$ , respectively. Good imaging is maintained, only slight blurring is observed, and no shadowing occurs by the deflection of the electron beam.

Although the improved settings in general enable for proper imaging at high temperatures, they make in situ LEEM measurements more complicated. First of all, using the CA makes switching between LEEM and LEED modes more time-consuming. Additionally, the positions of both CA and ES require readjustment due to the steady change in alignment caused by the thermal expansion of the objective lens. Finally, the use of CA and ES reduces the overall intensity.

## Appendix B

# Second Layer Formation of PTCDA Deposited on Ag(110)

Here, the discrepancy between the measured LEED pattern in this work and the simulated LEED pattern proposed by Willenbockel et al. [167] is discussed, which was found for two layers of PTCDA deposited on Ag(110) at room temperature. For clarification, the measured and simulated LEED patterns of Willenbockel et al. and this work are reproduced from Ref. [167] and Fig. 5.3, respectively, and compared in Fig. B.1. The LEED measurement in this work [cf. Fig. B.1 (b)] exhibits double spots for the second layer PTCDA structure where the simulated pattern by Willenbockel et al. [cf. Fig. B.1 (c)] suggests single spots. Since the double spots appear only for the second layer PTCDA spots and the measured pattern still exhibits  $90^\circ$  rotational symmetry, the spots are not artifacts. A closer look at the zoomed insets of Fig. B.1 (a) and (b) shows that both measurements are indeed in good agreement: The features of the second PTCDA layer that were identified as single spots by Willenbockel et al. are blurred, but their shape is elongated and similar to the double spot features observed in this work. Only the higher resolution in the latter reveals that these features consist of two spots that are very close to each other. Therefore, both measurements cannot be correctly described by a single herringbone structure with the matrix  $(-\frac{2}{3.3} \frac{3}{5})$ , as proposed by Willenbockel et al. [167]. Based on the latter, a corrected structure model is presented in Fig. B.1 (d): By preserving the size and dimensions of the unit cell and rotating it by  $2.5^\circ$  (light blue) and  $-2.5^\circ$  (dark blue), the double spots are reproduced.

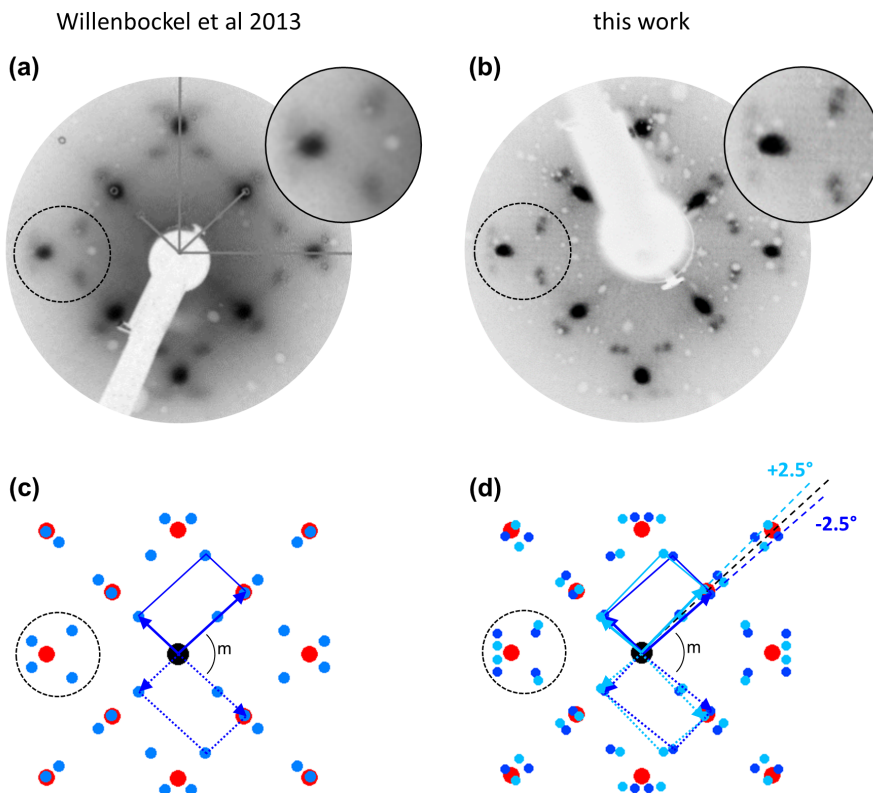


**Figure B.1:** Measured and simulated LEED images of the PTCDA bilayer structure on Ag(110). (a,c) LEED measurement at 19 eV and simulated LEED pattern as proposed by Willenbockel et al. [167]. Fig. B.1(a) adapted from Ref. [167], licensed under CC-BY 3.0. (b,d) LEED measurement at 16 eV and simulated LEED pattern within this work. The spots of the first layer PTCDA with brickwall structure are colored in red, the spots of the second PTCDA layer are colored in shades of blue. The reciprocal unit cells are shown as rectangles, the unit cells of the corresponding mirror domains as dashed lines.

## Appendix C

# Review: The Oxygen Reconstruction of the Cu(001) Surface

Since ion bombardment and subsequent annealing emerged in the 1950s as the standard surface cleaning procedure for LEED studies of metallic crystalline surfaces [239, 240], the oxygen reconstruction of the Cu(001) surface has been frequently studied and debated in the literature [82, 196–198, 200, 203, 205–223]. In particular, the observation of different oxygen adsorption structures was a point of discussion. Throughout many LEED studies in the 1960s and 1970s (e.g., [196–198, 200]), the existence of three different oxygen surface reconstructions was reported. These are identified by their characteristic LEED patterns, displayed schematically in Fig. C.1:

- A  $c(2 \times 2)$  pattern, which is also described by the primitive  $(\sqrt{2} \times \sqrt{2}) - R45^\circ$  unit cell [see Fig. C.1(b)].
- A so-called “4-spot” pattern, characterized by groups of four spots that appear instead of the half-order spot of the  $c(2 \times 2)$  pattern [see Fig. C.1(c)].
- The  $(\sqrt{2} \times 2\sqrt{2}) - R45^\circ$  pattern of the Cu(001)-MR-2O (missing-row) reconstruction with a rectangular real-space unit cell twice the size of the primitive  $(\sqrt{2} \times \sqrt{2}) - R45^\circ$  unit cell of the  $c(2 \times 2)$  structure [see Fig. C.1(d)].

The  $c(2 \times 2)$  pattern and the “4-spot” pattern have been reported to appear as pre-stages to the Cu(001)-MR-2O structure at an oxygen coverage of  $\theta_O < 0.5$ . Either only the  $c(2 \times 2)$  pattern [198, 206], or only the “4-spot” pattern [196, 197] or both of them were observed sequentially [200]. In other works, a disordered phase has been found as the only pre-stage to the Cu(001)-MR-2O reconstruction [205, 208, 211]. The experimental conditions under which these different structures were observed did not complement each other well. It is important to consider that different experimental setups may use different instrumentation and position it differently in the preparation chamber. This makes it difficult to quantitatively compare preparation parameters and resulting surface structures, even when the preparation procedures and parameters appear similar. Eventually, contamination of the experimental chamber or the sample surface may also play a role and cannot be excluded.

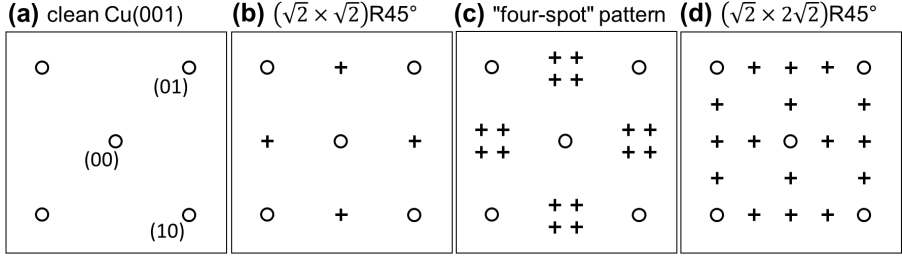


**Figure C.1: Schematic LEED patterns of different oxygen induced reconstructions of the Cu(001) surface.** Schematic LEED patterns of (a) the clean Cu(001) surface, (b) the “4-spot” pattern, (c) the  $c(2 \times 2)$  or  $(\sqrt{2} \times \sqrt{2}) - R45^\circ$  pattern, and (d) the  $(\sqrt{2} \times 2\sqrt{2}) - R45^\circ$  pattern Schematics in (a-d) based on Ref. [200].

Despite disagreement on the exact experimental conditions that lead to the respective oxygen reconstruction pre-stages, there is agreement on the following points:

- Overall, the  $c(2 \times 2)$  structure and the “4-spot” structure are accessible mainly for a combination of relatively low oxygen exposure and low preparation temperature [82, 200, 210, 217, 218]. Another way to obtain the  $c(2 \times 2)$  structure or the “4-spot” structure is to start with a Cu(001)-MR-2O reconstructed Cu(001) surface. The sample is then treated without oxygen exposure either by prolonged annealing [200] or by a combined process of bombardment with  $\sim 50\mu\text{C}$  of  $\sim 350\text{-eV}$   $\text{Ar}^+$  ions<sup>1</sup> and subsequent annealing [217].
- At saturation coverage  $\theta_O = 0.5$ , oxygen atoms occupy every second hollow-site on the Cu(001) surface, and in the topmost Cu layer a quarter of the Cu atoms are missing, forming the Cu(001)-MR-2O missing-row reconstruction.
- The oxygen reconstruction of the Cu(001) surface is a self-terminating process. At the beginning of the oxygen exposure, the sticking coefficient is large and the coverage increases rapidly. With increasing coverage, the sticking coefficient decreases such that it asymptotically approaches the saturation coverage of  $\theta_O = 0.5$ . [208, 221]
- The higher  $T_{O_2}^{\text{sample}}$ , the sample’s temperature during oxygen exposure, the lower the dosage required to obtain an oxygen saturated surface [200, 208, 221]. For a fixed  $T_{O_2}^{\text{sample}}$ , the characteristic dosage to obtain the Cu(001)-MR-2O structure is independent of the pressure [200].

<sup>1</sup>Note that for  $\text{Ar}^+$  sputtering during metal surface cleaning procedures, the parameters are typically in the order of  $\sim 1\text{mC}$  and  $1\text{-}2\text{keV}$ .

In the following, additional information on the structure and formation of the  $c(2 \times 2)$  structure and the “4-spot” structure is provided. For a detailed description of the structure of the Cu(001)-MR-2O reconstruction and its formation process, refer to Section 5.2.4. Finally, the order-disorder phase transition of the Cu(001)-MR-2O structure at elevated  $T_{O_2}^{sample}$  is discussed.

## The $c(2 \times 2)$ oxygen reconstruction and the “4-spot” pattern

The  $c(2 \times 2)$  pattern is frequently reported for oxygen reconstructed Cu(001) surfaces [82, 198–202, 204, 213]. In an idealized structure model of the  $c(2 \times 2)$  structure, the oxygen atoms would occupy every second hollow site on the Cu(001) surface, such that the surface is saturated for an oxygen coverage of  $\theta_O = 0.5$  as shown in Fig. C.2(a). However, in all experiments the  $(\sqrt{2} \times 2\sqrt{2}) - R45^\circ$  pattern of the Cu(001)-MR-2O reconstruction is observed when the coverage approaches  $\theta_O = 0.5$  [cf. Fig. 5.4]. Initiated by Mayer et al. [205] in 1986, the idea that the  $c(2 \times 2)$  structure does not exist on the Cu(001) surface became popular: Several works reported clear evidence for a disordered phase being the only pre-stage for  $\theta_O < 0.3$  and coexisting with the Cu(001)-MR-2O structure for  $0.3 \simeq \theta_O < 0.5$ , independent of the preparation temperature [205, 208, 211]. Because the LEED spots of the  $c(2 \times 2)$  structure represent a subset of the LEED spots of the Cu(001)-MR-2O reconstruction, it was concluded that LEED measurements of low quality Cu(001)-MR-2O structures were misinterpreted as  $c(2 \times 2)$ [210].

This conclusion demanded a more convincing proof of the existence of the  $c(2 \times 2)$  structure, which was provided, for example, by the STM study by Fujita et al. in 1996 [217]. Fig. C.2(b) displays a schematic structure model of a realistic  $c(2 \times 2)$  adsorption configuration, based on STM measurements of Fujita et al. [217]. The estimated local coverage is  $\theta_O \approx 0.16$ . The oxygen atoms occupy hollow sites on the Cu(001) surface and thus locally form a  $c(2 \times 2)$  structure. However, the domains are very small and larger areas of the Cu(001) surface remain uncovered. Due to the surface registry, two anti-phase  $c(2 \times 2)$  domains occur: Both the phase A domains (red oxygen atoms and unit cells) and the phase B domains (magenta oxygen atoms and unit cells) show the same fourfold symmetry and fulfill the rule that only every second hollow site of the Cu(001) surface is occupied by oxygen atoms. A unit cell of phase A can be transformed into a unit cell of phase B by translating it by one substrate lattice vector (the unit cell of the substrate is indicated in black). As the occupation of directly neighboring hollow sites is forbidden, domain boundaries between phase A and phase B domains of minimum width  $\sqrt{2}a_0$  are formed, where  $a_0$  is the lattice constant of the Cu(001) surface.

Experimentally observed  $c(2 \times 2)$  LEED spots are often described as diffuse and weak in intensity, as is the case for the LEED measurement by Scheidt et al. [82], displayed in Fig. C.2(d). This can easily be attributed to the low coverage and small domain size at which the  $c(2 \times 2)$  structure occurs. Additionally, an

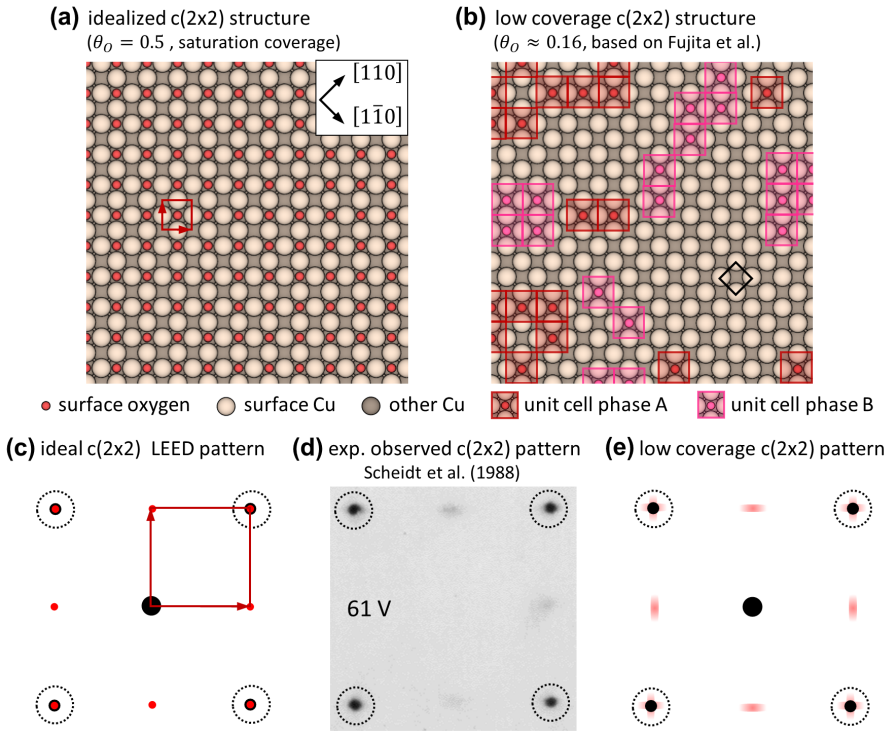


**Figure C.2: Structure of the  $c(2 \times 2)$  oxygen surface reconstruction.**

(a) Idealized  $c(2 \times 2)$  adsorption structure for saturation coverage  $\theta_O = 0.5$  with oxygen atoms occupying every second hollow site. The unit cell of the  $c(2 \times 2)$  structure is indicated in red. (b) Schematic structure model of a realistic  $c(2 \times 2)$  adsorption configuration, based on STM measurements of a  $c(2 \times 2)$  reconstructed Cu(001) surface with a local oxygen coverage of  $\theta_O \sim 0.16$  by Fujita et al. [217]. The unit cell of Cu(001) is marked with a black square. Due to the surface registry, two anti-phase domains of the  $c(2 \times 2)$  structure occur. These are highlighted in red (phase A) and magenta (phase B). For the original STM data, please refer to Fujita et al. [217]. (c) Simulated LEED pattern, as expected for the idealized  $c(2 \times 2)$  surface structure depicted in (a). (d) LEED pattern with faint  $(\frac{1}{2}\frac{1}{2})$  spots, as measured by Scheidt et al. [82] for oxygen-reconstructed Cu(001) with  $\theta_O < 0.5$ . The LEED spots are broad and of low intensity, most likely due to small domain size and low coverage. The elongated shape of the half-order spots can be attributed to anti-phase domain boundaries [204]. Panel (d) adapted from Ref. [82], © 1988, with permission from Elsevier. See License Notice. (e) Simulated LEED pattern of a realistic  $c(2 \times 2)$  adsorption configuration at low oxygen coverages such as suggested in panel (b). Based on Ref. [204].

elongation of the 1/2-order LEED spots perpendicular to the  $\langle 100 \rangle$  directions is observed. Generally, the elongation, broadening, or splitting of certain adsorbate LEED spots is caused by either anti-phase scattering from atomic steps that are misaligned with respect to the vicinal high-symmetry plane or anti-phase domains of the adsorbate. In the case of the  $c(2 \times 2)$  structure, the latter was found to be true [82, 204].

In the following, the effect of anti-phase domains on the LEED pattern, as introduced in Sec. 2.2.3, is discussed for the  $c(2 \times 2)$  reconstruction of Cu(001) and based on the work of Richter et al.[204]. In a simplified, one-dimensional picture, the periodicity of the  $c(2 \times 2)$  reconstruction is described by the distance  $a$  between two oxygen atoms, which leads to the appearance of first-order reflections for a momentum transfer of  $\Delta k = G_1 = \frac{2\pi}{a}$ . A periodic arrangement of alternating anti-phase domains of the  $c(2 \times 2)$  reconstruction with a length scale of  $d$  in one dimension results in anti-phase scattering. This means that the scattering amplitude vanishes at  $\Delta k = G_1$ , but scattering intensity appears at  $\Delta k = G_1 \pm \delta k = G_1 \pm \frac{\pi}{d}$ . Thus, the first-order reflection splits into two spots, separated by  $2\pi/d$ . Since LEED averages over an extended surface region, statistical variation in the size  $d$  will result in an elongation of the 1/2-order spot. Additionally, the total scattering amplitude is not zero at  $\Delta k = G_1$  because it includes in-phase contributions from the substrate [204]. Going back to the two-dimensional picture, the (10)-spot and the symmetrical equivalent spots suffer from anti-phase scattering for both the [100] and [010] directions. Therefore, they have a cross-like shape, as illustrated by the simulated LEED pattern in Fig. C.2(e).

The formation of ordered anti-phase domain structures is also believed to be the origin of the “4-spot” pattern [82, 200, 217]. Fig. C.3(a) presents a structure model of an oxygen reconstructed Cu(001) surface, based on STM measurements by Fujita et al. [217] for an estimated local oxygen coverage of  $\theta_O \approx 0.31$ . At this increased coverage, Fujita et al. observed that in  $c(2 \times 2)$  reconstructed surface areas, the anti-phase domains are preferentially arranged in such a way that sawtooth-shaped domain boundaries form along the  $\langle 110 \rangle$  directions [217]. Perpendicular to the phase boundaries, the domains are typically only one to two oxygen adsorption sites wide. Along the  $\langle 110 \rangle$  directions and perpendicular to the direction of the sawtooth-shaped domain boundaries, a periodic arrangement with a single distinct length scale  $d = 6a_0$  is found. Based on this structure model and the previously introduced effect of LEED spot splitting, the “4-spot” pattern in Fig. C.3(b) is derived. The substrate spots of the Cu(001) surface appear at distances  $G_0 = \frac{2\pi}{a_0}$  from the 00-spot along the  $\langle 110 \rangle$  directions. The  $c(2 \times 2)$  unit cell is spanned by unit vectors along the  $\langle 100 \rangle$  directions and length of  $G_1 = \frac{2\pi}{a}$ , with  $a = \sqrt{2}a_0$ . The periodic arrangement of the  $c(2 \times 2)$  anti-phase domains  $d$  along the  $\langle 110 \rangle$  directions results into a splitting of the  $c(2 \times 2)$  spots with  $\delta k = \frac{2\pi}{d} = \frac{2\pi}{6a_0}$  in the respective directions. Note that, in LEED measurements reported in literature (e.g. in the works of Fujita et al. [217] and Scheidt et al. [82]), the spots of the “4-spot” pattern are typically diffuse and of low intensity compared to the substrate’s first-order diffraction spots.

Appendix C Review: The Oxygen Reconstruction of the Cu(001) Surface

The STM data presented by Fujita et al. [217] also shows that  $c(2 \times 2)$  domains coexist with Cu(001)-MR-2O domains at oxygen exposures as low as 8 L ( $1 \times 10^{-7}$  Torr for 80 s) at  $\sim 180^\circ\text{C}$ . Due to the generally low structural quality of both the  $c(2 \times 2)$  and the “4-spot” structures, as well as the difficulty of producing samples with homogeneous  $c(2 \times 2)$  or “4-spot” surface structure, there is little interest in these two intermediate surface structures compared to the Cu(001)-MR-2O reconstruction. Nevertheless, these structures are important for understanding the formation mechanism of the desired Cu(001)-MR-2O reconstruction. When measurement techniques are employed that average over large areas, such as LEED, it is important to consider that less well-ordered  $c(2 \times 2)$  domains may coexist locally with the Cu(001)-MR-2O reconstruction.

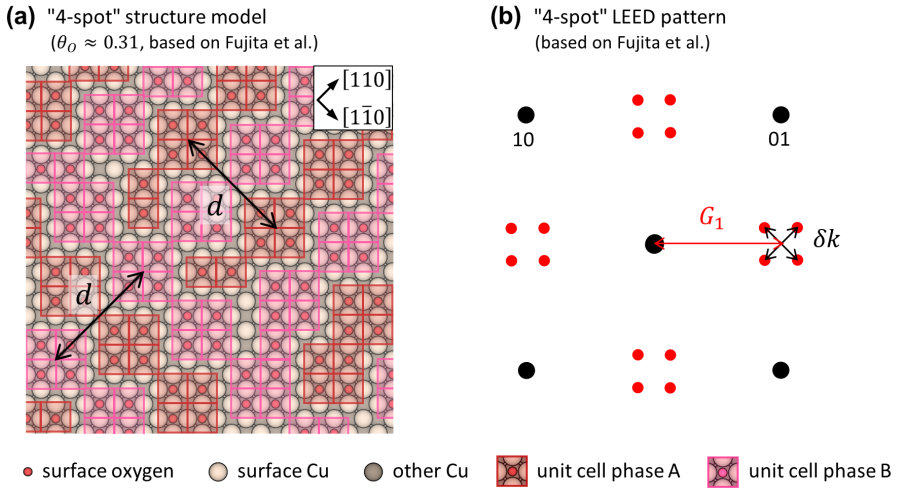


**Figure C.3: The “4-spot” surface structure and its LEED pattern.** (a) Schematic structure model of a possible configuration of the  $c(2 \times 2)$  structure for  $\theta_O \sim 0.31$ , showing a periodic anti-phase domain arrangement as suggested by Fujita et al. [217]. The structure repeats on the length scale  $d$ . Note that panel (a) is based on STM measurements of a  $c(2 \times 2)$  reconstructed Cu(001) surface and the discussion by Fujita et al. [217]. For the original STM data, please refer to Fujita et al. [217]. (b) Simulated “4-spot” LEED pattern for the structure suggested in panel (a). The  $1/2$ -order spots of the  $c(2 \times 2)$  structure at positions  $\Delta k = G_1$  are split into four spots. See main text for more information. Note that panel (b) is based on a simulated LEED pattern and the discussion by Fujita et al. [217].

# The order-disorder phase transition of the Cu(001)-MR-2O structure at elevated $T_{O_2}^{sample}$

The structure of the Cu(001)-MR-2O reconstruction and its formation process have been presented in detail in Section 5.2.4. As already mentioned in Section 5.2.4, higher  $T_{O_2}^{sample}$  during oxygen exposure [200] as well as post-annealing of the Cu(001)-MR-2O structure without oxygen exposure [196] makes the LEED spots of the Cu(001)-MR-2O structure become sharper, which is interpreted as an improvement of the Cu(001)-MR-2O structural order [196]. Extended post-annealing was found to remove the oxygen reconstruction [196, 220]. A more detailed study of the effect of an elevated annealing temperature during oxygen exposure was performed by Iddir et al. in 2007 [220]. While previous works investigated the oxygen reconstructed surface only after oxygen exposure and cooling to room temperature, Iddir et al. investigated the stable oxygen induced surface structure on Cu(001) in situ at high temperature and under equilibrium controlled oxygen exposure.

Fig. C.4(a) shows the phase diagram for the oxygen reconstruction on the Cu(001) surface, as determined by Iddir et al. [220] with an in situ X-ray scattering (XRD) experiment. Depending on the oxygen partial pressure and the temperature of the sample, three different surface structure phases occur:  $(1 \times 1)$ ,  $c(2 \times 2)$ , and

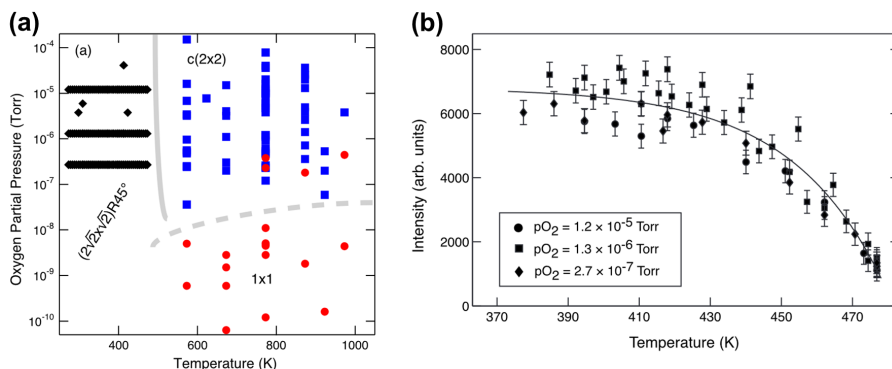


**Figure C.4: Experimental data on the order-disorder phase transition by Iddir et al. [220].** (a) Surface phase diagram for the oxygen reconstructed Cu(001) surface. The solid light gray line is an equilibrium phase boundary between the  $(\sqrt{2} \times 2\sqrt{2})R45^\circ$  and  $c(2 \times 2)$  surface phases. The dashed line is the hysteric boundary for oxygen adsorption and desorption. Data points are shown with symbols. (b) Temperature dependence of the  $(\frac{3}{4} \frac{3}{4} 0)$  XRD peak intensity at different oxygen partial pressures. Solid line is the best fit to a 2D Ising model. Fig. C.4(a,b) reprinted with permission from [220]. © 2007 by the American Physical Society. Courtesy of Argonne National Laboratory, managed and operated by UChicago Argonne, LLC, for the U.S. Department of Energy under Contract No. DE-AC02-06CH11357. See License Notice.

$(\sqrt{2} \times 2\sqrt{2})R45^\circ$ . Up to a temperature of 473 K, the  $(\sqrt{2} \times 2\sqrt{2})R45^\circ$  structure of the Cu(001)-MR-2O reconstruction is found to be stable. Above 473 K, the quarter-order superstructure spots, which are characteristic for the  $(\sqrt{2} \times 2\sqrt{2})R45^\circ$  structure, disappear completely. This results in the  $c(2 \times 2)$  structure, which has been observed to be stable up to a temperature of 1000 K (provided the oxygen partial pressure is high enough). At sufficiently high temperature and low oxygen partial pressure, oxygen desorbs from the surface and only the  $(1 \times 1)$  structure of the substrate is observed.[220]

Iddir et al. [220] studied the transition from the  $(\sqrt{2} \times 2\sqrt{2})R45^\circ$  phase to the  $c(2 \times 2)$  phase in more detail. In Fig. C.4(b) the temperature dependence of the peak intensity of a quarter-order reflection is displayed for different oxygen partial pressures  $P_{O_2}$  within the range where oxygen adsorbs. The intensity profile was found to be independent of  $P_{O_2}$  and fully reversible with temperature, showing little hysteresis. Above  $\sim 373$  K, the intensity begins to slowly decrease with increasing temperature. Towards the experimentally determined phase transition temperature of 473 K the decay rate increases. Further quantitative analysis of the XRD data revealed that the surface remains saturated with oxygen ( $\theta_O \sim 0.5$ ) and that the topmost Cu layer has a constant occupancy of  $3/4$ , not only for the  $(\sqrt{2} \times 2\sqrt{2})R45^\circ$  phase but also for the  $c(2 \times 2)$  phase and independent of temperature [220]. Therefore, the  $[c(2 \times 2)]_{highT}$  phase observed here cannot be described by the  $c(2 \times 2)$  structure model with  $\theta_O < 0.5$  and without Cu vacancies as introduced in the previous section.

Supported by first-principle calculations, Iddir et al. [220] describe the phase transition by an order-disorder transition of the Cu vacancy structure, as schematically illustrated in Fig. C.5. The starting point at low oxidation temperature is a Cu(001) surface with oxygen atoms occupying every second hollow site and well-defined rows of Cu vacancies [see Fig. C.5(a)]. With increasing temperature, the vacancies begin to rearrange, which gradually destroys the missing rows [cf. Figs. C.5(b,c)]. When the temperature exceeds the phase transition temperature, the vacancies arrange completely randomly [see Fig. C.5(d)]. During and after the phase transition, the adsorption positions of the oxygen atoms and the oxygen coverage  $\theta_O = 0.5$  did not change. Upon cool down, this order-disorder transition is fully reversible. Therefore, the  $[c(2 \times 2)]_{highT}$  structure model does not conflict with the  $c(2 \times 2)$  structure model introduced above. The  $[c(2 \times 2)]_{highT}$  structure cannot be observed at room temperature.

Finally, the process of structural order improvement of the Cu(001)-MR-2O reconstruction upon post-annealing or elevated preparation temperature is discussed in the context of the order-disorder transition. Experiments have shown that when exposed to oxygen at a temperature below the phase transition temperature, a coverage close to saturation  $\theta_O \sim 0.5$  ML can always be achieved if the dosage is sufficiently high. The resulting Cu(001)-MR-2O reconstructed surface was found to be of rather low structural quality, most likely due to small domain sizes. Strikingly, Cu atoms and vacancies were found to be very mobile on the Cu(001) surface at room temperature [241], and this effect is not expected to be

hindered by the adsorbed oxygen atoms [220]. Moreover, oxygen atoms are also mobile at room temperature, at least in the  $c(2 \times 2)$  configuration [217]. Indeed, experimental results show that at room temperature, the structural order of the Cu(001)-MR-2O reconstructed surface slowly improves with time [205].

However, each domain configuration is equivalent and represents a local minimum in the surface free energy [220]. Below the phase transition temperature, the missing rows are likely to form locally in different registries, resulting in relatively small anti-phase domain sizes. By annealing a Cu(001)-MR-2O reconstructed surface above the order-disorder phase transition temperature, the missing-row domains dissolve into the disordered vacancy structure. And if the preparation is done at a temperature above the order-disorder phase transition temperature, the disordered vacancy structure is formed directly. Upon cool down, the surface free energy can then be minimized on a larger scale and larger lateral missing-row domains are formed.

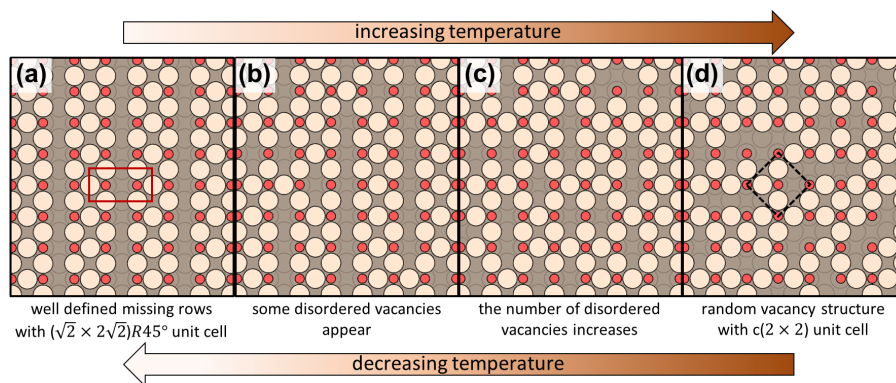


**Figure C.5: Structure model of the temperature-induced order-disorder phase transition of the Cu(001)-MR-2O structure.** (a) The starting point is the Cu(001)-MR-2O reconstruction. With increasing temperature the missing rows are gradually destroyed: (b) Single vacancies/Cu atoms have moved to another position. (c) The number of disordered vacancies increases, slowly removing the missing rows. (d) The Cu vacancies are randomly distributed. This transition is reversible upon cooldown. Schematics (a-d) based on the description by Iddir et al. [220].



# Bibliography

- [MR1] M. Raths, C. Schott, J. Knippertz, M. Franke, Y.-R. Lin, A. Haags, M. Aeschlimann, C. Kumpf, and B. Stadtmüller. “Growth, domain structure, and atomic adsorption sites of hBN on the Ni(111) surface”. *Physical Review Materials* **5**, 094001 (2021). DOI: 10.1103/PhysRevMaterials.5.094001.
- [MR2] M. Raths. “Real-time investigation of the growth of hexagonal boron nitride on metal surfaces using LEEM”. Master’s thesis. RWTH Aachen University, 2018.
- [MR3] J. Felter, M. Raths, M. Franke, and C. Kumpf. “In situ study of two-dimensional dendritic growth of hexagonal boron nitride”. *2D Materials* **6**, 045005 (2019). DOI: 10.1088/2053-1583/ab2926.
- [MR4] R. Wallauer, M. Raths, K. Stallberg, L. Münster, D. Brandstetter, X. Yang, J. Güdde, P. Puschnig, S. Soubatch, C. Kumpf, F. C. Bocquet, F. S. Tautz, and U. Höfer. “Tracing orbital images on ultrafast time scales”. *Science* **371**, 1056–1059 (2021). DOI: 10.1126/science.abf3286.
- [MR5] Y.-R. Lin, M. Franke, S. Parhizkar, M. Raths, V. W.-z. Yu, T.-L. Lee, S. Soubatch, V. Blum, F. S. Tautz, C. Kumpf, and F. C. Bocquet. “Boron nitride on SiC(0001)”. *Physical Review Materials* **6**, 064002 (2022). DOI: 10.1103/PhysRevMaterials.6.064002.
- [MR6] C. Herrmann, M. Raths, C. Kumpf, and K. L. Kavanagh. “Rotational epitaxy of h-BN on Cu (110)”. *Surface Science* **721**, 122080 (2022). DOI: 10.1016/j.susc.2022.122080.
- [MR7] A. Adamkiewicz, M. Raths, M. Stettner, M. Theilen, L. Münster, S. Wenzel, M. Hutter, S. Soubatch, C. Kumpf, F. C. Bocquet, R. Wallauer, F. S. Tautz, and U. Höfer. “Coherent and incoherent excitation pathways in time-resolved photoemission orbital tomography of CuPc/Cu(001)-2O”. *The Journal of Physical Chemistry C* **127**, 20411–20418 (2023). DOI: 10.1021/acs.jpcc.3c04859.
- [1] G. E. Moore. “Cramming more components onto integrated circuits”. *Electronics* **38**, 114–117 (1965). DOI: 10.1109/N-SSC.2006.4785860.

## Bibliography

- [2] J.-H. Kang, H. Shin, K. S. Kim, M.-K. Song, D. Lee, Y. Meng, C. Choi, J. M. Suh, B. J. Kim, H. Kim, A. T. Hoang, B.-I. Park, G. Zhou, S. Sundaram, P. Vuong, J. Shin, J. Choe, Z. Xu, R. Younas, J. S. Kim, S. Han, S. Lee, S. O. Kim, B. Kang, S. Seo, H. Ahn, S. Seo, K. Reidy, E. Park, S. Mun, M.-C. Park, S. Lee, H.-J. Kim, H. S. Kum, P. Lin, C. Hinkle, A. Ougazzaden, J.-H. Ahn, J. Kim, and S.-H. Bae. “Monolithic 3D integration of 2D materials-based electronics towards ultimate edge computing solutions”. *Nature Materials* **22**, 1470–1477 (2023). DOI: 10.1038/s41563-023-01704-z.
- [3] H. Ibach. *Physics of Surfaces and Interfaces*. Springer-Verlag, Berlin Heidelberg, 2006. DOI: 10.1007/3-540-34710-0.
- [4] J. Liu, Y. Ding, M. Zeng, and L. Fu. “Chemical insights into two-dimensional quantum materials”. *Matter* **5**, 2168–2189 (2022). DOI: 10.1016/j.matt.2022.05.034.
- [5] H. Kurebayashi, J. H. Garcia, S. Khan, J. Sinova, and S. Roche. “Magnetism, symmetry and spin transport in van der Waals layered systems”. *Nature Reviews Physics* **4**, 150–166 (2022). DOI: 10.1038/s42254-021-00403-5.
- [6] J. Maggiora, X. Wang, and R. Zheng. “Superconductivity and interfaces”. *Physics Reports* **1076**, 1–49 (2024). DOI: 10.1016/j.physrep.2024.05.001.
- [7] A. K. Geim and I. V. Grigorieva. “Van der Waals heterostructures”. *Nature* **499**, 419–425 (2013). DOI: 10.1038/nature12385.
- [8] G. Fiori, F. Bonaccorso, G. Iannaccone, T. Palacios, D. Neumaier, A. Seabaugh, S. K. Banerjee, and L. Colombo. “Electronics based on two-dimensional materials”. *Nature Nanotechnology* **9**, 768–779 (2014). DOI: 10.1038/nnano.2014.207.
- [9] F. Boschini, M. Zonno, and A. Damascelli. “Time-resolved ARPES studies of quantum materials”. *Reviews of Modern Physics* **96**, 015003 (2024). DOI: 10.1103/RevModPhys.96.015003.
- [10] K. S. Novoselov, A. K. Geim, S. V. Morozov, D. Jiang, Y. Zhang, S. V. Dubonos, I. V. Grigorieva, and A. A. Firsov. “Electric field effect in atomically thin carbon films”. *Science* **306**, 666–669 (2004). DOI: 10.1126/science.1102896.
- [11] K. S. Novoselov, A. K. Geim, S. V. Morozov, D. Jiang, M. I. Katsnelson, I. V. Grigorieva, S. V. Dubonos, and A. A. Firsov. “Two-dimensional gas of massless Dirac fermions in graphene”. *Nature* **438**, 197–200 (2005). DOI: 10.1038/nature04233.
- [12] A. H. Castro Neto, F. Guinea, N. M. R. Peres, K. S. Novoselov, and A. K. Geim. “The electronic properties of graphene”. *Reviews of Modern Physics* **81**, 109–162 (2009). DOI: 10.1103/RevModPhys.81.109.

- [13] A. R. Urade, I. Lahiri, and K. S. Suresh. “Graphene properties, synthesis and applications: A review”. *JOM* **75**, 614–630 (2023). DOI: 10.1007/s11837-022-05505-8.
- [14] Y. Zhang, Y.-W. Tan, H. L. Stormer, and P. Kim. “Experimental observation of the quantum Hall effect and Berry’s phase in graphene”. *Nature* **438**, 201–204 (2005). DOI: 10.1038/nature04235.
- [15] K. S. Novoselov, Z. Jiang, Y. Zhang, S. V. Morozov, H. L. Stormer, U. Zeitler, J. C. Maan, G. S. Boebinger, P. Kim, and A. K. Geim. “Room-temperature quantum Hall effect in graphene”. *Science* **315**, 1379–1379 (2007). DOI: 10.1126/science.1137201.
- [16] R. R. Nair, P. Blake, A. N. Grigorenko, K. S. Novoselov, T. J. Booth, T. Stauber, N. M. R. Peres, and A. K. Geim. “Fine structure constant defines visual transparency of graphene”. *Science* **320**, 1308–1308 (2008). DOI: 10.1126/science.1156965.
- [17] K. F. Mak, M. Y. Sfeir, Y. Wu, C. H. Lui, J. A. Misewich, and T. F. Heinz. “Measurement of the optical conductivity of graphene”. *Physical Review Letters* **101**, 196405 (2008). DOI: 10.1103/PhysRevLett.101.196405.
- [18] T. Stauber, N. M. R. Peres, and A. K. Geim. “Optical conductivity of graphene in the visible region of the spectrum”. *Physical Review B* **78**, 085432 (2008). DOI: 10.1103/PhysRevB.78.085432.
- [19] V. Kumar. “Linear and nonlinear optical properties of graphene: A review”. *Journal of Electronic Materials* **50**, 3773–3799 (2021). DOI: 10.1007/s11664-021-08904-w.
- [20] A. A. Balandin, S. Ghosh, W. Bao, I. Calizo, D. Teweldebrhan, F. Miao, and C. N. Lau. “Superior thermal conductivity of single-layer graphene”. *Nano Letters* **8**, 902–907 (2008). DOI: 10.1021/nl10731872.
- [21] J. H. Seol, I. Jo, A. L. Moore, L. Lindsay, Z. H. Aitken, M. T. Pettes, X. Li, Z. Yao, R. Huang, D. Broido, N. Mingo, R. S. Ruoff, and L. Shi. “Two-dimensional phonon transport in supported graphene”. *Science* **328**, 213–216 (2010). DOI: 10.1126/science.1184014.
- [22] G. Fugallo, A. Cepellotti, L. Paulatto, M. Lazzeri, N. Marzari, and F. Mauri. “Thermal conductivity of graphene and graphite: Collective excitations and mean free paths”. *Nano Letters* **14**, 6109–6114 (2014). DOI: 10.1021/nl502059f.
- [23] C. Lee, X. Wei, J. W. Kysar, and J. Hone. “Measurement of the elastic properties and intrinsic strength of monolayer graphene”. *Science* **321**, 385–388 (2008). DOI: 10.1126/science.1157996.
- [24] G. Tsoukleri, J. Parthenios, K. Papagelis, R. Jalil, A. C. Ferrari, A. K. Geim, K. S. Novoselov, and C. Galotis. “Subjecting a graphene monolayer to tension and compression”. *Small* **5**, 2397–2402 (2009). DOI: 10.1002/smll.200900802.

## Bibliography

- [25] G. Cao. “Atomistic studies of mechanical properties of graphene”. *Polymers* **6**, 2404–2432 (2014). DOI: 10.3390/polym6092404.
- [26] A. K. Geim. “Graphene: Status and prospects”. *Science* **324**, 1530–1534 (2009). DOI: 10.1126/science.1158877.
- [27] D. Akinwande, N. Petrone, and J. Hone. “Two-dimensional flexible nanoelectronics”. *Nature Communications* **5**, 5678 (2014). DOI: 10.1038/ncomms6678.
- [28] L. A. Ponomarenko, A. K. Geim, A. A. Zhukov, R. Jalil, S. V. Morozov, K. S. Novoselov, I. V. Grigorieva, E. H. Hill, V. V. Cheianov, V. I. Fal’ko, K. Watanabe, T. Taniguchi, and R. V. Gorbachev. “Tunable metal-insulator transition in double-layer graphene heterostructures”. *Nature Physics* **7**, 958–961 (2011). DOI: 10.1038/nphys2114.
- [29] G.-H. Lee, Y.-J. Yu, C. Lee, Cory Dean, K. L. Shepard, P. Kim, and J. Hone. “Electron tunneling through atomically flat and ultrathin hexagonal boron nitride”. *Applied Physics Letters* **99**, 243114 (2011). DOI: 10.1063/1.3662043.
- [30] I. Meric, C. R. Dean, N. Petrone, L. Wang, J. Hone, P. Kim, and K. L. Shepard. “Graphene field-effect transistors based on boron-nitride dielectrics”. *Proceedings of the IEEE* **101**, 1609–1619 (2013). DOI: 10.1109/JPROC.2013.2257634.
- [31] G. Yang, L. Li, W. B. Lee, and M. C. Ng. “Structure of graphene and its disorders: a review”. *Science and Technology of Advanced Materials* **19**, 613–648 (2018). DOI: 10.1080/14686996.2018.1494493.
- [32] I. N. Yakovkin. “Dirac cones in graphene, interlayer interaction in layered materials, and the band gap in MoS<sub>2</sub>”. *Crystals* **6**, 143 (2016). DOI: 10.3390/cryst6110143.
- [33] E. Y. Andrei and A. H. MacDonald. “Graphene bilayers with a twist”. *Nature Materials* **19**, 1265–1275 (2020). DOI: 10.1038/s41563-020-00840-0.
- [34] K. Kim, A. DaSilva, S. Huang, B. Fallahazad, S. Larentis, T. Taniguchi, K. Watanabe, B. J. LeRoy, A. H. MacDonald, and E. Tutuc. “Tunable moiré bands and strong correlations in small-twist-angle bilayer graphene”. *PNAS* **114**, 3364–3369 (2017). DOI: 10.1073/pnas.1620140114.
- [35] Y. Cao, V. Fatemi, S. Fang, K. Watanabe, T. Taniguchi, E. Kaxiras, and P. Jarillo-Herrero. “Unconventional superconductivity in magic-angle graphene superlattices”. *Nature* **556**, 43–50 (2018). DOI: 10.1038/nature26160.

- [36] X. Lu, P. Stepanov, W. Yang, M. Xie, M. A. Aamir, I. Das, C. Urgell, K. Watanabe, T. Taniguchi, G. Zhang, A. Bachtold, A. H. MacDonald, and D. K. Efetov. “Superconductors, orbital magnets and correlated states in magic-angle bilayer graphene”. *Nature* **574**, 653–657 (2019). DOI: 10.1038/s41586-019-1695-0.
- [37] L. Rademaker, I. V. Protopopov, and D. A. Abanin. “Topological flat bands and correlated states in twisted monolayer-bilayer graphene”. *Physical Review Research* **2**, 033150 (2020). DOI: 10.1103/PhysRevResearch.2.033150.
- [38] S. Chen, M. He, Y.-H. Zhang, V. Hsieh, Z. Fei, K. Watanabe, T. Taniguchi, D. H. Cobden, X. Xu, C. R. Dean, and M. Yankowitz. “Electrically tunable correlated and topological states in twisted monolayer-bilayer graphene”. *Nature Physics* **17**, 374–380 (2021). DOI: 10.1038/s41567-020-01062-6.
- [39] S. S. Dindorkar, A. S. Kurade, and A. H. Shaikh. “Magical moiré patterns in twisted bilayer graphene: A review on recent advances in graphene twistrionics”. *Chemical Physics Impact* **7**, 100325 (2023). DOI: 10.1016/j.chphi.2023.100325.
- [40] W. Yao, E. Wang, C. Bao, Y. Zhang, K. Zhang, K. Bao, C. K. Chan, C. Chen, J. Avila, M. C. Asensio, J. Zhu, and S. Zhou. “Quasicrystalline 30° twisted bilayer graphene as an incommensurate superlattice with strong interlayer coupling”. *PNAS* **115**, 6928–6933 (2018). DOI: 10.1073/pnas.1720865115.
- [41] S. J. Ahn, P. Moon, T.-H. Kim, H.-W. Kim, H.-C. Shin, E. H. Kim, H. W. Cha, S.-J. Kahng, P. Kim, M. Koshino, Y.-W. Son, C.-W. Yang, and J. R. Ahn. “Dirac electrons in a dodecagonal graphene quasicrystal”. *Science* **361**, 782–786 (2018). DOI: 10.1126/science.aar8412.
- [42] P. Moon, M. Koshino, and Y.-W. Son. “Quasicrystalline electronic states in 30° rotated twisted bilayer graphene”. *Physical Review B* **99**, 165430 (2019). DOI: 10.1103/PhysRevB.99.165430.
- [43] M. J. Park, H. S. Kim, and S. Lee. “Emergent localization in dodecagonal bilayer quasicrystals”. *Physical Review B* **99**, 245401 (2019). DOI: 10.1103/PhysRevB.99.245401.
- [44] M. J. Park, Y. Kim, G. Y. Cho, and S. Lee. “Higher-order topological insulator in twisted bilayer graphene”. *Physical Review Letters* **123**, 216803 (2019). DOI: 10.1103/PhysRevLett.123.216803.
- [45] C. Yan, D.-L. Ma, J.-B. Qiao, H.-Y. Zhong, L. Yang, S.-Y. Li, Z.-Q. Fu, Y. Zhang, and L. He. “Scanning tunneling microscopy study of the quasicrystalline 30° twisted bilayer graphene”. *2D Materials* **6**, 045041 (2019). DOI: 10.1088/2053-1583/ab3b16.

## Bibliography

- [46] E. Koren and U. Duerig. “Superlubricity in quasicrystalline twisted bilayer graphene”. *Physical Review B* **93**, 201404 (2016). DOI: 10.1103/PhysRevB.93.201404.
- [47] T. Suzuki, T. Iimori, S. J. Ahn, Y. Zhao, M. Watanabe, J. Xu, M. Fujisawa, T. Kanai, N. Ishii, J. Itatani, K. Suwa, H. Fukidome, S. Tanaka, J. R. Ahn, K. Okazaki, S. Shin, F. Komori, and I. Matsuda. “Ultrafast unbalanced electron distributions in quasicrystalline 30° twisted bilayer graphene”. *ACS Nano* **13**, 11981–11987 (2019). DOI: 10.1021/acsnano.9b06091.
- [48] G. Yu, Z. Wu, Z. Zhan, M. I. Katsnelson, and S. Yuan. “Dodecagonal bilayer graphene quasicrystal and its approximants”. *npj Computational Materials* **5**, 122 (2019). DOI: 10.1038/s41524-019-0258-0.
- [49] P. Avouris and C. Dimitrakopoulos. “Graphene: Synthesis and applications”. *Materials Today* **15**, 86–97 (2012). DOI: 10.1016/S1369-7021(12)70044-5.
- [50] S. Forti and U. Starke. “Epitaxial graphene on SiC: from carrier density engineering to quasi-free standing graphene by atomic intercalation”. *Journal of Physics D: Applied Physics* **47**, 094013 (2014). DOI: 10.1088/0022-3727/47/9/094013.
- [51] G. R. Yazdi, T. Iakimov, and R. Yakimova. “Epitaxial graphene on SiC: A review of growth and characterization”. *Crystals* **6**, 53 (2016). DOI: 10.3390/cryst6050053.
- [52] H.-C. Shin, Y. Jang, Tae-H. Kim, J.-H. Lee, D.-H. Oh, S. J. Ahn, J. H. Lee, Y. Moon, J.-H. Park, S. J. Yoo, C.-Y. Park, D. Whang, C.-W. Yang, and J. R. Ahn. “Epitaxial growth of a single-crystal hybridized boron nitride and graphene layer on a wide-band gap semiconductor”. *Journal of the American Chemical Society* **137**, 6897–6905 (2015). DOI: 10.1021/jacs.5b03151.
- [53] F. C. Bocquet, Y.-R. Lin, M. Franke, N. Samiseresht, S. Parhizkar, S. Soubatch, T.-L. Lee, C. Kumpf, and F. S. Tautz. “Surfactant-mediated epitaxial growth of single-layer graphene in an unconventional orientation on SiC”. *Physical Review Letters* **125**, 106102 (2020). DOI: 10.1103/PhysRevLett.125.106102.
- [54] H. Yin, M. Hutter, C. Wagner, F. S. Tautz, F. C. Bocquet, and C. Kumpf. “Epitaxial growth of mono- and (twisted) multilayer graphene on SiC(0001)”. *Physical Review Materials* **9**, 044003 (2025). DOI: 10.1103/PhysRevMaterials.9.044003.
- [55] J. A. Sobota, Y. He, and Z.-X. Shen. “Angle-resolved photoemission studies of quantum materials”. *Reviews of Modern Physics* **93**, 025006 (2021). DOI: 10.1103/RevModPhys.93.025006.

- [56] H. Zhang, T. Pincelli, C. Jozwiak, T. Kondo, R. Ernstorfer, T. Sato, and S. Zhou. “Angle-resolved photoemission spectroscopy”. *Nature Reviews Methods Primers* **2**, 1–22 (2022). DOI: 10.1038/s43586-022-00133-7.
- [57] P. Puschnig, S. Berkebile, A. J. Fleming, G. Koller, K. Emtsev, T. Seyller, J. D. Riley, C. Ambrosch-Draxl, F. P. Netzer, and M. G. Ramsey. “Reconstruction of molecular orbital densities from photoemission data.” *Science* **326**, 702–706 (2009). DOI: 10.1126/science.1176105.
- [58] P. Puschnig, G. Koller, C. Draxl, and M. G. Ramsey. “The structure of molecular orbitals investigated by angle-resolved photoemission”. In: *Small Organic Molecules on Surfaces: Fundamentals and Applications*. Ed. by H. Sitter, C. Draxl, and M. Ramsey. Springer Series in Materials Science. Springer, Berlin, Heidelberg, 2013, pp. 3–23. DOI: 10.1007/978-3-642-33848-9\_1.
- [59] M. Dauth, M. Wiessner, V. Feyer, A. Schöll, P. Puschnig, F. Reinert, and S. Kümmel. “Angle resolved photoemission from organic semiconductors: orbital imaging beyond the molecular orbital interpretation.” *New J. Phys.* **16**, 103005 (2014). DOI: 10.1088/1367-2630/16/10/103005.
- [60] P. Puschnig and M. G. Ramsey. “Photoemission tomography: Valence band photoemission as a quantitative method for investigating molecular films”. In: *Encyclopedia of Interfacial Chemistry*. Ed. by K. Wandelt. Elsevier, Oxford, 2018, pp. 380–391. DOI: 10.1016/B978-0-12-409547-2.13782-5.
- [61] S. R. Forrest. “The path to ubiquitous and low-cost organic electronic appliances on plastic”. *Nature* **428**, 911–918 (2004). DOI: 10.1038/nature02498.
- [62] Y. Yang and F. Wudl. “Organic electronics: From materials to devices”. *Advanced Materials* **21**, 1401–1403 (2009). DOI: 10.1002/adma.200900844.
- [63] Q. Zhang, W. Hu, H. Sirringhaus, and K. Müllen. “Recent progress in emerging organic semiconductors”. *Advanced Materials* **34**, 2108701 (2022). DOI: 10.1002/adma.202108701.
- [64] V. Bhat, C. P. Callaway, and C. Risko. “Computational approaches for organic semiconductors: From chemical and physical understanding to predicting new materials”. *Chemical Reviews* **123**, 7498–7547 (2023). DOI: 10.1021/acs.chemrev.2c00704.
- [65] T. Rohwer, S. Hellmann, M. Wiesenmayer, C. Sohrt, A. Stange, B. Slomski, A. Carr, Y. Liu, L. M. Avila, M. Källäne, S. Mathias, L. Kipp, K. Rossnagel, and M. Bauer. “Collapse of long-range charge order tracked by time-resolved photoemission at high momenta.” *Nature* **471**, 490–493 (2011). DOI: 10.1038/nature09829.

## Bibliography

- [66] R. Wallauer, J. Reimann, N. Armbrust, J. Güdde, and U. Höfer. “Intervalley scattering in MoS<sub>2</sub> imaged by two-photon photoemission with a high-harmonic probe”. *Applied Physics Letters* **109**, 162102 (2016). DOI: 10.1063/1.4965839.
- [67] S. Eich, M. Plötzing, M. Rollinger, S. Emmerich, R. Adam, C. Chen, H. C. Kapteyn, M. M. Murnane, L. Plucinski, D. Steil, B. Stadtmüller, M. Cinchetti, M. Aeschlimann, C. M. Schneider, and S. Mathias. “Band structure evolution during the ultrafast ferromagnetic-paramagnetic phase transition in cobalt.” *Sci. Adv.* **3**, e1602094 (2017). DOI: 10.1126/sciadv.1602094.
- [68] C. W. Nicholson, A. Lücke, W. G. Schmidt, M. Puppini, L. Rettig, R. Ernstorfer, and M. Wolf. “Beyond the molecular movie: Dynamics of bands and bonds during a photoinduced phase transition.” *Science* **362**, 821–825 (2018). DOI: 10.1126/science.aar4183.
- [69] M. X. Na, A. K. Mills, F. Boschini, M. Michiardi, B. Nosarzewski, R. P. Day, E. Razzoli, A. Sheyerman, M. Schneider, G. Levy, S. Zhdanovich, T. P. Devereaux, A. F. Kemper, D. J. Jones, and A. Damascelli. “Direct determination of mode-projected electron-phonon coupling in the time domain.” *Science* **366**, 1231–1236 (2019). DOI: 10.1126/science.aaw1662.
- [70] D. P. Woodruff. *Modern Techniques of Surface Science*. 3rd edition. Cambridge Solid State Science Series. Cambridge University Press, Cambridge, 2016. DOI: 10.1017/CB09781139149716.
- [71] E. Bauer. “Low energy electron microscopy”. *Reports on Progress in Physics* **57**, 895–938 (1994). DOI: 10.1088/0034-4885/57/9/002.
- [72] K. Pussi and R. D. Diehl. “Low-energy electron diffraction”. In: *Characterization of Materials*. Ed. by E. N. Kaufmann. John Wiley & Sons, Inc, 2012, pp. 1841–1853. DOI: <https://doi.org/10.1002/0471266965.com085.pub2>.
- [73] M. P. Seah and W. A. Dench. “Quantitative electron spectroscopy of surfaces: A standard data base for electron inelastic mean free paths in solids”. *Surface and Interface Analysis* **1**, 2–11 (1979). DOI: 10.1002/sia.740010103.
- [74] E. Bauer. “LEEM and SPLEEM”. In: *Science of Microscopy*. Ed. by P. W. Hawkes and J. C. H. Spence. Springer Nature, New York, 2007, pp. 605–656. DOI: 10.1007/978-0-387-49762-4\_8.
- [75] H.-J. Herlt. “Elastische Rückstreuung sehr langsamer Elektronen an reinen und gasbedeckten Wolfram-Einkristalloberflächen”. PhD thesis. Technische Universität Clausthal, 1982. URL: <https://www.deutsche-digitale-bibliothek.de/item/GPBTUNADE2YCVUZNVCUYVAL7QJBUVOKM>.

- [76] J. I. Flege, W. X. Tang, and M. S. Altman. “Low-energy electron microscopy”. In: *Characterization of Materials*. Ed. by E. N. Kaufmann. John Wiley & Sons, Inc, 2012, pp. 1808–1827. DOI: 10.1002/0471266965.com157.
- [77] M. A. Van Hove, W. H. Weinberg, and C.-M. Chan. *Low-Energy Electron Diffraction: Experiment, Theory and Surface Structure Determination*. Springer Series in Surface Sciences, vol 6. Springer-Verlag, Berlin Heidelberg, 1986. DOI: 10.1007/978-3-642-82721-1.
- [78] S. Mizuno, F. Rahman, and M. Iwanaga. “Low-energy electron diffraction patterns using field-emitted electrons from tungsten tips”. *Japanese Journal of Applied Physics* **45**, L178 (2006). DOI: 10.1143/JJAP.45.L178.
- [79] H. Lüth. *Solid Surfaces, Interfaces and Thin Films*. 6th edition. Series: Graduate Texts in Physics. Springer International Publishing, Cham, 2015. DOI: 10.1007/978-3-319-10756-1.
- [80] K. Oura, M. Katayama, A. V. Zotov, V. G. Lifshits, and A. A. Saranin. *Surface Science: An Introduction*. Series: Advanced Texts in Physics. Springer-Verlag, Berlin Heidelberg, 2003. DOI: 10.1007/978-3-662-05179-5.
- [81] M. Henzler. “Electron diffraction and surface defect structure”. In: *Electron Spectroscopy for Surface Analysis*. Ed. by H. Ibach. Series: Topics in Current Physics, vol 4. Springer-Verlag, Berlin Heidelberg, 1977, pp. 117–149. DOI: 10.1007/978-3-642-81099-2\_4.
- [82] A. Scheidt, H. Richter, and U. Gerhardt. “The structure of oxygen adsorbed on spherical Cu and Ni surfaces at and close to the (001) pole”. *Surface Science* **205**, 38–58 (1988). DOI: 10.1016/0039-6028(88)90163-X.
- [83] H. Zi-Pu, D. F. Ogletree, M. A. Van Hove, and G. A. Somorjai. “Leed theory for incommensurate overlayers: application to graphite on Pt(111)”. *Surface Science* **180**, 433–459 (1987). DOI: 10.1016/0039-6028(87)90219-6.
- [84] M. J. Hamer, A. Giampietri, V. Kandyba, F. Genuzio, T. O. Menteş, A. Locatelli, R. V. Gorbachev, A. Barinov, and M. Mucha-Kruczyński. “Moiré superlattice effects and band structure evolution in near-30-degree twisted bilayer graphene”. *ACS Nano* **16**, 1954–1962 (2022). DOI: 10.1021/acsnano.1c06439.
- [85] D. Martocchia, P. R. Willmott, T. Brugger, M. Björck, S. Günther, C. M. Schlepütz, A. Cervellino, S. A. Pauli, B. D. Patterson, S. Marchini, J. Wintterlin, W. Moritz, and T. Greber. “Graphene on Ru(0001): A 25×25 supercell”. *Physical Review Letters* **101**, 126102 (2008). DOI: 10.1103/PhysRevLett.101.126102.

## Bibliography

- [86] E. Bauer, M. Mundschau, W. Swiech, and W. Telieps. “Surface studies by low-energy electron microscopy (LEEM) and conventional UV photoemission electron microscopy (PEEM)”. *Ultramicroscopy* **31**, 49–57 (1989). DOI: 10.1016/0304-3991(89)90033-8.
- [87] E. Bauer. “Low energy electron reflection microscopy”. In: *Fifth international congress for electron microscopy*. Academic Press, New York, 1962, pp. 11–12.
- [88] W. Telieps and E. Bauer. “An analytical reflection and emission UHV surface electron microscope”. *Ultramicroscopy* **17**, 57–65 (1985). DOI: [https://doi.org/10.1016/0304-3991\(85\)90177-9](https://doi.org/10.1016/0304-3991(85)90177-9).
- [89] *Manual for the Elmitec AC-SPELEEM III*. Technical Report. Elmitec Elektronenmikroskopie GmbH. 2008.
- [90] E. Bauer. *Surface Microscopy with Low Energy Electrons*. Springer New York, New York, 2014. DOI: 10.1007/978-1-4939-0935-3.
- [91] E. Bauer. “The resolution of the low energy electron reflection microscope”. *Ultramicroscopy* **17**, 51–56 (1985). DOI: 10.1016/0304-3991(85)90176-7.
- [92] Th. Schmidt, S. Heun, J. Slezak, J. Diaz, K. C. Prince, G. Lilienkamp, and E. Bauer. “SPELEEM: Combining LEEM and spectroscopic imaging”. *Surface Review and Letters* **05**, 1287–1296 (1998). DOI: 10.1142/S0218625X98001626.
- [93] M. S. Altman, W. F. Chung, and C. H. Liu. “LEEM phase contrast”. *Surface Review and Letters* **05**, 1129–1141 (1998). DOI: 10.1142/S0218625X98001468.
- [94] J. I. Flege, B. Kaemena, A. Meyer, J. Falta, S. D. Senanayake, J. T. Sadowski, R. D. Eithiraj, and E. E. Krasovskii. “Origin of chemical contrast in low-energy electron reflectivity of correlated multivalent oxides: The case of ceria”. *Physical Review B* **88**, 235428 (2013). DOI: 10.1103/PhysRevB.88.235428.
- [95] J. I. Flege and E. E. Krasovskii. “Intensity-voltage low-energy electron microscopy for functional materials characterization”. *Phys. Status Solidi RRL* **8**, 463–477 (2014). DOI: 10.1002/pssr.201409102.
- [96] J. Jobst, J. Kautz, D. Geelen, R. M. Tromp, and S. J. van der Molen. “Nanoscale measurements of unoccupied band dispersion in few-layer graphene”. *Nature Communications* **6**, 8926 (2015). DOI: 10.1038/ncomms9926.
- [97] J. Jobst, A. J. H. van der Torren, E. E. Krasovskii, J. Balgley, C. R. Dean, R. M. Tromp, and S. J. van der Molen. “Quantifying electronic band interactions in van der Waals materials using angle-resolved reflected-electron spectroscopy”. *Nature Communications* **7**, 13621 (2016). DOI: 10.1038/ncomms13621.

- [98] W. F. Chung, Y. J. Feng, H. C. Poon, C. T. Chan, S. Y. Tong, and M. S. Altman. “Layer spacings in coherently strained epitaxial metal films”. *Physical Review Letters* **90**, 216105 (2003). DOI: 10.1103/PhysRevLett.90.216105.
- [99] T. Duden, A. Thust, C. Kumpf, and F. S. Tautz. “Focal-series reconstruction in low-energy electron microscopy”. *Microscopy and Microanalysis* **20**, 968–973 (2014). DOI: 10.1017/S1431927614000403.
- [100] P. L. Lévesque, H. Marchetto, T. Schmidt, F. C. Maier, H.-J. Freund, and E. Umbach. “Correlation between substrate morphology and the initial stages of epitaxial organic growth: PTCDA/Ag(111)”. *The Journal of Physical Chemistry C* **120**, 19271–19279 (2016). DOI: 10.1021/acs.jpcc.6b06781.
- [101] C. Henneke. “Kinetic and thermodynamic considerations on the formation of heteromolecular layers on metal surfaces”. PhD thesis. RWTH Aachen University, 2015. URL: <https://juser.fz-juelich.de/record/834675>.
- [102] H. Hertz. “Ueber einen Einfluss des ultravioletten Lichtes auf die elektrische Entladung”. *Annalen der Physik* **267**, 983–1000 (1887). DOI: 10.1002/andp.18872670827.
- [103] W. Hallwachs. “Ueber den Einfluss des Lichtes auf electrostatisch geladene Körper”. *Annalen der Physik* **269**, 301–312 (1888). DOI: 10.1002/andp.18882690206.
- [104] A. Einstein. “Über einen die Erzeugung und Verwandlung des Lichtes betreffenden heuristischen Gesichtspunkt”. *Annalen der Physik* **322**, 132–148 (1905). DOI: 10.1002/andp.19053220607.
- [105] S. Hüfner. *Photoelectron Spectroscopy*. 3rd edition. Series: Advanced Texts in Physics. Springer-Verlag, Berlin Heidelberg, 2003. DOI: 10.1007/978-3-662-09280-4.
- [106] A. Damascelli. “Probing the electronic structure of complex systems by ARPES”. *Physica Scripta* **2004**, 61 (2004). DOI: 10.1238/Physica.Topical.109a00061.
- [107] C. M. Schneider. “F03 photoelectron emission spectroscopy”. In: *43rd IFF Spring School: ”Scattering Methods for Condensed Matter Research: Towards Novel Applications at Future Sources”*. Ed. by M. Angst, T. Brückel, D. Richter, and R. Zorn. Schriften des Forschungszentrums Jülich / Reihe Schlüsseltechnologien / Key Technologies, vol 33. Forschungszentrum Jülich GmbH, JCNS, PGI, ICS, IAS, 2012, F3.1–F3.45. URL: <https://juser.fz-juelich.de/record/134956>.
- [108] F. Reinert and S. Hüfner. “Photoemission spectroscopy - from early days to recent applications”. *New Journal of Physics* **7**, 97 (2005). DOI: 10.1088/1367-2630/7/1/097.

## Bibliography

- [109] B. Lv, T. Qian, and H. Ding. “Angle-resolved photoemission spectroscopy and its application to topological materials”. *Nature Reviews Physics* **1**, 609–626 (2019). DOI: 10.1038/s42254-019-0088-5.
- [110] M. Staab, D. Kutnyakhov, R. Wallauer, S. Chernov, K. Medjanik, H. J. Elmers, M. Kläui, and G. Schönhense. “Energy- and k -resolved mapping of the magnetic circular dichroism in threshold photoemission from Co films on Pt(111)”. *Physical Review B* **95**, 165437 (2017). DOI: 10.1103/PhysRevB.95.165437.
- [111] M. Weinelt. “Time-resolved two-photon photoemission from metal surfaces”. *Journal of Physics: Condensed Matter* **14**, R1099–R1141 (2002). DOI: 10.1088/0953-8984/14/43/202.
- [112] J. Felter, J. Wolters, F. C. Bocquet, F. S. Tautz, and C. Kumpf. “Momentum microscopy on the micrometer scale: Photoemission microtomography applied to single molecular domains”. *Journal of Physics: Condensed Matter* **31**, 114003 (2019). DOI: 10.1088/1361-648X/aafc45.
- [113] P. Puschnig, E.-M. Reinisch, T. Ules, G. Koller, S. Soubatch, M. Ostler, L. Romaner, F. S. Tautz, C. Ambrosch-Draxl, and M. G. Ramsey. “Orbital tomography: Deconvoluting photoemission spectra of organic molecules”. *Physical Review B* **84**, 235427 (2011). DOI: 10.1103/PhysRevB.84.235427.
- [114] T. Fauster and W. Steinmann. “Chapter 8 - Two-photon photoemission spectroscopy of image states”. In: *Photonic Probes of Surfaces*. Ed. by P. Halevi. Series: Electromagnetic Waves: Recent Developments in Research. Elsevier, Amsterdam, 1995, pp. 347–411. DOI: <https://doi.org/10.1016/B978-0-444-82198-0.50015-1>.
- [115] X.-Y. Zhu. “Electronic structure and electron dynamics at molecule-metal interfaces: implications for molecule-based electronics”. *Surface Science Reports* **56**, 1–83 (2004). DOI: 10.1016/j.surfrep.2004.09.002.
- [116] Y. J. Dappe, A. A. Villaeys, and F. P. Lohner. “Description of the coherent and incoherent processes in two-photon photoemission on Cu(111) surface”. *Applied Surface Science* **168**, 41–43 (2000). DOI: 10.1016/S0169-4332(00)00576-6.
- [117] J. Güdde, M. Rohleder, and U. Höfer. “Time-resolved two-color interferometric photoemission of image-potential states on Cu(100)”. *Applied Physics A* **85**, 345–350 (2006). DOI: 10.1007/s00339-006-3711-0.
- [118] H. Ueba and T. Mii. “Theory of energy- and time-resolved two-photon photoemission from metal surfaces – influence of pulse duration and excitation condition.” *Appl. Phys. A Mater. Sci. Process.* **71**, 537–545 (2000). DOI: 10.1007/s003390000711.

- [119] T. Klamroth, P. Saalfrank, and U. Höfer. “Open-system density-matrix approach to imagepotential dynamics of electrons at Cu(100): energy- and time-resolved two-photon photoemission spectra.” *Phys. Rev. B* **64**, 035420 (2001). DOI: 10.1103/PhysRevB.64.035420.
- [120] H. Ueba and B. Gumhalter. “Theory of two-photon photoemission spectroscopy of surfaces”. *Progress in Surface Science* **82**, 193–223 (2007). DOI: 10.1016/j.progsurf.2007.03.002.
- [121] C. M. Heyl, J. GÜdde, A. L’Huillier, and U. Höfer. “High-order harmonic generation with  $\mu\text{J}$  laser pulses at high repetition rates.” *J. Phys. B At. Mol. Opt. Phys.* **45**, 074020 (2012). DOI: 10.1088/0953-4075/45/7/074020.
- [122] H. Wang, Y. Xu, S. Ulonska, J. S. Robinson, P. Ranitovic, and R. A. Kaindl. “Bright high-repetition-rate source of narrowband extreme-ultraviolet harmonics beyond 22 eV.” *Nat. Commun.* **6**, 7459 (2015). DOI: 10.1038/ncomms8459.
- [123] C. Tusche, P. Goslawski, D. Kutnyakhov, M. Ellguth, K. Medjanik, H. J. Elmers, S. Chernov, R. Wallauer, D. Engel, A. Jankowiak, and G. Schönhense. “Multi-MHz time-of-flight electronic bandstructure imaging of graphene on Ir(111).” *Appl. Phys. Lett.* **108**, 261602 (2016). DOI: 10.1063/1.4955015.
- [124] H. Yin. “On the way to twisted bilayer graphene: In-situ investigation of template-mediated growth of graphene on 6H-SiC(0001)”. Master’s thesis. RWTH Aachen University, 2021.
- [125] W. Auwärter. “Hexagonal boron nitride monolayers on metal supports: versatile templates for atoms, molecules and nanostructures”. *Surface Science Reports* **74**, 1–95 (2019). DOI: 10.1016/j.surfrep.2018.10.001.
- [126] W. Auwärter, T. J. Kreuzt, T. Greber, and J. Osterwalder. “XPD and STM investigation of hexagonal boron nitride on Ni(111)”. *Surface Science* **429**, 229–236 (1999). DOI: 10.1016/S0039-6028(99)00381-7.
- [127] P. Sutter, J. Lahiri, P. Albrecht, and E. Sutter. “Chemical vapor deposition and etching of high-quality monolayer hexagonal boron nitride films”. *ACS Nano* **5**, 7303–7309 (2011). DOI: 10.1021/nn202141k.
- [128] F. Orlando, R. Larciprete, P. Lacovig, I. Boscarato, A. Baraldi, and S. Lizzit. “Epitaxial growth of hexagonal boron nitride on Ir(111)”. *The Journal of Physical Chemistry C* **116**, 157–164 (2012). DOI: 10.1021/jp207571n.
- [129] F. Müller and S. Grandthyll. “Monolayer formation of hexagonal boron nitride on Ag(001)”. *Surface Science* **617**, 207–210 (2013). DOI: 10.1016/j.susc.2013.07.024.

## Bibliography

- [130] J. E. Felter. “Different growth modes of molecular adsorbate systems and 2D materials investigated by low-energy electron microscopy”. PhD thesis. RWTH Aachen University, 2019. URL: <https://juser.fz-juelich.de/record/866243>.
- [131] K. Heinz, J. Bernhardt, J. Schardt, and U. Starke. “Functional surface reconstructions of hexagonal SiC”. *Journal of Physics: Condensed Matter* **16**, S1705–S1720 (2004). DOI: 10.1088/0953-8984/16/17/013.
- [132] C. H. Park, Byoung-Ho Cheong, Keun-Ho Lee, and K. J. Chang. “Structural and electronic properties of cubic, 2H, 4H, and 6H SiC”. *Physical Review B* **49**, 4485–4493 (1994). DOI: 10.1103/PhysRevB.49.4485.
- [133] J. C. Koepke, J. D. Wood, C. M. Horvath, J. W. Lyding, and S. Barraza-Lopez. “Preserving the  $7\times 7$  surface reconstruction of clean Si(111) by graphene adsorption”. *Applied Physics Letters* **107**, 071603 (2015). DOI: 10.1063/1.4928930.
- [134] M. A. Kulakov, G. Henn, and B. Bullemer. “SiC(0001) $3\times 3$ -Si surface reconstruction – a new insight with a STM”. *Surface Science* **346**, 49–54 (1996). DOI: 10.1016/0039-6028(95)00919-1.
- [135] J. Schardt, J. Bernhardt, U. Starke, and K. Heinz. “Crystallography of the  $(3\times 3)$  surface reconstruction of 3C-SiC(111), 4H-SiC(0001) and 6H-SiC(0001) surfaces retrieved by low-energy electron diffraction”. *Physical Review B* **62**, 10335–10344 (2000). DOI: 10.1103/PhysRevB.62.10335.
- [136] D. Momeni Pakdehi, P. Schädlich, T. T. N. Nguyen, A. A. Zakharov, S. Wundrack, E. Najafidehaghani, F. Speck, K. Pierz, T. Seyller, C. Tegenkamp, and H. W. Schumacher. “Silicon carbide stacking-order-induced doping variation in epitaxial graphene”. *Advanced Functional Materials* **30**, 2004695 (2020). DOI: 10.1002/adfm.202004695.
- [137] A. Nakajima, H. Yokoya, Y. Furukawa, and H. Yonezu. “Step control of vicinal 6H-SiC(0001) surface by  $H_2$  etching”. *Journal of Applied Physics* **97**, 104919 (2005). DOI: 10.1063/1.1901838.
- [138] V. Borovikov and A. Zangwill. “Step bunching of vicinal 6H-SiC{0001} surfaces”. *Physical Review B* **79**, 245413 (2009). DOI: 10.1103/PhysRevB.79.245413.
- [139] G. C. Büke. “Epitaxial graphene and carbon nanotubes on silicon carbide”. In: *Nanomaterials Handbook*. Ed. by Y. Gogotsi. 2nd edition. CRC Press, 2017, pp. 63–82. DOI: 10.1201/9781315371795-3.
- [140] N. Ooi, V. Rajan, J. Gottlieb, Y. Catherine, and J. B. Adams. “Structural properties of hexagonal boron nitride”. *Modelling and Simulation in Materials Science and Engineering* **14**, 515 (2006). DOI: 10.1088/0965-0393/14/3/012.
- [141] D. D. L. Chung. “Review graphite”. *Journal of Materials Science* **37**, 1475–1489 (2002). DOI: 10.1023/A:1014915307738.

- [142] P. C. Mende, J. Li, and R. M. Feenstra. “Substitutional mechanism for growth of hexagonal boron nitride on epitaxial graphene”. *Applied Physics Letters* **113**, 031605 (2018). DOI: 10.1063/1.5039823.
- [143] K. V. Emtsev, F. Speck, Th. Seyller, L. Ley, and J. D. Riley. “Interaction, growth, and ordering of epitaxial graphene on SiC{0001} surfaces: A comparative photoelectron spectroscopy study”. *Physical Review B* **77**, 155303 (2008). DOI: 10.1103/PhysRevB.77.155303.
- [144] K. V. Emtsev, A. Bostwick, K. Horn, J. Jobst, G. L. Kellogg, L. Ley, J. L. McChesney, T. Ohta, S. A. Reshanov, J. Röhrl, E. Rotenberg, A. K. Schmid, D. Waldmann, H. B. Weber, and T. Seyller. “Towards wafer-size graphene layers by atmospheric pressure graphitization of silicon carbide”. *Nature Materials* **8**, 203–207 (2009). DOI: 10.1038/nmat2382.
- [145] C. Riedl, C. Coletti, T. Iwasaki, A. A. Zakharov, and U. Starke. “Quasi-free-standing epitaxial graphene on SiC obtained by hydrogen intercalation”. *Physical Review Letters* **103**, 246804 (2009). DOI: 10.1103/PhysRevLett.103.246804.
- [146] H. Hibino, H. Kageshima, F. Maeda, M. Nagase, Y. Kobayashi, and H. Yamaguchi. “Microscopic thickness determination of thin graphite films formed on SiC from quantized oscillation in reflectivity of low-energy electrons”. *Physical Review B* **77**, 075413 (2008). DOI: 10.1103/PhysRevB.77.075413.
- [147] K. L. Man and M. S. Altman. “Low energy electron microscopy and photoemission electron microscopy investigation of graphene”. *Journal of Physics: Condensed Matter* **24**, 314209 (2012). DOI: 10.1088/0953-8984/24/31/314209.
- [148] F. C. Bocquet, Y.-R. Lin, M. Franke, N. Samiseresht, S. Parhizkar, S. Soubatch, T.-L. Lee, C. Kumpf, and F. S. Tautz. Data used in: “Surfactant-mediated epitaxial growth of single-layer graphene in an unconventional orientation on SiC”. Jülich DATA. 2020. DOI: 10.26165/JUELICH-DATA/VGEHRD.
- [149] H. Yin, M. Hutter, C. Wagner, F. S. Tautz, F. C. Bocquet, and C. Kumpf. Data used in: “Epitaxial growth of mono- and (twisted) multilayer graphene on SiC(0001)”. Jülich DATA. 2025. DOI: 10.26165/JUELICH-DATA/F1JRQW.
- [150] C. Virojanadara, M. Syväjarvi, R. Yakimova, L. I. Johansson, A. A. Zakharov, and T. Balasubramanian. “Homogeneous large-area graphene layer growth on 6H-SiC(0001)”. *Physical Review B* **78**, 245403 (2008). DOI: 10.1103/PhysRevB.78.245403.
- [151] R. B. Woodward and R. Hoffmann. “Stereochemistry of electrocyclic reactions.” *J. Am. Chem. Soc.* **87**, 395–397 (1965). DOI: 10.1021/ja01080a054.

## Bibliography

- [152] K. Fukui. “Role of frontier orbitals in chemical reactions.” *Science* **218**, 747–754 (1982). DOI: 10.1126/science.218.4574.747.
- [153] J. Itatani, J. Levesque, D. Zeidler, H. Niikura, H. Pépin, J. C. Kieffer, P. B. Corkum, and D. M. Villeneuve. “Tomographic imaging of molecular orbitals.” *Nature* **432**, 867–871 (2004). DOI: 10.1038/nature03183.
- [154] J. Repp, G. Meyer, S. M. Stojković, A. Gourdon, and C. Joachim. “Molecules on insulating films: scanning-tunneling microscopy imaging of individual molecular orbitals.” *Phys. Rev. Lett.* **94**, 026803 (2005). DOI: 10.1103/PhysRevLett.94.026803.
- [155] M. Meckel, D. Comtois, D. Zeidler, A. Staudte, D. Pavičić, H. C. Bandulet, H. Pépin, J. C. Kieffer, R. Dörner, D. M. Villeneuve, and P. B. Corkum. “Laser-induced electron tunneling and diffraction.” *Science* **320**, 1478–1482 (2008). DOI: 10.1126/science.1157980.
- [156] T. L. Cocker, D. Peller, P. Yu, J. Repp, and R. Huber. “Tracking the ultrafast motion of a single molecule by femtosecond orbital imaging.” *Nature* **539**, 263–267 (2016). DOI: 10.1038/nature19816.
- [157] M. Wießner, D. Hauschild, C. Sauer, V. Feyer, A. Schöll, and F. Reinert. “Complete determination of molecular orbitals by measurement of phase symmetry and electron density.” *Nat. Commun.* **5**, 4156 (2014). DOI: 10.1038/ncomms5156.
- [158] D. Lüftner, T. Ules, E. M. Reinisch, G. Koller, S. Soubatch, F. S. Tautz, M. G. Ramsey, and P. Puschnig. “Imaging the wave functions of adsorbed molecules.” *Proc. Natl. Acad. Sci. U.S.A.* **111**, 605–610 (2014). DOI: 10.1073/pnas.1315716110.
- [159] S. Weiß, D. Lüftner, T. Ules, E. M. Reinisch, H. Kaser, A. Gottwald, M. Richter, S. Soubatch, G. Koller, M. G. Ramsey, F. S. Tautz, and P. Puschnig. “Exploring three-dimensional orbital imaging with energy-dependent photoemission tomography.” *Nat. Commun.* **6**, 8287 (2015). DOI: 10.1038/ncomms9287.
- [160] A. Stolow, A. E. Bragg, and D. M. Neumark. “Femtosecond time-resolved photoelectron spectroscopy.” *Chem. Rev.* **104**, 1719–1758 (2004). DOI: 10.1021/cr020683w.
- [161] A. von Conta, A. Tehlar, A. Schletter, Y. Arasaki, K. Takatsuka, and H. J. Wörner. “Conical-intersection dynamics and ground-state chemistry probed by extreme-ultraviolet time-resolved photoelectron spectroscopy.” *Nat. Commun.* **9**, 3162 (2018). DOI: 10.1038/s41467-018-05292-4.
- [162] C. Z. Bisgaard, O. J. Clarkin, G. Wu, A. M. D. Lee, O. Gessner, C. C. Hayden, and A. Stolow. “Time-resolved molecular frame dynamics of fixed-in-space CS<sub>2</sub> molecules.” *Science* **323**, 1464–1468 (2009). DOI: 10.1126/science.1169183.

- [163] L. Holmegaard, J. L. Hansen, L. Kalhøj, S. L. Kragh, H. Stapelfeldt, F. Filsinger, J. Küpper, G. Meijer, D. Dimitrovski, M. Abu-samha, C. P. J. Martiny, and L. B. Madsen. “Photoelectron angular distributions from strong-field ionization of oriented molecules.” *Nat. Phys.* **6**, 428–432 (2010). DOI: 10.1038/nphys1666.
- [164] A. Trabatttoni, J. Wiese, U. De Giovannini, J.-F. Olivieri, T. Mullins, J. Onvlee, S.-K. Son, B. Frusteri, A. Rubio, S. Trippel, and J. Küpper. “Setting the photoelectron clock through molecular alignment.” *Nat. Commun.* **11**, 2546 (2020). DOI: 10.1038/s41467-020-16270-0.
- [165] C. Seidel, C. Awater, X. D. Liu, R. Ellerbrake, and H. Fuchs. “A combined STM, LEED and molecular modelling study of PTCDA grown on Ag(110).” *Surface Science* **371**, 123–130 (1997). DOI: 10.1016/S0039-6028(96)00981-8.
- [166] J. Ziroff, F. Forster, A. Schöll, P. Puschnig, and F. Reinert. “Hybridization of organic molecular orbitals with substrate states at interfaces: PTCDA on silver.” *Phys. Rev. Lett.* **104**, 233004 (2010). DOI: 10.1103/PhysRevLett.104.233004.
- [167] M. Willenbockel, B. Stadtmüller, K. Schönauer, F. C. Bocquet, D. Lüftner, E. M. Reinisch, T. Ules, G. Koller, C. Kumpf, S. Soubatch, P. Puschnig, M. G. Ramsey, and F. S. Tautz. “Energy offsets within a molecular monolayer: the influence of the molecular environment”. *New Journal of Physics* **15**, 033017 (2013). DOI: 10.1088/1367-2630/15/3/033017.
- [168] Y. Zou, L. Kilian, A. Schöll, Th. Schmidt, R. Fink, and E. Umbach. “Chemical bonding of PTCDA on Ag surfaces and the formation of interface states”. *Surface Science* **600**, 1240–1251 (2006). DOI: 10.1016/j.susc.2005.12.050.
- [169] O. Bauer, G. Mercurio, M. Willenbockel, W. Reckien, C. H. Schmitz, B. Fiedler, S. Soubatch, T. Bredow, F. S. Tautz, and M. Sokolowski. “Role of functional groups in surface bonding of planar  $\pi$ -conjugated molecules”. *Physical Review B* **86**, 235431 (2012). DOI: 10.1103/PhysRevB.86.235431.
- [170] G. Mercurio, O. Bauer, M. Willenbockel, N. Fairley, W. Reckien, C. H. Schmitz, B. Fiedler, S. Soubatch, T. Bredow, M. Sokolowski, and F. S. Tautz. “Adsorption height determination of nonequivalent C and O species of PTCDA on Ag(110) using X-ray standing waves”. *Physical Review B* **87**, 045421 (2013). DOI: 10.1103/PhysRevB.87.045421.
- [171] M. Willenbockel, D. Lüftner, B. Stadtmüller, G. Koller, C. Kumpf, S. Soubatch, P. Puschnig, M. G. Ramsey, and F. S. Tautz. “The interplay between interface structure, energy level alignment and chemical bonding strength at organic–metal interfaces”. *Physical Chemistry Chemical Physics* **17**, 1530–1548 (2015). DOI: 10.1039/C4CP04595E.

## Bibliography

- [172] K. Stallberg, A. Namgalies, and U. Höfer. “Photoluminescence study of the exciton dynamics at PTCDA/noble-metal interfaces”. *Physical Review B* **99**, 125410 (2019). DOI: 10.1103/PhysRevB.99.125410.
- [173] K. Stallberg, A. Namgalies, S. Chatterjee, and U. Höfer. “Ultrafast exciton dynamics and charge transfer at PTCDA/metal interfaces”. *The Journal of Physical Chemistry C* **126**, 12728–12734 (2022). DOI: 10.1021/acs.jpcc.2c04696.
- [174] S. Maier and M. Stöhr. “Molecular assemblies on surfaces: towards physical and electronic decoupling of organic molecules”. *Beilstein Journal of Nanotechnology* **12**, 950–956 (2021). DOI: 10.3762/bjnano.12.71.
- [175] X. Yang, I. Krieger, D. Lüftner, S. Weiß, T. Heepenstrick, M. Hollerer, P. Hurdax, G. Koller, M. Sokolowski, P. Puschnig, M. G. Ramsey, F. S. Tautz, and S. Soubatch. “On the decoupling of molecules at metal surfaces.” *Chem. Commun.* **54**, 9039–9042 (2018). DOI: 10.1039/C8CC03334J.
- [176] M. Hollerer, D. Lüftner, P. Hurdax, T. Ules, S. Soubatch, F. S. Tautz, G. Koller, P. Puschnig, M. Sterrer, and M. G. Ramsey. “Charge transfer and orbital level alignment at inorganic/organic interfaces: the role of dielectric interlayers”. *ACS Nano* **11**, 6252–6260 (2017). DOI: 10.1021/acsnano.7b02449.
- [177] X. H. Qiu, G. V. Nazin, and W. Ho. “Vibrationally resolved fluorescence excited with submolecular precision”. *Science* **299**, 542–546 (2003). DOI: 10.1126/science.1078675.
- [178] T. Miyamachi, M. Gruber, V. Davesne, M. Bowen, S. Boukari, L. Joly, F. Scheurer, G. Rogez, T. K. Yamada, P. Ohresser, E. Beaurepaire, and W. Wulfhekel. “Robust spin crossover and memristance across a single molecule”. *Nature Communications* **3**, 938 (2012). DOI: 10.1038/ncomms1940.
- [179] F. Schulz, R. Drost, S. K. Hämäläinen, and P. Liljeroth. “Templated self-assembly and local doping of molecules on epitaxial hexagonal boron nitride”. *ACS Nano* **7**, 11121–11128 (2013). DOI: 10.1021/nn404840h.
- [180] C. Brülke, T. Heepenstrick, I. Krieger, B. Wolff, X. Yang, A. Shamsadindlou, S. Weiß, F. C. Bocquet, F. S. Tautz, S. Soubatch, and M. Sokolowski. “Quantitative analysis of the electronic decoupling of an organic semiconductor molecule at a metal interface by a monolayer of hexagonal boron nitride”. *Physical Review B* **99**, 121404 (2019). DOI: 10.1103/PhysRevB.99.121404.
- [181] A. Kumar, K. Banerjee, and P. Liljeroth. “Molecular assembly on two-dimensional materials”. *Nanotechnology* **28**, 082001 (2017). DOI: 10.1088/1361-6528/aa564f.
- [182] J. M. MacLeod and F. Rosei. “Molecular self-assembly on graphene”. *Small* **10**, 1038–1049 (2014). DOI: 10.1002/smll.201301982.

- [183] A. Riss, S. Wickenburg, L. Z. Tan, H.-Z. Tsai, Y. Kim, J. Lu, A. J. Bradley, M. M. Ugeda, K. L. Meaker, K. Watanabe, T. Taniguchi, A. Zettl, F. R. Fischer, S. G. Louie, and M. F. Crommie. “Imaging and tuning molecular levels at the surface of a gated graphene device”. *ACS Nano* **8**, 5395–5401 (2014). DOI: 10.1021/nn501459v.
- [184] N. Krane, C. Lotze, G. Reeht, L. Zhang, A. L. Briseno, and K. J. Franke. “High-resolution vibronic spectra of molecules on molybdenum disulfide allow for rotamer identification”. *ACS Nano* **12**, 11698–11703 (2018). DOI: 10.1021/acsnano.8b07414.
- [185] R. Forcker, D. Kasemann, T. Dienel, C. Wagner, R. Franke, K. Müllen, and T. Fritz. “Electronic decoupling of aromatic molecules from a metal by an atomically thin organic spacer”. *Advanced Materials* **20**, 4450–4454 (2008). DOI: 10.1002/adma.200801112.
- [186] K. J. Franke, G. Schulze, N. Henningsen, I. Fernández-Torrente, J. I. Pascual, S. Zarwell, K. Rück-Braun, M. Cobian, and N. Lorente. “Reducing the molecule-substrate coupling in C<sub>60</sub>-based nanostructures by molecular interactions”. *Physical Review Letters* **100**, 036807 (2008). DOI: 10.1103/PhysRevLett.100.036807.
- [187] Z. Liu, K. Sun, X. Li, L. Li, H. Zhang, and L. Chi. “Electronic decoupling of organic layers by a self-assembled supramolecular network on Au(111)”. *The Journal of Physical Chemistry Letters* **10**, 4297–4302 (2019). DOI: 10.1021/acs.jpcllett.9b01167.
- [188] A. Rastgoo-Lahrood, J. Björk, M. Lischka, J. Eichhorn, S. Kloft, M. Fritton, T. Strunskus, D. Samanta, M. Schmittel, W. M. Heckl, and M. Lackinger. “Post-synthetic decoupling of on-surface-synthesized covalent nanostructures from Ag(111)”. *Angewandte Chemie International Edition* **55**, 7650–7654 (2016). DOI: 10.1002/anie.201600684.
- [189] S. Gärtner, B. Fiedler, O. Bauer, A. Marele, and M. M. Sokolowski. “Lateral ordering of PTCDA on the clean and the oxygen pre-covered Cu(100) surface investigated by scanning tunneling microscopy and low energy electron diffraction.” *Beilstein J. Org. Chem.* **10**, 2055–2064 (2014). DOI: 10.3762/bjoc.10.213.
- [190] M. Böhlinger, W. -D. Schneider, K. Glöckler, E. Umbach, and R. Berndt. “Adsorption site determination of PTCDA on Ag(110) by manipulation of adatoms”. *Surface Science* **419**, L95–L99 (1998). DOI: 10.1016/S0039-6028(98)00733-X.
- [191] K. Glöckler, C. Seidel, A. Soukopp, M. Sokolowski, E. Umbach, M. Böhlinger, R. Berndt, and W.-D. Schneider. “Highly ordered structures and submolecular scanning tunnelling microscopy contrast of PTCDA and DM-PBDCI monolayers on Ag(111) and Ag(110)”. *Surface Science* **405**, 1–20 (1998). DOI: 10.1016/S0039-6028(97)00888-1.

## Bibliography

- [192] C. Seidel, J. Poppensieker, and H. Fuchs. “Real-time monitoring of phase transitions of vacuum deposited organic films by molecular beam deposition LEED”. *Surface Science* **408**, 223–231 (1998). DOI: 10.1016/S0039-6028(98)00231-3.
- [193] F. S. Tautz, S. Sloboshanin, J. A. Schaefer, R. Scholz, V. Shklover, M. Sokolowski, and E. Umbach. “Vibrational properties of ultrathin PTCDA films on Ag(110)”. *Physical Review B* **61**, 16933–16947 (2000). DOI: 10.1103/PhysRevB.61.16933.
- [194] D. Braun, A. Schirmeisen, and H. Fuchs. “Molecular growth and sub-molecular resolution of a thin multilayer of PTCDA on Ag(110) observed by scanning tunneling microscopy”. *Surface Science* **575**, 3–11 (2005). DOI: 10.1016/j.susc.2004.10.032.
- [195] M. Wießner, D. Hauschild, A. Schöll, F. Reinert, V. Feyer, K. Winkler, and B. Krömker. “Electronic and geometric structure of the PTCDA/Ag(110) interface probed by angle-resolved photoemission”. *Physical Review B* **86**, 045417 (2012). DOI: 10.1103/PhysRevB.86.045417.
- [196] R.N. Lee and H.E. Farnsworth. “LEED studies of adsorption on clean (100) copper surfaces”. *Surface Science* **3**, 461–479 (1965). DOI: 10.1016/0039-6028(65)90026-9.
- [197] G. Ertl. “Untersuchung von Oberflächenreaktionen mittels Beugung langsamer Elektronen (LEED): I. Wechselwirkung von O<sub>2</sub> und N<sub>2</sub>O mit (110)-, (111)- und (100)-Kupfer-Oberflächen”. *Surface Science* **6**, 208–232 (1967). DOI: 10.1016/0039-6028(67)90005-2.
- [198] A. Oustry, L. Lafourcade, and A. Escaut. “Étude par del de l’interaction de l’oxygène avec les faces (110), (100) et (111) de monocristaux de cuivre”. *Surface Science* **40**, 545–554 (1973). DOI: 10.1016/0039-6028(73)90143-X.
- [199] L. McDonnell and D.P. Woodruff. “A LEED study of oxygen adsorption on copper (100) and (111) surfaces”. *Surface Science* **46**, 505–536 (1974). DOI: 10.1016/0039-6028(74)90322-7.
- [200] P. Hofmann, R. Unwin, W. Wyrobisch, and A.M. Bradshaw. “The adsorption and incorporation of oxygen on Cu(100) at  $T \geq 300$  K”. *Surface Science* **72**, 635–644 (1978). DOI: 10.1016/0039-6028(78)90351-5.
- [201] S. Kono, S. M. Goldberg, N. F. T. Hall, and C. S. Fadley. “Azimuthal Anisotropy in core-level X-ray photoemission from  $c(2 \times 2)$  oxygen on Cu(001): experiment and single-scattering theory”. *Physical Review Letters* **41**, 1831–1835 (1978). DOI: 10.1103/PhysRevLett.41.1831.
- [202] J. H. Onuferko and D. P. Woodruff. “Leed structural study of the adsorption of oxygen on Cu {100} surfaces”. *Surface Science* **95**, 555–570 (1980). DOI: 10.1016/0039-6028(80)90195-8.

- [203] D. J. Godfrey and D. P. Woodruff. "A low energy ion scattering study of the adsorption of oxygen on Cu{100} surfaces". *Surface Science* **105**, 459–468 (1981). DOI: 10.1016/0039-6028(81)90011-X.
- [204] H. Richter and U. Gerhardt. "Adsorption sites of oxygen on Cu(001) and Ni(001) determined from the shape of the low-energy electron-diffraction spots". *Physical Review Letters* **51**, 1570–1572 (1983). DOI: 10.1103/PhysRevLett.51.1570.
- [205] R. Mayer, Chun-Si Zhang, and K. G. Lynn. "Evidence for the absence of a  $c(2\times 2)$  superstructure for oxygen on Cu(100)". *Physical Review B* **33**, 8899–8902 (1986). DOI: 10.1103/PhysRevB.33.8899.
- [206] M. Wuttig, R. Franchy, and H. Ibach. "Oxygen on Cu(100): a new type of an adsorbate induced reconstruction". *Journal of Electron Spectroscopy and Related Phenomena* **44**, 317–323 (1987). DOI: 10.1016/0368-2048(87)87032-9.
- [207] H. C. Zeng, R. A. McFarlane, R. N. S. Sodhi, and K. A. R. Mitchell. "LEED crystallographic studies for the chemisorption of oxygen on the (100) surface of copper". *Canadian Journal of Chemistry* **66**, 2054–2062 (1988). DOI: 10.1139/v88-330.
- [208] M. Wuttig, R. Franchy, and H. Ibach. "Oxygen on Cu(100) – a case of an adsorbate induced reconstruction." *Surf. Sci.* **213**, 103–136 (1989). DOI: 10.1016/0039-6028(89)90254-9.
- [209] H. C. Zeng, R. A. McFarlane, and K. A. R. Mitchell. "A LEED crystallographic investigation of some missing row models for the Cu(100)- $(2\sqrt{2}\times\sqrt{2})R45^\circ$ -O surface structure". *Surf. Sci.* **208**, L7–L14 (1989). DOI: 10.1016/0039-6028(89)90023-X.
- [210] M. C. Asensio, M. J. Ashwin, A. L. D. Kilcoyne, D. P. Woodruff, A. W. Robinson, Th. Lindner, J. S. Somers, D. E. Ricken, and A. M. Bradshaw. "The structure of oxygen adsorption phases on Cu(100)". *Surface Science* **236**, 1–14 (1990). DOI: 10.1016/0039-6028(90)90755-W.
- [211] F. Jensen, F. Besenbacher, E. Laegsgaard, and I. Stensgaard. "Dynamics of oxygen-induced reconstruction of Cu(100) studied by scanning tunneling microscopy". *Physical Review B* **42**, 9206–9209 (1990). DOI: 10.1103/PhysRevB.42.9206.
- [212] H. C. Zeng and K. A. R. Mitchell. "Further LEED investigations of missing row models for the Cu(100)- $(2\sqrt{2}\times\sqrt{2})R45^\circ$ -O surface structure". *Surface Science* **239**, L571–L578 (1990). DOI: [https://doi.org/10.1016/0039-6028\(90\)90220-3](https://doi.org/10.1016/0039-6028(90)90220-3).
- [213] M. Sotro. "Oxygen induced reconstruction of ( $h11$ ) and (100) faces of copper". *Surface Science* **260**, 235–244 (1992). DOI: 10.1016/0039-6028(92)90037-7.

## Bibliography

- [214] F. Besenbacher and J. K. Nørskov. “Oxygen chemisorption on metal surfaces: General trends for Cu, Ni and Ag”. *Progress in Surface Science* **44**, 5–66 (1993). DOI: 10.1016/0079-6816(93)90006-H.
- [215] F. M. Leibsle. “STM studies of oxygen-induced structures and nitrogen coadsorption on the Cu(100) surface: evidence for a one-dimensional oxygen reconstruction and reconstructive interactions”. *Surface Science* **337**, 51–66 (1995). DOI: 10.1016/0039-6028(95)00519-6.
- [216] W. Liu, K. C. Wong, H. C. Zeng, and K. A. R. Mitchell. “What determines the structures formed by oxygen at low index surfaces of copper?” *Progress in Surface Science* **50**, 247–257 (1995). DOI: 10.1016/0079-6816(95)00059-3.
- [217] T. Fujita, Y. Okawa, Y. Matsumoto, and K.-I. Tanaka. “Phase boundaries of nanometer scale  $c(2 \times 2)$ -O domains on the Cu(100) surface”. *Physical Review B* **54**, 2167–2174 (1996). DOI: 10.1103/PhysRevB.54.2167.
- [218] M. Kittel, M. Polcik, R. Terborg, J.-T. Hoeft, P. Baumgärtel, A.M. Bradshaw, R.L. Toomes, J.-H. Kang, D.P. Woodruff, M. Pascal, C.L.A. Lamont, and E. Rotenberg. “The structure of oxygen on Cu(100) at low and high coverages”. *Surface Science* **470**, 311–324 (2001). DOI: 10.1016/S0039-6028(00)00873-6.
- [219] J. A. Eastman, P. H. Fuoss, L. E. Rehn, P. M. Baldo, G.-W. Zhou, D. D. Fong, and L. J. Thompson. “Early-stage suppression of Cu(001) oxidation”. *Applied Physics Letters* **87**, 051914 (2005). DOI: 10.1063/1.2005396.
- [220] H. Iddir, D. D. Fong, P. Zapol, P. H. Fuoss, L. A. Curtiss, G.-W. Zhou, and J. A. Eastman. “Order-disorder phase transition of the Cu(001) surface under equilibrium oxygen pressure”. *Phys. Rev. B* **76**, 241404(R) (2007). DOI: 10.1103/PhysRevB.76.241404.
- [221] K. Lahtonen, M. Hirsimäki, M. Lampimäki, and M. Valden. “Oxygen adsorption-induced nanostructures and island formation on Cu{100}: Bridging the gap between the formation of surface confined oxygen chemisorption layer and oxide formation”. *The Journal of Chemical Physics* **129**, 124703 (2008). DOI: 10.1063/1.2980347.
- [222] X. Duan, O. Warschkow, A. Soon, B. Delley, and C. Stampfl. “Density functional study of oxygen on Cu(100) and Cu(110) surfaces.” *Phys. Rev. B* **81**, 075430 (2010). DOI: 10.1103/PhysRevB.81.075430.
- [223] M. Li, M. T. Curnan, W. A. Saidi, and J. C. Yang. “Uneven oxidation and surface reconstructions on stepped Cu(100) and Cu(110)”. *Nano Letters* **22**, 1075–1082 (2022). DOI: 10.1021/acs.nanolett.1c04124.

- [224] H. Mönig, M. Todorović, M. Z. Baykara, T. C. Schwendemann, L. Rodrigo, E. I. Altman, R. Pérez, and U. D. Schwarz. “Understanding scanning tunneling microscopy contrast mechanisms on metal oxides: A case study”. *ACS Nano* **7**, 10233–10244 (2013). DOI: 10.1021/nn4045358.
- [225] S. J. Tjung, Q. Zhang, J. J. Repicky, S. F. Yuk, X. Nie, N. M. Santagata, A. Asthagiri, and J. A. Gupta. “STM and DFT studies of CO<sub>2</sub> adsorption on O-Cu(100) surface”. *Surface Science* **679**, 50–55 (2019). DOI: 10.1016/j.susc.2018.08.013.
- [226] X. Yang. “Investigating the interaction between  $\pi$ -conjugated organic molecules and metal surfaces with photoemission tomography”. PhD thesis. RWTH Aachen University, 2021. URL: <https://juser.fz-juelich.de/record/902299>.
- [227] S. Wenzel and M. Stettner. Peter-Grünberg-Institut 3, Forschungszentrum Jülich GmbH. *Private Communications*.
- [228] F. S. Tautz. “Structure and bonding of large aromatic molecules on noble metal surfaces: The example of PTCDA”. *Progress in Surface Science* **82**, 479–520 (2007). DOI: 10.1016/j.progsurf.2007.09.001.
- [229] D. Shin, Z. Wei, H. Shim, and G. Lee. “Adsorption and ordering of PTCDA on various reconstruction surfaces of In/Si(111)”. *Applied Surface Science* **372**, 87–92 (2016). DOI: 10.1016/j.apsusc.2016.03.033.
- [230] D. Brandstetter, X. Yang, D. Lüftner, F. S. Tautz, and P. Puschnig. “kMap.py: A Python program for simulation and data analysis in photoemission tomography”. *Computer Physics Communications* **263**, 107905 (2021). DOI: 10.1016/j.cpc.2021.107905.
- [231] P. Puschnig. “Molekülorbital-Datenbank”. Universität Graz. URL: <https://homepage.uni-graz.at/de/peter.puschnig/research-1/> (visited on 08/23/2025).
- [232] P. M. Echenique, R. Berndt, E. V. Chulkov, Th. Fauster, A. Goldmann, and U. Höfer. “Decay of electronic excitations at metal surfaces.” *Surf. Sci. Rep.* **52**, 219–317 (2004). DOI: 10.1016/j.surfrep.2004.02.002.
- [233] X. Cui, C. Wang, A. Argondizzo, S. Garrett-Roe, B. Gumhalter, and H. Petek. “Transient excitons at metal surfaces.” *Nat. Phys.* **10**, 505–509 (2014). DOI: 10.1038/nphys2981.
- [234] M. Dantus, R. M. Bowman, and A. H. Zewail. “Femtosecond laser observations of molecular vibration and rotation”. *Nature* **343**, 737–739 (1990). DOI: 10.1038/343737A0.
- [235] H. Yin. “Investigation of 2D materials using low energy electron microscopy (LEEM)”. PhD thesis. RWTH Aachen University, 2025. Defended but not yet published.
- [236] S. Tautz, U. Höfer, R. Huber, and P. Puschnig. “Orbital Cinema”. URL: <https://orbital-cinema.eu/> (visited on 09/07/2025).

## Bibliography

- [237] B. Stadtmüller, T. Sueyoshi, G. Kichin, I. Kröger, S. Soubatch, R. Temirov, F. S. Tautz, and C. Kumpf. “Commensurate registry and chemisorption at a hetero-organic interface”. *Physical Review Letters* **108**, 106103 (2012). DOI: 10.1103/PhysRevLett.108.106103.
- [238] “Twenty-nine groups backed by ERC Synergy Grants to tackle complex research questions”. European Research Council. URL: <https://erc.europa.eu/news/erc-2022-synergy-grants-results> (visited on 09/07/2025).
- [239] H. E. Farnsworth, R. E. Schlier, T. H. George, and R. M. Burger. “Ion bombardment-cleaning of germanium and titanium as determined by low-energy electron diffraction”. *Journal of Applied Physics* **26**, 252–253 (1955). DOI: 10.1063/1.1721972.
- [240] H. E. Farnsworth, R. E. Schlier, T. H. George, and R. M. Burger. “Application of the ion bombardment cleaning method to titanium, germanium, silicon, and nickel as determined by low-energy electron diffraction”. *Journal of Applied Physics* **29**, 1150–1161 (1958). DOI: 10.1063/1.1723393.
- [241] R. Van Gastel, E. Somfai, S. B. Van Albada, W. Van Saarloos, and J. W. M. Frenken. “Nothing moves a surface: vacancy mediated surface diffusion”. *Physical Review Letters* **86**, 1562–1565 (2001). DOI: 10.1103/PhysRevLett.86.1562.

# List of Own Publications

- A. Adamkiewicz, **M. Raths**, M. Stettner, M. Theilen, L. Münster, S. Wenzel, M. Hutter, S. Soubatch, C. Kumpf, F. C. Bocquet, R. Wallauer, F. S. Tautz, and U. Höfer. “Coherent and Incoherent Excitation Pathways in Time-Resolved Photoemission Orbital Tomography of CuPc/Cu(001)-2O.” *The Journal of Physical Chemistry C* **127**, 20411 (2023).
- C. Herrmann, **M. Raths**, C. Kumpf, and K. L. Kavanagh. “Rotational epitaxy of h-BN on Cu(110).” *Surface Science* **721**, 122080 (2022).
- Y.-R. Lin, M. Franke, S. Parhizkar, **M. Raths**, V. W.-z. Yu, T.-L. Lee, S. Soubatch, V. Blum, F. S. Tautz, C. Kumpf, and François C. Bocquet. “Boron nitride on SiC(0001).” *Physical Review Materials* **6**, 064002 (2022).
- **M. Raths\***, C. Schott\*, J. Knippertz, M. Franke, Y.-R. Lin, A. Haags, M. Aeschlimann, C. Kumpf, and B. Stadtmüller. “Growth, domain structure, and atomic adsorption sites of hBN on the Ni(111) surface.” *Physical Review Materials* **5**, 094001 (2021).
- R. Wallauer, **M. Raths**, K. Stallberg, L. Münster, D. Brandstetter, X. Yang, J. Güdde, P. Puschnig, S. Soubatch, C. Kumpf, F. C. Bocquet, F. S. Tautz, and U. Höfer. “Tracing orbital images on ultrafast time scales.” *Science* **371**, 1056 (2021).
- J. Felter, **M. Raths**, M. Franke, and C. Kumpf. “In-situ study of two-dimensional dendritic growth of hexagonal boron nitride.” *2D Materials* **6**, 045005 (2019).

---

\*These authors contributed equally.



# Acknowledgments

This work would not have been possible without the assistance and contribution of many people. At this point, I would like to express my gratitude to everyone who has supported me in different ways during my doctoral studies and beyond. While it is not possible to mention everyone individually, I would like to take this opportunity to name a few of those who helped me along my journey and express my gratitude for their invaluable support.

First and foremost, I am deeply grateful to my doctoral supervisor, Prof. Dr. Christian Kumpf, for his outstanding supervision, invaluable advice, and continuous support during my master's and PhD studies. His warm and open manner, encouraging attitude, and constructive feedback have been a constant source of motivation. I particularly appreciate his patience and his curiosity to understand every detail of my work, which always made me feel supported and reassured. I am thankful for the trust he placed in me – for example, by sending me alone to an international conference at the beginning of my PhD, which gave me confidence and valuable experience. Whenever I encountered difficulties, he was always available to discuss problems and provide guidance, for which I am sincerely thankful.

I would also like to express my appreciation to Prof. Dr. Joachim Mayer for kindly agreeing to serve as the second supervisor and for taking the time to co-referee both this thesis and my master's thesis.

My thanks go to Janina Felter for her supervision during my master's thesis and her support during the first months of my PhD. You did an excellent job preparing me for all the troubleshooting that the LEEM instrument had in store for me. I greatly enjoyed the time we spent together in the lab, in the work café, and on our trips to Marburg, especially our walks along the *Grimm-Dich-Pfad*.

I would also like to thank François Posseik, who generously shared his time, knowledge, and enthusiasm with me. Thank you for welcoming me into your lab and encouraging me in your kind and supportive way.

My thanks go to Hao Yin for his company, reliability, and support during his time as my master's student at the LEEM and beyond. I am happy to see the LEEM instrument in such capable hands, and I feel honored by the deep gratitude you have expressed toward me as your supervisor.

I am deeply grateful to my fellow doctoral and postdoctoral colleagues, especially Anja Meier, Mark Hutter, Jose Martinez Castro, Sabine Wenzel, You-Ron Lin, and Monja Stettner, for the time we shared at work, conferences, and at after-work dinners, for the more or less spontaneous carpools, and for proofreading first drafts of my thesis. Your friendship and support have made my time as PhD student both enjoyable and truly memorable.

## *Acknowledgments*

I would like to thank the Elmitec team, especially Helder Marchetto, Florian Schütz, and Torsten Franz, for their fast and thorough support in dealing with all the small and big challenges the LEEM instrument had in store for me. It means a great deal to know that help was always just one call away.

My thanks also go to Ulrich Höfer and his group for including me in the time-resolved POT experiments. I am especially grateful to Robert Wallauer and Klaus Stallberg for welcoming me into their lab and for many discussions on the experimental setup and data analysis. I hope I was able to support you as best as I could. I am also very grateful for the warm welcome from the Marburg PhD students, especially Alexa Adamkiewicz and Marleen Axt, and thank them for inviting me to their barbecues and game nights.

I thank Prof. Dr. Stefan Tautz for giving me the opportunity to conduct my PhD research at PGI-3. I am especially grateful to him for including me in the SFB project on realizing tr-POT and for his encouragement to dig into the density matrix formalism.

I would like to thank all members of the PGI-3 for creating a warm and welcoming atmosphere. I am grateful for their support in many different ways, such as lending a helping hand in the lab, discussing my data with me, and solving scientific and organizational issues.

Finally, my heartfelt thanks go to my family and my friends, who have always supported me over the years and brought fun and joy to my life. I thank my parents for their silent dedication and steady support throughout all the years of my studies. I thank my brother, Johannes, and my friends – especially Alexandra and Teresa – for their loving support and encouraging words throughout every condition of my life. Last but certainly not least, I would like to thank my boyfriend, Nils, whose incredible belief in me, constant encouragement, and loving presence have been a great source of strength throughout this journey.

# Eidesstattliche Erklärung

Miriam Elisabeth Raths

erklärt hiermit, dass diese Dissertation und die darin dargelegten Inhalte die eigenen sind und selbstständig, als Ergebnis der eigenen originären Forschung, generiert wurden.

Hiermit erkläre ich an Eides statt:

1. Diese Arbeit wurde vollständig oder größtenteils in der Phase als Doktorand dieser Fakultät und Universität angefertigt;
2. Sofern irgendein Bestandteil dieser Dissertation zuvor für einen akademischen Abschluss oder eine andere Qualifikation an dieser oder einer anderen Institution verwendet wurde, wurde dies klar angezeigt;
3. Wenn immer andere eigene- oder Veröffentlichungen Dritter herangezogen wurden, wurden diese klar benannt;
4. Wenn aus anderen eigenen- oder Veröffentlichungen Dritter zitiert wurde, wurde stets die Quelle hierfür angegeben. Diese Dissertation ist vollständig meine eigene Arbeit, mit der Ausnahme solcher Zitate;
5. Alle wesentlichen Quellen von Unterstützung wurden benannt;
6. Wenn immer ein Teil dieser Dissertation auf der Zusammenarbeit mit anderen basiert, wurde von mir klar gekennzeichnet, was von anderen und was von mir selbst erarbeitet wurde;
7. Ein Teil oder Teile dieser Arbeit wurden zuvor veröffentlicht und zwar in:
  - R. Wallauer, M. Raths, K. Stallberg, L. Münster, D. Brandstetter, X. Yang, J. Güdde, P. Puschnig, S. Soubatch, C. Kumpf, F. C. Bocquet, F. S. Tautz, and U. Höfer. “Tracing orbital images on ultrafast time scales.” *Science* **371**, 1056 (2021).

Monheim am Rhein, 3. April 2026

Miriam Elisabeth Raths



Band / Volume 111

**Characteristics of plastically deformed *fcc* and *bcc* High-Entropy Alloys**

T. Meenen (2025), x, 115 pp

ISBN: 978-3-95806-820-9

Band / Volume 112

**Software-Configurable Analog-To-Digital Converters for Configurable Pulse Detection**

L. Krystofiak (2025), xvii, 113 pp, xxix

ISBN: 978-3-95806-826-1

Band / Volume 113

**Development of Superparamagnetic Based Biological Sensor for the Detection of *Brucella* DNA Using Frequency Mixing Magnetic Detection**

A. Abuawad (2025), X, 129 pp

ISBN: 978-3-95806-836-0

Band / Volume 114

**A System for the Cryogenic Power Management of Quantum Computing Electronics: Development, Integration, and Test**

A. R. Cabrera Galicia (2025), xxv, 110, lviii pp

ISBN: 978-3-95806-844-5

Band / Volume 115

**Investigation of 2D Materials using Low Energy Electron Microscopy (LEEM)**

H. Yin (2025) viii, 137 pp

ISBN: 978-3-95806-848-3

Band / Volume 116

**Topotactic phase transition in  $\text{La}_{0.6}\text{Sr}_{0.4}\text{CoO}_{3-\delta}$  thin films: oxygen content, dynamics and reversibility**

S. He (2025) ix, 137 pp

ISBN: 978-3-95806-868-1

Band / Volume 117

**Electrical anisotropy and shear-resistant topology in the quasi one-dimensional van-der-Waals material  $\alpha\text{-Bi}_4\text{Br}_4$**

J.K. Hofmann (2025) xv, 129 pp

ISBN: 978-3-95806-869-8

Band / Volume 118

**Spin-orbital mixing in the topological ladder of the two-dimensional metal PtTe<sub>2</sub>**

M. Qahosh (2025), ix, 170 pp

ISBN: 978-3-95806-872-8

Band / Volume 119

**Functions of SNNs constrained by biology**

A. Korcsak-Gorzo (2025), xvi, 145 pp

ISBN: 978-3-95806-876-6

Band / Volume 120

**On Scalable Integrated Charge State Tuning for Semiconductor Quantum Dot Devices**

F. A. Hader (2026), xx, 145 pp

ISBN: 978-3-95806-884-1

Band / Volume 121

**Efficient Massively Space-Time-Parallel Simulations with Adaptive Spectral Deferred Correction**

T. Saupe (2026), v, 149 pp

ISBN: 978-3-95806-886-5

Band / Volume 122

**Controlled single-molecule manipulation**

P. Kopp (2026), viii, 136 pp

ISBN: 978-3-95806-887-2

Band / Volume 123

**Growth and Excitation Dynamics of Epitaxial 2D Materials and Molecular Layers Studied by Electron and Momentum Microscopy**

M. E. Raths (2026), xvi, 161, XXIX pp

ISBN: 978-3-95806-892-6

Weitere **Schriften des Verlags im Forschungszentrum Jülich** unter  
<http://www.zb1.fz-juelich.de/verlagextern1/index.asp>



Information

Band / Volume 123

ISBN 978-3-95806-892-6

Mitglied der Helmholtz-Gemeinschaft

